SYNTHESIS OF NANOSTRUCTURED GRAPHITIC CARBONS BY IRON-CATALYZED GRAPHITIZATION OF BIOMASS

by

ROBERT DUNCAN HUNTER

A thesis submitted to the University of Birmingham for the degree of
DOCTOR OF PHILOSOPHY

School of Chemistry
College of Engineering and Physical Sciences
University of Birmingham
July 2022

ABSTRACT

Porous carbon materials have a wide range of applications, finding use as anode materials for batteries, electrocatalyst supports, supercapacitors and adsorbents for water treatment. High performance in these applications is achieved through features such as high thermal and electrical conductivity and high surface area. Therefore, considerable effort has gone into developing simple and scalable means of producing carbon materials with precise porosity as well as tailored bulk and surface structure.

Porous carbons with a high graphitic content are particularly attractive due to their high chemical stability and electronic conductivity, and a good route to make these materials is through catalytic graphitization. Here, organic precursors are combined with a metal compound, often iron, before heating in an inert atmosphere to produce iron-based nanoparticles *in situ*, which catalyze the conversion of amorphous carbon to graphitic nanostructures.

Throughout the literature, organic precursors vary widely and depending on the precursors and reaction conditions, catalytic graphitization has produced various graphitic nanostructures, however, the underlying reasons as to why some structures are preferred over others is not known. In this thesis, a systematic study of the effect of organic precursor structure is explored as a means of controlling the catalyst particle size, which has a direct effect on the porosity of the material. This study is extended to investigate a selection of nitrogen-containing, biomass-derived organic precursors and the presence of nitrogen was found to have an inhibiting effect on the iron-catalyzed graphitization process.

The precise chemical and physical nature of the catalytic species in iron-catalyzed graphitization systems is also an area of dispute. To address this, iron-catalyzed graphitization is studied *in situ* on both the bulk and nano-scale, using experimental techniques such as synchrotron X-ray diffraction and environmental transmission electron microscopy, in combination with molecular dynamics simulations to probe the underlying mechanism of graphitization.

ACKNOWLEDGEMENTS

Firstly, I would like to give a huge thanks to Dr Zoe Schnepp for giving me the opportunity to join her research group and for all the invaluable support and encouragement throughout my PhD. I would like to thank the School of Chemistry at the University of Birmingham, EPSRC, the RSC and Universitas U21 for providing funding for my work.

Within the School of Chemistry there are many other people I would like to thank. I would like to give a special mention to Professor Roy Johnston, while unfortunately we only had the chance to work together for a relatively short time, I really appreciated his support and how welcome he made me feel within his group, and I’m sure he will be fondly remembered by everyone at Birmingham. I would also like to thank Dr Phoebe Allan for stepping in to provide supervision and Dr Alessio Alexiadis for helping out with various computational problems. And of course, I am extremely grateful to everybody on Floor 5 past and present for all their help and constant entertainment over the years!

I have been very fortunate to have had the chance to collaborate with experts at some amazing research institutes around the world and there are many people I would like to thank: Dr Dmitri Zakharov for hosting me at Brookhaven National Laboratory and helping to perform some fascinating TEM experiments. Dr Brian Pauw and Dr Glen Smales for inviting me to attend the “Better with Scattering workshop” at BAM and helping to battle through lots of SAXS data. Professor Valeska Ting and Dr Jemma Rowlandson at the University of Bristol for letting me use their nitrogen sorption instrument. Dr Joaquín Ramírez-Rico, Sol Fernández-Muñoz and Dr Aleksandr Missiul for an awesome trip to the ALBA synchrotron. Dr Alex Kulak at the University

of Leeds for collecting some beautiful SEM images, and Professor Shaun Hendy and Dr Kannan Ridings at the University of Auckland for helping me to get up and running with molecular dynamics.

Finally, I would like to give a big thank you to Mary for keeping me sane over the past few years and for the endless proofreading that she has done for me to get my thesis into a presentable state!

List of abbreviations

BCC – body-centred cubic

BET – Brunauer-Emmett-Teller

CBS – circular backscatter

CCD – charge coupled device

CVD – chemical vapour deposition

DI – deionized

DMF – dimethylformamide

EA – elemental analysis

EAM – embedded atom model

ETEM – environmental transmission electron microscopy

FCC – face-centred cubic

FEG-SEM – field emission gun – scanning electron microscope

FWHM – full width at half maximum

HCP – hexagonally-close packed

ISO – International Organization for Standardization

IUPAC – International Union of Pure and Applied Chemistry

LAMMPS – large-scale atomic/molecularly massively parallel simulator

MDF – medium-density fibreboard

MEAM – modified embedded atom model

MEMS – microelectromechanical systems

MOF – metal-organic framework

MS – mass spectrometry

NLDFT – non-linear density functional theory

OVITO – open visualization tool

PXRD – powder X-ray diffraction

SAXS – small angle X-ray scattering

SEM – scanning electron microscopy/microscope

TEM – transmission electron microscopy/microscope

TGA – thermogravimetric analysis

TGA-MS – thermogravimetric analysis – mass spectrometry

THF – tetrahydrofuran

XPS – X-ray photoelectron spectroscopy

XRD – X-ray diffraction

Contents

List of figures

List of publications

Work included in this thesis

Chapter 1 – R. D. Hunter, J. Ramirez-Rico and Z. Schnepp, *J. Mater. Chem. A*, 2022, **10**, 4489-4516.

Chapter 3 - R. D. Hunter, J. L. Rowlandson, G. J. Smales, B. R. Pauw, V. P. Ting, A. Kulak and Z. Schnepp, *Mater. Adv.*, 2020, **1**, 3281–3291.

Related work not included in this thesis

M. S. Chambers, R. D. Hunter, M. J. Hollamby, B. R. Pauw, A. J. Smith, T. Snow, A. E. Danks and Z. Schnepp, *Inorg. Chem.,* 2022, **61**, 6742-6749.

R. D. Hunter, J. Davies, S. J. A. Hérou, A. Kulak and Z. Schnepp, *Philos. Trans. R. Soc., A*, 2021, **379**, 20200336.

D. C. Fletcher, R. D. Hunter, W. Xia, G. J. Smales, B. R. Pauw, E. Blackburn, A. Kulak, H. Xin and Z. Schnepp, *J. Mater. Chem.,* 2019, **7**, 19506-19512.

Chapter 1 – Introduction

1.1 Introduction

Research into new materials has the potential to contribute to the development of sustainable technological processes, combatting our overreliance on fossil fuels. One such material is nanostructured graphitic carbon, which boasts a wide variety of useful properties that include high chemical stability, large accessible surface areas and high thermal and electronic conductivity. This makes nanostructured graphitic carbon materials valuable in technologies such as batteries,[1] fuel cells[2] and separation science,[3] where they can be employed to replace traditional, less abundant materials, leading to more efficient and eco-friendly production processes.

Since their discovery, considerable research has been conducted into how to develop nanostructured graphitic carbon materials, and numerous new production methods have been established as a result. The first reported synthesis of carbon nanotubes, for example, was carried out by Iijima using arc discharge,[4] a method in which an electrical arc is used to vaporize a solid carbon precursor that is then deposited in the form of graphitic carbon nanostructures. A similar principle is used in laser ablation, first reported by Guo *et al*, in which a laser beam is used instead of a high temperature plasma.[5] However, these methods require an extremely high amount of energy and are therefore not appropriate for industrial processes. The past few years have seen a move towards research into cheaper, scalable and more environmentally friendly methods of producing nanostructured graphitic carbon materials that can be adapted to suit a particular requirement.

This thesis focuses on the method of catalytic graphitization, which is described by IUPAC as “the transformation of non-graphitic carbon into graphite by heat treatment in the presence of certain metals or minerals".[6] While various transition metals have been used to promote catalytic graphitization processes, this work primarily focuses on the use of iron, due to its wide availability and low toxicity. Iron-catalyzed graphitization methods have been reported using a range of organic precursors, including cheap and widely available biomass products such as sawdust. Therefore, iron-catalyzed graphitization may be viewed as an attractive route to producing nanostructured graphitic carbon materials from both an environmental and economic perspective. In addition, because of the wide variety of precursors available, there is potential for this method to be adapted to suit a particular need.

This introduction chapter examines the current field of research into iron-catalyzed graphitization, starting with a brief introduction to the key carbon structures and the current applications in which they are employed. It then compares iron-catalyzed graphitization with other methods of synthesizing nanostructured graphitic carbons, before evaluating the wide range of organic precursors that have been employed in the literature, focusing on the advantages and disadvantages of each. Finally, the chapter investigates the current challenges facing the iron-catalyzed graphitization method, looking particularly at the limitations of the current understanding of the mechanistic aspects of graphitization, with a view to outlining where research in this field might progress.

1.2 Key carbon structures

Porous carbon structures may have an amorphous and/or graphitic composition. Amorphous carbons contain a mixture of sp^2 and sp^3 hybridized carbon atoms and display limited long-range order throughout the structure.[7] Their surface consists of many reactive, dangling π-bonds, which leads to decreased stability.[8]

Graphitic carbons are often more desirable due to their greater electronic conductivity and higher stability.[9] They contain a significant degree of sp^2 hybridized carbon atoms, arranged in hexagonal layers, and include ideal structures such as graphite. The term “graphitic carbon” is applied to describe carbon structures that consist of a similar interplanar spacing to graphite, which results in a characteristic peak in PXRD patterns.[10] Therefore, nanostructured carbons such as fullerenes – the discovery of which earned Kroto, Curl and Smalley the 1996 Nobel Prize for chemistry[11] – and carbon nanotubes – discovered by Iijima in 1991[4] – can also be classified as having a graphitic composition due to their high sp^2 carbon content and because the multi-walled variants display a similar interlayer spacing to graphite. Further graphitic carbons that have been widely reported in the literature include onion- or shell-like carbons, which consist of roughly spherical layers of graphitic carbon surrounding a central core that can either be hollow or contain a nanoparticle.

Along with graphitic and amorphous carbons, intermediate carbon nanostructures referred to as “turbostratic carbons” are commonly reported. This class of carbon material also consists of graphitic layers but with less long-range ordering than graphitic carbons. Rather than the perfect stacking displayed in graphite, turbostratic carbons may exhibit random translation of the graphitic layers along with rotational disorder, resulting in areas of larger interlayer spacing, as shown in figure 1.1.[12] This can be observed in PXRD as a broadening and/or a small shift to a lower 2θ value of the characteristic (002) reflection peak.

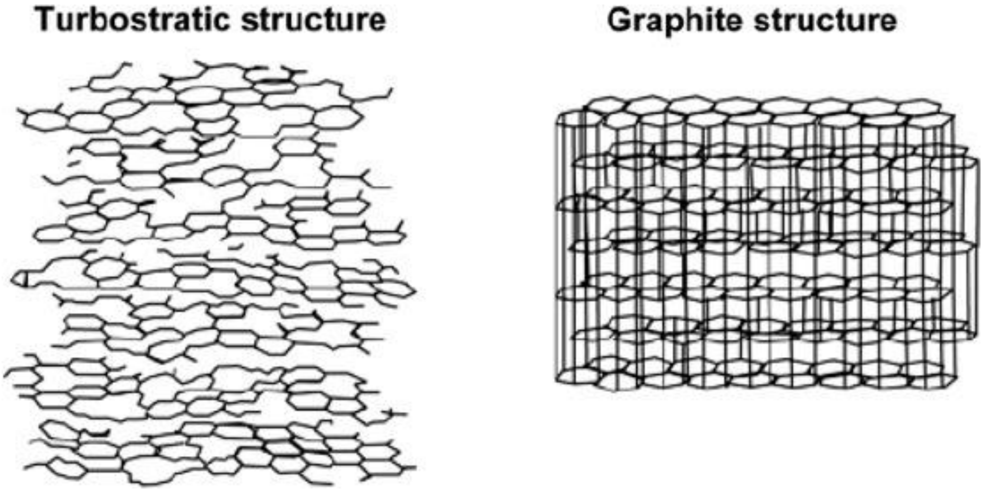

Figure 1.1: Schematic illustration of turbostratic and graphitic structure of carbons. Images modified with permission from ref. 13.

Carbon materials can also be roughly categorized according to whether they will undergo conversion into graphite by heat treatment. Graphitizable carbons, or soft carbons, will convert to graphite by heating to temperatures of up to approximately 2500 °C, whereas non-graphitizable carbons, or hard carbons, do not undergo this conversion and remain non-graphitic even at high temperatures. Various models have been used to describe the structure of graphitizable and non-graphitizable carbons, the first of which was reported by Franklin in 1951 (figures 1.2a, and b).[14] Franklin found that carbon sources such as polyvinyl chloride and petroleum coke would form graphite upon heating to 2200 °C, while polyvinylidene chloride and sucrose would remain amorphous. She proposed that for soft carbon precursors, small graphitic domains were arranged in an almost parallel arrangement that allowed for graphitization, whereas hard carbon precursors consisted of many cross-links and random orientations of the graphitic domains, preventing conversion to graphite.[14] More recent studies have reported fullerene-like models in which hard carbon precursors consist of a disordered array of six-membered and non-six-membered rings, resulting in a curved, microporous structure that resists graphitization upon heating (figure 1.2c and d).[15,16,17]

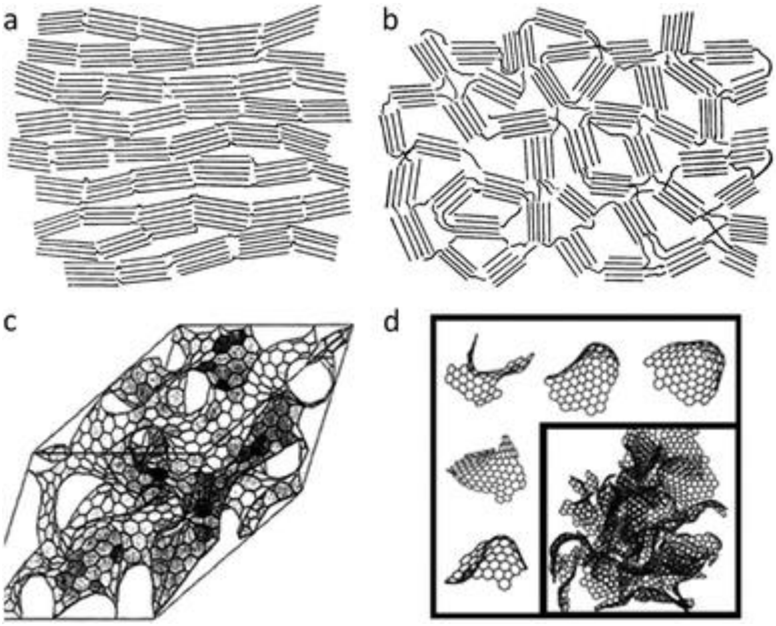

Figure 1.2: Structures of a) graphitizable and b) non-graphitizable carbons proposed by Franklin and c) curved graphitic sheet and d) fullerene-like structural models of amorphous carbon. Composite figure re-produced with permission from ref. 18.

1.3 Applications of carbon materials

A wide range of applications have been reported for carbon materials. This section discusses a few key applications that are relevant to the nanostructured graphitic carbons produced by catalytic graphitization.

1.3.1 Batteries

Graphite remains the most common choice of anode material in lithium-ion battery technology. The interlayer spacing in graphite is such that lithium ions can easily move into the structure without being so strongly bound that is not possible to subsequently remove them, allowing for reversible charge and discharge of the battery.[19] However, graphite is now listed as a critical material, so developing routes to graphite or alternative materials is a growing area of research. So far, there are relatively few examples of products produced *via* catalytic graphitization being used as lithium-ion battery anodes. However, due to the possible use of sustainable carbon sources, further interest in catalytic graphitization routes is likely.[20,21] In recent years, interest in other battery technologies such as sodium-ion batteries has also been growing, particularly for stationary power sources where the gravimetric penalty of using heavier sodium ions is less important. Sodium ions do not easily intercalate into graphite, so much research has been directed towards the development of alternative anode materials.[22] Hard carbons are a class of material that have shown to be promising anode materials for sodium-ion batteries.[23] While the exact sodium storage mechanism within hard carbons remains an area of dispute, recent studies have suggested that the small graphitic domains within a hard carbon structure can be beneficial for sodium storage.[24]

1.3.2 Fuel cells

Graphitic carbon materials have also attracted interest in the field of fuel cells.[25] A key reaction in fuel cell technologies is the oxygen reduction reaction. This occurs at the cathode within a fuel cell to reduce oxygen from the air. At the anode, a fuel such as hydrogen is supplied, which is oxidized so that the sole product of the reaction is water. The oxygen reduction reaction generally requires the use of a noble metal-based catalyst such as platinum decorated on porous carbon. Because of the cost of platinum, however, the replacement of these noble metal catalysts is now an extremely active field of research involving a vast number of variations to porous carbon materials. Various authors have proposed the used of heteroatom doping to improve the catalytic activity,[26] while others favour the use of different types of nanoparticles – for example, transition metals such as iron encapsulated in graphitic carbon shells.[2] The graphitic carbon shell may provide protection and increase the stability of the transition metal species against the often strongly acidic or alkaline conditions used in fuel cells.[2]

1.3.3 Adsorbents

Because of their greater potential for non-covalent interactions such as electrostatics and *π*-*π* interactions, various graphitic carbon structures have also been proposed as adsorbents for water treatment to remove pollutants including heavy metals[27] and organic dyes.[28] Finding the balance between degree of graphitization and porosity is important for optimum adsorptive performance. This was highlighted by the work of Wang *et al*, in which the authors found that pristine multi-walled carbon nanotubes displayed limited adsorption capacity for the uptake of lead ions.[29] However, by increasing the surface area of the multi-walled carbon nanotubes through acid treatment, a tenfold increase in the adsorption capacity was achieved.

1.4 Production of carbon materials

One of the earlier methods of synthesizing complex graphitic carbons is arc discharge, which was the method that Iijima used to synthesize the first-reported carbon nanotubes.[4] An electrical arc is used to vaporize a solid carbon precursor, which is then deposited as graphitic carbon upon cooling. The process occurs inside a vacuum chamber through which inert gas is supplied to avoid oxidation. Within the chamber, a potential difference is applied between two electrodes. The anode contains a powdered carbon precursor along with a catalytic material – usually a transition metal such as nickel or iron – while the cathode is generally composed of pure graphite. These electrodes are gradually brought closer together until the distance between them is such that an electrical arc forms between them through the non-conductive gas. The arc current generates an extremely high temperature that ionizes the gas particles to create a plasma. The high temperature plasma vaporizes the solid carbon precursor within the anode, which then deposits onto the cooled cathode as structures such as carbon nanotubes[30] and fullerenes.[31]

Using a similar principle to arc discharge, another route that has been explored for the synthesis of nanostructured graphitic carbons is laser ablation. First reported by Guo *et al*,[5] rather than using a high temperature plasma, a pulsed laser beam is used to vaporize the carbon source. Under an inert atmosphere, the beam is fired onto a graphite target embedded with metal catalyst particles. As in arc discharge, the airborne carbon vapour particles condense onto a cooled copper collector and grow to form structures such as fullerenes and nanotubes with the aid of the metal catalyst nanoparticles.[32]

Both arc discharge and laser ablation require a large amount of energy to produce graphitic carbons and scaling up the processes is challenging. A more recently developed method is CVD, which is commonly used for the industrial production of carbon nanotubes. Unlike arc discharge and laser ablation, pure graphite is not required as a source of carbon. Instead, a carbonaceous gas such as acetylene is flowed over a two-dimensional substrate, coated in metal catalyst nanoparticles such as iron, cobalt and nickel. Upon heating, the gas decomposes and dissolves into the catalyst nanoparticles. Graphitic carbon is then deposited onto the surface of the nanoparticles, which may grow into carbon nanotubes.[33] Compared with arc discharge and laser ablation, CVD processes can produce a relatively high purity product in a high yield in a less energy-intensive manner. By changing various experimental parameters such as reaction temperature or the chemical nature of the catalyst or substrate, it is possible to influence the structure of the final product.[34]

It is important to note that in the synthesis methods discussed, a combination of a catalyst based on transition metals such as iron, cobalt and nickel and a carbon source is used to produce nanostructured graphitic carbons, so all may be considered examples of catalytic graphitization. This thesis, however, focuses on the use of solid or solution-based organic precursors (figure 1.3), rather than the gaseous organic precursors used in CVD. Graphitizable carbon precursors eventually convert to graphitic carbons when heated to high temperatures of approximately 2500 °C. With the addition of an iron catalyst, the temperature of this graphitization process can be reduced considerably to approximately 800 °C. Classically non-graphitizable carbon precursors can also be graphitized.

The solid or solution-based organic precursor is typically mixed with an iron salt solution such as iron chloride, iron acetate or iron nitrate and heated under an inert atmosphere. Upon heating, the organic precursor thermally decomposes to form amorphous carbon. The iron source also decomposes, in many cases initially forming iron oxide nanoparticles, before carbothermal reduction by the surrounding carbonaceous material results in the *in situ* formation of catalytically active iron or iron carbide nanoparticles. While the exact mechanism of the graphitization process remains an area of dispute, multiple variations of iron-catalyzed graphitization have been used to produce nanostructured graphitic carbon products.

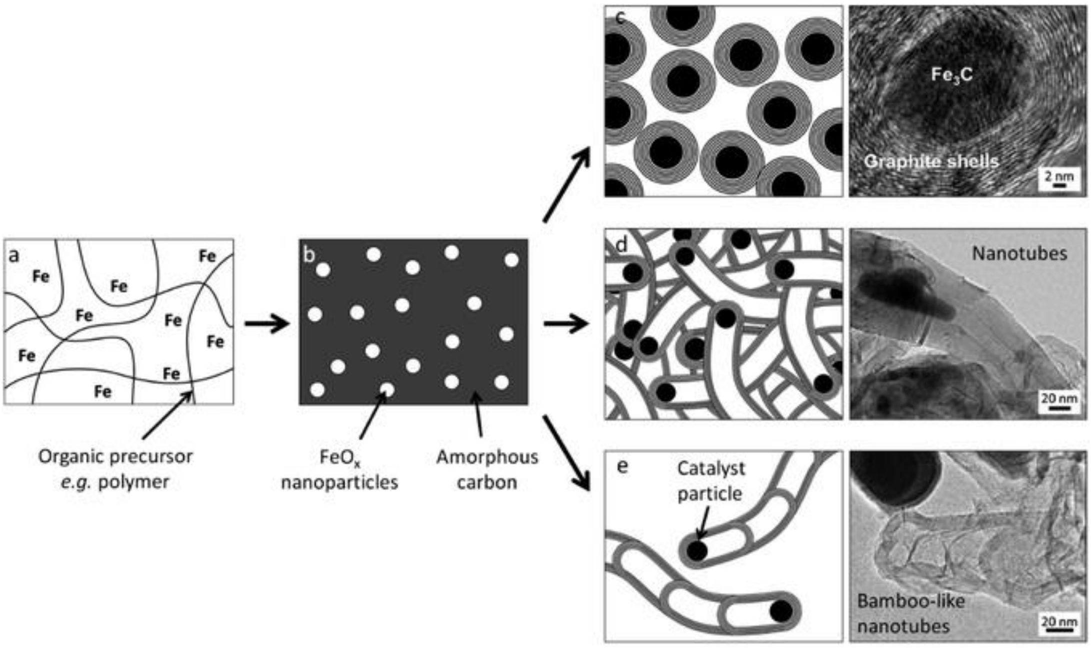

Figure 1.3: Schematic of a typical iron-catalyzed graphitization process of pyrolyzing a) an organic/iron mixture to initially produce b) amorphous carbon and iron oxide nanoparticles then a variety of graphitic nanostructures such as c) shells, d) nanotubes and e) bamboo-like nanotubes. Figure reproduced with permission from ref. 18.

1.5 Organic precursors used in iron-catalyzed graphitization

This section presents the main categories of organic precursor that have been used in iron-catalyzed graphitization. A few examples from the literature are discussed to highlight the diversity of the method, focusing particularly on those in which effort has been made to explain or influence the formation of the graphitic carbon product.

1.5.1 Small organic molecules

The simplest class of organic precursor used in iron-catalyzed graphitization processes are small molecules such as the sugars, sucrose and glucose. Sugar molecules are mono- or disaccharides and are generally highly soluble in water, so can simply be combined with an aqueous iron salt solution such as iron nitrate to produce a homogeneous mixture. The mixture can then be dried and pyrolyzed to produce nanostructured graphitic carbons. An example of this can be seen in the work of Yang *et al*, who synthesized graphitic shell-like structures containing metal particles by pyrolyzing sucrose and iron (III) nitrate at 700 °C.[35] The metal particles were then removed through acid-washing to leave graphitic nanocapsules, alongside a smaller number of graphitic nanotubes, highlighting the possibility of the formation of different nanostructures within the same product.

Comparing the nature of the graphitic nanostructures in different studies can be challenging due to the varying nature of the precise reaction conditions (table 1.1). For example, Sevilla *et al* reported the formation of filamentous multi-walled nanotubes in a similar system, using a combination of glucose and iron nitrate, suggesting that the catalyst particle was highly mobile.[36] It is difficult to say with certainty the exact reasons for the variation in graphitic nanostructure. However, it seems likely that the metal:organic ratio has an effect. The synthesis of shell-like structures by Yang *et al* used a greater amount of iron nitrate (3 mmol of iron per 1 g of sucrose) than Sevilla *et al* (0.4 or 0.8 mmol of iron per 1 g of glucose). Therefore, the higher metal:organic ratio may favour the formation of shell-like structures. In the glucose system, there may be more amorphous carbon available for the catalyst particle to “consume”, promoting movement to form tubular structures. Also, the nanoparticles in the sucrose study by Yang *et al* are likely to have been larger, which may have affected their mobility.

Variations on iron-catalyzed graphitization routes have been used to control the size of the catalyst nanoparticles to maintain structural uniformity in the resulting nanostructured graphitic carbon. For example, Xie *et al* used sucrose as the source of carbon, but rather than simply mixing with an iron source, the sucrose was polymerized to form a soft carbon template through self-assembly.[37] The carbon template was then hydrothermally treated with iron nitrate solution to disperse the iron uniformly throughout the structure before pyrolysis.

Table 1.1: List of examples of nanostructured graphitic carbons produced from small molecule organic precursors.

Product description	**Organic precursor**	**Iron source**	**Synthesis temperature (°C)**	**Comments**
Graphitic tubes/shells[38]	Glucose	$Fe(NO_3)_3$	800	Structure of glucose-derived carbon compared to starch- and cellulose-derived carbons. S_{BET} 343 m^2g^{-1}.
Graphite[39]	Glucose	Fe powder	1200	Glucose pyrolyzed to form hard carbon before grinding with Fe powder.
Carbon-encapsulated magnetic nanoparticles, core-shell structure[40]	Glucose	Fe_3O_4 nanoparticles	700-850	S_{BET} 134-202 m^2g^{-1}.
Graphene-like carbon shell encapsulating Fe_3C nanoparticles[41]	Glucose	$Fe(NO_3)_3$	800	KNO_3 added as a promoter. S_{BET} 238 m^2g^{-1}.
Graphitic mesoporous carbon, carbon nanotubes[35]	Sucrose	$Fe(NO_3)_3$	700/800	S_{BET} 198 m^2g^{-1}.
Nanoporous graphitic carbon, wormlike porous structure[37]	Sucrose	$Fe(NO_3)_3$	600-900	Initial hydrothermal treatment. F123 copolymer template. S_{BET} 329 m^2g^{-1}.
Graphitic nanoribbons[42]	Sucrose	$Fe(NO_3)_3$	800	Initial hydrothermal treatment.
Hollow carbon nanospheres[43]	Sucrose	Fe oxide nanoparticles	450	Very broad peak in XRD.
Fe_3C or Fe nanoparticles with graphitic shells[44]	Glucose, sucrose or urea	$Fe(C_5H_7O_2)_3$	800	S_{BET} 40-240 m^2g^{-1}.

Graphite encapsulated Fe_3C/Fe nanosheet composites[45]	Glucose and glycine	$Fe(NO_3)_3$	700-1000	S_{BET} 75-260 m^2g^{-1}.
Fe particles with graphitic carbon shells[46]	Glucose + dicyandiamide or urea	$K_3[Fe(CN)_6]$	800/900	NaCl template. Dicyandiamide or urea for N-doping.
Fe- and N-doped carbon nanostructures [47]	Glycine	$FeCl_3$	900	Additional template of silica beads. S_{BET} 740 m^2g^{-1}.
Fe-doped porous carbons, graphene sheets, particles wrapped by graphitic carbon[48]	L-Histidine	Fe_2O_3 and $FeCl_3$	1000 then 1000	Ball milling and acid wash after first pyrolysis. S_{BET} 200-315 m^2g^{-1}.
Metallic nanoparticles in graphitic shells[49]	Citric acid	$Fe(NO_3)_3$	800	Initial formation of metal citrate gel at 120 °C.
Fe_3C encapsulated in graphitic layers[50]	1,8-Diaminonaphthalene	$FeCl_3$	700-1000	Initial polymerization step. S_{BET} 510-920 m^2g^{-1}.

1.5.2 Synthetic polymers

Along with small organic molecules, a variety of synthetic polymers have been used as organic precursors for the production of nanostructured graphitic carbons (table 1.2). As with small organic molecules, many synthetic polymers are water-soluble so can be simply dissolved in water and mixed with an aqueous iron salt solution. For example, Huang *et al* combined the water-soluble polymer polyethylene glycol with iron sulfate solution to synthesize bamboo-like hollow carbon fibres.[51]

Alternatively, an iron source may be mixed with a monomer, which is subsequently polymerized before the resulting mixture is pyrolyzed. A commonly used class of synthetic polymers used in catalytic graphitization are phenolic resins. These are thermosetting polymers that are generally synthesized from the reaction of phenols with formaldehyde and are commonly used as industrial adhesives. Inomata *et al* investigated the effect of varying the mixing method on carbons prepared from the catalytic graphitization of phenolic resin, using ferrocene as the source of iron.[52] Similar graphitic carbon nanostructures were observed in electron microscopy. However, gas sorption data revealed that mechanical mixing of solid precursors resulted in a more microporous product, while homogeneous mixing of solvated precursors resulted in greater mesoporosity.[52] This variation in porosity is likely due to the size of the catalyst nanoparticle.

Another means of introducing porosity into nanostructured graphitic carbons is using either hard or soft templating routes. Sevilla *et al* carbonized silica and phenolic resin to produce a silica xerogel, followed by pyrolysis and treatment with hydrofluoric acid to remove the silica component.[53] The carbonaceous component was then impregnated with ethanolic iron nitrate and further pyrolyzed to produce a graphitic carbon with a high surface area. Similarly, Li *et al* synthesized mesoporous SBA-15 silica with embedded iron oxide nanoparticles and infiltrated with phenolic resin before pyrolysis.[54] Both of these methods produced highly ordered porous graphitic carbon materials with a high specific surface area. However, the main disadvantage of hard templating routes such as these is the removal of the silica template to reveal the pure carbon material, which requires the addition of a strong acid or base such as hydrofluoric acid or sodium hydroxide respectively, so an extra step is added to the synthesis.

Soft templating routes based on self-assembly have also been explored. Wang *et al* combined phenolic resin with ammonium iron citrate as the iron source, along with a surfactant, Pluronic P123, to introduce mesoporosity.[55] Soft templates are burnt off during the pyrolysis procedure so eliminate the need for a template removal step, streamlining the synthesis route.

Table 1.2: List of examples of nanostructured graphitic carbons produced from synthetic polymers.

Product description	**Organic precursor**	**Iron source**	**Synthesis temperature (°C)**	**Comments**
Turbostratic carbon shells and tubes surrounding Fe nanoparticles[56]	Furfuryl alcohol	Ferrocene	450-820	Initial polymerization step to polyfurfuryl alcohol.
Turbostratic carbon, shell-like structures[57]	Furfuryl alcohol	Ferrocene	700	S_{BET} 200 m^2g^{-1}.
Graphitic mesoporous carbons[53]	Phenolic resin	$Fe(NO_3)_3$	900	Silica xerogel template. S_{BET} 1010 m^2g^{-1}.
Graphitic mesoporous carbon[58]	Phenolic resin	$Fe(NO_3)_3$ or ferrocene	700	S_{BET} 607 m^2g^{-1} and 248 m^2g^{-1}.
Onion-like carbon[59]	Phenol/formaldehyde	Ferrocene	1000	Different mixing methods compared.
Microporous carbons, graphitic layers[52]	Phenol/formaldehyde	Ferrocene	1000	Mechanical mixing compared to solution mixing. S_{BET} 216-632 m^2g^{-1}.
Mesoporous carbon[54]	Phenol/formaldehyde resin	$Fe(NO_3)_3$	900	SBA-15 silica nanocast. S_{BET} 670 m^2g^{-1}.
Mesoporous graphite-like carbon[55]	Phenol/formaldehyde	$(NH_4)_5[Fe(C_6H_4O_7)_2]$	700	Pluronic P123 as templating agent.
Ordered mesoporous carbons with partially	Phenol/formaldehyde	$FeCl_3/FeSO_4$	800	Initial hydrothermal treatment and

graphitized network[60]				copolymer P123.
Graphitic mesoporous carbon[61]	Resorcinol/formaldehyde	$FeC_6H_6O_7$	900	Silica sol template. Surface area depends on Fe content.
Highly ordered Fe-containing mesoporous carbon[62]	Resorcinol/formaldehyde	$Fe(NO_3)_3$	800	Triblock copolymer Pluronic F127 as templating agent.
Metal-doped carbon aerogels[63]	Resorcinol/formaldehyde	$Fe(CO_2CH_3)_2$	900	S_{BET} 461 m^2g^{-1}.
Graphitic carbon spheres[64]	Resorcinol/formaldehyde	Prussian blue	1000	S_{BET} 381 m^2g^{-1}.
Macroporous monolithic graphitic carbon[65]	Resorcinol/formaldehyde xerogel	$FeCl_3$	1000	Spinodal decomposition during polymerization introduces microporosity. S_{BET} 465 m^2g^{-1}.
Onion-like or nanocapsule-like graphitic carbon[66]	Resorcinol/formaldehyde	$Fe(CO_2CH_3)_2$	1100	Two step pyrolysis to minimize cracking.
Monolithic porous graphitic carbons[67]	Resorcinol, furfural xerogel	$FeCl_3$	1050	S_{BET} 400 m^2g^{-1}.
Carbon nanotubes and shells[68]	Polyethylene/polyvinyl alcohol	$Fe(OH)_2$ needles	750	
Carbon nanofibers with bamboo-like hollow fibril morphology[51]	Polyethylene glycol	$FeSO_4$	750	Graphitization believed to be facilitated by sulfur dissolution into the catalyst particles.
Carbon nanotubes[69]	Polypropylene	Fe nanoparticles	700	Dissolution of precursor in xylene.
Multilayer graphitic nanosheets/nanoshells[70]	Poly(4-ethylstyrene-*co*-divinylbenzene)	$Fe(C_5H_7O_2)_3$	850	

1.5.3 Biopolymers

Polymers derived from biomass, known as “biopolymers”, offer a potentially cheaper and more environmentally friendly alternative to synthetic polymers, Therefore, these materials have also been explored for use in catalytic graphitization systems (table 1.3). Many biopolymers are also waste products of industrial processes. Cellulose, for example, is the most abundant biopolymer found in nature as it is the primary component of the cell walls of green plants, as well as being a waste product in paper production, so is viewed as an attractive feedstock. Cellulose is a polysaccharide consisting of linear chains of β-linked glucose monomer units, which form a hydrogen bonding network between themselves, resulting in strong microfibrils. Because of the strong hydrogen bonding network, cellulose is difficult to dissolve in water. Therefore, iron-catalyzed graphitization routes generally involve soluble iron salts being infiltrated into the solid cellulose matrix.

A variety of different iron sources have been used to induce graphitic character into the structure of cellulose-derived carbons. A study by Hoekstra *et al* examined the graphitization of microcrystalline cellulose spheres in combination with three trivalent iron salts: iron (III) nitrate, ammonium iron (III) citrate and iron (III) chloride.[71] The study found that it was possible to produce graphitic carbon with all three of the iron salts, with PXRD patterns showing the presence of iron and iron carbide. However, the carbons produced using iron nitrate and ammonium iron citrate showed a greater amount of shell-like and tubular graphitic nanostructures compared with the carbon produced from iron chloride. Nitrogen sorption results showed the presence of mesopores in the carbons produced from iron nitrate and ammonium iron citrate, whereas the carbon produced from iron chloride only displayed microporosity. A mechanistic study of each system was carried out using temperature dependent

PXRD and showed the formation of small iron oxide nanoparticles before reduction to iron and iron carbide in the iron nitrate and ammonium iron citrate systems. A similar route was observed with iron chloride. However, the peaks corresponding to iron oxide phases were much sharper, indicating a larger particle size, which was consistent with results from electron microscopy. The authors suggested that the variation in particle sizes was due to the volatility of iron chloride, resulting in larger particles being deposited onto the surface of the microcrystalline spheres.[71] The results of this study again suggest that the graphitization behaviour is highly dependent on the size of the catalyst nanoparticles.

The other major component of many plant-based biomass sources is lignin. Lignin is a highly abundant polyaromatic molecule and a by-product of the Kraft wood pulping process. Like cellulose, lignin is insoluble in water. However, lignin is soluble in some organic solvents such as THF, so some authors have mixed lignin in THF solutions with aqueous iron nitrate solutions to homogeneously disperse the iron throughout the lignin.[72,73] After pyrolysis, shell-like encapsulated metal nanoparticles were found in the carbon products. A similar study by Zhang *et al* used a combination of lignin and iron nitrate, but rather than producing a homogeneous dispersion, solid lignin powder was coated in the iron solution.[74] While the resulting product contained similar shell-like structures, the catalyst particles were polydisperse, as the iron was coated on the surface of the lignin.

Various other biopolymers have been used as feedstock for graphitization. Their common characteristic is the presence of functionality, such as hydroxyl groups, which enables the strong binding of iron ions. Agar, for example, is a mixture of two polysaccharides that contain hydroxyl groups, agarose and agaropectin, and has also been used as a precursor for catalytic graphitization.[75] As well as purely carbon-, hydrogen- and oxygen-based precursors, biopolymers with nitrogen functionality have been explored. Chitosan, for example, is a polysaccharide derived from crustacean shells that contains hydroxyl groups as well as an amine group in its monomer unit, which can be exploited to introduce nitrogen into the final graphitic carbon structure.[76] Another example is gelatin, a polypeptide that is a waste product of the meat industry, which has been shown to strongly interact with iron nitrate solution to produce a microporous foam-like structure. Upon pyrolysis, graphitic carbon encapsulated iron carbide nanoparticles are formed, while the foam structure remains intact to give a hierarchical graphitic carbon product.[77]

Table 1.3: List of examples of nanostructured graphitic carbons produced from biopolymer precursors

Product description	**Organic precursor**	**Iron source**	**Synthesis temperature (°C)**	**Comments**
Turbostratic carbon with a ribbon morphology[78]	Microcrystalline cellulose spheres	$Fe(NO_3)_3$	800	Detailed mechanism study.
Graphitic carbon shells and tube-like structures[79]	Cellulose filter paper	$Fe(NO_3)_3$	800	*In situ* TEM images of graphitization.
Fe or Fe_3C nanoparticles embedded in graphitic carbon matrix[80]	Cellulose	Fe oxide nanoparticles	Up to 800	Initial hydrothermal treatment.
Mesoporous graphitic carbon[81]	Microcrystalline cellulose spheres	$Fe(NO_3)_3$	800	Various metals compared.
Carbon encapsulated Fe_3C nanoparticles[82]	Cellulose	Fe_3O_4 nanoparticles from $FeCl_2/FeCl_3$	800-1600	Thicker graphitic shell at higher temperature.
Mesoporous graphite-containing carbon[83]	Cellulose	$FeCl_2/Fe(NO_3)_3$	500-1000	Various cellulose precursors.
Mesoporous graphitic carbon[38]	Cellulose fibres	$Fe(NO_3)_3$	800	Cellulose-derived carbon compared to glucose- and

				starch-derived carbon. S_{BET} 358 m^2g^{-1}.
Porous graphitic carbon[84]	Cellulose	$Fe(NO_3)_3$	850	Liquid, gaseous and solid products characterized.
Microporous or mesoporous carbon[38]	Potato starch	$Fe(NO_3)_3$	800	Graphitization very slow compared to cellulose or glucose.
Graphitic carbon nanostructures[36]	Starch	$Fe(NO_3)_3$	900	Comparison of starch-, glucose- and sucrose-derived carbons.
Graphitic-carbon encapsulated Fe nanoparticles[74]	Kraft lignin	$Fe(NO_3)_3$	700-1000	Larger particles believed to create thicker graphitic shells.
Graphene-encapsulated Fe particles, multilayer graphene sheets/flakes, core-shell structure[72]	Kraft lignin	$Fe(NO_3)_3$	1000	Lignin dissolved in THF.
Graphene-encapsulated Fe particles[73]	Kraft lignin	$Fe(NO_3)_3$	1000	Different Fe:lignin ratios.
Graphene-encapsulated Fe nanoparticles[85]	Kraft lignin	$Fe(NO_3)_3$	1000	Effect of pyrolysis gases (Ar, CO_2, H_2, CH_4) investigated.
Carbon-encapsulated Fe nanoparticles and carbon tubules[86]	Kraft lignin	Fe nanoparticles or $Fe(NO_3)_3$	1000	Comparison of solid and aqueous Fe precursors.
Core shell structures[87]	Lignin, cellulose and hemicellulose	$Fe(NO_3)_3$	1000	Biomass pyrolyzed before Fe addition and second pyrolysis step.

				Limited graphitization for lignin.
Porous carbon sheets[75]	Agar	$Fe(NO_3)_3$	800	$Al(NO_3)_3$ as templating agent.
Graphitic mesoporous capsules, graphitized carbon[77]	Gelatin	$Fe(NO_3)_3$	800	Addition of $Mg(NO_3)_2$ to prevent sintering.
Sponge-like graphitic carbon[76]	Chitosan	$FeCl_3$, $FeCl_2$ or $(Fe(Phen)_3Cl_2)$	900	Freeze drying of chitosan gel introduces macroporosity.
N-doped carbon with a high degree of graphitization[88]	Chitosan	$FeCl_3$	800-1000	Graphitic N functionality

1.5.4 Raw biomass

As well as using polymers that can be derived from biomass as feedstocks for graphitization, there has been interest in using raw biomass as a source of carbon (table 1.4). Upon pyrolysis, the biological macrostructure of biomass generally remains intact even with iron treatment, resulting in carbons with complex pore networks that can give good performance in applications such as supercapacitors.[89] Biomass sources are generally insoluble in water, so syntheses usually consist of coating the surface of the biomass in an iron solution. For example, Thompson *et al* coated softwood sawdust in iron nitrate solution and heated the mixture to 800 °C under a nitrogen atmosphere.[90] Woody biomass such as sawdust mostly consists of a mixture of cellulose, hemi-cellulose and lignin, with surface hydroxyl groups allowing for interaction with iron ions. Upon pyrolysis of the sawdust/iron nitrate mixture, iron and/or iron carbide nanoparticles formed on the surface of the resulting amorphous carbon, which burrowed through the carbon matrix to produce a mixture of continuous and bamboo-like nanotubes. In this study, the size of the iron or iron carbide catalyst nanoparticles were shown to dictate the porosity of the carbon. Nitrogen sorption data showed that a higher metal:organic ratio resulted in a larger pore size. This could also be seen in TEM, which showed larger catalyst particles in the samples with a higher metal:organic ratio.[90]

An important factor in iron-catalyzed graphitization of a biomass precursor is the dispersion of the iron source. A study by Hunter *et al* demonstrated that milling a range of solid lignocellulosic biomass sources to maximize the coating of iron nitrate before pyrolysis resulted in porous graphitic carbons with consistent adsorptive properties.[91]

Table 1.4: List of examples of nanostructured graphitic carbons produced from biomass sources

Product description	**Organic precursor**	**Iron source**	**Synthesis temperature (°C)**	**Comments**
Continuous and bamboo-like graphitic nanotubes[90]	Softwood sawdust	$Fe(NO_3)_3$	800	Porosity depends on Fe:biomass ratio.
Nanofibers/mesoporous carbon composites[92]	Sawdust	$FeCl_3$	600-800	Fast pyrolysis process. Carbon structure compared with those produced from $Fe(NO_3)_3$ and $Fe_2(SO_4)_3$.
Graphitic carbon nanostructures[93]	Pine wood sawdust	$Fe(NO_3)_3$	900/1000	Carbon structures compared to those produced using Ni.
Onion-like structure, curved graphitic shells[94]	Beech wood	$FeCl_3$	1000/1300	Impregnation with $FeCl_3$ solution in isopropanol.
Porous graphitic carbons[95]	Beech wood	$FeCl_3$	1000-1600	Slow pyrolysis to 500 °C to reduce cracking.
Onion-like graphitic shells[96]	MDF wood	$FeCl_3$	850-2000	Slow pyrolysis to 500 °C to reduce cracking.
Mesoporous graphitic carbons[91]	Bamboo, nut shells,	$Fe(NO_3)_3$	800	Mechanical milling increases

	grasses, wood			graphitization for hard biomass.
Carbon microfibres with iron nanoparticles[97]	Bamboo	$Fe(NO_3)_3$	800	Hydrothermal pre-treatment of bamboo in NaOH.
Porous graphitic carbon[98]	Bamboo	K_2FeO_4	800	Bamboo pyrolyzed to 400 °C before infiltration with Fe precursor.
Porous graphene-shell nanosheets[99]	Coconut shell	$FeCl_3$	900	$ZnCl_2$ used for simultaneous activation and graphitization. S_{BET} 1874 m^2g^{-1}.
Porous graphitic carbon[100]	Coconut shell	$Fe(NO_3)_3$	1000	Coconut shell milled to a powder before infiltration with $Fe(NO_3)_3$.
Magnetic nanofibers/porous carbon composites[101]	Rice husks	$FeCl_3$	600	Various pre-treatments of rice husks including hydrothermal and NaOH.
Fe/N-doped carbon[102]	Soybean milk	$FeCl_3$	600-1000	S_{BET} 879-1164 m^2g^{-1}.
Onion-like graphitic carbon[103]	Cotton	$Fe(C_5H_7O_2)_3$	650	DMF used as solvent.
Nanoporous carbon@carbon fibre composites[104]	Cotton	$FeCl_3$	500-600	MOF precursor. Initial activation step.
Mesoporous carbon/Fe nanocomposite[105]	Cotton fabric	$Fe(NO_3)_3$	800	S_{BET} 154-410 m^2g^{-1}.
N-doped porous graphitic carbon[106]	Water hyacinth	$Fe(NO_3)_3$	700	Dopamine hydrochloride as N source.
Hierarchically porous carbon nanosheets[107]	Moringa Oleifera stems	$Fe(NO_3)_3$	800	$ZnCl_2$ as activation catalyst.
Graphitic core-shell structures[108]	Miscanthus grass powder	$Fe(NO_3)_3$	900	Graphitization enhanced with Co.
Magnetic carbon nanocages[109]	Pine tree resin	$Fe(NO_3)_3$	1000	Fe_3C catalyst.
Hierarchical porous graphitic carbon[110]	Chopsticks	$Fe(NO_3)_3$	850	$K_2C_2O_4$ as activating agent.
Worm-like structures, carbon nano-capsule[111]	Chinese chestnuts	$Fe(NO_3)_3$	400-800	Gas and liquid by-products also characterized.

Graphitized carbon nanosheets[112]	Citrus grandis skins	$FeCl_3$	1200	Biomass milled. $ZnCl_2$ used as co-catalyst.
Carbon-shell coated Fe nanoparticles[113]	Coffee grounds	$Fe(NO_3)_3$	800	Coffee grounds washed before infiltration with $Fe(NO_3)_3$.
Mesoporous graphitic carbon[114]	Chestnut shell, bamboo, poplar, cotton, lotus	$Fe(NO_3)_3$	800	Different Fe loading and pyrolysis conditions investigated.
Graphite-shell-chains[115]	Wood, coffee, tofu residue, cotton	$Fe(NO_3)_3$	850	Electron microscopy shows tube-like structures.
Graphitic structures[116]	Oil palm frond	$Fe(NO_3)_3$	1000-1400	Silica also added.
Graphitized porous carbon[117]	Phoenix tree leaves	K_2FeO_4	650-950	Biomass initially pyrolyzed to 400 °C before mixing with K_2FeO_4 powder.
Carbon shells/tubes[118]	*Oryza sativa* pulp	$FeCl_3$	800	NaOH pre-treatment.
Porous graphitic carbon microtubes[119]	Willow catkins	$K_4Fe(CN)_6$	900	Carbon structure compared to that produced using $FeCl_2$.

1.5.5 Organometallics

The examples discussed in the preceding sections have all used a separate organic and metal precursor. An alternative method is to use a single reactant containing both components, such as an iron-containing organometallic complex. This route has been less explored than other organic precursors; however, there are some examples of pyrolysis of materials such as iron gluconates[120] and ferrocene[121] in the literature (table 1.5). The use of organometallic precursors brings its own challenges, as organometallics can have a relatively low thermal stability. Therefore, some routes have included an initial polymerization step. For example, Li *et al* heated ferrocene under reflux with aluminium chloride to introduce cross-links between the cyclopentadienyl rings to improve the stability before subjecting to pyrolysis.[122]

Table 1.5: List of examples of nanostructured graphitic carbons produced from organometallic precursors.

Product description	Precursor	Synthesis temperature (°C)	Comments
Mesoporous graphitic carbon[123]	Fe phthalocyanine	900	Mesoporous silica template. S_{BET} 877 m^2g^{-1}.
Multi-walled carbon nanotubes[124]	Fe phthalocyanine	850	Initial vaporization at 650 °C, then flow of gas into second high temperature furnace with Ar.
Graphitic carbon nanostructures, nanocapsules, nanopipes[120]	Fe (II) gluconate	900-1000	Addition of $KMnO_3$ post-treatment to remove Fe species and amorphous carbon.
Graphitic porous carbons with 3D nanonetwork[122]	Ferrocene	700-900	Initial reflux in CCl_4/$AlCl_3$ to drive cross-linking of cyclopentadienyl rings.
Fe-filled carbon nanotubes[121]	Ferrocene	860-920	Initial sublimation of ferrocene at 150 °C, then flow of gas into second high furnace with Ar.
Graphitic nanocages[125]	$Fe(CO)_5$, C_2H_2 and NH_3	750-1050	Carbon product doped with N.
Graphitic nanocages[126]	$Fe(CO)_5$ and C_2H_5OH	900	Vertical tube furnace with three heating zones.
Carbon-encapsulated Fe_3C nanoparticles[127]	Ferrocene	600-1600	High pressure, mechanism study.
Core@shell nanocomposites[128]	Ferrocene	900	High pressure.

1.6 Mechanism of iron-catalyzed graphitization

One of the current drawbacks of catalytic graphitization is the limited understanding of the fundamental mechanism of graphitization. As shown in the previous section, many examples throughout the literature use a combination of an organic precursor and an iron source to produce a nanostructured graphitic carbon material. However, the choice of precursor and synthesis conditions vary greatly between studies, both of which can significantly affect the graphitic carbon structure. As a result, it is difficult to compare different systems directly or predict which may result in materials with enhanced properties. Therefore, further research is required to understand the underlying mechanism of the graphitization process to develop the method as an industrially viable route to sustainable nanostructured graphitic carbons. While there are few mechanistic studies of iron-catalyzed graphitization, the process has many similarities with carbon nanotube growth *via* CVD so the more extensive literature regarding CVD is a good starting point for study.

1.6.1 Nucleation and growth of carbon nanotubes

In CVD, a substrate is decorated with metal catalyst nanoparticles upon which amorphous carbon is deposited as the carbonaceous gas feedstock decomposes. The amorphous carbon dissolves into the metal catalyst particle and is redeposited as graphitic carbon. A popular theory regarding the initial carbon nanotube nucleation is the “yarmulke” mechanism, first proposed by Dai *et al*.[129] The first step involves the formation of a graphene cap over the catalyst nanoparticle. The basal plane of graphite has a lower surface energy than most metals, so in combination with the unfavourably high surface: bulk ratio of nanoparticles due to their extremely small size, the formation of a graphene cap reduces the overall surface energy of the system. As more carbon is introduced, the cap lifts off the catalyst nanoparticle and elongates to form a single-walled carbon nanotube (figure 1.4), believed to be driven by the high energy of dangling carbon bonds at the edge of the graphitic planes.[130]

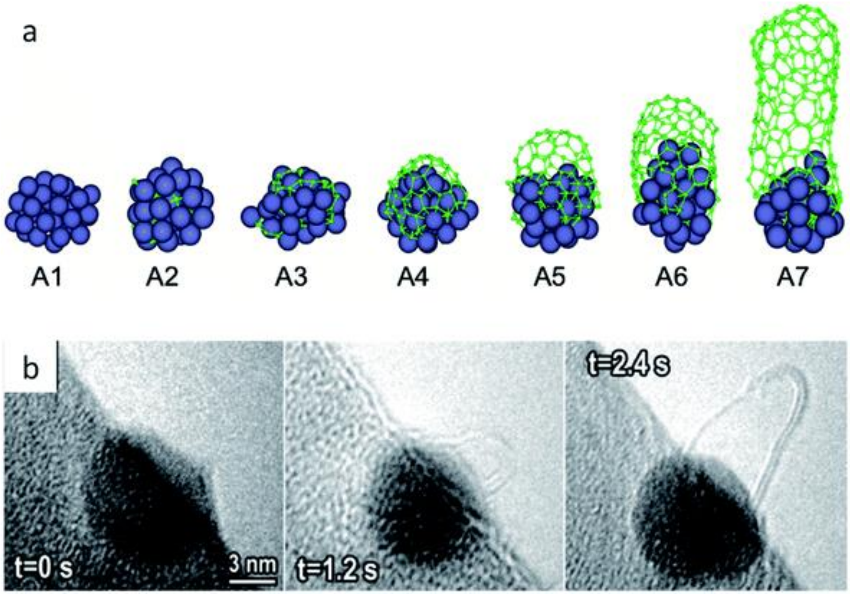

Figure 1.4: a) Molecular dynamics simulation of a carbon cap formation and lift-off and b) still images taken from environmental TEM video footage of carbon nanotube growth from an iron catalyst. Composite figure reproduced with permission from ref. 18.

Dai *et al* also observed that the diameter of a single-walled carbon nanotube was related to the diameter of the catalyst nanoparticle, consistent with the "yarmulke" mechanism, where the size of the catalyst nanoparticle determines the size of the graphitic cap.[129] Molecular dynamics simulations such as those carried out in a study by Ding *et al* showed a similar correlation between the size of the catalyst nanoparticle and the likelihood of multi-walled carbon nanotube formation.[131] In their model, single-walled carbon nanotubes were formed by small catalyst nanoparticles and the number of graphitic layers increased with the size of the catalyst nanoparticle. An earlier study by the same group also observed a similar size dependence, and that with extremely small nanoparticles (≤ 20 atoms), the resulting carbon nanotubes have a poorly ordered structure with a large number of defects and energetically unfavourable dangling bonds. This suggests the catalyst particles must reach a critical size before they become active,[132] similar to some experimental observations in CVD.[133]

Simulations have also shown the possibility of catalyst particle encapsulation, as has been observed in experiment with the formation of shell-like nanostructures. Ding *et al* modelled the early stages of nanotube nucleation in CVD and showed the formation of small graphitic “islands” on the surface of the iron nanoparticle, most of which would redissolve into the nanoparticle.[131] Eventually, a larger cap would form that does not redissolve or lift off to form a carbon nanotube. At lower synthesis temperatures (< 700 K), a graphitic cap that forms on the surface does not have enough energy to overcome the interfacial energy between the cap and the catalyst nanoparticle so remains on the surface. More graphitic caps then nucleate on the surface of the catalyst particle surface until it is completely encapsulated, and the catalyst becomes deactivated. In Ding *et al*’s model, only at temperatures above 800 K was there enough energy in the system to overcome the interfacial energy in order for the cap to lift off and elongate to form a carbon nanotube (figure 1.5).[131] This is similar to observations in CVD where encapsulated particles tend to be found in lower temperature regions of CVD ovens. An additional factor that may influence the nature of the graphitic nanostructure is particle size, as small particles tend not to become encapsulated. Both tubular and shell-like structures are also commonly reported in catalytic graphitization systems, often within the same sample, suggesting a similar graphitization mechanism may be occurring. In reality, the same sample may have variations in temperature and polydispersity, which may contribute to the formation of both tubular and shell-like graphitic nanostructures.

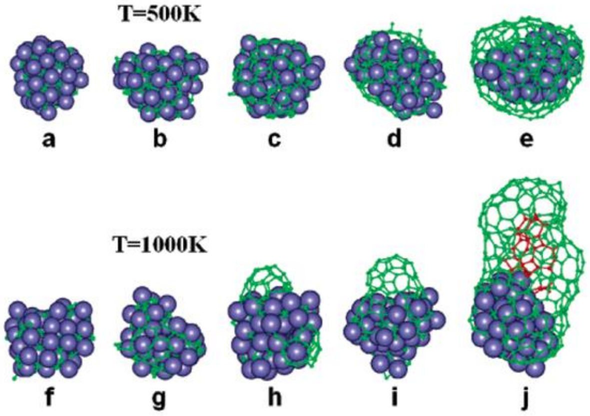

Figure 1.5: Snapshots from typical molecular dynamics simulations of iron-catalyzed formation of carbon species at 500 K (a-e) and 1000 K (f-j). At low temperatures, the particle is encapsulated by a graphitic layer, whereas SWCNTs are nucleated at intermediate temperatures. Images modified with permission from ref. 131.

1.6.2 Types of carbon nanotube growth

Nanotube growth in CVD can proceed in two different ways, depending on the specific reaction conditions. One possibility is tip-growth, otherwise known as “float-growth”, in which the catalyst nanoparticle detaches from the substrate and leaves a carbon nanotube trail between itself and the substrate (figure 1.6a).[134] Alternatively, growth can proceed *via* base-growth, in which the catalyst nanoparticle remains in contact with the substrate and the nanotube forms and grows outwards from the nanoparticle (figure 1.6b).[135] The dominating path is dependent on the interactions between the catalyst nanoparticle and the substrate, demonstrated by the work of Wang *et al* in which iron was used as a catalyst and the nature of the substrate was varied.[136] They suggested that if the interfacial energy between the catalyst nanoparticle and the substrate is greater than the surface energy of the substrate itself, tip-growth would dominate, which they observed with a silica substrate. Conversely, with a tantalum substrate, the iron/tantalum interfacial energy was lower than the surface energy of pure tantalum so base-growth was the dominant pathway.[136]

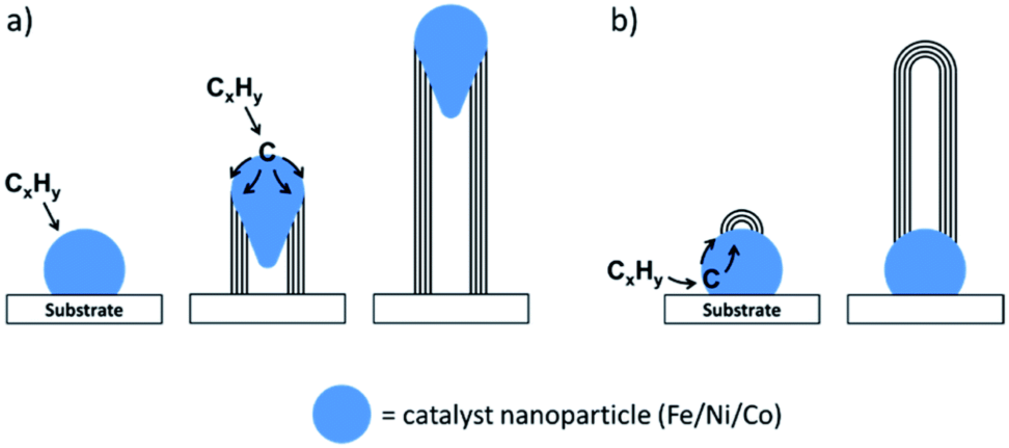

Figure 1.6: Schematic of a) tip-growth and b) base-growth mechanisms of carbon nanotube growth in chemical vapour deposition, driven by decomposition of a hydrocarbon gas and dissolution of carbon into a catalyst particle. Figure reproduced with permission from ref. 18.

In CVD, the structure of the nanotube can also vary between systems. In some examples, continuous nanotubes are observed, whereas in other systems, so-called “bamboo-like” carbon nanotubes are reported. Bamboo-like nanotubes contain layers of graphitic carbon within the nanotube structure, similar to bamboo, rather than a straight channel as in continuous nanotubes.[137] The formation of bamboo-like carbon nanotubes has been observed *in situ* using ETEM. In a CVD study by Ichihasi *et al,* the authors were able to observe the formation of both continuous and bamboo-like nanotubes within the same sample (figure 1.7).[138] Continuous nanotubes were formed by constant tip-growth of the catalyst nanoparticle, leaving a nanotube in its path. However, in some cases, the catalyst nanoparticle would stop moving for a short amount of time and deposit a layer of graphitic carbon before becoming mobile again, resulting in the formation of a bamboo-like carbon nanotube.[138]

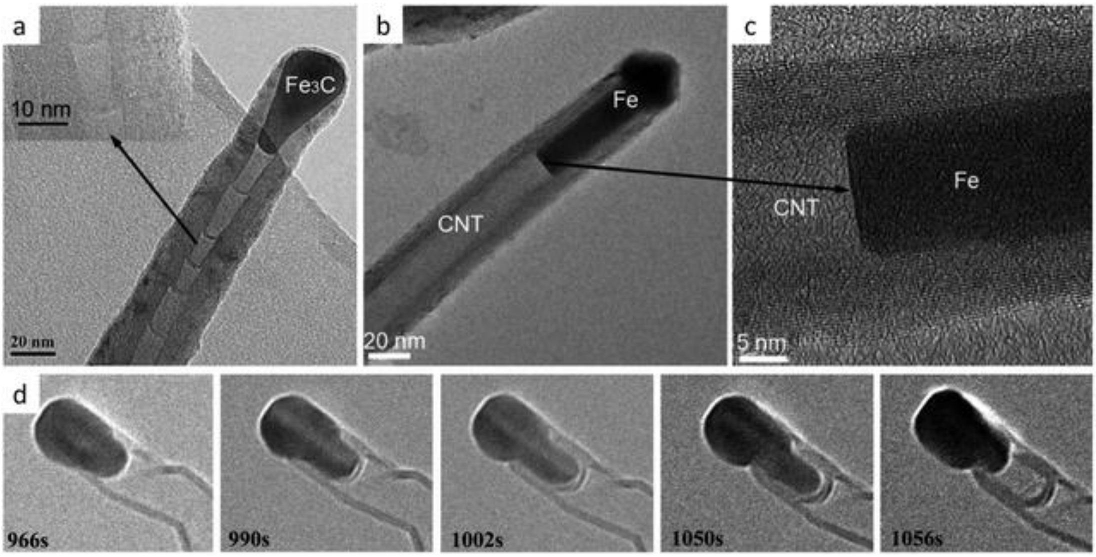

Figure 1.7: TEM images of a) bamboo-like and b) and c) continuous carbon nanotubes and d) in situ growth of a bamboo-like carbon nanotube. Composite figures reproduced with permission from ref. 18.

1.6.3 Chemical nature of the catalyst

An area of debate in both CVD and catalytic graphitization systems is the chemical nature of the catalyst nanoparticle during graphitization. Some authors argue that iron carbide (Fe_3C) hinders the growth of nanotubes,[139] while others believe that it is a necessary phase.[140] Other reports have suggested that the different phases result in different graphitic nanostructures, with iron producing continuous nanotubes and iron carbide producing bamboo-like nanotubes.[137]

The high activity of iron-based catalyst particles is commonly credited to the high carbon solubility of iron (up to 2.14 wt%) at temperatures of around 700-800 °C. One of the proposed mechanisms of graphitic carbon formation is a dissolution-precipitation mechanism. The iron particle dissolves carbon atoms until it reaches a point of supersaturation, before depositing graphitic carbon onto its surface. This hypothesis has been used to explain why transition metals with a low carbon solubility such as copper show poor catalytic activity for graphitization, while metals with high carbon solubility such as iron and nickel show high activity.[72] An alternative theory suggests that the formation of metastable carbides is crucial for graphitization, with graphitic carbon being deposited as a result of the decomposition of these metastable carbides into the more thermodynamically stable metal species along with graphitic carbon. As well as having a low carbon solubility, copper does not form metastable carbides, thought to be as a result of its completely filled electronic d-shell not allowing for the formation of bonds with carbon. Therefore, the carbide decomposition mechanism may also explain the low activity of copper.[72,141] The nature of the mechanism in iron systems is difficult to determine as both iron and iron carbide are commonly observed in CVD and catalytic graphitization systems. Therefore, both dissolution-precipitation and carbide decomposition mechanisms have been reported. A study by Yan *et al* proposed that as iron carbide is stable at the temperatures involved in catalytic graphitization, it is unlikely that the formation of graphitic carbon is due to metal carbide decomposition.[72] Instead, they suggested that the iron carbide and iron species may both act as dissolution-precipitation catalysts, contributing to a high catalytic activity in iron species.

1.6.4 Physical nature of the catalyst

Determining the physical state of the catalyst particle during graphitization has also proven to be an area of contention. A commonly cited theory describing the physical state of the catalyst in CVD processes is the vapour-liquid-solid mechanism first proposed by Wagner and Ellis to explain the growth of silicon whiskers.[142] This mechanism suggests that the catalyst particle must be in a liquid state to promote growth. However, the melting temperature of bulk iron is 1538 °C,[143] much higher than the reaction temperatures used in CVD and catalytic graphitization processes. The melting point of iron carbide is less simple to define as it is metastable, so does not have a well-defined melting point – it generally decomposes into elemental iron and carbon at 1227 °C.[143] Even so, some authors have observed liquid-like behaviour during *in situ* studies using ETEM.[144] A study by Harutyunyan *et al* proposed that the formation of a liquid phase is essential for growth of carbon nanotubes in CVD and the formation of a solid particle hinders growth.[145] While the heating effects of the high energy electron beam within the ETEM may be a factor in these studies, similar tubular nanostructures – likely formed by the movement of catalyst nanoparticles – are commonly observed *ex situ* as well, suggesting that this behaviour is not exclusively as a result of the electron beam. Other authors, however, argue that the catalyst particle remains in the solid state, and that the liquid-like behaviour is due to the constant fluctuation of the catalyst nanoparticle phase.[140] While many of these ETEM experiments have been performed to study CVD syntheses, similar liquid-like behaviour has been observed in the catalytic graphitization of cellulose filter paper with iron nitrate solution.[79] Using ETEM, the catalyst particle was observed to move through the solid amorphous carbon matrix, leaving behind a trail of tubular graphitic carbon.

As well as *in situ* experimental studies, modelling studies have been used to provide insight on the melting behaviour of iron-based nanoparticles. Methods such as molecular dynamics have shown that the melting temperature of metal nanoparticles can be considerably lower than the corresponding bulk melting temperature.[146] Therefore, the melting temperatures stated in binary phase diagrams such as the iron-carbon phase diagram may not be applicable to nanosized objects, raising the possibility that the catalyst nanoparticles may be in a liquid or liquid-like state. One model, carried out by Ding *et al*, suggests that both states are possible.[147] Their study modelled the growth of single-walled carbon nanotubes on both solid and liquid iron nanoparticles and found that the two routes had similar growth mechanisms. The main difference was that the main diffusion pathway of the carbon atoms through liquid nanoparticles was through the bulk, while surface diffusion dominated in solid nanoparticles.[147] In real systems, both routes may take place at the same time as the nanoparticles are unlikely to be completely uniform in size. Therefore, it is possible that smaller particles are in a liquid state and larger particles are in a solid state at the same temperature, but the resulting nanostructure may be the same in both scenarios.

A further factor to consider is that some metals, including iron, are known to undergo surface melting. This may explain the liquid-like behaviour of the catalyst nanoparticles in some systems. Ding *et al* have used molecular dynamics to demonstrate that surface melting occurs at temperatures below the melting temperature in both free[148] and supported iron nanoclusters,[149] with the depth of the surface melt increasing with temperature until the cluster undergoes complete melting. Therefore, as well as both solid and liquid states, it is possible that the nanoparticles occupy “in-between” states in the process of graphitization.

The presence of a surface is also an important aspect to consider in the melting behaviour of the catalyst nanoparticles in CVD and catalytic graphitization. Modelling results have shown that the interaction strength can significantly affect the melting temperature,[149] and favourable epitaxy between the nanoparticle and the substrate can raise the melting temperature by hundreds of degrees.[150] This implies that the suggested variation in melting temperature may not be a purely size-based argument.

1.7 Conclusions and perspective

Iron-catalyzed graphitization has shown the potential to be a scalable and economic route to nanostructured graphitic carbon materials. Significantly, it opens up the possibility of using natural organic precursors such as cellulose or sawdust, rather than precursors that originate from fossil fuel sources or indeed a pure carbon source, as is required in some other synthesis routes. The catalyst particles are also formed *in situ* from a cheap iron source such as iron nitrate, resulting in a straightforward synthesis route.

However, a number of obstacles must still be overcome before iron-catalyzed graphitization may be widely used to produce truly tailorable graphitic carbon nanostructures to match the precise requirements of a real-world application. The wide variety of combinations of organic precursors and iron sources has shown the apparent flexibility of iron-catalyzed graphitization routes, but there are few examples of systematic studies of the process in which the effect of different reaction conditions has been examined. Without such studies, it is difficult to assess the impact of the choice of organic or metal precursor – as well as experimental parameters such as temperature, dwell time and heating rate – on the final graphitic carbon nanostructure.

Another challenge is the limited understanding of the fundamental mechanism of the graphitization process. The reasons why the catalyst particles sometimes become mobile and produce tubular nanostructures and sometimes remain stationary and form shell-like structures is unclear. Further questions relating to the exact chemical nature (iron or iron carbide) and physical nature (solid or liquid) of the catalyst nanoparticle during graphitization also remain unanswered. Improved understanding of the behaviour of the catalyst particles during graphitization may allow for control over the structure of the resulting nanostructured graphitic carbons, which would enable the structures to be tailored to match the requirements of real-world applications.

Much of the existing research of the mechanism of graphitization has been focused on CVD processes, and while some of the same ideas may be applied, further studies specifically related to iron-catalyzed graphitization systems are required. *In situ* experiments, such as synchrotron PXRD or ETEM, along with increasingly sophisticated computational methods will likely offer significant insight into the fundamental mechanistic aspects of iron-catalyzed graphitization. However, on a simpler scale, systematic studies of factors affecting the structure of the resulting carbons will also be important to identify optimal precursors and reaction conditions.

Chapter 2 – Solid state characterization methods

2.1 XRD

2.1.1 Crystallography

Crystalline solids contain repeating units of atomic arrangements, and the smallest repeating unit is known as the "unit cell". The unit cell can be described by three cell edge lengths – a, b and c – and three angles – α, β, γ. The various possible values of these lengths and angles give rise to seven primitive lattice types, where atoms occupy the corners of the unit cell. These are listed in table 2.1. Centring – namely, primitive (P), body centring (I), face centring (F) or base centring (C) (table 2.2) – gives a total of 14 unique lattice types, known as "Bravais lattices". Crystal structures with a particular Bravais lattice will share a common collection of mirror planes and rotational symmetry axes. Each crystal system has a set of essential symmetries, which limits the types of centring which are "allowed". For example, attempting to construct a cubic lattice with C centring, will disrupt the essential symmetry of a cubic system and inadvertently create a primitive tetragonal cell. Therefore, a base centred cubic lattice is not a unique lattice type.

Introducing different atoms into a unit cell leads to additional symmetry elements which can be used to describe the specific crystal structure. These include screw axes and glide planes. The inclusion of all possible symmetry elements results in 230 possible space groups, which can be used to describe the symmetry of all crystal systems. Planes of atoms within a lattice are described by values known as "Miller indices" (*hkl)*. The h, k and l values are equal to the reciprocal of the intercepts along each of the unit cell edge lengths.

Table 2.1: Details of the Bravais lattices.

Crystal system	Unit cell lengths	Unit cell angles (°)	Allowed centring
Cubic	a = b = c	$\alpha = \beta = \gamma = 90$	P, I, F
Tetragonal	a = b ≠ c	$\alpha = \beta = \gamma = 90$	P, I
Orthorhombic	a ≠ b ≠ c	$\alpha = \beta = \gamma = 90$	P, I, F, C
Rhombohedral	a = b = c	$\alpha = \beta = \gamma \neq 90$	R
Hexagonal	a = b ≠ c	$\alpha = \beta = 90$ °, $\gamma = 120$	P
Monoclinic	a ≠ b ≠ c	$\alpha = \gamma = 90$ °, $\beta \neq 90$	P, C
Triclinic	a ≠ b ≠ c	$\alpha \neq \beta \neq \gamma \neq 90$	P

Table 2.2: Unit cell types

Type of centring	Description
Primitive (P)	Lattice points only at corners of the unit cell
Rhombohedral (R)	Also has no centring, but is a trigonal shape
Body centred (I)	Lattice points at the corners and the centre of the unit cell
Face centred (F)	Lattice points at each corner and in the centre of each face of the unit cell
Base centred (C)	Lattice points at each corner and at the centre of opposite faces

2.1.2 Diffraction experiment

In a typical powder X-ray diffraction experiment, X-rays are generated by passing a current through a tungsten cathode, resulting in thermionic emission of electrons. The electrons are accelerated towards a cooled metal anode under vacuum by applying a potential difference of approximately 40 kV. Collisions of the electrons with the metal anode causes ionisation of the core electrons. As the electrons relax down to lower orbitals, thermal energy is released alongside the emission of X-rays with energies characteristic of the anode material. A continuous “background” spectrum is also observed due to Bremsstrahlung, or “braking radiation”, which is produced as the electrons decelerate as they approach the metal anode.

For a diffraction experiment, it is important to have an X-ray source with a single, defined wavelength. However, anode materials generally give rise to multiple characteristic emission lines. Copper, for example, gives rise to three characteristic emission lines. Therefore, filters or monochromators are generally used to remove part of the emission spectra.

X-rays are scattered by areas of electron density. Therefore, lattice planes are able to scatter an incident X-ray beam. Parallel planes allow for diffraction to occur as the atomic distances are similar in magnitude to the wavelength of the incident X-ray beam. If a monochromatic X-ray beam is fired at two parallel planes, the beam must travel further to reach the second plane than the first plane. As a result, the beam becomes phase shifted and destructive interference will occur between the waves of the two diffracted beams and no intensity will be observed in the diffraction pattern. However, if the difference in path length is equal to a multiple of the incident wavelength of the X-ray beam, constructive interference will occur, and a peak will be observed in the diffraction pattern. This relationship is described by Bragg’s law:

$$n\lambda = 2d_{hkl}\, sin\, \theta \tag{2.1}$$

Where n is an integer, λ is the wavelength of the incident X-rays, d_{hkl} is the interplanar spacing and 2θ is the diffracted angle of the beam relative to the incident X-ray beam. Peaks are present at specific values of 2θ and correspond to particular interplanar spacings. These are related to the unit cell parameters a, b, c, α, β *and* γ, which allows for characterization of the crystal structure. For example, in a structure with a tetragonal unit cell, where $a = b \neq c$ and $\alpha = \beta \neq \gamma$, the d_{hkl} values can be described using the following expression:

$$\frac{1}{d_{hkl}^2} = \frac{h^2 + k^2}{a^2} + \frac{l^2}{c^2}$$

(2.2)

The intensity, I_{hkl} of each Bragg reflection is described by the following equation:

$$I_{hkl} = K_{hkl} F_{hkl}^2 m_{hkl} A_{hkl} Lp_{hkl}$$

(2.3)

Where K_{hkl} is a proportionality constant, F_{hkl} is the structure factor, m_{hkl} is the multiplicity of the Bragg reflection, A_{hkl} is an absorption correction factor (which is dependent on the composition and thickness of the sample) and Lp_{hkl} is the Lorentz factor (corrects for the probability of observing a Bragg reflection at a certain angle, and a radiation polarization factor).

The structure factor for each peak is dependent on the atom type and positions within the unit cell and is expressed using the following equation:

$$F_{hkl} = \sum_j t_j f_j exp\left[2\pi i\left(hx_j + ky_j + lz_i\right)\right]$$

(2.4)

Where x_j, y_j and z_j are fractional atomic coordinates, f_j is the atomic scattering factor of atom j and t_j accounts for atomic vibrations around their average positions.

2.1.3 Scherrer analysis

The widths of peaks in a diffraction pattern can be used to extract information about the size of crystallites within a powder sample using the Scherrer equation:

$$\tau = \frac{K\lambda}{\beta cos\theta} \tag{2.5}$$

Where the mean crystallite size, τ, is related to the shape factor, K, which typically has a value of 0.9 assuming spherical crystallites, the wavelength of the incident X-rays, λ, the line broadening at the full width at half maximum after subtracting the instrumental broadening, β and the diffracted angle, θ.

2.1.4 Rietveld refinement

Rietveld refinement is a whole pattern method for analysing PXRD data.[151,152,153] In a single crystal XRD experiment, discrete diffraction spots with easily measurable intensities are obtained, whereas a powder sample consists of many small crystals in random orientations, results in rings of scattering. Therefore, peaks with similar d-spacings can overlap and information regarding the individual intensities may be lost. Taking a whole pattern approach to PXRD analysis and comparing to a structural model along with parameters to describe peak shapes and the background allows for crystallographic information to be calculated.

A least squares method is used to minimize the difference between a model diffraction pattern. This difference is referred to as the residual, S_y, and is described by equation 2.6:

$$S_y = \sum_i w_i (y_i - y_{ci})^2$$

(2.6)

where w_i is equal to $1/y_i$, y_i is the observed intensity at the *i*th step and y_{ci} is the calculated intensity at the *i*th step.

The quality of the refinement can be followed using factors such as the weighted profile R factor, R_{wp}, which should decrease as the calculated diffraction pattern becomes more similar to the experimental data (equation 2.7).

$$R_{wp} = \sqrt{\frac{\sum w_i (y_i - y_{ci})^2}{\sum w_i (y_i)^2}}$$

(2.7)

Common parameters that are refined during the fitting procedure include unit cell parameters, atomic occupancies, atomic positions and thermal displacement parameters.

2.2 Electron microscopy

2.2.1 TEM

Rather than using a conventional optical microscope, which is limited by the wavelength of visible light, features on the nanoscale can be probed using TEM by exploiting the small wavelength of electrons, described by the de Broglie equation (equation 2.8), in which λ refers to the wavelength of the electrons, *h* is Planck's constant, *m* is the particle's mass and *v* is its velocity. The wavelength of electrons is similar to the interatomic distances in solids so will undergo diffraction when passed through a crystalline material. In a TEM, the electron beam is fired through the sample and the transmitted electrons are used to create an image.

$$\lambda = \frac{h}{mv}$$

(2.8)

In electron microscopes, the electrons are usually generated through thermionic emission. A filament commonly made of tungsten or lanthanum boride is used as a source of electrons and acts as the cathode. Accelerating voltage (100-300 kV) is applied to the surrounding cathode cap, known as a “Wehnelt cylinder”. A small emission current is then applied to the filament to produce heat and once the filament is supplied with enough energy, electrons are ejected from the filament and attracted towards a positively charged anode. The negatively charged Wehnelt cylinder acts a convergent lens to initially focus the electron beam as the filament will produce electrons in all directions.

As electrons are easily scattered by air particles, the whole column of the microscope is held under vacuum with a liquid nitrogen cold trap attached to condense any contaminants that may have entered the system.

After passing through the Wehnelt cylinder, the electron beam is further focused by various sets of lenses. These act in the same way as glass lenses are used to focus the beam of light in an optical microscope, but rather than glass, each lens is a coil of copper wire through which a current is passed to generate an electromagnetic field that directs the beam. There are three sets of these lenses in a TEM: the condenser lens that focuses the beam onto the sample, the objective lens, which helps to focus and magnify the beam after it has passed through the sample and the projector lens, which further magnifies the beam so that it can hit a phosphorescent screen that can be used to produce an image of the sample (figure 2.1). A CCD can then be used to capture a digital image.

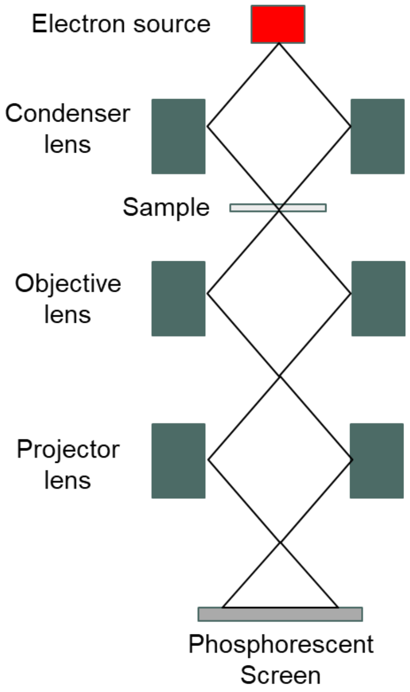

Figure 2.1: Schematic of a TEM.

In order to generate an image, the electrons must be able to penetrate through the whole sample, so it is important to produce a very thin sample (100-200 nm), especially if the components are particularly highly scattering. There are various ways to achieve this; however, most of the samples in this thesis were prepared by dispersing a small amount of solid sample in a solvent and depositing onto a thin copper grid. Copper is the most common material used for TEM grids as it is electronically conductive, stable in the electron beam and relatively inexpensive. The grids are often coated with a carbon film, which allows the electron beam to pass through and stops the sample from falling between the gaps in the grid.

The majority of the electrons in the beam pass straight through the sample. These transmitted electrons are used to construct the standard type of images in TEM, known as “bright field images”. Darker areas in these images indicate more electron-dense regions of the sample where the electrons have been scattered away from the primary beam axis, such as areas that contain heavier elements.

Alternatively, the user can view the scattered electrons to produce a dark field image where the more electron-dense regions appear lighter and the regions which let the beam pass straight through appear dark. It is often not necessary to obtain both dark and bright field images; however, in some cases, the dark field image can provide greater structural detail, such as the possibility to view crystal defects.

As well as imaging, a TEM can be used to gain some crystallographic information about the sample. Just as with X-rays in XRD experiments, crystalline samples can act as diffraction gratings for electrons. If the portion of sample that is being analysed consists of a single crystal, then a spot diffraction pattern will be observed, as in single crystal XRD. If the area of sample consists of a random orientation of crystal directions, then a ring pattern will be produced. These diffraction patterns can be extremely useful to determine the exact phases present in different regions of a sample.

2.2.2 SEM

Many of the general principles of TEM can also be applied to SEM; however, the accelerating voltage used is a lot lower, 5-20 kV compared to 100-300 kV in TEM. As inside a TEM, it is vital that the column is kept under vacuum so that the electron beam does not interact with anything other than the actual sample being analysed.

The electron beam is generated in the same way as in a TEM, using either thermionic emission from a tungsten filament or lanthanum boride crystal or using a field emission device. The beam is then subjected to focusing through sets of electromagnetic lenses (figure 2.2).

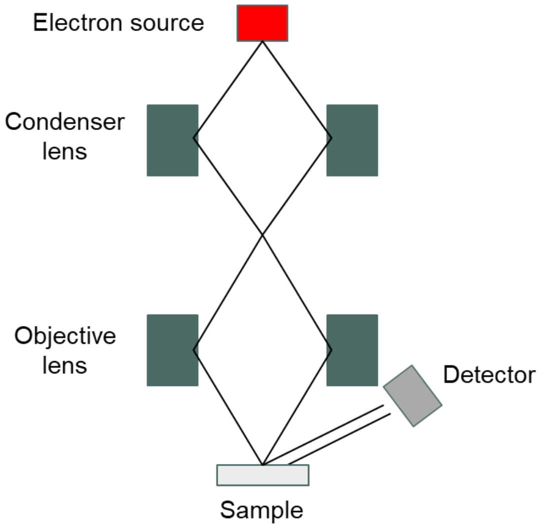

Figure 2.2: Schematic of a SEM.

The beam is first passed through a condenser lens which demagnifies it, meaning the size of the beam is decreased. This helps to improve the image resolution. Rather than passing through the sample at this point, as in TEM, the beam then travels through an objective lens which is used for further demagnification along with focusing before the beam finally hits the sample located at the bottom of the column (figure 2.2) Various interactions can occur when the electron comes into contact with the sample, and these interactions lead to different signals, as shown in figure 2.3..

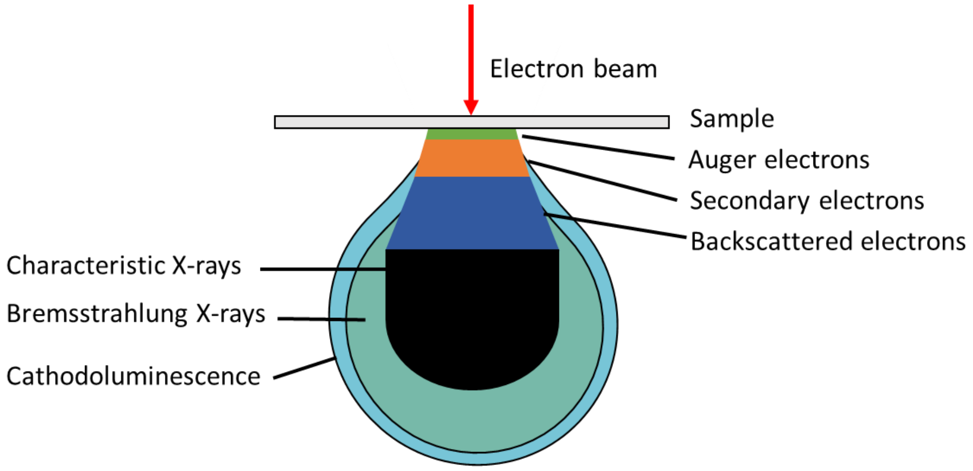

Figure 2.3: Possible signals emitted by a sample in SEM.

The signals that are of primary interest for SEM are secondary electrons and backscattered electrons. Secondary electrons, which can be used to produce high-resolution images of the surface, are generated by collisions between the electron beam and the loosely bound outer electrons of the atoms within the sample. These are low in energy, so can only give information on atoms near the surface of the sample – secondary electrons produced by atoms further into the bulk will get absorbed. Secondary electrons are affected by atomic number as heavier elements produce a greater number of secondary electrons, and also by curvature of the sample surface (figure 2.4) so can provide detailed topographical information about the sample.

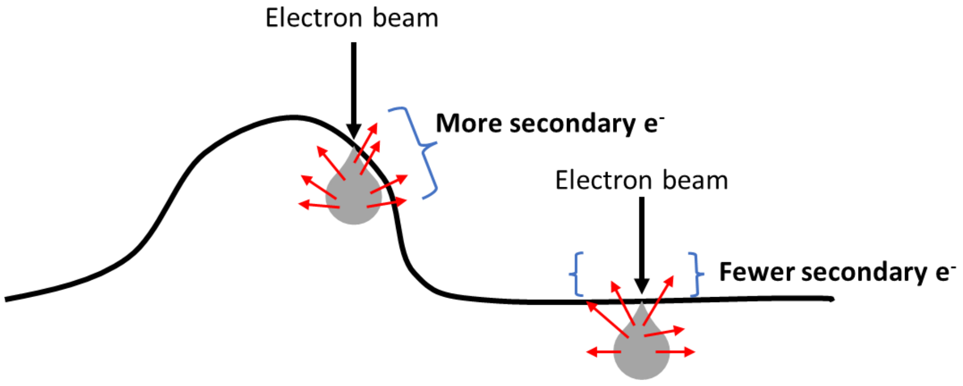

Figure 2.4: Schematic of secondary electrons on curved and flat surfaces.

Some of the electron beam interacts with the nucleus of the atoms in the sample and elastically scattered at an angle of up to 180 °. The electrons produced in this interaction are known as “backscattered electrons” and display a much higher energy than secondary electrons. However, the likelihood of the electrons from the beam hitting an atomic nucleus is relatively low, so there are fewer backscattered electrons produced than secondary electrons. The number of backscattered electrons produced is greater for elements with a higher atomic number due to the larger nucleus so backscattered electrons can provide extra information on the sample composition.

2.3 Raman spectroscopy

Raman spectroscopy is a non-destructive technique based on the scattering of monochromatic light to probe the vibrational modes within a sample. The majority of scattering events are elastic, in which the energy of the incident photon is conserved (known as “Rayleigh scattering”), whereas Raman scattering is an inelastic process in which the energy of the scattered photon is shifted to either a higher or lower wavelength, known as “Stokes” and “anti-Stokes” Raman scattering, respectively. For a vibrational mode to be Raman active, the vibration must induce a change in polarizability of the molecule.

In the context of carbon materials, Raman spectroscopy can be used to probe the hybridization of the carbon atoms on the surface of the sample, therefore allowing for the degree of graphitization to be determined.

2.4 SAXS

SAXS is a non-destructive technique that can probe the average structure in a bulk material and provide information on features in the 1-100 nm size range.

In a standard setup, collimated monochromatic X-rays are irradiated through a sample in transmission mode. The majority of the incident X-ray beam will pass through the sample so a beamstop is used to block the incident beam that does not undergo scattering. The X-rays scattered to low angles (typically 0.1 to 10 °) can be measured.

Scattering occurs when there is an electron density contrast within the sample. Atoms in the sample scatter incident radiation in all directions, giving a background radiation that is almost constant at small angles. The particles inside the sample provide additional scattering due to contrasts within the sample and scatter to different angles depending on the size of the scattering feature. Larger features will scatter to smaller angles than smaller features and features with a larger electron density contrast with the surrounding matrix will generally contribute more to the scattering pattern. Scattering patterns are usually presented as a function of the scattering vector q, as given by equation 2.9, where θ is the scattering angle and λ is the wavelength of the X-ray source.

$$q = \frac{4\pi \sin \theta}{\lambda} \tag{2.9}$$

In the context of this thesis, SAXS is generally used to extract size distributions of iron-based particles with a relatively high atomic number within a matrix of carbon, which has a low atomic number. SAXS can be used to extract information about the size, shape or packing of scattering features within a sample, assuming that two of these are known quantities. For example, the packing of a sample can be calculated prior to a SAXS experiment, if the density of the components within the sample are known, by measuring the X-ray absorbance of the sample. Then, if the shape of the scattering features of interest is also known, from results of techniques such as electron microscopy, the size distribution can subsequently be extracted.

The size range of scattering features (D_{min} to D_{max}) that can be measured is dependent on the q range of the SAXS measurement as described in equations 2.10 and 2.11.

$$D_{min} \approx \frac{\pi}{q_{max}} \tag{2.10}$$

$$D_{max} \approx \frac{\pi}{q_{min}} \tag{2.11}$$

2.5 Nitrogen sorption

Nitrogen sorption measurements are used to assess the porosity of the materials in this thesis. Isotherms were collected using the static volumetric method. In this method, a known amount of nitrogen gas is dosed into the sample bulb, and the gas adsorbs onto the sample and the pressure in the sample bulb decreases until equilibrium is reached. The amount of gas adsorbed at the equilibrium pressure is the difference between the amount of gas dosed in and the amount of gas required to fill the space around the sample. An adsorption isotherm is constructed by gradually dosing in more nitrogen gas stepwise until a relative pressure, p/p^0, ≈ 1. A desorption isotherm is then constructed in the same manner by the stepwise removal of nitrogen gas from the sample bulb.

Isotherms are grouped into six general classes by IUPAC, shown in Figure 2.5.[154] Type I isotherms are commonly observed in microporous solids with relatively small external surfaces and display a characteristic rapid increase in the amount of gas adsorbed over the low relative pressure range. A subsequent horizontal or near horizontal plateau indicates that the micropores are filled and that little or no further adsorption takes place. Type I(a) indicates a narrow range of small micropores (with a width of less than 1 nm), whereas type I(b) indicates a broader range including wider micropores and possibly narrow mesopores (with a width of less than 2.5 nm). Type II isotherms are characteristic of non-porous or macroporous adsorbents and point B indicates the formation of a monolayer. Type III and type V isotherms are uncommon and suggest weak gas-solid interactions. Type III isotherms indicate non-porous and microporous adsorbents and type V isotherms indicate mesoporous adsorbents. Type IV isotherms are commonly observed for mesoporous adsorbents and are accompanied by hysteresis as a result of capillary condensation within the mesopores. Type IV(b) isotherms indicate narrow mesopore widths. The type of hysteresis loop can also be categorized and used to describe the nature of the mesoporosity. Finally, type VI is another uncommon isotherm and signifies layer-by-layer adsorption on a highly uniform nonporous surface.

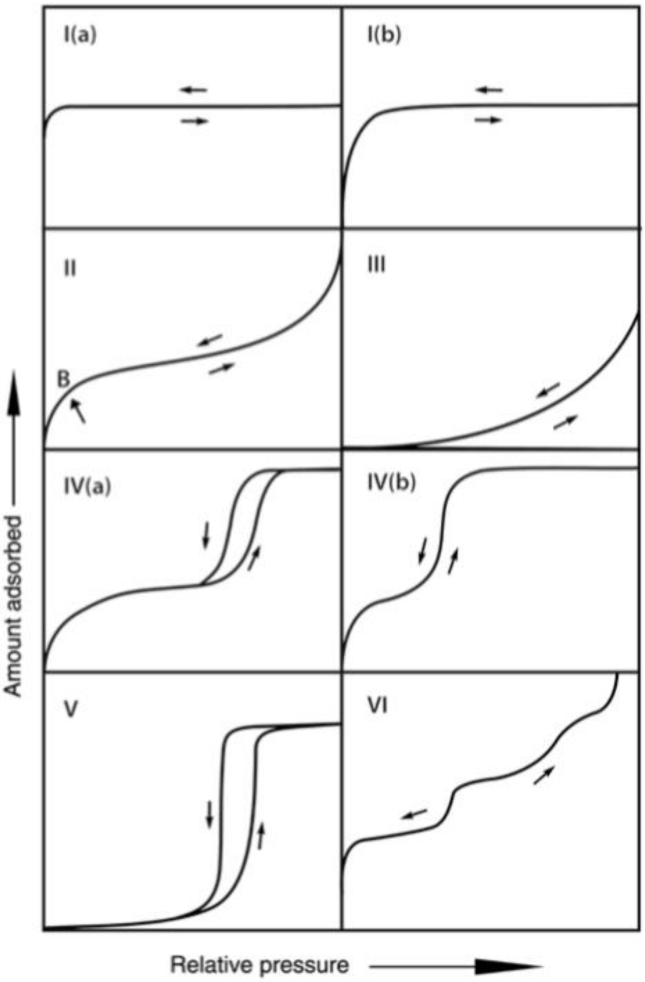

Figure 2.5: The six main types of physisorption isotherms. Figure reproduced with permission from ref. 154.

2.5.1 Determining total pore volume

The total pore volume, V_{tot} can be calculated from nitrogen sorption isotherms by taking the mass of gas adsorbed at the isotherm plateau, m_a, and using equation 2.12, where m_s is the mass of solid sample and ρ_l is the liquid density at the operational temperature.

$$V_{tot} = \frac{m_a}{\rho_l m_s} \tag{2.12}$$

2.5.2 Measuring specific surface area

The BET method is the most widely used method for evaluating the surface area of porous materials.[155] Two stages are involved in implementing the BET method to extract a specific surface area value:

1. Transform a physisorption isotherm into a linear BET plot using equation 2.13 and derive a value of the BET monolayer capacity, n_m, where n is the specific amount of gas adsorbed at the relative pressure p/p^0.
2. The BET surface area is calculated from n_m using equation 2.14 by adopting an appropriate value of the molecular cross-sectional area, σ (0.162 nm^2 for nitrogen at 77 K). N_A in the equation corresponds to Avogadro's number and m_{sample} is the mass of the sample.

$$\frac{p/p^0}{n(1-p/p^0)} = \frac{1}{n_m C} + \frac{C-1}{n_m C}(p/p^0) \tag{2.13}$$

$$S_{BET} = \frac{n_m \sigma N_A}{m_{sample}} \tag{2.14}$$

The range of linearity of the BET plot is always restricted to a limited part of the isotherm, often within the p/p^0 range of 0.05-0.30 for type II and type IV(a) isotherms. Values of the BET area are dependent on the adsorptive gas and operational temperature and the procedure used to locate the pressure range in applying the BET equation. The molecular cross-sectional area of nitrogen is assumed to be 0.162 nm^2 (assuming a closed-packed monolayer). However, it is now recognised that due to its quadrupole moment, the orientation of a nitrogen molecule is dependent on the surface chemistry of the adsorbent. This may lead to uncertainty in the value of σ (possibly 20 % for some surfaces).

It is also important to consider the following assumptions made by BET theory when calculating a value for the specific surface area of a sample:

- The model only considers adsorbate-adsorbent interactions – lateral adsorbate-adsorbate interactions of molecules within the same layer are excluded.
- All molecules in subsequent layers following the initial monolayer are assumed to be identical – instead, interactions between these molecules and the adsorbate will decrease with increasing distance from the surface.
- All adsorption sites are assumed to be energetically identical.

2.5.2.1 Application of the BET method to microporous materials

Caution is needed in the presence of micropores – it may be impossible to separate the processes of monolayer-multilayer adsorption and micropore filling. Therefore, it is often difficult to locate the appropriate linear range of a BET plot. Rouquerol *et al* developed a set of criteria to identify the appropriate linear pressure range to calculate the BET surface area, which is now widely used for the analysis of microporous materials:[155]

- The BET constant, C, should be positive.
- Application of the BET equation should be restricted to the range in which the term $n(1-p/p^0)$ continuously increases with p/p^0.
- The p/p^0 value corresponding to n_m should be within the selected BET range.

2.5.3 Micropore analysis using the t-plot

The micropore volume and micropore surface area can be calculated using the *t*-plot method.[156] In this method, gas adsorption isotherms of a sample are compared with a non-porous reference material of similar chemical surface composition. The amount of gas adsorbed on the sample at p/p^0 is plotted against t, the thickness of the adsorbed layer of the non-porous reference at the corresponding p/p^0 (equation 2.15)

$$t = \frac{V_a}{S_{BET}} = \frac{n_a}{n_m}\sigma_t \tag{2.15}$$

The parameter n_a refers to the amount of gas adsorbed on the sample at p/p^0, n_m is the monolayer amount, σ_t is the thickness of a single monolayer and V_a is the pore volume.

A non-porous sample identical to the reference would give a linear plot and the difference between the pore structures is shown as a non-linear region on the *t*-plot. The specific surface area can then be calculated from the gradient of a linear section and the pore volumes from the extrapolated intercept.

As the *t*-plot method uses the BET equation to calculate the value for *t*, it has the same limitations and assumptions as the BET specific surface area calculations so it can be useful to compare similar samples, but the absolute values may not be a true representation of the sample’s pore structure.

2.6 XPS

XPS is a spectroscopic technique based on the photoelectric effect that can be used to determine elemental composition and the chemical states of elements on the surface of a material. In XPS, a sample is irradiated with an X-ray beam of a specific energy (hv) and the kinetic energy (E_K) of the emitted secondary photoelectron is measured. Using equation 2.16, where φ refers to the work function of the element, the binding energy (E_B) of the released photoelectron can be calculated, which can be used as a fingerprint to identify specific elements and chemical states.

$$E_B = h\nu - E_K - \varphi \tag{2.16}$$

The peak intensity in an XPS spectrum is proportional to the elemental concentration so can be used to quantify the composition of the sample surface.

Chapter 3 - The effect of precursor structure on porous carbons produced by iron-catalyzed graphitization of biomass

3.1 Introduction

In chapter 1, the range of different types of organic precursors and synthesis conditions used in iron-catalyzed graphitization routes was discussed, highlighting factors that can influence the resulting porous carbon structure. Previous work has shown that subjecting solid lignocellulosic biomass sources to milling, before soaking in iron nitrate solution and subsequently pyrolyzing, resulted in a more consistent graphitic product.[91] This was attributed to the more consistent coverage of the biomass sources with iron irons in the milled biomass samples. However, variation in the degree of graphitization and the subsequent adsorptive capacity for methylene blue remained after milling, likely due to the structural differences between the biomass sources.

The precise structure of biomass is complex and often varies between different plant species, or in different parts of the plant.[157] Therefore, in this chapter, the structural complexity and variation is minimized by focusing on three compositionally similar but structurally different organic materials, glucose, starch and cellulose, all of which are commonly found in biomass. Glucose is a monosaccharide with the molecular formula $C_6H_{12}O_6$, figure 3.1a, and is highly soluble in water. Starch is a mixture of two polysaccharides, amylose and amylopectin, shown in figures 3.1b and c. The amylose and amylopectin contents in starch can vary depending on its origin. There is typically around 20-35 % amylose in common starches such as potato and corn, but it can range from 3-50 %.[158] Amylose is a linear polymer with a molecular weight of 1×10^5

– 1 x 10^6 $gmol^{-1}$, consisting of *α*(1→4) linked glucose units. Similarly, amylopectin also comprises of *α*(1→4) linked glucose units but approximately 5 % of the glucose units have an *α*(1→6) linked chain, resulting in a more branched structure. Starch consists of a granular structure, with regions of amorphous and crystalline lamellae. Unlike glucose, starch is not truly water soluble – the granules undergo swelling in hot water, resulting in a colloidal gel.[159] Finally cellulose, figure 3.1d, is also a polysaccharide, consisting of a single linear polymer made up of *β*(1→4) linked glucose units. Cellulose is insoluble in water and the linear polymer chains tend to assemble into fibres and fibrils due to the strong intermolecular hydrogen bonding between the cellulose polymers.[160]

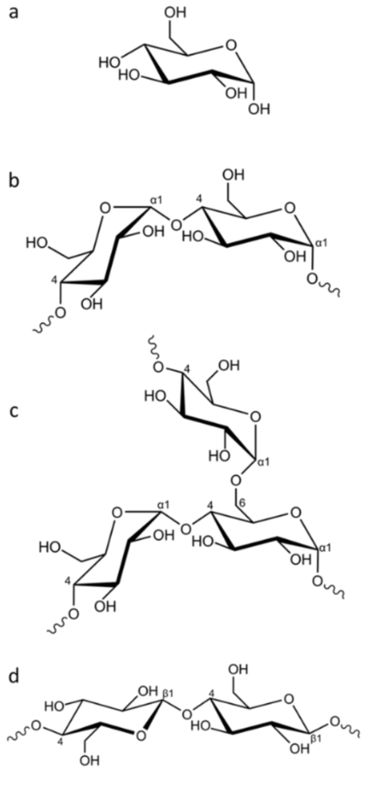

Figure 3.1: Structures of a) glucose, b) amylose, c) amylopectin and d) cellulose

3.2 Experimental

3.2.1 Materials

Table 3.1: Details of materials used in this chapter.

Material	Supplier	CAS number
D-(+)-glucose	Sigma-Aldrich	50-99-7
Starch, from potato	Sigma-Aldrich	9005-25-8
Cellulose fibres, (medium)	Sigma-Aldrich	9004-34-6
Iron (III) nitrate nonahydrate, ≥98 %	Sigma-Aldrich	7782-61-8
Starch from corn (S4126)	Sigma-Aldrich	9005-25-8
Starch from corn (S9679)	Sigma-Aldrich	9005-25-8
Amylose from potato	Sigma-Aldrich	9005-82-7
Hydrochloric acid, 37 wt% in H_2O	Sigma-Aldrich	7647-01-0
Ethanol, absolute, ≥99.8 %	Fisher Scientific	64-17-5
Hydrogen peroxide, 30% w/v	VWR Chemicals	7722-84-1

3.2.2 Catalytic graphitization

For glucose samples, 5 g of D-(+)-glucose was dissolved in 20 ml DI water in a beaker with gentle heating to 40 °C and stirring for 10 min, 0.27 g (0.68 mmol) of iron nitrate nonahydrate was dissolved in 4 ml of DI water and this was added to the glucose solution, followed by stirring for 10 min. The mixture was dried in an oven at 70 °C for 24 hr. The resulting brown, caramel-like sample was placed in an alumina boat crucible then heated in a tube furnace at a rate of 5 °C/min under a nitrogen atmosphere with a flow rate of 1 l/min to 800 °C. The samples were dwelled at 800 °C for 1 hr before cooling completely to room temperature.

For starch samples, the procedure was the same except 5 g of potato/corn starch was dissolved in 45 ml of DI water at 70 °C and stirred for 10 min. 0.27 g (0.68 mmol) of iron nitrate nonahydrate was again dissolved in 4 ml of DI water and this was added to the starch mixture, followed by stirring for 10 min. The mixture was dried (as in glucose samples) to produce an orange solid, which was subjected to the same heating procedure as glucose samples.

For cellulose samples, 0.27 g (0.68 mmol) of iron nitrate nonahydrate was dissolved in 15 ml of DI water at room temperature and the resulting solution was added to a beaker containing 5 g of cellulose fibres (powder). The mixture was manually stirred for 10 min until the solution had been absorbed. The sample was dried to give a yellow powder and pyrolyzed as above. The amount of water was kept to a minimum in each of these samples to reduce the energy requirements in the drying step.

3.2.2.1 Reason for different preparation methods for glucose, starch and cellulose

Different amounts of water were used in each of the three systems, depending on the amount needed to achieve solubility or saturation. The aim of each preparation method was to combine a certain molar amount of iron nitrate with a certain mass of biomass, so this ratio was kept constant across the three samples. The challenge was to achieve a homogeneous mixing of the iron with each of the three biomass precursors. Glucose is highly soluble in water, so it was possible to completely dissolve 5 g in 20 ml DI water and combine this with iron nitrate, followed by drying. Gentle heating to 40 °C was used simply to speed up dissolution. Potato starch is less soluble, so required more DI water (45 ml) and a greater amount of heating (to 70 °C) to get a homogeneous “solution” of starch that could be combined with iron nitrate (the starch granules swell rather than truly dissolve). Cellulose fibres are insoluble in water. Soaking cellulose powder in iron nitrate solution with an excess of solution would have led to pooling of the solution around the solid sample and an unclear amount of iron nitrate on the actual cellulose. Therefore, the amount of water needed to completely saturate 5 g of cellulose was tested, and the required amount of iron nitrate was dissolved in this volume of water and added to the cellulose. The mixture was stirred to ensure an even coating of iron nitrate on the cellulose.

3.2.3 Acid-washing

0.2 g of carbon/iron carbide sample was sonicated in 20 ml of 0.1 M hydrochloric acid for 1 hr. The mixture was then magnetically stirred for 24 hr. The solid sample was collected by centrifugation and washed three times with DI water and once with ethanol, then left to dry at room temperature in air for 24 hr.

3.2.4 PXRD

Samples were ground into a powder and placed on low-background silicon wafer sample holders. Measurements were performed using a PANalytical Empyrean diffractometer with a copper anode (wavelengths: $K_{\alpha 1}$ = 1.5406 Å, $K_{\alpha 2}$ = 1.5443 Å) and a Pixel 2D detector. The diffractometer did not have a monochromator but the K_{β} radiation was removed with a nickel filter.

3.2.5 Raman spectroscopy

Samples were ground into a fine powder and placed on a glass slide. Raman spectroscopy measurements were collected using a Renishaw inVia Raman microscope using a red laser at 10 % power with a wavelength of 633 nm. Peak fitting was performed assuming a 4 peak Voigt function.

3.2.6 SEM

Samples were mounted on a SEM stub using an adhesive copper tape and viewed with a FEG-SEM FEI Nova using a CBS detector at the School of Chemistry, University of Leeds, operating at 5 kV with deceleration mode.

3.2.7 TEM

Small portions of samples (≈ 50 mg) were dispersed in ethanol (≈ 1 ml) by sonication for 10 min. One drop of the dispersion was pipetted onto a carbon-coated copper TEM grid. The images were obtained using a JEOL 2100 TEM containing a tungsten filament and a CCD detector within the School of Metallurgy and Materials at the University of Birmingham.

3.2.8 SAXS

Samples were ground into a fine powder and distributed across a hole in a paper sample holder between two pieces of Scotch® Magic™ tape. The wide-range SAXS experiments were performed using the Multi-scale Analyser for Ultrafine Structures at the Federal Institute for Materials Research and Testing, Berlin. Copper and molybdenum anodes (8 eV and 17 eV photons, respectively) were used to measure over a wide *q*-range.

3.2.9 Nitrogen sorption

Nitrogen sorption measurements were carried out at 77 K using a 3Flex volumetric gas sorption analyser from Micromeritics at the University of Bristol. 100-300 mg of sample was degassed at 300 °C for 4 hr under 10^{-7} mbar vacuum. Nitrogen (AirProducts, 99.999 %) isotherms were collected with filler rods over the range p/p^0 10^{-8} – 1.0 and helium was used to calculate the free space following isotherm collection.

3.3 Results and discussion

3.3.1 Graphitization of glucose, starch and cellulose

Carbon samples prepared by iron-catalyzed graphitization were analysed by PXRD (figure 3.2). A peak at approximately 26 ° 2θ, characteristic of graphitic carbon, is present in all the diffraction patterns, showing that it was possible to introduce some degree of graphitization in all three organic precursors. The peaks at 26 ° 2θ are all relatively broad, broader than would be expected for a pure graphite sample (assuming an interlayer spacing of 0.334 nm, the peak corresponding to the (002) reflection would be sharp and centred around 26.7° 2θ) suggesting a considerable amount of disorder remained in the carbon structure.

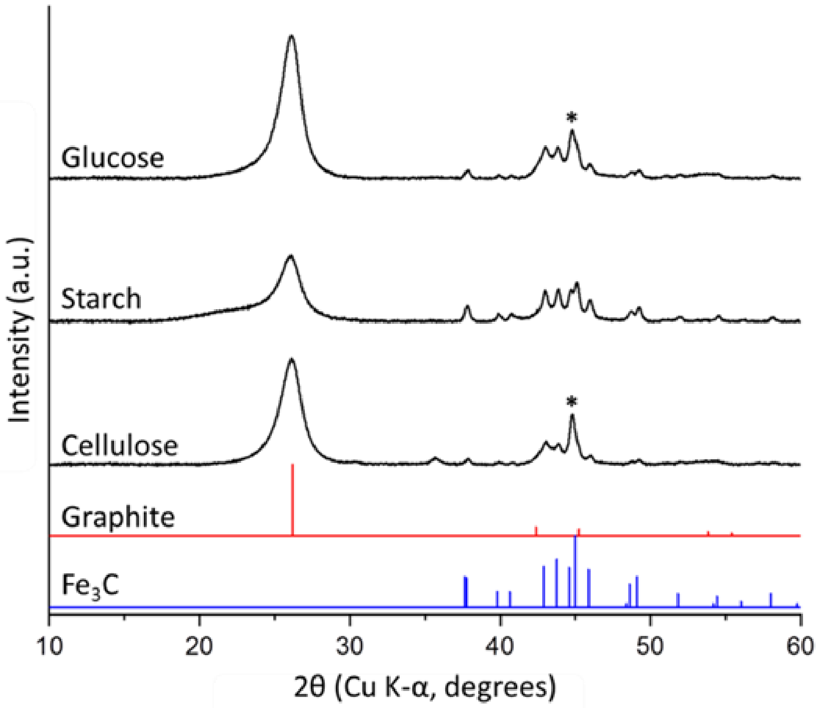

Figure 3.2: PXRD patterns for carbons produced from glucose, starch, and cellulose (5 g) and iron nitrate (0.68 mmol), dwelled at 800 °C for 1 hr. (*) indicates the presence of α-Fe.

The peaks at higher 2θ correspond to iron carbide, present in all three of the carbon samples. In the glucose- and cellulose-derived carbons, the sharper peak at approximately 45 ° 2θ corresponds to a the *α*-Fe phase, ferrite. The relative intensity of the graphitic carbon peak relative to the peaks for the iron phases in the starch-derived carbon is slightly lower than in the glucose- and cellulose-derived carbons, suggesting a lower degree of graphitization. The graphitic peak also shows slight broadening to lower 2θ in the starch-derived carbon sample. This peak corresponds to the basal plane of graphite, (i.e. the interlayer spacing of the graphitic layers). Therefore, as 2θ is inversely proportional to d-spacing, this shift to a lower 2θ suggests that the interlayer spacing between the layers may be greater in the starch-derived carbon, indicative of a more disordered, turbostratic carbon structure.

The structure of the carbons was further characterized using Raman spectroscopy (figure 3.3). The Raman spectra show the presence of two prominent peaks at approximately 1325 and 1600 cm^{-1}, corresponding to the D1 and G bands respectively. The G band is present in all carbon materials that display any graphitic character, indicating the presence of sp^2 hybridized carbon atoms. The D1 band is forbidden in perfect graphite so indicates disorder within the carbon structure. To extract quantitative information about the samples, the spectra were deconvoluted into four peaks with a Voigt peak shape as used previously by Rowlandson *et al* (figure 3.4).[161] The D2 and D3 bands used in the fitting procedure are also due to defects in the carbon structure. The D2 band has been ascribed tentatively in previous studies to polyene-like structures and the D3 band to amorphous carbon.[162] In some fitting procedures, an additional band at approximately 1610 cm^{-1} is used; however, this band has significant overlap with the G band so was not employed in this study as it did not improve the fit.[162] The results of the fitting procedure are reported in table 3.2.

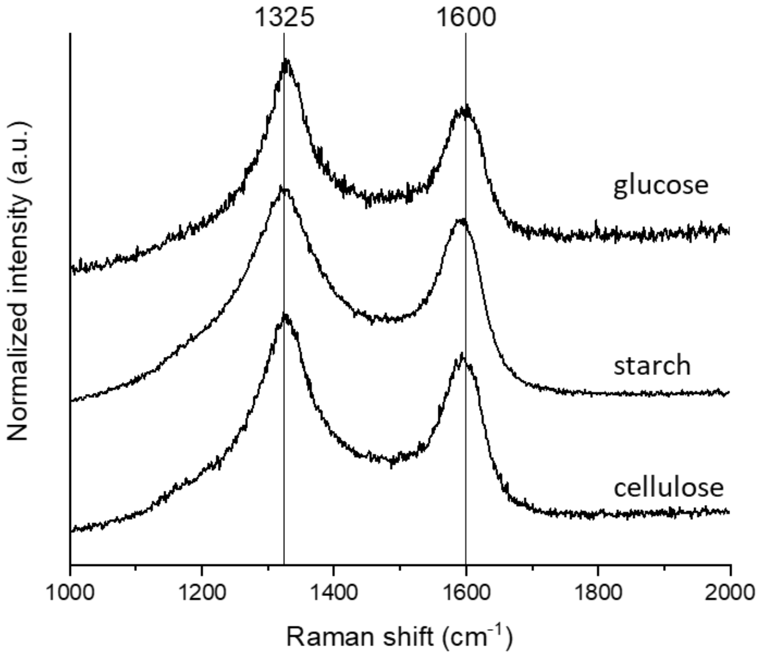

Figure 3.3: Raman spectra of carbons produced from glucose, starch and cellulose (5 g) and iron nitrate (0.68 mmol), dwelled at 800 °C for 1 hr.

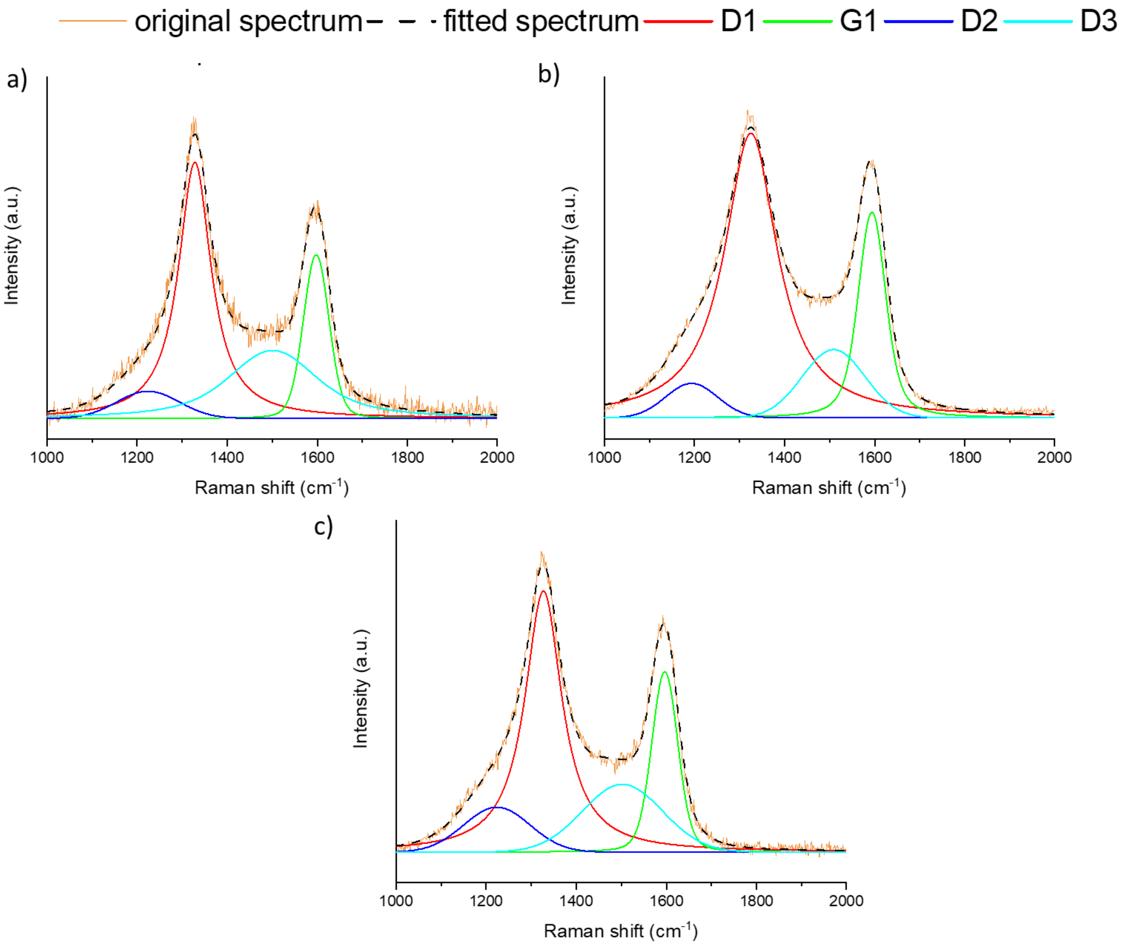

Figure 3.4: Deconvolution of peaks in Raman spectra of carbons produced from glucose, starch and cellulose (5 g) and iron nitrate (0.68 mmol), dwelled at 800 °C for 1 hr.

Table 3.2: Results from fitting of Raman spectra in Figure 3.4. All measurements were collected in triplicate on different locations and the average values are reported with uncertainty values.

Organic precursor	**Band**	**Peak position (cm^{-1})**	**FWHM (cm^{-1})**	**I_D/I_G**
Glucose	D1	1329 +/- 1	96 +/- 8	1.59 +/- 0.02
	G	1599 +/- 1	67 +/- 1	
Potato starch	D1	1325 +/- 1	133 +/- 9	1.34 +/- 0.14
	G	1596 +/- 3	70 +/- 4	
Cellulose	D1	1328 +/- 1	106 +/- 6	1.53 +/- 0.08
	G	1597 +/- 2	69 +/- 1	

In ideal graphite, the G peak is centred around 1581 cm^{-1}. However, in the glucose-, starch- and cellulose-derived carbons, the G peak is shifted to a higher value of approximately 1600 cm^{-1}, indicating the presence of nanocrystalline graphitic domains.[163] Therefore, the graphitization process in these carbons may be assumed to fit into stage two of the three-stage model proposed by Ferrari and Robertson, which describes the conversion of amorphous carbon to nanocrystalline graphite.[163] Generally, when considering graphitic materials, the intensity of the D1 band compared to the G band (I_D/I_G) is used as an indicator of the degree of graphitization of the carbon material, and a lower I_D/I_G value indicates greater graphitic character. However, this interpretation is only valid for stage three of the three-stage model as nanocrystalline graphite is converted to graphite. In stage two, the opposite trend is observed.[163] Shimodaira and Masui suggested that a sharp G and D1 peak in the Raman spectra of activated carbons was due to the carbon structure containing winding short basal planes, rather than a regularly ordered graphite lattice.[164] Therefore, the higher I_D/I_G calculated for the glucose- and cellulose-derived carbons compared to the starch-derived carbons may indicate a greater number of nanocrystalline graphitic domains, which is consistent with the greater graphitic character shown in PXRD.[163]

The surface structure of the carbons was investigated using SEM (figures 3.5a-c). All three of the carbons show complex carbon nanostructures. Iron-containing particles can be observed throughout the sample as bright spots in the images collected with a CBS detector due to their greater electron density compared to the surrounding carbons. Although most clearly visible in the cellulose-derived carbon, all three of the samples show tubular nanostructures, similar in nature to those observed in a previous study of iron-catalyzed graphitization of lignocellulosic sawdust.[90]

The hollow nanostructures could be observed more clearly in all three samples using TEM (figures 3.5d-f). All three of the samples show the presence of graphitic nanotubes alongside graphitic shells, suggesting that each system does not appear to favour the formation of one kind of graphitic product over the other. In the TEM images, the iron carbide nanoparticles can be seen as dark spots, again due to their greater electron density resulting in greater scattering of the electron beam.

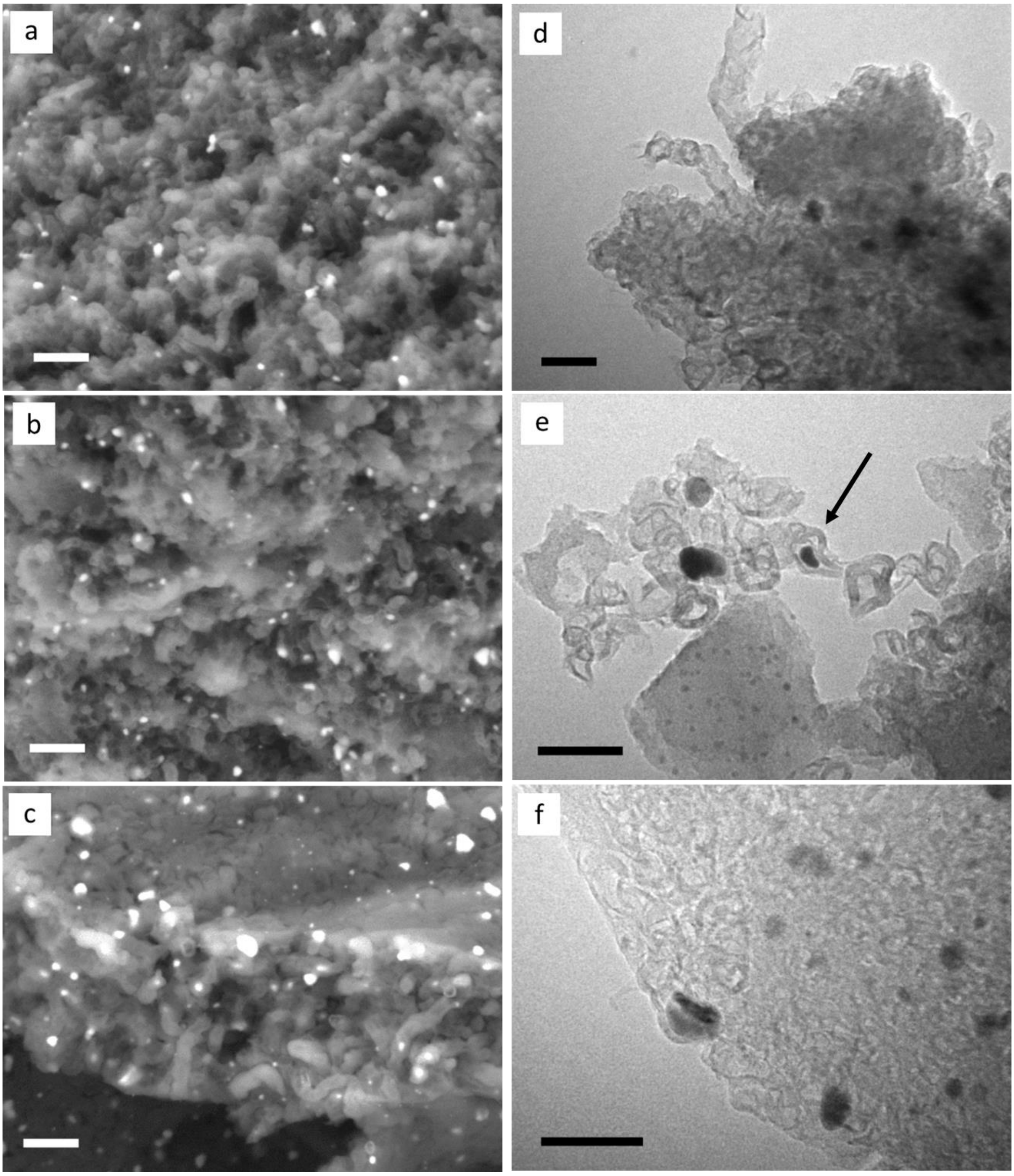

Figure 3.5: SEM (backscattered electron detector) a-c) and TEM images d-f) of carbons produced from a, d) glucose, b, e) starch and c, f) cellulose (5 g) and iron nitrate (0.68 mmol), held at 800 °C for 1 hr. Scale bars in SEM images = 200 nm. Scale bar in TEM images = 100 nm. Arrow in e) indicates a catalyst nanoparticle trapped "mid-flow" inside a graphitic nanotube.

Importantly, in all three of the carbons there is evidence for catalyst particle movement. For example, figure 3.5e shows an iron carbide nanoparticle trapped "mid-flow" inside of a graphitic nanotube. Also, "empty" graphitic pores can be observed, likely to have been filled by an iron carbide nanoparticle before it moved away and left a pore of approximately the same size as the nanoparticle.

Table 3.3: Average crystallite size calculated by Scherrer analysis of PXRD patterns in figure 3.2.

Organic precursor	**Average crystallite size (nm)**	
	Fe_3C	**α-Fe**
Glucose	36	13
Starch	25	33
Cellulose	31	20

Electron microscopy can be used to give an indication of the size of the iron carbide nanoparticles within the carbons. However, the main limitation with this method is that only a small portion of the sample may be imaged at one time. An average crystallite size for each phase present can be calculated from PXRD using the Scherrer equation. These values are listed in table 3.3. SAXS was also used to generate a size distribution of the iron-based particles throughout the bulk of the carbon matrix rather than just the average to give a statistically significant representation of the whole sample. Figure 3.6 shows the raw SAXS patterns for the glucose-, starch- and cellulose-derived carbons. The data was fitted using McSAS, a fitting program that uses a Monte Carlo method to extract form-free size distributions.[165]

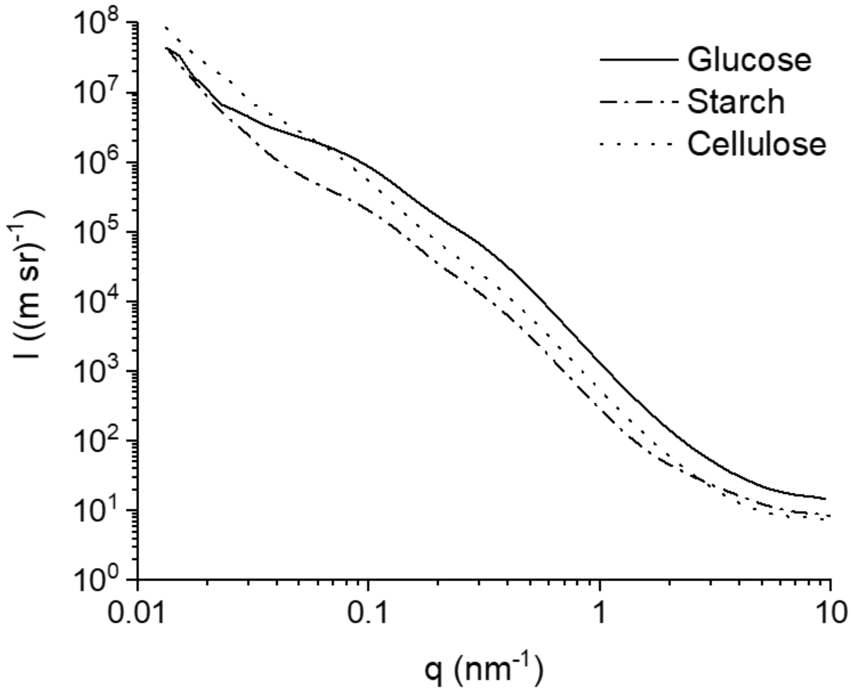

Figure 3.6: Small angle X-ray scattering data for carbons produced from glucose, starch, and cellulose (5 g) and iron nitrate (0.68 mmol), held at 800 °C for 1 hr.

The form is an important factor to consider during SAXS analysis and refers to the specific shape of the scattering feature of interest. SAXS analysis requires two parameters out of the size, shape and packing to be known quantities in order to determine the third unknown parameter. If the densities of the components of the sample are known, the packing of the sample can be determined experimentally by measuring the absorption of the X-ray beam. Then either the size or shape of the scattering features must be determined using a secondary technique such as electron microscopy. In the case of the carbon samples in this study, the shape of the scattering features was chosen to be spherical for the Monte Carlo fits as TEM showed the iron/iron carbide nanoparticles to be approximately spherical in shape. Selection of a good model scattering feature for the particular system is important as McSAS will almost always produce a “perfect” fit of the data regardless of the shape selected (i.e.

a “good” fit may be achieved for the same data using spheres/rods, but will likely give different results) but the resulting size distributions may not be a true representation of the sample.

Figure 3.7 shows the comparison of the raw SAXS data for glucose-derived carbon with the Monte Carlo fit as an example to illustrate the good agreement between the data and the fit. For completeness, the data fits for starch- and cellulose-derived carbons are included in appendix A. Figure 3.8a shows the resulting size distribution of the scattering features in the glucose-derived carbon. A trimodal distribution of scattering features is observed, similar to a previous study of catalytic graphitization in a gelatin/iron nitrate system.[77]

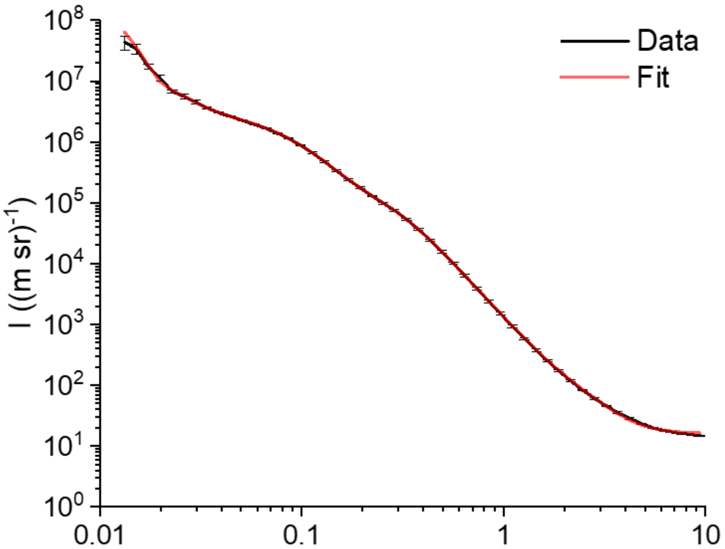

Figure 3.7: Raw SAXS data vs Monte Carlo fit for carbon produced from glucose (5 g) and iron nitrate (0.68 mmol), held at 800 °C for 1 hr.

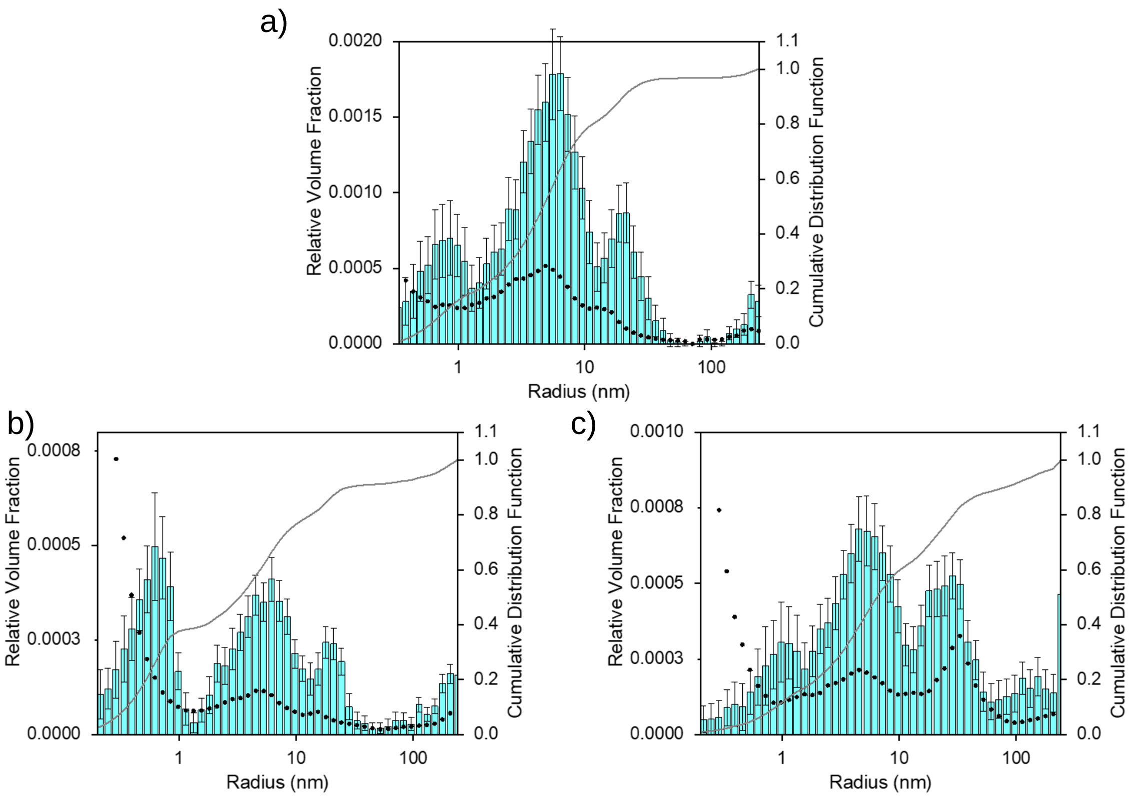

Figure 3.8: Scattering feature size distribution histogram coupled with visibility limits (black dots, left y-axis) and cumulative distribution function (grey line, right y-axis) for carbons produced from a) glucose, b) starch and c) cellulose (5 g) and iron nitrate (0.68 mmol), held at 800 °C for 1 hr.

SAXS arises from regions of contrasting electron density so various possible areas of the sample could have contributed to the scattering pattern. In order to determine which distribution was due to the iron carbide/carbon scattering interface, the carbon samples were washed with 0.1 M hydrochloric acid, as iron carbide is soluble in acid. PXRD of the glucose-derived carbon after acid-washing shows that the characteristic peaks corresponding to iron carbide were partially removed, indicating the dissolution of some of the iron carbide nanoparticles, while the graphitic carbon peak remains unchanged (figure 3.9).

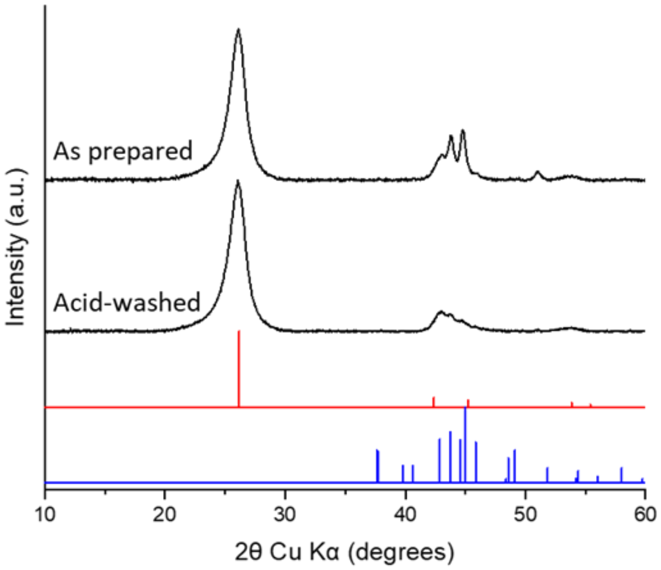

Figure 3.9: PXRD patterns of as prepared and acid-washed carbons produced from glucose (5 g) and iron nitrate (0.68 mmol), held at 800 °C for 1 hr.

The resulting size distribution calculated from a Monte Carlo fit of the acid-washed glucose-derived carbon shows that the peak in the histogram for the scattering features with the largest radii (10-100 nm) decreased upon acid-washing, suggesting that these features are due to the iron carbide/carbon scattering interface (figure 3.10). This size range is also consistent with the sizes observed in electron microscopy and Scherrer analysis (approximately 10-40 nm). The other scattering features are more difficult to assign; however, it seems likely that the scattering features with radii in the range of approximately 1-10 nm are likely to be due to the carbon/air interface and various mesopores within the sample, while the even smaller features (< 1 nm) are likely due to surface roughness from micropores.

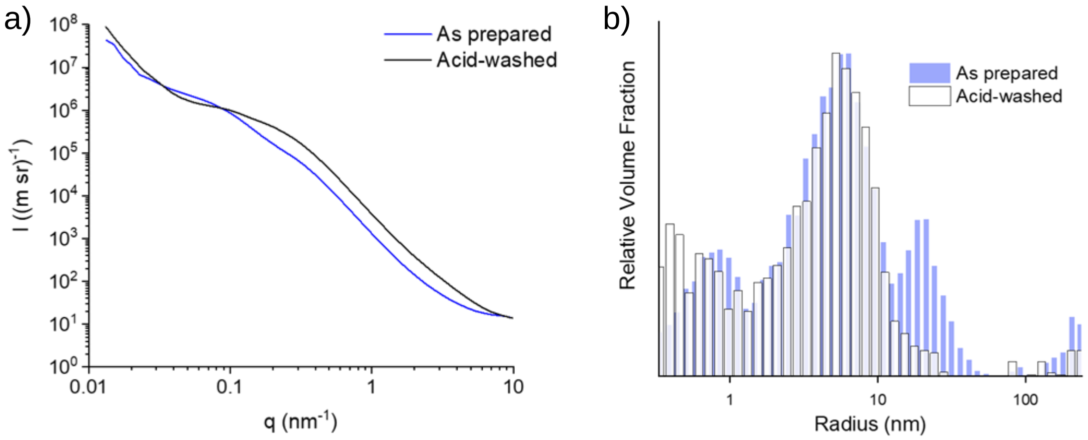

Figure 3.10: a) Raw SAXS data and b) resulting size distribution histograms for as prepared and acid-washed carbons produced from glucose (5 g) and iron nitrate (0.68 mmol), held at 800 °C for 1 hr.

Acid-washing was also used to remove iron carbide particles from the starch- and cellulose-derived carbons (figures 3.11a and b). It is worth noting that not all of the iron carbide particles were removed from the carbon matrix as some peaks corresponding to iron carbide remained in the PXRD patterns after washing (particularly visible in the starch-derived carbon). This may be due to some of the nanoparticles being embedded deep within the carbon matrix and inaccessible to the acid. However, the purpose of the acid-washing procedure used here was to identify which size distribution in the SAXS data was due to the iron carbide nanoparticles so removal of all of the nanoparticles was not vital. However, optimization of the washing procedure, for example by varying the concentration of hydrochloric acid used or the treatment time, would likely improve the efficiency of the washing. For example, a characterization method such as atomic absorption spectroscopy or inductively coupled plasma - mass spectrometry/optical emission spectroscopy, where the sample is digested, could be used to determine a reliable iron content in a range of samples washed using different hydrochloric acid concentrations and/or treatment times so the precise conditions to achieve the maximum dissolution of iron could be identified.

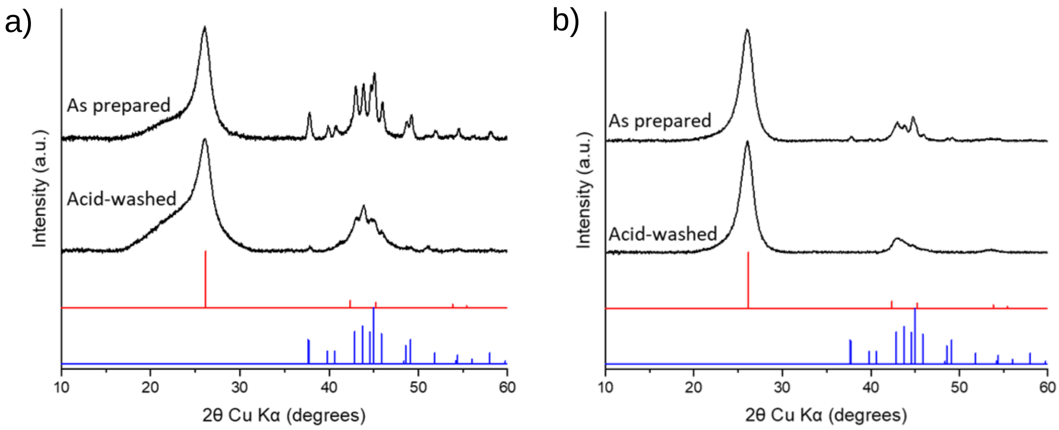

Figure 3.11: PXRD patterns of as prepared and acid-washed carbons produced from a) starch and b) cellulose (5 g) and iron nitrate (0.68 mmol), held at 800 °C for 1 hr.

Size distribution histograms for the starch- and cellulose-derived carbons before and after acid-washing again show that a large proportion of the scattering features are removed by the acid-washing procedure, hence these can be assigned to the iron carbide/carbon scattering interface.

The size distribution histogram for the cellulose-derived carbons shows a similar trimodal distribution, of which the population of scattering features with radii of 10-100 nm significantly decreases upon acid-washing, suggesting this is the approximate size of the iron carbide particles (figure 3.12b and d). This is again consistent with Scherrer analysis, which showed an average crystallite size of 31 nm for Fe_3C and 20 nm for *α*-Fe (table 3.3) In the starch-derived carbons, the decrease in the relative volume of scattering features decreases across a greater length scale (figure 3.12a and c). The relative volume fraction of scattering features with radii of approximately 10-50 nm decreases, as well as the relative volume fraction of scattering features with radii of 5-10 nm, suggesting the starch-derived carbon contains iron carbide nanoparticles of a smaller size than the glucose- and cellulose-derived carbons, although the average crystallite size calculated from the Scherrer equation is similar to the glucose- and cellulose-derived carbons (table 3.3).

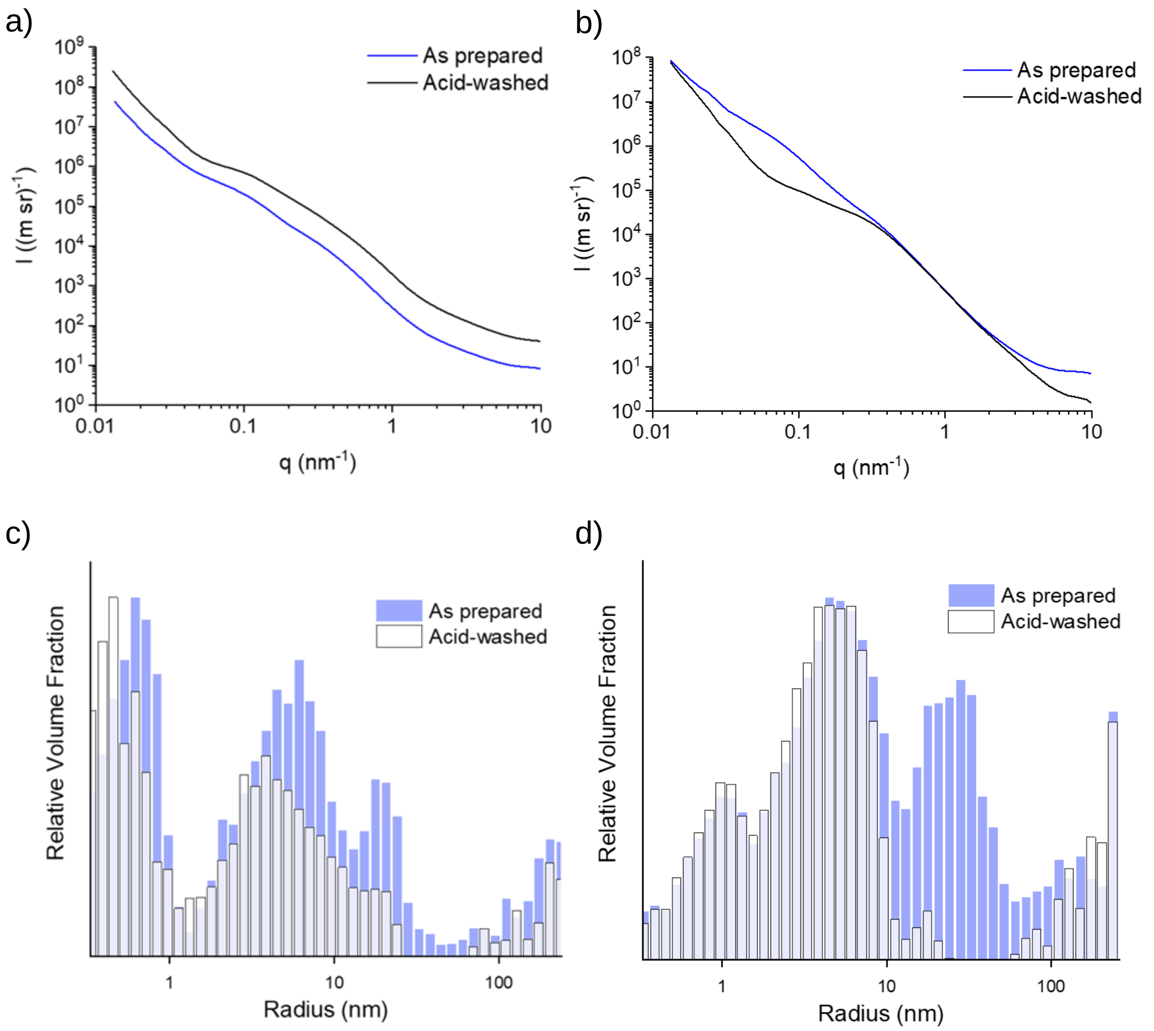

Figure 3.12: Raw SAXS data and resulting size distribution histograms for as prepared and acid-washed carbons produced from a,c) starch and b,d) cellulose (5 g) and iron nitrate (0.68 mmol), held at 800 °C for 1 hr.

Nitrogen sorption measurements were used to assess the porosity profiles of the glucose-, starch- and cellulose-derived carbons (figure 3.13). All three carbons display an isotherm with type IV characteristics, including hysteresis due to capillary condensation, characteristic of mesoporous materials. The isotherms do not quite reach saturation at p/p^0 = 1, suggesting that the pore size extends into the macroporous size range, > 50 nm, outside the measurement window of the nitrogen sorption experiment. Capillary condensation refers to when a gaseous species condenses into a liquid-like phase within a pore at a pressure lower than the saturation pressure of the pure liquid resulting in delayed desorption. The nature of the hysteresis loops in the three carbons seems to be most closely matched to type H4 as the sharp changes in adsorption and desorption branches observed in type H1 and H2 isotherms are not observed.[166] The isotherms all display a distinct region for micropore filling at low p/p^0 and the desorption branches have a fairly sharp decrease between 0.4-0.5 p/p^0, again consistent with type H4 behaviour. This particular isotherm shape is commonly displayed by aggregated zeolite crystals, some mesoporous zeolites and micro-mesoporous carbons, so appears to be an appropriate assignment to the glucose-, starch- and cellulose-derived carbons in this study.[154,166] Although the nitrogen sorption isotherms for the three carbons all display a similar type of hysteresis, the exact shape of the isotherm for the starch-derived carbon is notably different to the other two samples. A considerably smaller hysteresis loop and greater micropore filling is observed, suggesting fewer mesopores and more micropores are present in the starch-derived carbon.

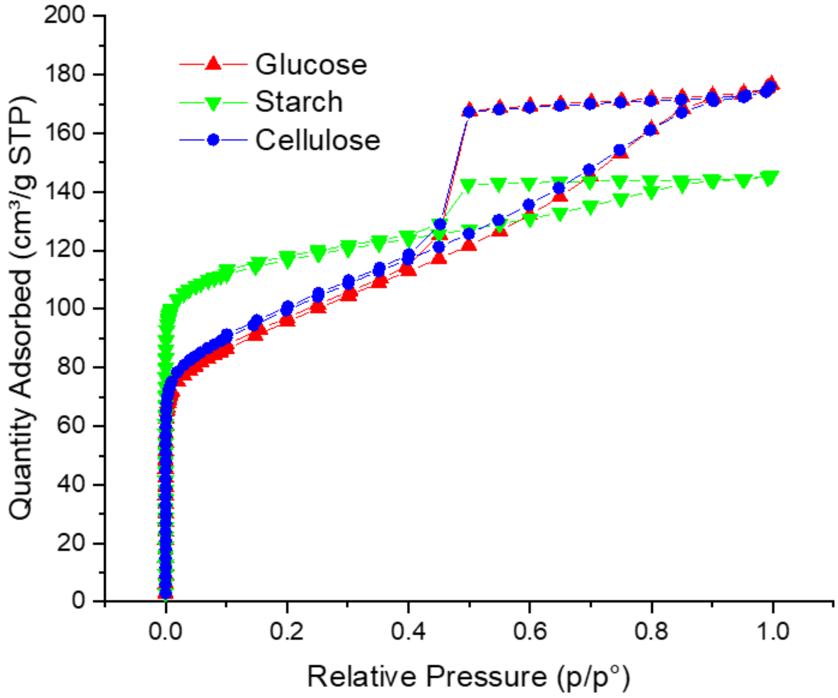

Figure 3.13: Nitrogen sorption isotherms for carbons produced from glucose, starch, and cellulose (5 g) and iron nitrate (0.68 mmol), held at 800 °C for 1 hr.

The adsorptive characteristics of the carbons were calculated from the isotherms using a variety of methods and listed in table 3.4 and displayed in a radar plot in figure 3.14. The specific surface areas of the samples were calculated using BET theory. Due to the presence of micropores in the carbons, it was necessary to apply the Rouquerol correction in order to select an appropriate pressure range for the BET plots.[155] The specific surface area values were calculated to be 342, 450 and 357 m^2g^{-1} for the glucose-, starch- and cellulose-derived carbons respectively.

The higher specific surface area value for the starch-derived carbon is due to the greater microporosity. This can be observed in the sorption isotherms as a greater increase in the amount of nitrogen adsorbed in the low-pressure region, which corresponds to micropore filling. The microporosity was also quantified using the *t*-plot method, with starch-derived carbon displaying a much greater micropore surface area of 342 m^2g^{-1}, compared to 132 and 142 m^2g^{-1} for glucose- and cellulose-derived carbons respectively.[156]

Table 3.4: Adsorptive properties calculated from nitrogen sorption isotherms for carbons produced from glucose, starch and cellulose (5 g) and iron nitrate (0.68 mmol), held at 800 °C for 1 hr: maximum quantity of nitrogen adsorbed (Q_{ads}), total pore volume (V_{tot}), micropore volume (V_{micro}), micropore surface area (S_{micro}), volume-weighted average pore size (w_{avg}) and BET surface area (S_{BET}). A full isotherm (p/p^0) was recorded for each material and in duplicate for glucose and cellulose samples. The mean values are shown and the uncertainty values represent the largest deviation from the mean.

Precursor	**Max Q_{ads} ($cm^3\ g^{-1}$)**	**V_{tot} ($cm^3\ g^{-1}$)**	**V_{micro} (cm^3g^{-1})**	**S_{micro} ($cm^3\ g^{-1}$)**	**w_{avg}:2D-NLDFT (Å)**	**S_{BET} ($m^2\ g^{-1}$)**
Glucose	177 +/- 1	0.27 +/- <0.01	0.06 +/- < 0.01	133 +/- 1	30.9 +/- 0.6	343 +/- 1
Starch	145	0.22	0.13	342	13.2	450
Cellulose	176 +/- 1	0.27 +/- < 0.01	0.06 +/- < 0.01	143 +/- 1	29.7 +/- 0.7	358 +/- 1

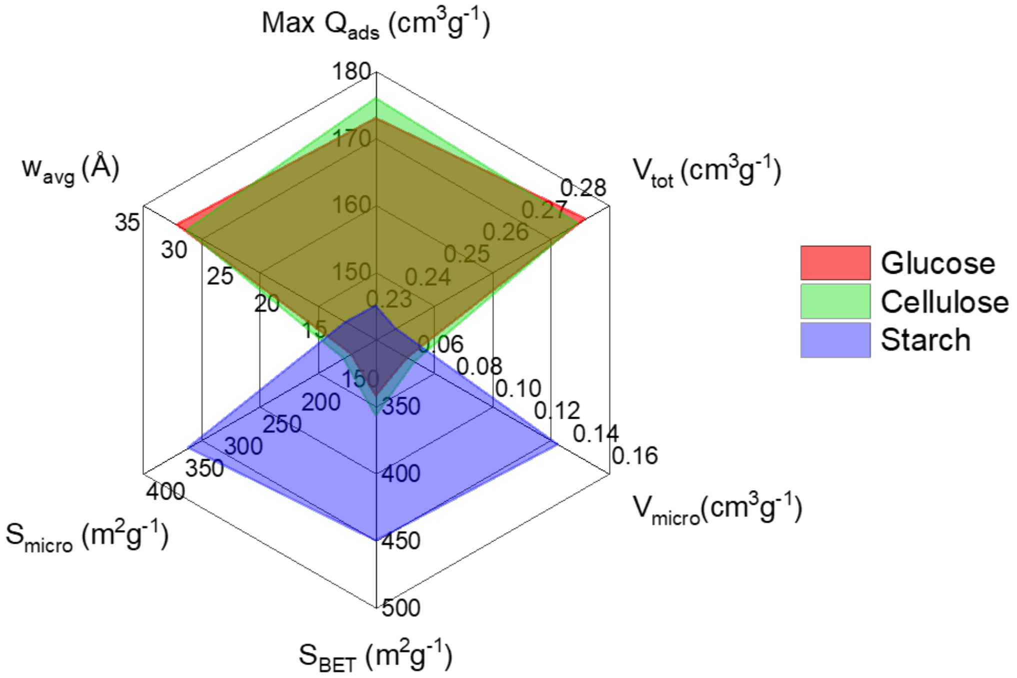

Figure 3.14: Radar plot of adsorptive properties of carbons produced from glucose, starch and cellulose (5 g) and iron nitrate (0.68 mmol), held at 800 °C for 1 hr.

The greater microporosity in the starch-derived carbon can also be visualized in pore size distributions calculated using NLDFT, in which the glucose- and cellulose-derived carbons display a greater range of pore widths (figure 3.15). The volume-weighted average pore size, w_{avg} was calculated from the pore size distributions using equation 3.1, as described by Laudisio *et al*, where V_i is the pore volume and w_i is the pore width at a certain data point *i*. The w_{avg} shows a lower value of 13.2 Å for the starch-derived carbon compared to 30.9 and 29.7 Å for glucose- and cellulose-derived carbons.[167]

$$w_{avg} = \frac{\sum_{i=1}^{n} w_i V_i}{\sum_{i=1}^{n} V_i} \tag{3.1}$$

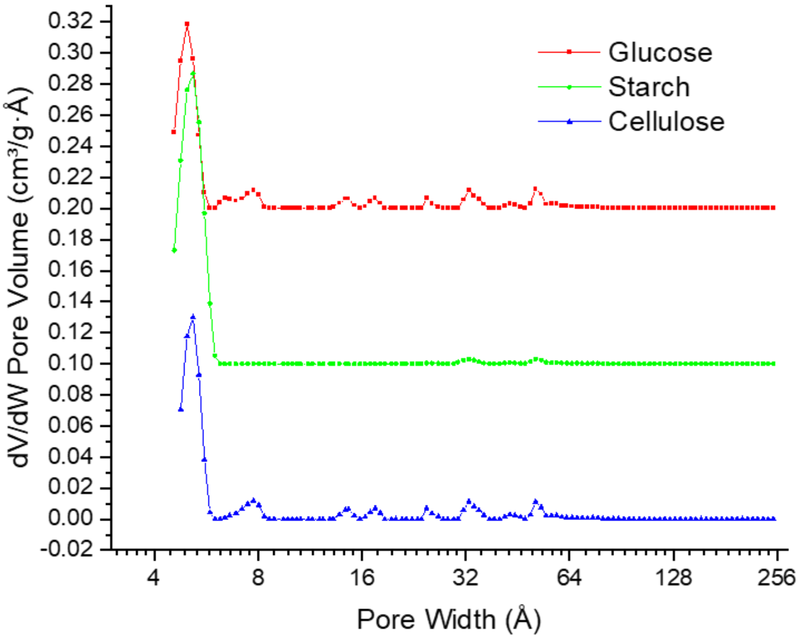

Figure 3.15: Pore size distributions calculated using NLDFT for carbons produced from glucose, starch and cellulose (5 g) and iron nitrate (0.68 mmol), held at 800 °C for 1 hr.

Full repeat isotherms for the glucose- and cellulose-derived carbons were run to calculate uncertainty values for the adsorptive properties. It was not possible to run a full repeat isotherm for the starch-derived carbon sample due to time constraints. However, a partial isotherm without the microporous region was collected to verify the general isotherm shape, which was in good agreement with the full isotherm data.

The greater microporosity in the starch-derived carbon is in agreement with the smaller particle sizes observed in SAXS. Furthermore, the broad graphitic carbon peak observed in PXRD suggests that the starch-derived carbon contains a mixture of turbostratic carbon, which results in microporosity and graphitic carbon nanostructures that give rise to the mesoporosity. The larger catalyst particle sizes observed in glucose- and cellulose-derived carbons results in a greater degree of graphitization and therefore greater mesoporosity due to the formation of more graphitic carbon nanostructures.

3.3.2 Effect of iron nitrate concentration

To examine the effect of the concentration of iron nitrate solution added to the organic precursor, a series of glucose-, starch- and cellulose-derived carbons were synthesized using varying concentrations of iron nitrate solution.

PXRD patterns of the resulting carbons derived from glucose and cellulose show that varying the iron concentration has little effect on the degree of graphitization, suggesting a low amount of iron is sufficient to drive graphitization (figure 3.16). The glucose-derived carbon synthesized using 0.34 mmol of iron nitrate shows low intensity peaks corresponding to magnetite, indicating that not all of the oxide underwent carbothermal reduction to form iron carbide or iron. In both glucose- and cellulose-derived carbons synthesized using 3.4 mmol of iron nitrate, the PXRD patterns show a larger peak corresponding to *α*-Fe alongside iron carbide.

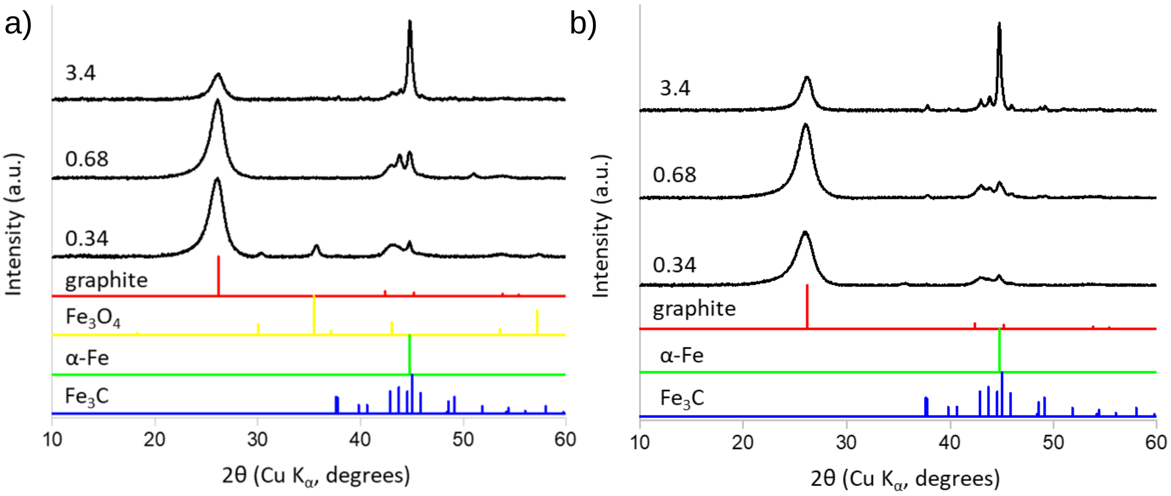

Figure 3.16: PXRD patterns for carbons produced from a) glucose and b) cellulose (5 g) and various amounts of iron nitrate (in mmol), held at 800 °C for 1 hr.

The influence of the iron nitrate concentration is greater in the starch-derived carbons. Increasing the concentration of iron nitrate solution leads to sharper, better-resolved peaks corresponding to iron carbide, suggesting a greater degree of crystallinity and/or an increase in particle size (figure 3.17). A decrease in the crystallinity of the graphitic carbon phase is also observed with decreasing iron content concentration, with a more significant contribution from the turbostratic carbon component in the starch-derived carbon synthesized with the lowest iron nitrate concentration.

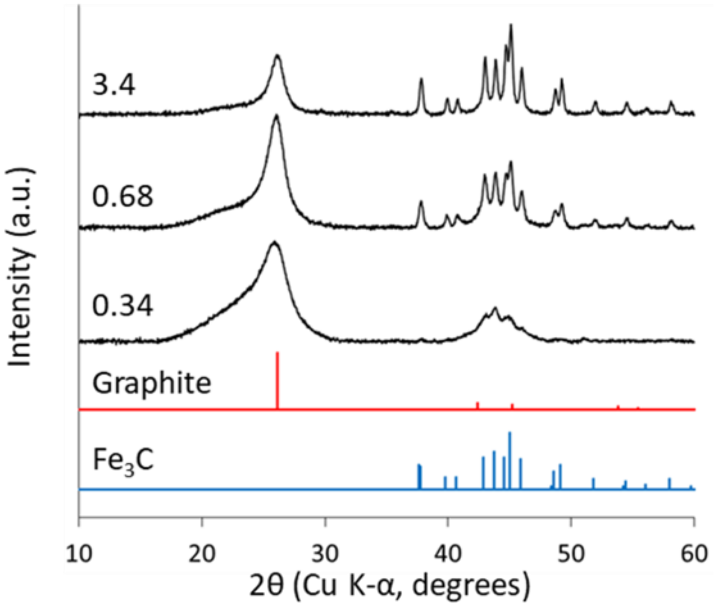

Figure 3.17: PXRD patterns for carbons produced from starch (5 g) and various amounts of iron nitrate (in mmol), held at 800 °C for 1 hr.

SAXS was again used to assess the iron carbide/iron particle sizes within the carbons. The increasing size of the scattering features with increasing iron content can be observed in the raw SAXS data as a shift of the shoulder feature at around 0.4 nm^{-1} in the 0.34 mmol sample to a lower q value of approximately 0.07-0.08 nm^{-1} in the 3.4 mmol sample (figure 3.18a). This observation translates as an increase in the relative volume fraction of the scattering features with radii between 10-100 nm in the resulting size distribution histograms (figures 3.18b-d), clearly showing the growth of the iron-based particles. The growth of the iron-based particles with increasing iron nitrate concentration is expected as there is less biomass surrounding the iron-based particles and the particles are likely to be closer together initially, resulting in more growth and sintering during pyrolysis and this trend is mirrored in average crystallite size calculated using Scherrer analysis of PXRD data (table 3.5).

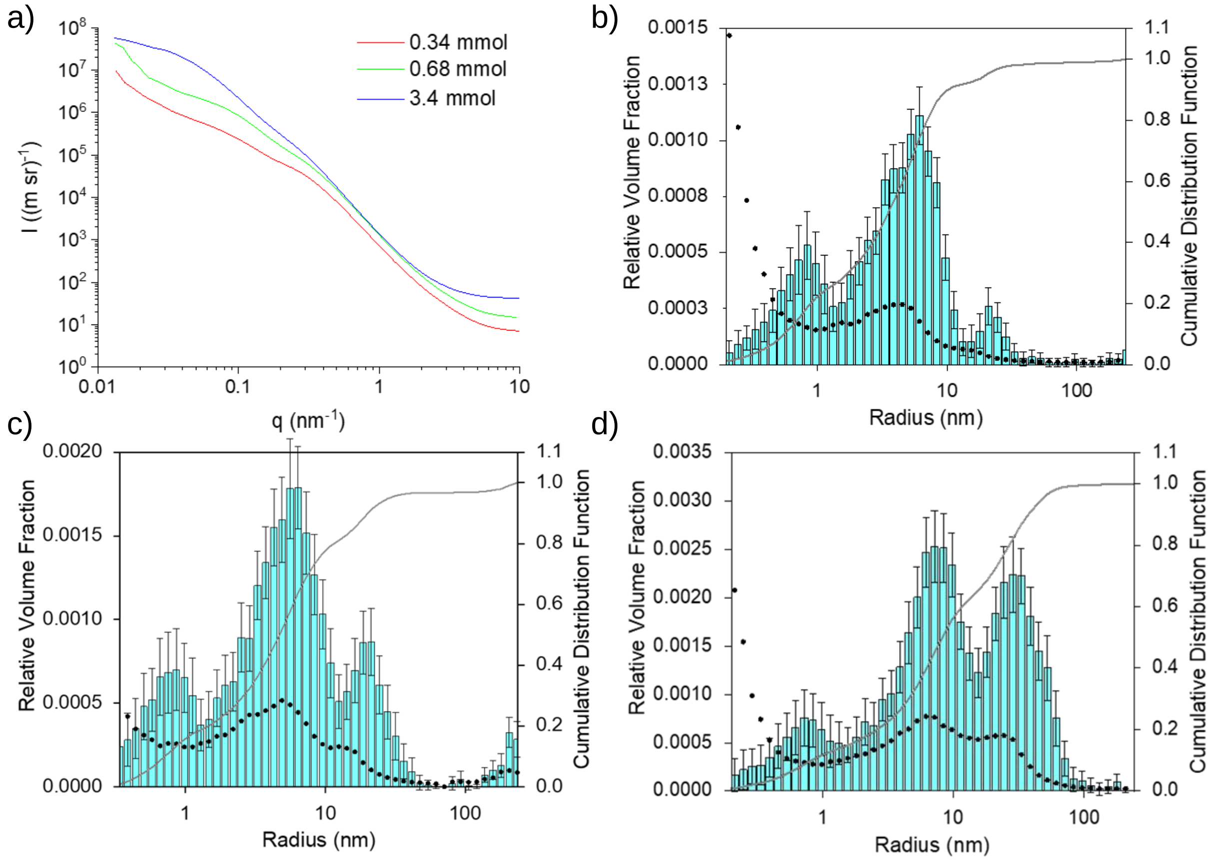

Figure 3.18: a) Raw SAXS data and resulting size distributions for glucose-derived carbons synthesized using b) 0.34 mmol, c) 0.68 mmol and d) 3.4 mmol of iron nitrate

Table 3.5: Average crystallite size of iron phases in glucose-derived carbons synthesized using different concentrations of iron nitrate solution, calculated from Scherrer analysis of PXRD patterns (figure 3.16a).

Iron concentration (mmol)	**Average crystallite size (nm)**		
	Fe_3O_4	**Fe_3C**	***α*-Fe**
0.34	21	-	20
0.68	-	36	13
3.4		52	19

SAXS data of the cellulose-derived carbons show similar results, as the centre of the main feature in the SAXS data moves from approximately 0.6 nm^{-1} to a lower q value of approximately 0.1 nm^{-1}, signifying a larger particle size in the sample with the higher iron content (3.19a), a trend that is also observed in Scherrer analysis of PXRD data (table 3.6). In the resulting size distribution histograms, the relative volume fraction of the population of scattering features with radii between 10-100 nm increases with increasing iron nitrate concentration (figures 3.19b-d). The middle population of scattering features, centred between 1-10 nm in the sample synthesized using 0.34 mmol of iron nitrate also shifts to being centred at approximately 10 nm in the sample synthesized using 3.4 mmol of iron nitrate. This population was earlier assigned to being due to the carbon/air interface in mesopores. In a previous study of iron-catalyzed graphitization of softwood sawdust, as shown here, the particle size was observed to increase with increasing iron nitrate concentration.[90] This in turn resulted in larger tubular graphitic nanostructures. The size of the graphitic nanostructures is dependent on the size of the catalyst particle; therefore, it is likely that the larger catalyst particles also result in graphitic nanostructures of a greater diameter.

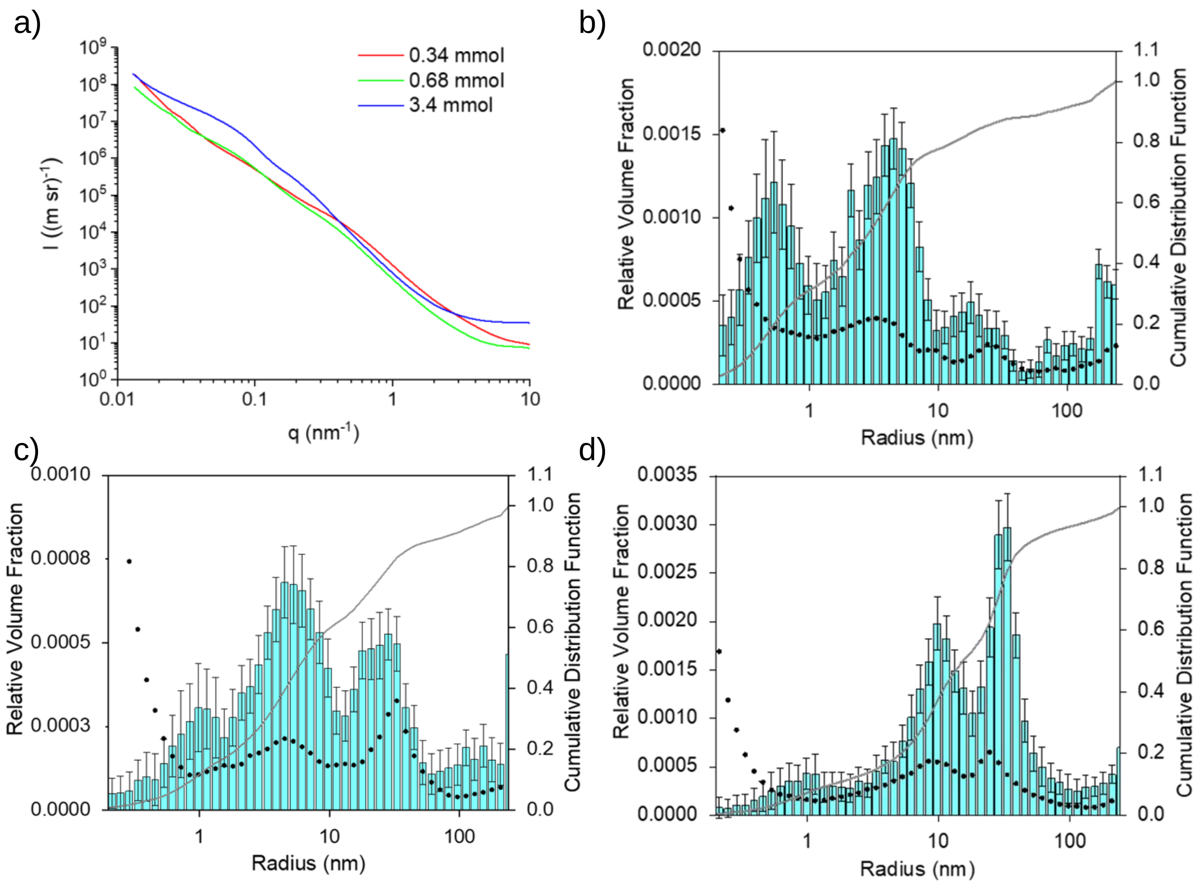

Figure 3.19: a) Raw SAXS data and resulting size distributions for cellulose-derived carbons synthesised using b) 0.34 mmol, c) 0.68 mmol and d) 3.4 mmol of iron nitrate.

Table 3.6: Average crystallite size of iron phases in cellulose-derived carbons synthesized using different concentrations of iron nitrate solution, calculated from Scherrer analysis of PXRD patterns (figure 3.16b).

Iron concentration (mmol)	**Average crystallite size (nm)**		
	Fe_3O_4	**Fe_3C**	***α*-Fe**
0.34	14	-	13
0.68	-	31	20
3.4	-	51	26

Results from SAXS measurements for starch-derived carbons again shows a growth in the size of the scattering features with increasing iron nitrate concentration (figures 3.20a-d). In the sample synthesized using 0.34 mmol of iron nitrate, there are very few scattering features within the 10-100 nm size range, consistent with the low degree of graphitization and broad, poorly resolved peaks corresponding to iron carbide in PXRD, making it difficult to calculate an average crystallite size using Scherrer analysis (table 3.7). As the amount of iron nitrate is increased, the relative volume fraction of the population of scattering features increases, resulting in greater crystallinity and/or size of the iron carbide nanoparticles (figures 3.20b-d). A greater degree of graphitization is also observed as the iron carbide nanoparticles increase in size, further indicating that the catalyst particles may have to reach a critical size in order to become catalytically active. Importantly, the size of the scattering features in the starch-derived carbons is generally smaller than those observed in glucose- and cellulose-derived carbons, particularly at low iron concentration, suggesting that starch provides a greater degree of control over the catalyst particle size.

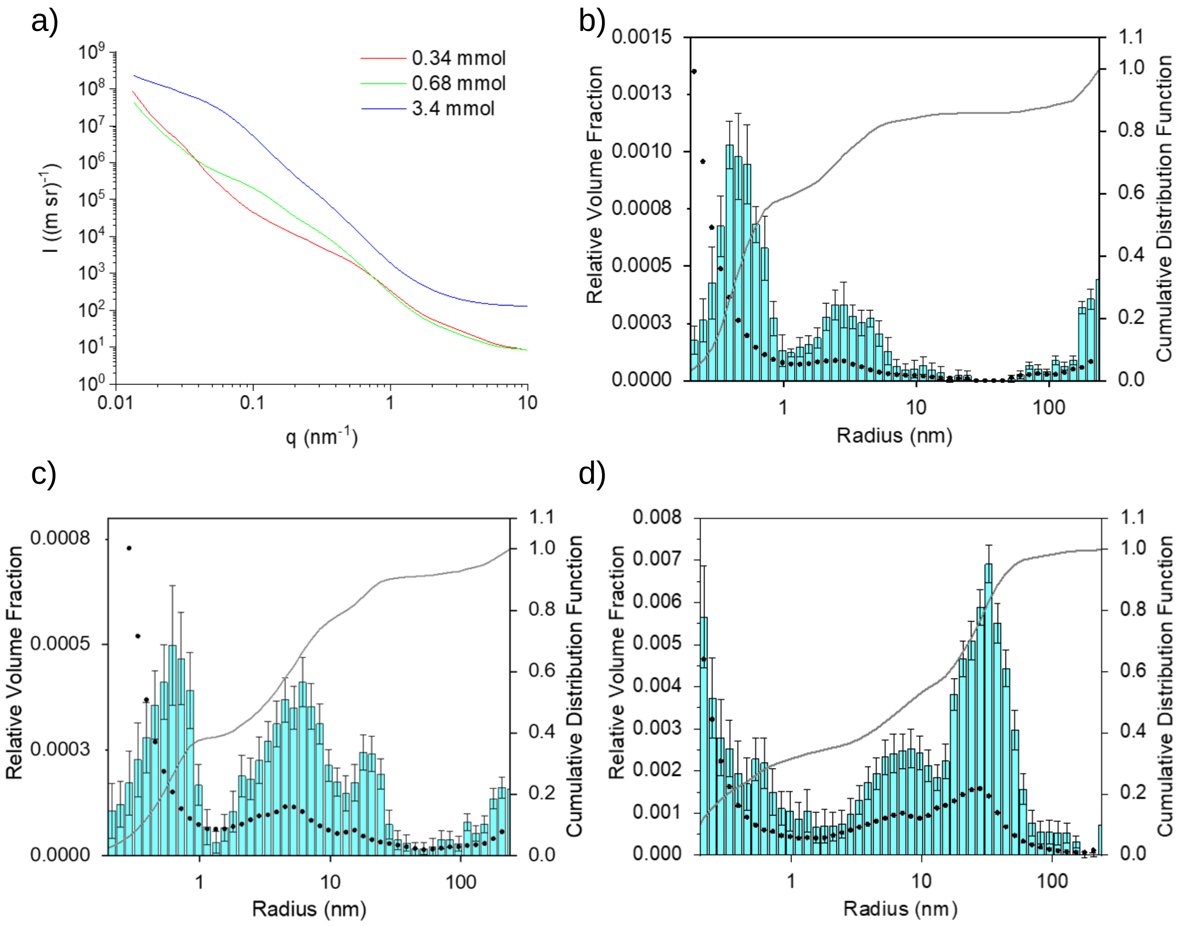

Figure 3.20: a) Raw SAXS data and resulting size distributions for starch-derived carbons synthesised using b) 0.34 mmol, c) 0.68 mmol and d) 3.4 mmol of iron nitrate

Table 3.7: Average crystallite size of iron phases in starch-derived carbons synthesized using different concentrations of iron nitrate solution, calculated from Scherrer analysis of PXRD patterns (figure 3.17).

Iron concentration (mmol)	**Average crystallite size (nm)**		
	Fe_3O_4	**Fe_3C**	***α*-Fe**
0.34	-	-	-
0.68	-	25	33
3.4	-	39	40

3.3.3 Effect of synthesis conditions

Due to the different behaviour observed in the starch system, a study of the effect of synthesis conditions was carried out to provide some insight into the graphitization mechanism in each of the three systems examined. In a previous *in situ* synchrotron PXRD study of a gelatin/iron nitrate system, small magnetite (Fe_3O_4) nanoparticles were initially formed, which underwent carbothermal reduction to wüstite (FeO_x), followed by transformation to iron nitride (Fe_3N) and finally iron carbide.[168] A simplified lab-based investigation was carried out to determine whether a similar mechanistic path was being followed in the glucose-, starch- and cellulose-based systems. The organic precursor/iron nitrate mixtures were pyrolyzed to various temperatures between 500 °C and 800 °C and held at that temperature for 1 hr, unless otherwise stated, and allowed to cool to room temperature.

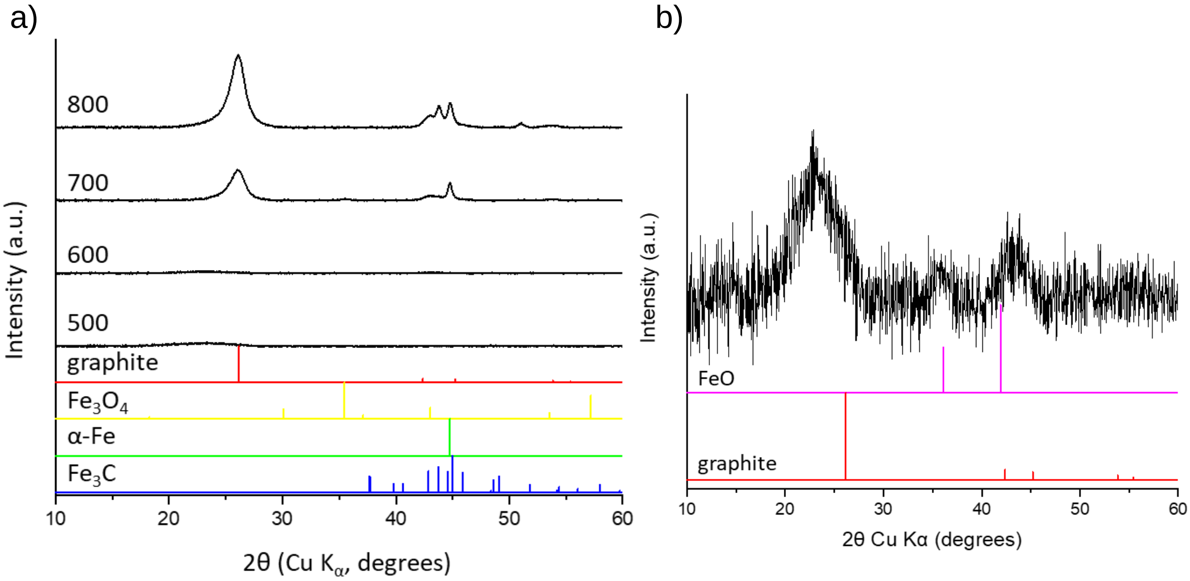

Figure 3.21: a) PXRD patterns for carbons produced from glucose (5 g) and iron nitrate (0.68 mmol), heated to various temperatures (in °C) and dwelled for 1 hr. b) Magnified PXRD pattern of glucose-derived carbon heated to 600 °C.

Glucose- and cellulose-derived carbons yielded similar PXRD results (figures 3.21 and 3.22 respectively). At temperatures of 500 and 600 °C, the samples appear to be largely amorphous, with an extremely broad feature at approximately 24 ° 2θ corresponding to amorphous carbon, and no clear peaks for crystalline iron phases. However, magnification of the PXRD pattern of glucose-derived carbon heated to 600 °C shows evidence of the presence of wüstite, suggesting that the initial stage of the reaction pathway is the formation of iron oxide phases, as in the gelatin/iron nitrate system.[168] These wüstite peaks are weak and relatively broad, suggesting that these nanoparticles are small and/or poorly crystalline. The gelatin/iron nitrate study was performed using a synchrotron X-ray source, so the diffraction data collected on a lab-based diffractometer is always likely to be of a lesser quality and may not be able to pick up all of the peaks present. However, a lower ratio of metal:organic precursors was also used in this study, so the iron-based nanoparticles are likely to be of a smaller size, as the iron nitrate concentration has been shown to affect the particle size of the iron species.

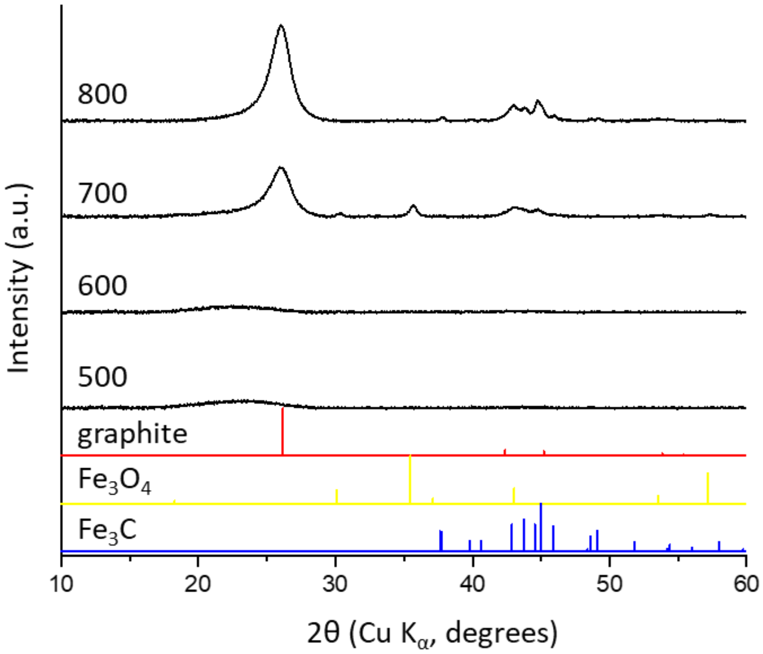

Figure 3.22: PXRD patterns for carbons produced from cellulose (5 g) and iron nitrate (0.68 mmol), heated to various temperatures (in °C), and dwelled for 1 hr.

In the starch system, a sharp peak for graphitic carbon does not appear until a higher temperature of 800 °C (figure 3.23). Peaks corresponding to *α*-Fe are visible in the PXRD pattern of the sample heated to 600 °C, which grow in intensity upon heating to 700 °C, along with the emergence of iron carbide. Peaks corresponding to magnetite are less visible in the PXRD patterns of the starch-derived carbons, however, it may be that any iron oxide nanoparticles present are extremely small and/or poorly crystalline so difficult to identify on the lab diffractometer.

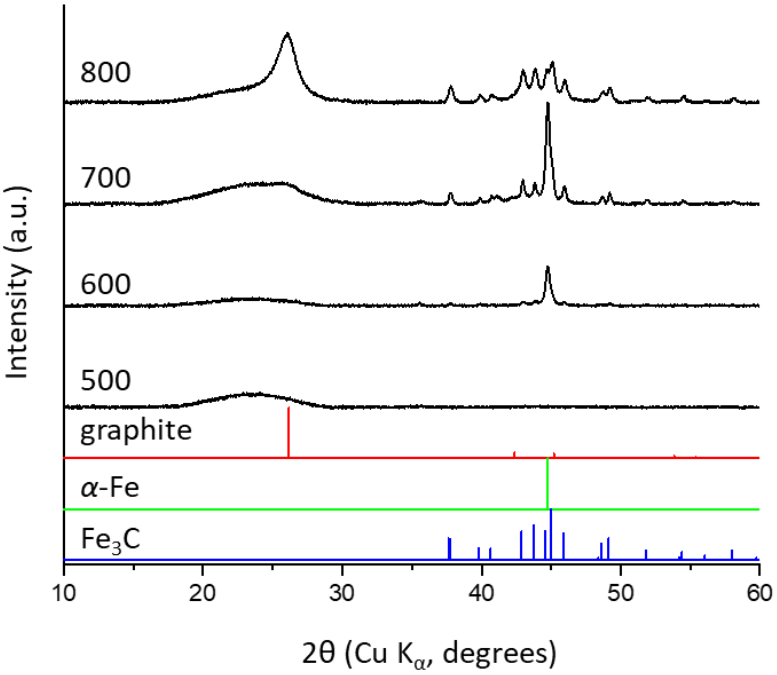

Figure 3.23: PXRD patterns for carbons produced from starch (5 g) and iron nitrate (0.68 mmol), heated to various temperatures (in °C) and held for 1 hr.

Unlike the gelatin/iron nitrate system, no Bragg peaks that can be assigned to iron nitride phases are observed in the glucose-, cellulose- and starch-derived carbon systems. Glucose, starch and cellulose consist of only carbon, hydrogen and oxygen, whereas gelatin is a polypeptide, so contains a considerable amount of nitrogen functionality, which appeared to be acting as the source of nitrogen for the formation of iron nitride. The carbons in this study and the gelatin work were all heated under a nitrogen atmosphere, but the lack of nitride phases here indicates that the nitrogen in the atmosphere is not participating in the reaction mechanism.

The observation that graphitic carbon appears to form at 700 °C in the glucose- and cellulose-derived carbons, but not to a great extent until 800 °C in the starch-derived carbons, shows that the process of graphitization occurs slower in the starch system. To further investigate this, a series of glucose-, starch- and cellulose-derived carbons were synthesized at 800 °C and held at the maximum temperature for 0, 0.5, 1 and 2 hr to determine whether the furnace dwell time had an influence on the graphitic carbon structure.

Similar results are observed in the PXRD patterns for glucose- and cellulose-derived carbons (figures 3.24a and b respectively). For all of the dwell times tested, a significant graphitic carbon peak is observed alongside peaks for iron carbide and *α*-Fe. The intensity of the graphitic carbon peak does not significantly change as the dwell time is varied, suggesting that the graphitization process proceeds quickly upon reaching 800 °C. Peaks corresponding to iron oxide phases such as magnetite are visible in the diffraction pattern of the glucose-derived carbons at the shorter dwell times, as there may not have been enough time for the iron oxide nanoparticles to undergo complete carbothermal reduction to form iron carbide or iron. As the hold time is increased, the intensity of the iron oxide peaks decrease in intensity as more of the iron oxide nanoparticles are reduced.

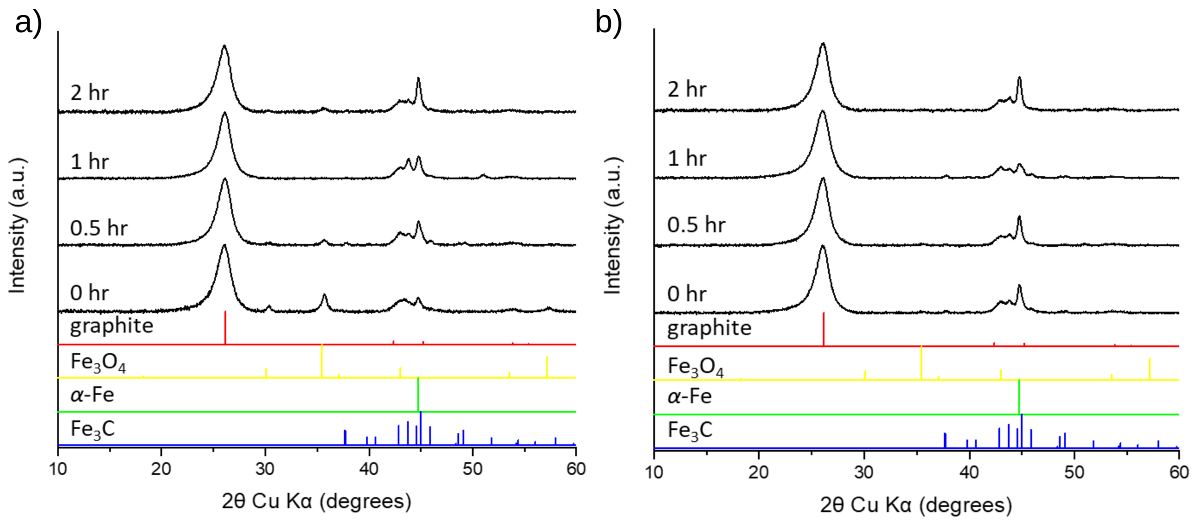

Figure 3.24: PXRD patterns for carbons produced from a) glucose and b) cellulose (5 g) and iron nitrate (0.68 mmol), heated to 800 °C and dwelled for various lengths of time.

The effect of the dwell time at 800 °C in the series of starch-derived carbons is much more pronounced. This is particularly noticeable when the amount of iron nitrate added to the potato starch was increased to 3.4 mmol. The PXRD pattern for the starch-derived carbon held at 800 °C for 0 hr shows an extremely broad, poorly resolved peak at approximately 45 ° 2θ (figure 3.25), likely corresponding to very small iron carbide nanoparticles with low crystallinity. With increasing hold time, the broad amorphous peak transforms into crystalline peaks corresponding to iron carbide, suggesting an increase in the size of the nanoparticles. This can also be observed as a small increase in crystallite size calculated by Scherrer analysis (table 3.8). Furthermore, at 0 hr, the carbon structure is largely amorphous, with the PXRD pattern showing a broad feature centred around 24 ° 2θ. As the hold time increases, and the iron carbide phase becomes increasingly crystalline, a peak at a slightly higher 2θ begins to emerge and grow.

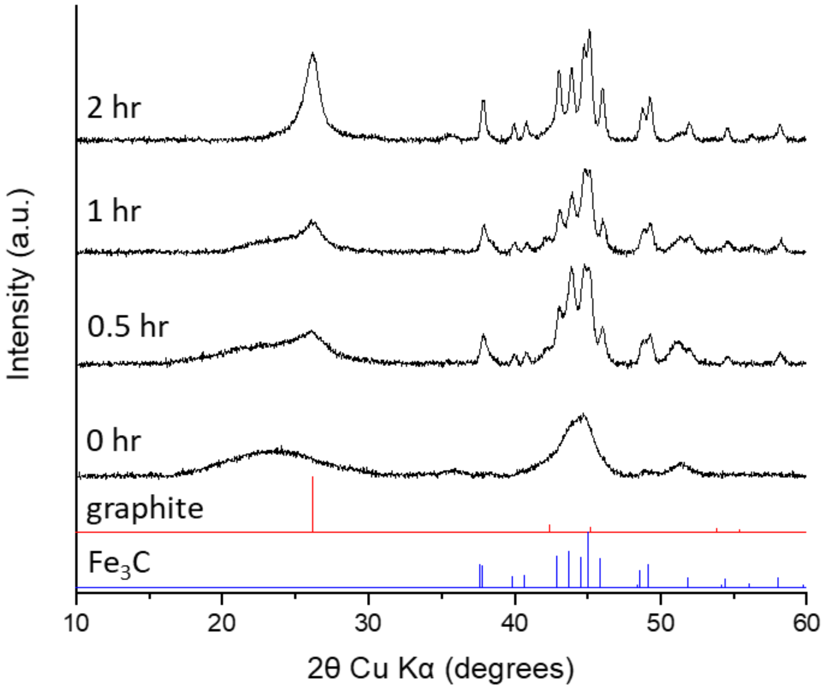

Figure 3.25: PXRD patterns for carbons produced from starch (5 g) and iron nitrate (3.4 mmol), heated to 800 °C and dwelled for various lengths of time.

Table 3.8: Average crystallite size of iron phases in starch-derived carbons synthesized using different dwell times at 800 °C, calculated from Scherrer analysis of PXRD patterns (figure 3.25).

Dwell time at 800 °C (hr)	**Average crystallite size (nm)**	
	Fe$_3$C	***α*-Fe**
0	-	-
0.5	28	-
1	27	27
2	34	33

SAXS results of the starch-derived carbons held at 800 °C for different times show a clear difference in the size of the scattering features with the varying hold times. This can be observed in the raw SAXS patterns as a shift of the broad feature at a q value of approximately 0.4 nm^{-1} in the sample held for 0 hr to a lower q value of approximately 0.1 nm^{-1} after the hold time was increased to 0.5 hr (figure 3.26a). Fitting the data further highlights this growth and shows a considerable increase in the size of the scattering features between the samples held for 0 and 0.5 hr (figure 3.26b-c). It is at this point that a low intensity graphitic carbon peak begins to emerge in PXRD. Gradual growth of the scattering features is then observed with increasing hold time to 2 hr (figure 3.26e), while the carbon structure becomes more graphitic in nature, further suggesting that the iron-based catalyst nanoparticles must reach a critical size in order to become catalytically active.

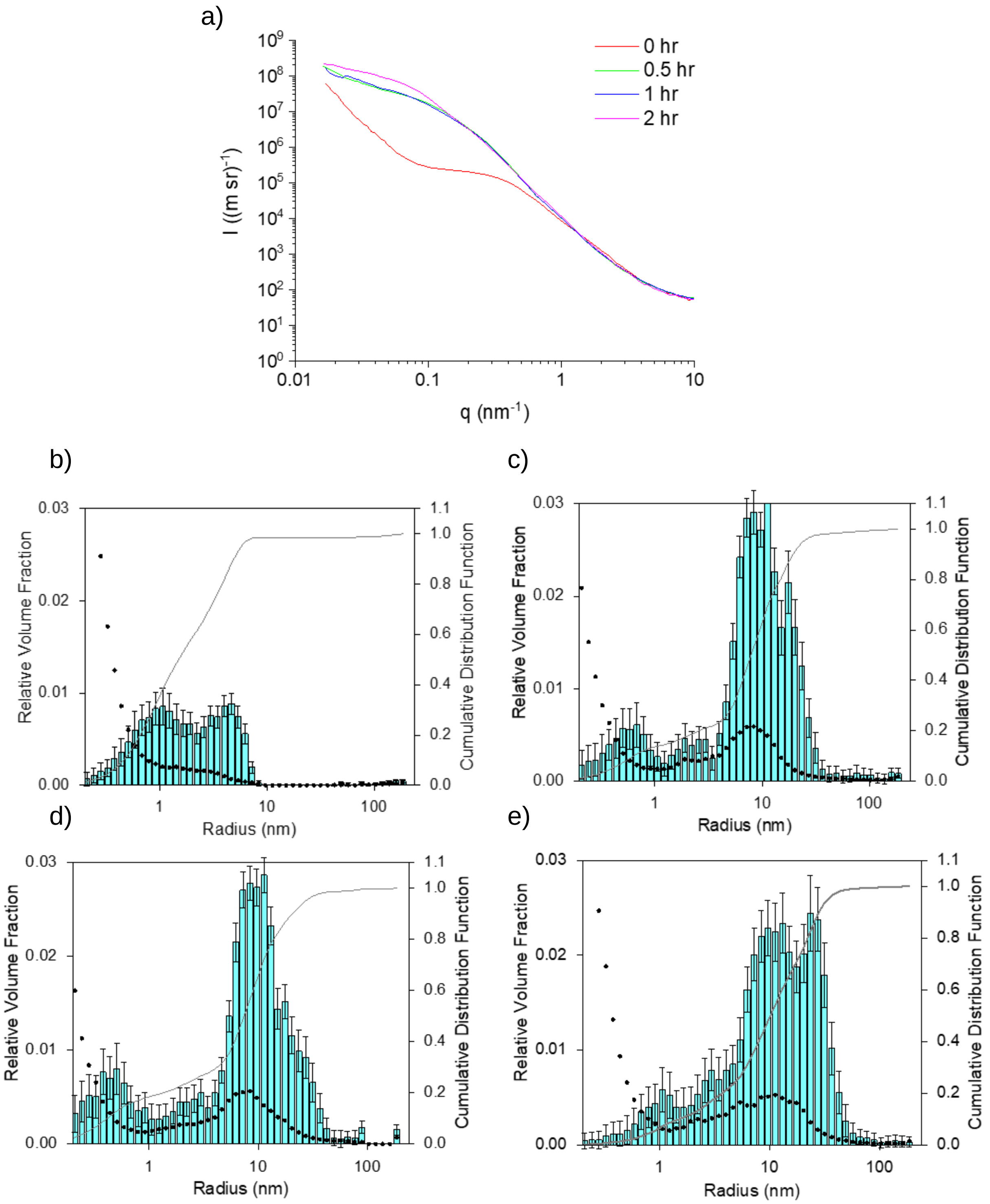

Figure 3.26: a) Raw SAXS data and resulting size distribution histograms calculated using McSAS, including visibility limits (black dots, left y-axis) and cumulative distribution functions (right y-axis), for carbons produced from starch (5 g) and iron nitrate (3.4 mmol), heated to 800 °C and dwelled for b) 0, c) 0.5, d) 1 and e) 2 hr.

Nitrogen sorption measurements were collected to assess the development of the porosity of the starch-derived carbons with increasing hold time (figure 3.27). The samples held at 800 °C for 0 and 0.5 hr show a similar type I shape isotherm with little hysteresis, indicating a distinct lack of mesoporosity. In contrast, the isotherm for the sample held for 1 hr displays hysteresis, indicating the development of mesoporosity in the carbons. The increase in mesoporosity is continued in the sample held for 2 hr, mirroring the iron carbide particle size growth observed in PXRD and SAXS.

The jump from micropores to mesopores seen in the isotherms can be highlighted by the decrease in the BET surface area values as the hold time is increased from 474 m^2g^{-1} for the sample held for 0 hr to 260 m^2g^{-1} for the sample held for 2 hr. This trend is also visible in other adsorptive properties calculated from the isotherms (table 3.9 and figure 3.28) as well as pore size distributions (figure 3.29). These results are consistent with the PXRD data, as the graphitic carbon emerges as mesoporosity is introduced into the carbon structure. In the samples held for 0 and 0.5 hr, the porosity is likely to be predominantly due to the largely disordered turbostratic carbon component, whereas the mesoporosity in the samples held for 1 and 2 hr is due to the newly formed graphitic carbon nanostructures. The size of these nanostructures is dictated by the size of the catalyst nanoparticles. As graphitization induces the formation of mesopores, it seems reasonable to suggest that the critical size that the iron-based catalyst particle must reach in order to become catalytically active is within the mesopore range (2-50 nm).

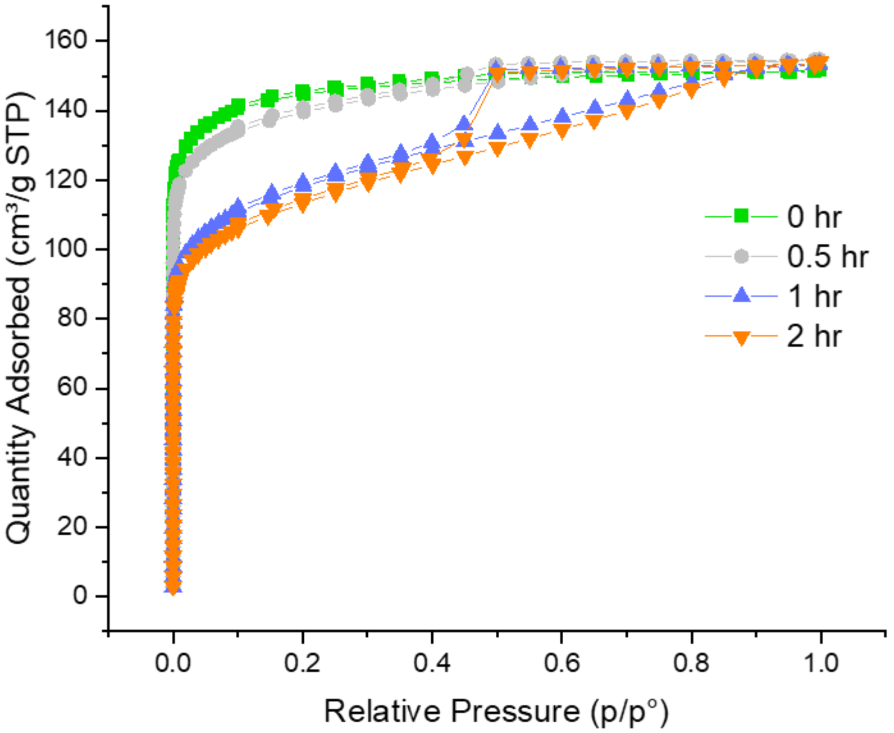

Figure 3.27: Nitrogen sorption isotherms for carbons produced from starch (5 g) and iron nitrate (3.4 mmol), heated to 800 °C and dwelled for various lengths of time.

Table 3.9: Adsorptive properties calculated from nitrogen sorption isotherms of carbons produced from starch (5 g) and iron nitrate (3.4 mmol), heated to 800 °C and dwelled for various lengths of time.

Hold time (hr)	**Max Q_{ads} (cm^3 g^{-1})**	**V_{tot} (cm^3 g^{-1})**	**V_{micro} (cm^{3}g^{-1})**	**S_{micro} (cm^3 g^{-1})**	**W_{avg}:2D-NLDFT (Å)**	**S_{BET} (m^2 g^{-1})**
0	152	0.23	0.18	474	4.8	566
0.5	155	0.24	0.16	418	7.2	539
1	153	0.24	0.11	280	14.8	441
2	154	0.24	0.10	260	17.6	422

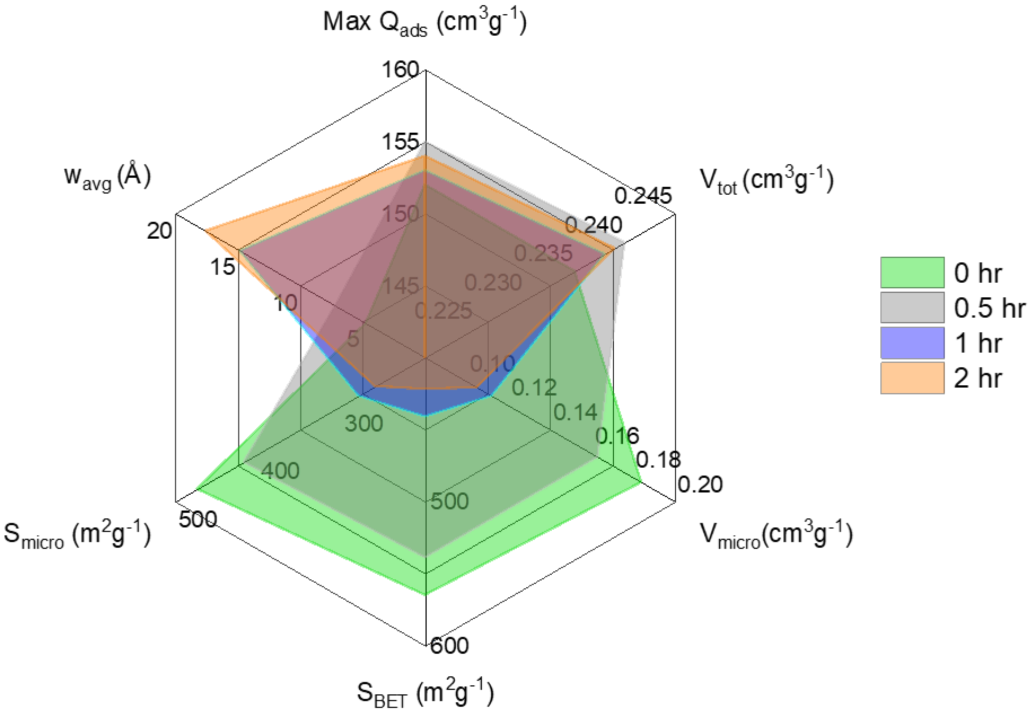

Figure 3.28: Radar plot of adsorptive properties of carbons produced from starch (5 g) and iron nitrate (3.4 mmol), dwelled at 800 °C for various lengths of time.

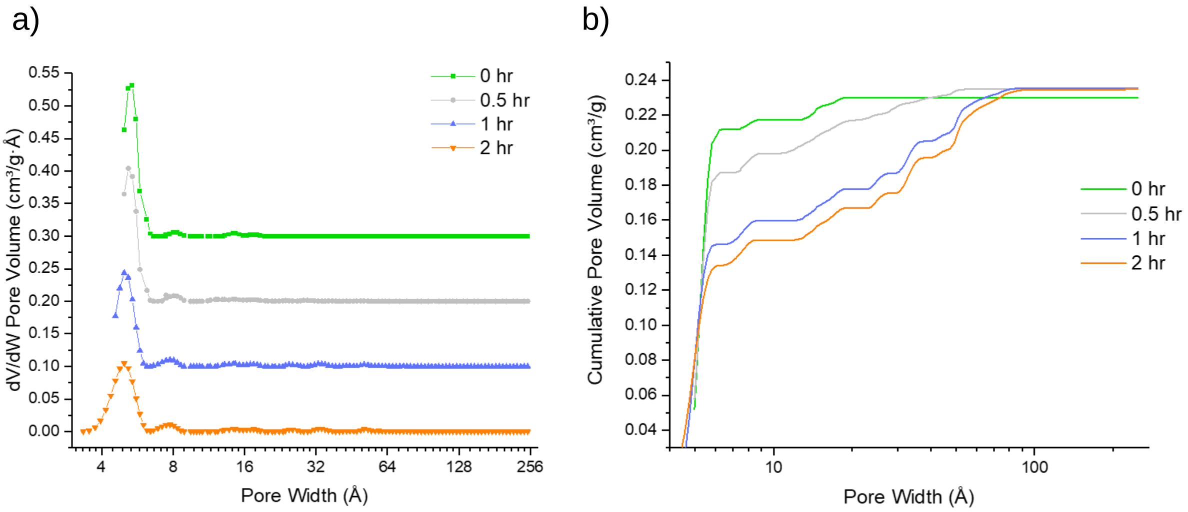

Figure 3.29: a) Pore size distributions and b) cumulative pore size distributions calculated using NLDFT for carbons produced from starch (5 g) and iron nitrate (3.4 mmol), heated to 800 °C and dwelled for various lengths of time.

3.3.4 Mechanism of graphitization

The data suggests that starch restricts the growth of the iron carbide nanoparticles to a greater extent than glucose and cellulose, which appears to result in a slower graphitization process in the starch-derived carbon system. The study of synthesis conditions showed that the initial stage of the reaction pathway was the formation of small iron oxide nanoparticles, similar to previous results in a gelatin/iron nitrate system.[168] These nanoparticles are carbothermally reduced from magnetite to wüstite before further reduction to iron carbide, and in some cases iron. Due to the compositional similarity of the three precursors tested, the reasons for the difference in the size of the iron carbide nanoparticles between glucose/cellulose and starch is likely due to the physical properties of the precursors and their decomposition pathways.

Cellulose fibres are highly hydrophilic, due to the many hydroxyl groups within the polymer structure but are insoluble in water as cellulose polymers form a strong hydrogen bonding network between themselves, resulting in long fibres. Therefore, it is likely that the iron ions from the iron nitrate solution are only able to coat the surface of these fibres, rather than penetrating through the structure (figure 3.30a). As a result, initial nucleation of the iron oxide nanoparticles will also occur on the surface of the cellulose fibres. Upon further heating, and as the iron oxide nanoparticles are carbothermally reduced to form iron carbide nanoparticles, these nanoparticles are free to grow quickly.

Glucose is readily soluble in water so forms a homogeneous solution with the iron nitrate during the initial preparation (figure 3.30b). Therefore, iron ions can be dispersed uniformly throughout the glucose mixture. Iron nitrate is known to thermally decompose into iron oxide at temperatures between 130 and 160 °C. Because glucose is a small molecule, it decomposes at a relatively low temperature of 200 °C. Cellulose and starch, meanwhile, have major decomposition steps between 300 and 350 °C.[169] A large proportion of the carbonaceous material may therefore have already decomposed by the time at which the initial nucleation of small iron oxide nanoparticles occurs. Upon further heating, these iron oxide nanoparticles may grow and sinter relatively easily as there is little carbonaceous material surrounding them to maintain separation of the nanoparticles and restrict growth. Therefore, by the time the iron oxide nanoparticles are reduced to iron carbide, they are relatively large in size and quickly become catalytically active.

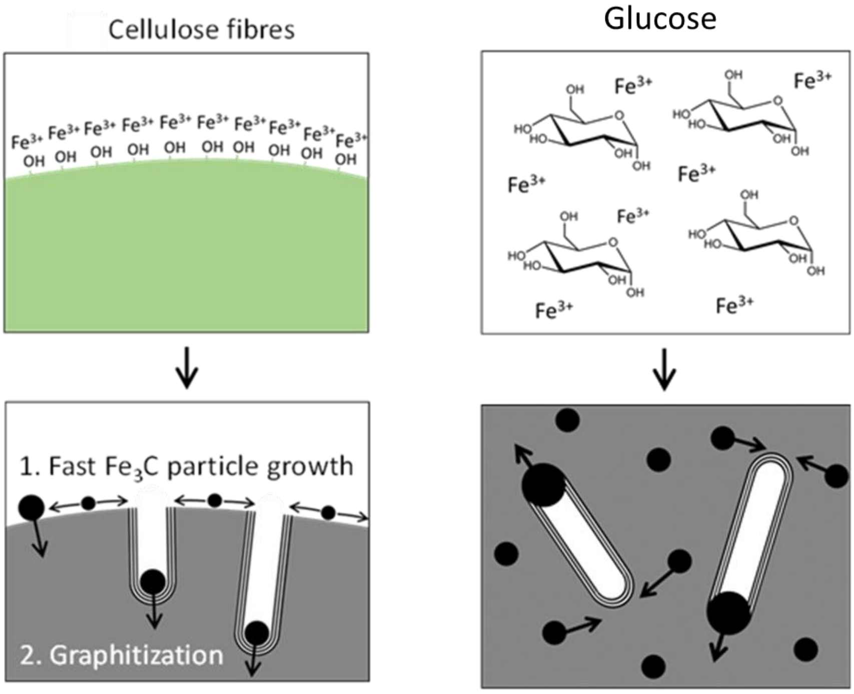

Figure 3.30: Schematic of proposed mechanism of graphitization in cellulose and glucose-derived carbons

The behaviour of starch, however, is considerably different to glucose and cellulose. Starch molecules self-assemble into a granular structure, with alternating layers of amorphous and crystalline regions. The amorphous regions primarily consist of amylose, while the crystalline regions consist of amylopectin double helices. Rather than truly dissolving in water, starch granules undergo swelling upon heating in a process known as “gelatinization”.[170] At this point, the starch granule loses crystallinity and amylose molecules leach out, allowing water molecules to diffuse into the granular structure. In the case of the starch-derived carbon preparation, the starch was heated to the gelatinization point, approximately 70 °C, and the iron nitrate solution was added. Therefore, as well as water molecules, Fe^{3+} ions may have entered the starch granules, forming a thick gel (figure 3.31). Starch undergoes thermal decomposition in a nitrogen atmosphere at approximately 300 °C, considerably higher than glucose.[170] Therefore, as iron nitrate decomposes to form iron oxide, there is significantly more surrounding carbonaceous material that likely prevents sintering and growth of the iron oxide nanoparticles. This appears to also translate to the later growth of Fe_3C nanoparticles, where PXRD, SAXS and nitrogen sorption show slower particle growth.

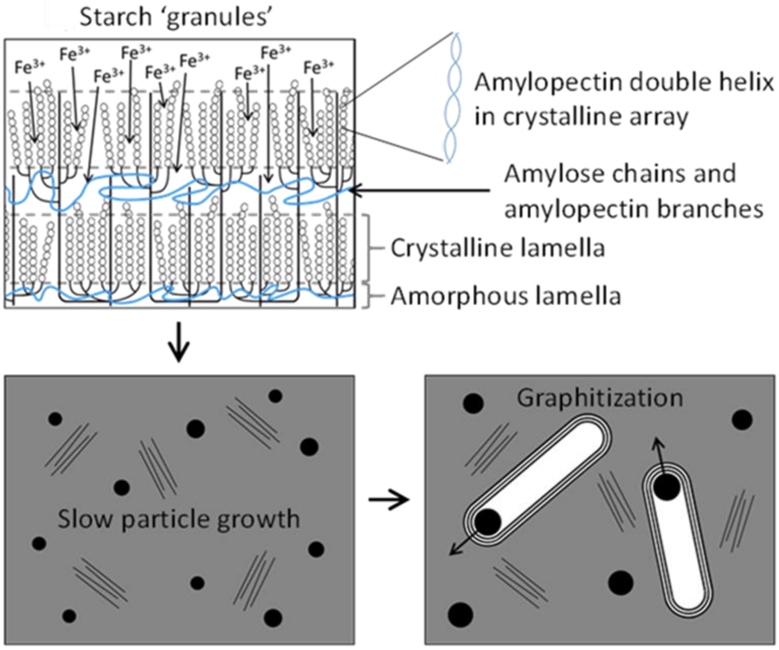

Figure 3.31: Schematic of proposed mechanism of graphitization in starch-derived carbons

The origin of the starch does not appear to affect this behaviour. PXRD results of carbons derived from potato and corn starch both display a significant turbostratic carbon content (figure 3.32). Both starch sources consist of a similar ratio of amylose:amylopectin, approximately 20:80 and 25:75 in potato and corn starch respectively, so this is to be expected. However, carbons derived from waxy corn starch (which consists of almost pure amylopectin with trace amounts of amylose) and pure amylose show different results. The waxy corn starch gives a carbon product with a greater graphitic character than the potato and corn starch-derived carbons, more similar to that of glucose- or cellulose-derived carbon, while pure amylose shows little graphitization. Therefore, it may be concluded that the combination of both amylose and amylopectin within the starch precursor is important for the controlled growth of catalyst nanoparticles.

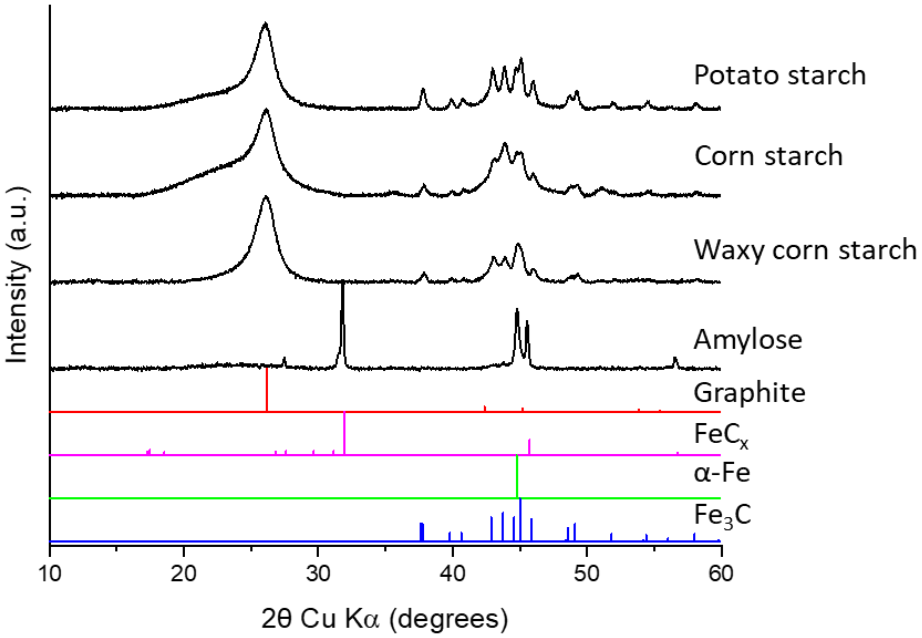

Figure 3.32: PXRD patterns for carbons produced from potato starch, corn starch, waxy corn starch and amylose (5 g) and iron nitrate (0.68 mmol), dwelled at 800 °C for 1 hr.

3.4 Conclusions

Nanostructured graphitic carbons were synthesized from three compositionally similar but structurally different organic precursors: glucose, starch and cellulose. All three organic precursors are composed of the same sugar monomer unit but resulted in graphitic carbon products with different structural and textural properties.

The size of the iron carbide catalyst nanoparticles is understood to be a key factor in the different graphitic carbon structures. This observation is similar to previous reports of carbon nanotube synthesis *via* chemical vapour deposition, in which it was suggested that the catalyst nanoparticle must reach a critical size in order to become catalytically active, and the diameter of the resulting carbon nanotube is then dependent on the size of the catalyst nanoparticles. In this work, fast catalyst particle growth is observed in glucose- and cellulose-derived carbon systems, resulting in a predominantly mesoporous graphitic carbon product as evidenced by nitrogen sorption measurements. PXRD and SAXS data suggest that catalyst particle growth is much slower in starch-derived carbons, resulting in slower graphitization and a graphitic carbon product with a greater degree of microporosity. However, results presented in this chapter are all based on *ex situ* data and *in situ* experiments are required to further probe the kinetics of the graphitization process.

The differences in the structure of the carbon products are believed to be due to the physical properties of the organic precursor, with the combination of both amylose and amylopectin within the granule structure seemingly playing a key role in controlling graphitization. The controllable nature of the starch system, with the degree of graphitization and porosity being dependent on simple reaction conditions such as the furnace dwell time at 800 °C, suggests that the starch system is a promising avenue to explore for the production of tailorable porous graphitic carbons by iron-catalyzed graphitization. However, further investigation of the role of factors such as the amylose:amylopectin ratio and swelling behaviour in the graphitization process is required to fully understand the complex nature of the starch system. Future work should also be directed towards testing the carbons in applications – for example, the performance of the carbons as metal-ion battery anodes – and assessing how the structural differences highlighted in this chapter affect the properties of the carbon when employed in different applications.

Table 3.10: Summary of key findings in chapter 3.

Key Finding	**Evidenced by:**
Possible to synthesize graphitic carbons using iron-catalyzed graphitization of glucose, starch and cellulose.	• Appearance of characteristic peak for graphitic carbon in PXRD • Presence and growth of G band in Raman spectra
Glucose, starch and cellulose produced tubular graphitic carbon nanostructures	• SEM • TEM
Smaller Fe/Fe_3C particle sizes produced in starch-derived carbon under same reaction conditions	• Size distribution histograms extracted from SAXS data
Glucose and cellulose produced predominantly mesoporous carbons. Under the same reaction conditions, starch produced predominantly microporous carbons	• N_2 sorption isotherms and calculated adsorptive characteristics
Graphitization process occurs faster in glucose- and cellulose-derived carbons under the same reaction conditions as starch-derived carbons.	• Growth of characteristic peak for graphitic carbon in PXRD • Development of mesoporosity in N_2 sorption experiments

Chapter 4 - The influence of nitrogen in the synthesis of porous carbons by iron-catalyzed graphitization

4.1 Introduction

The results of the previous chapter highlighted the possible variation in the resulting carbon nanostructure from compositionally similar organic precursors. An additional challenge in identifying trends in the literature is that precursor materials may be impure or contain various heteroatoms within the structure, which could influence graphitization. In many cases, the addition of heteroatoms is deliberate and beneficial. The synthesis of porous carbons doped with heteroatoms such as nitrogen,[171] sulfur[172] and phosphorus[173] is a large area of research, as these materials have been shown to improve performance in various energy applications, such as electrocatalysis,[174,175] supercapacitors[176] and carbon capture.[177] Considerable effort has gone into optimizing the precise structure of heteroatom-doped carbon materials. For example, Menga *et al* selectively introduced tetrapyrrolic Fe-N_4 sites, promising catalytically active sites for polymer exchange membrane fuel cell reactions.[178] A zinc-porphyrin was initially pyrolyzed before exchanging the zinc ions for iron ions, which, if added at the start of the syntheses, would preferentially from less catalytically active pyridinic structures.

From a green chemistry perspective, the use of raw biomass or materials derived from biomass as a precursor is a particularly attractive avenue to explore as they are renewable and often a waste product of industrial processes. However, the structure of biomass is often disordered, with a somewhat random distribution of heteroatom arrangements throughout the structure, making control of the heteroatom chemistry a greater challenge. This chapter investigates iron-catalyzed graphitization of a selection of bio-derived nitrogen-containing organic precursors in combination with iron nitrate solution, examining the effect of the presence of nitrogen within the precursor's structure on the graphitization mechanism. In a previous study by Schnepp *et al* investigating a gelatin and iron nitrate system, only shell-like nanostructures were observed so it may be that the presence of nitrogen has an influence on the nature of the graphitic product.[77]

In this work, two categories of nitrogen-containing organic precursors are examined: amino acid-based precursors (glycine and gelatin) and saccharide-based precursors (N-acetylglucosamine, chitosan and chitin). Of the amino acid-based precursors, glycine is a water-soluble amino acid with the molecular formula $C_2H_5NO_2$ (figure 4.1a), while gelatin is a water-soluble polypeptide that primarily consists of glycine, proline and hydroxyproline residues (figure 4.1b) and is a major waste product of the meat industry.

With regard to the saccharide-based precursors, N-acetylglucosamine is a water-soluble monosaccharide, similar to glucose, with an amide functional group and the molecular formula $C_8H_{15}NO_6$ (figure 4.2a). Chitosan, a highly abundant polysaccharide that can be derived from crustacean shells, is a linear polymer consisting of a mixture of predominantly D-glucosamine along with some N-acetyl-D-glucosamine residues (figure 4.2b). Chitosan has poor solubility in water but can be dissolved in 2 wt% acetic acid solutions. Chitosan is generally produced by the deacetylation of chitin, the final precursor investigated in this study, which is a similar linear polymer consisting of N-acetyl-D-glucosamine residues (figure 4.2c). Chitin is, however, insoluble in both water and weak acetic acid solutions.

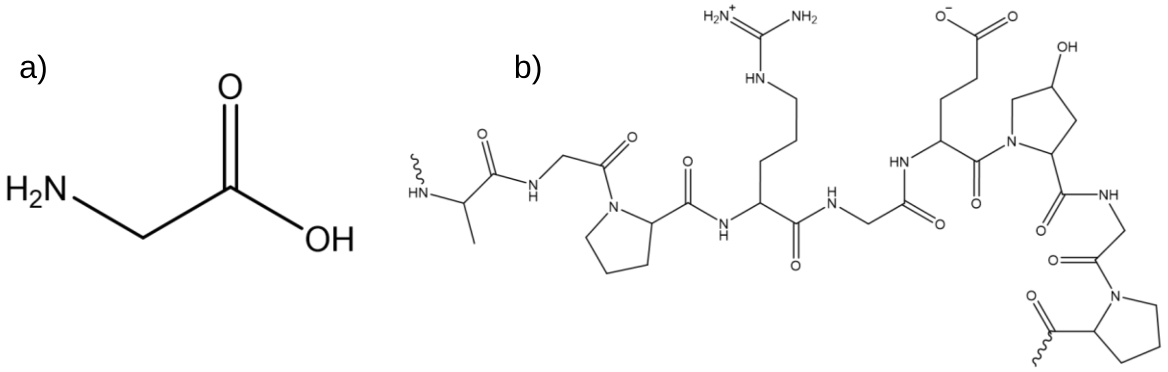

Figure 4.1: a) Structure of glycine and b) representative structure of gelatin.

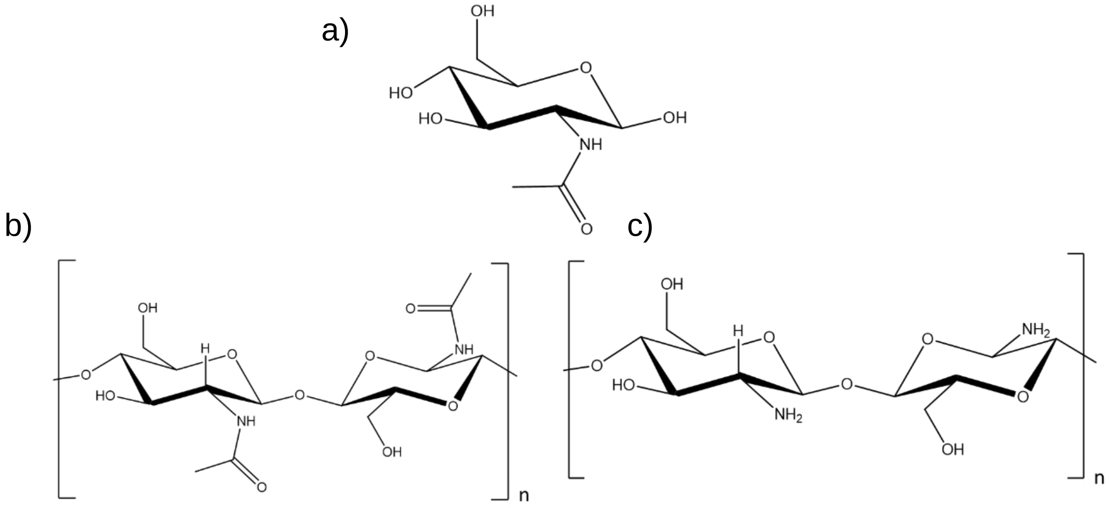

Figure 4.2: Structures of a) N-acetylglucosamine, b) chitosan and c) chitin.

4.2 Experimental

4.2.1 Materials

Table 4.1: Details of materials used in this chapter.

Material	Supplier	CAS Number
Glycine ≥98.5 %	Alfa Aesar	56-40-6
Gelatin, from porcine skin, G2500	Sigma-Aldrich	9000-70-8
N-acetylglucosamine	Sigma-Aldrich	7512-17-6
Chitosan, from shrimp shells	Sigma-Aldrich	9012-76-4
Chitin, from shrimp shells	Sigma-Aldrich	1398-61-4
Iron (III) nitrate nonahydrate, ≥98 %	Sigma-Aldrich	7782-61-8
Acetic acid, glacial, ≥99 %	Sigma-Aldrich	64-19-7

4.2.2 Catalytic graphitization

For glycine samples, 25 ml of deionized water was gently heated in a beaker and 5 g of glycine was added with magnetic stirring until the glycine had completely dissolved. 0.27 g (0.68 mmol) of iron (III) nitrate nonahydrate was dissolved in 4 ml of DI water and this was added to the glycine solution, followed by stirring for 10 min. The mixture was dried in an air oven at 70 °C for 24 hr or until constant mass. The resulting brown, caramel-like material was placed in an alumina boat crucible and heated in a tube furnace at a rate of 5 °C min^{-1} under a nitrogen atmosphere with a flow rate of 1 lmin^{-1} to 800 °C. The samples were held at 800 °C for 1 hr, unless otherwise stated, before cooling completely to room temperature.

For gelatin samples, the same procedure was followed except 5 g of gelatin was dissolved in 50 ml of DI water and heating to 70 °C was required to achieve dissolution before the addition of iron nitrate solution.

For chitosan samples, 5 g of chitosan was dissolved in 250 ml, 2 wt% acetic acid solution and stirred for 3 hr before the addition of iron nitrate solution.

For chitin samples, 0.27 g (0.68 mmol) of iron (III) nitrate nonahydrate was dissolved in 20 ml of DI water at room temperature and the resulting solution was added to a beaker containing 5 g of chitin. The mixture was manually stirred until the solution had been absorbed. The sample was dried and pyrolyzed as above.

Control samples from each organic precursor were prepared using the same method but without the addition of iron nitrate solution.

4.2.3 PXRD

Samples were ground into a fine powder and placed on low-background silicon wafer sample holders. PXRD experiments were performed using a PANalytical Empyrean diffractometer with a copper anode (wavelengths: $K_{\alpha 1}$ = 1.5406 Å, $K_{\alpha 2}$ = 1.5443 Å) and a Pixel 2D detector. The diffractometer did not have a monochromator fitted but the K_{β} radiation was removed with a nickel filter.

4.2.4 Raman spectroscopy

Samples were ground into a fine powder and placed on a glass slide. Raman spectroscopy measurements were collected using a Renishaw inVia Raman microscope with a green laser (wavelength of 532 nm) at 10 % power for 10 accumulations for each sample. Deconvolution of the resulting spectra was performed using Voigt peak shapes.

4.2.5 SEM

Samples were mounted on an SEM stub using an adhesive carbon tape. Samples were viewed with a FEG-SEM FEI Nova 450 in secondary electron mode operating at 5 kV.

4.2.6 Elemental analysis

Elemental analysis data was collected using a Thermo Scientific FlashSmart CHNS Elemental analyser.

4.2.7 XPS

XPS measurements were performed using a Thermo Scientific Nexsa X-ray photoelectron spectrometer system utilizing aluminium K_{α} X-rays. A Shirley background was subtracted from all spectra and fitted in CasaXPS.[179]

4.2.8 SAXS

Samples were ground into a fine powder and distributed across a hole in a paper sample holder between two pieces of Scotch® Magic™ tape. The wide-range SAXS experiments were performed using the Multi-scale Analyser for Ultrafine Structures at the Federal Institute for Materials Research and Testing, Berlin. Copper and molybdenum anodes (8 eV and 17 eV photons, respectively) were used to measure over a wide *q*-range.

4.2.9 Nitrogen sorption

Nitrogen sorption measurements were carried out at 77 K using a Quantachrome Nova 1000 series volumetric gas sorption analyser. 50-200 mg of sample was degassed at 150 °C for 24 hr under vacuum. Isotherms were collected with filler rods over the range p/p^0 0.015 – 0.95. BET surface areas were calculated by applying the Rouquerol correction to select an appropriate p/p^0 using the method recommended by ISO 9277.[155] The total pore volume measurable by nitrogen sorption was obtained from the isotherm plateau at p/p^0 0.95 and the micropore volume and micropore surface area were calculated using the *t*-plot method, according to ISO 15901-3.[156]

4.2.10 TGA

TGA data was obtained using a Q50 - Thermogravimetric Analyzer (TA instruments). Thermograms were recorded under a nitrogen atmosphere at a heating rate of 10 $\mathrm{Kmin^{-1}}$, from 25-800 °C, with an average sample weight of approximately 10 mg.

4.2.11 TGA-MS

TGA-MS data was obtained using a NETZSCH STA 449F3 Jupiter instrument, the samples were run from 40-800 °C under a nitrogen atmosphere with a 10 $\mathrm{Kmin^{-1}}$ ramp rate.

4.2.12 TEM

Small portions of sample (≈ 50 mg) were dispersed in ethanol (≈ 1 ml) by sonication for 10 min. One drop of the dispersion was pipetted on to a carbon-coated copper TEM grid. The images were obtained using a JEM 1400 TEM.

4.3 Results and discussion

4.3.1 Catalytic graphitization of N-containing organic precursors

Carbon samples were prepared by iron-catalyzed graphitization, with glycine, gelatin (from porcine skin), N-acetylglucosamine, chitosan (from shrimp shells) and chitin (from shrimp shells) as the sources of carbon, and iron nitrate solution as the source of iron. Figure 4.3 shows PXRD patterns of the resulting black powders, displaying predominantly broad peaks centred at approximately 25° and 45° 2θ, consistent with an amorphous carbon structure. PXRD patterns for carbons produced from glucose, starch and cellulose in the previous chapter (all precursors that only consist of carbon, hydrogen and oxygen) using the same reaction conditions are included as a comparison. These show a much greater degree of graphitization than the carbons produced from the nitrogen-containing precursors, suggesting that the presence of nitrogen in the precursor structure reduces the degree of graphitization.

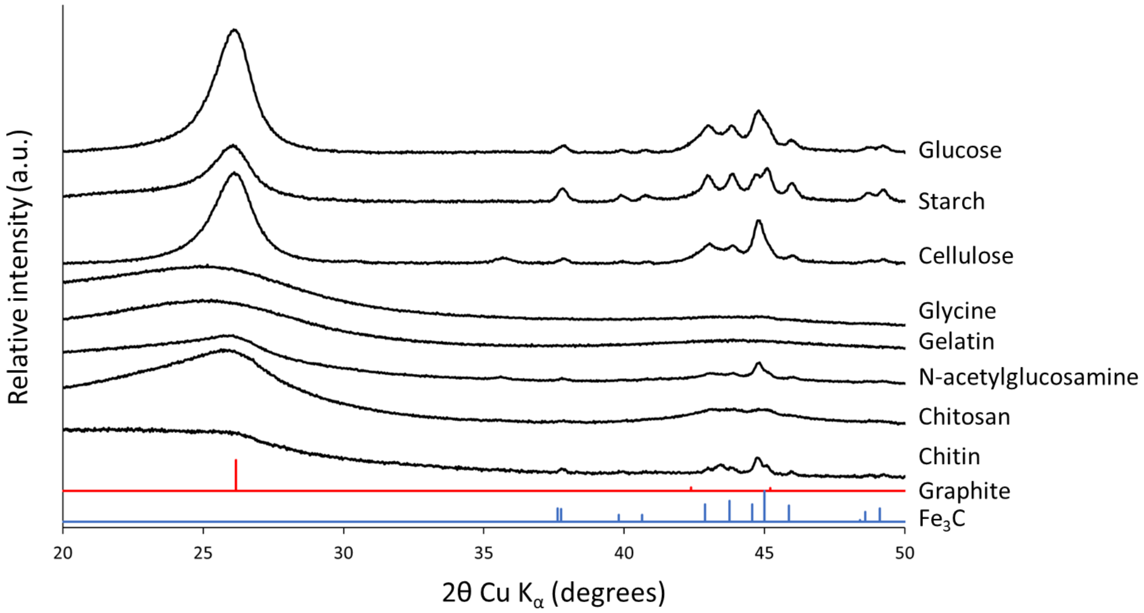

Figure 4.3: PXRD patterns for carbon samples produced from glucose, starch, cellulose, glycine, gelatin, N-acetylglucosamine, chitosan and chitin (5 g) and iron nitrate solution (0.68 mmol), dwelled at 800 °C for 1 hr.

The diffraction patterns of glycine- and gelatin-derived carbons show particularly broad features and no peaks corresponding to any crystalline iron phases, suggesting either that any iron species present in these samples are amorphous, or that the crystallite size is too small to contribute enough Bragg scattering to be measured by a lab powder X-ray diffractometer. The peak at approximately 25° 2θ, which corresponds to the (002) reflection of graphite, is shifted to a slightly higher diffraction angle in the N-acetylglucosamine, chitosan and chitin-derived carbons, suggestive of a more turbostratic carbon structure. These samples also display low intensity peaks at approximately 45° 2θ, which are likely to correspond to iron carbide.

Further characterization of the carbons was carried out using Raman spectroscopy. All spectra exhibit peaks at approximately 1325 and 1600 cm^{-1}, corresponding to the D (noted as D1) and G bands respectively (figure 4.4), similar to the spectra observed in chapter 3.

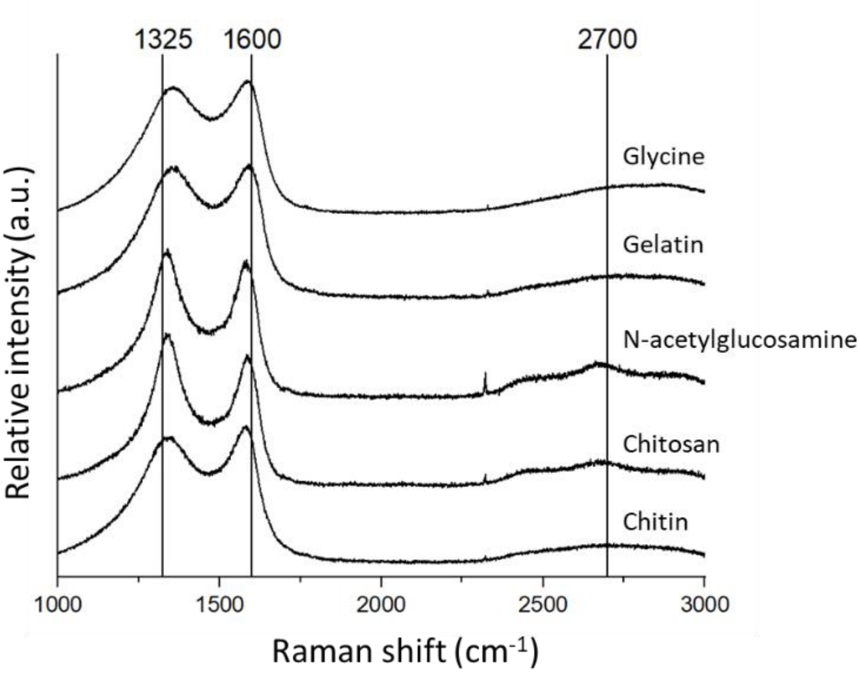

Figure 4.4: Raman spectra for carbon samples produced from glycine, gelatin, N-acetylglucosamine, chitosan and chitin (5 g) and iron nitrate solution (0.68 mmol), dwelled at 800 °C for 1 hr.

Values calculated from fitting of the spectra show sharper peaks corresponding to the D1 and G bands in the chitosan- and N-acetylglucosamine-derived carbons (table 4.2). Previous Raman spectroscopy studies of carbon materials have used the FWHM of the G band as an indicator of increased bond-angle ordering at sp^2 sites. Therefore, suggesting a greater degree of graphitization.[180,181] This is consistent with PXRD results, which showed a shift in the (002) reflection peak to a higher diffraction angle.

Table 4.2: Results from fitting of Raman spectra in figure 4.4. All measurements were collected in triplicate on different locations and the average values are reported with uncertainty values.

Organic precursor	**Band**	**Peak position (cm^{-1})**	**FWHM (cm^{-1})**	**I_D/I_G**
Glycine	D1	1357 +/- 4	167 +/- 17	1.18 +/- 0.08
	G	1595 +/- 2	93 +/- 5	
Gelatin	D1	1358 +/- 1	176 +/- 7	1.24 +/- 0.04
	G	1599 +/- 1	92 +/- 2	
N-acetylglucosamine	D1	1336 +/- 1	127 +/- 7	1.32 +/- 0.01
	G	1585 +/- 2	78 +/- 2	
Chitosan	D1	1344 +/- 3	136 +/- 22	1.31 +/- 0.03
	G	1591 +/- 3	81 +/- 5	
Chitin	D1	1345 +/- 2	163 +/- 4	1.04 +/- 0.01
	G	1587 +/- 1	91 +/- 1	

SEM images of the carbons (Figure 4.5) generally show relatively smooth surfaces coated in bright spots, potentially corresponding to iron carbide particles or due to charging of the surface. Chitosan forms a thick hydrogel when it is mixed with weak acetic acid and SEM images show that the porosity of the gel is maintained in the resulting chitosan-derived carbon. PXRD and Raman spectroscopy showed little graphitization in the chitosan-derived carbon, so these large pores are unlikely to be a result of iron-catalyzed graphitization. SEM images of chitin-derived carbon show a wrinkled, fibrous structure.

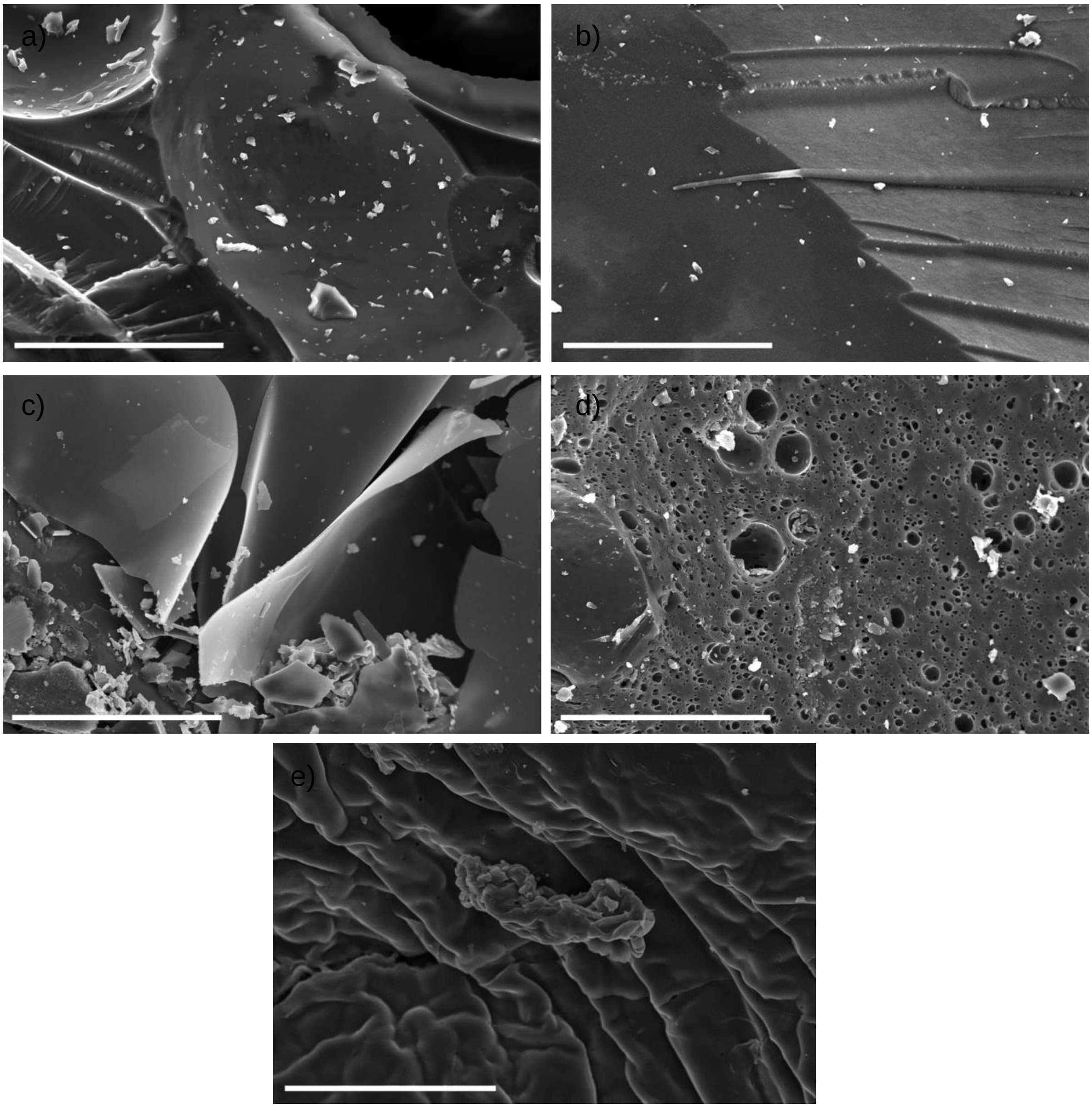

Figure 4.5: SEM images of carbons produced from a) glycine, b) gelatin, c) N-acetylglucosamine, d) chitosan and e) chitin (5 g) and iron nitrate (0.68 mmol), heated to 800 °C and dwelled for 1 hr. Scale bar = 10 μm

Elemental analysis and XPS measurements of the various carbons show that the nitrogen content of the initial starting material is retained in the final carbon material (table 4.3). Therefore, the amino acid-based glycine and gelatin-derived carbons contain a greater proportion of nitrogen than the saccharide-based N-acetylglucosamine-, chitosan- and chitin-derived carbons. The low iron content in all of the samples shown in XPS suggest that the mixing procedure generally results in iron being dispersed throughout the bulk of the carbon structure with little remaining on the surface (figure 4.6a).

Table 4.3: Atomic compositions of carbon samples produced from glycine, gelatin, N-acetylglucosamine, chitosan and chitin (5 g) and iron nitrate solution (0.68 mmol), heated to 800 °C and dwelled for 1 hr.

Precursor	**C%**		**N%**		**H%**	**O%**	**Fe%**
	EA	**XPS**	**EA**	**XPS**	**EA**	**XPS**	**XPS**
Glycine	70.7	84.1	15.1	9.8	0.8	5.7	0.4
Gelatin	69.6	87.3	13.8	6.3	3.5	6.0	0.4
N-acetylglucosamine	80.5	94.2	5.0	2.0	0.6	3.6	0.3
Chitosan	82.3	88.1	9.1	4.5	1.0	7.3	0.1
Chitin	79.0	91.9	5.8	3.2	0.8	4.8	0.1

Deconvolution of high-resolution nitrogen 1s spectra show four types of nitrogen species within the carbon samples (figure 4.6b). The peaks at approximately 398.1, 399.5, 400.8 and 402.5 eV can be ascribed to pyridinic-N, pyrrolic-N, graphitic-N and oxidized-N, respectively (appendix B – figure 8.3-8.7).[182] The presence of pyridinic, pyrrolic and graphitic-N shows that nitrogen is doped into the carbon structure. N-acetylglucosamine- and chitin-derived carbons show a greater proportion of graphitic-N and a lower proportion of pyrrolic-N, consistent with the greater degree of graphitization observed in PXRD. The higher content of pyrrolic-N is likely to disrupt the graphitic layers, consistent with the greater disorder observed in PXRD and Raman spectroscopy in glycine-, gelatin- and chitosan-derived carbons.

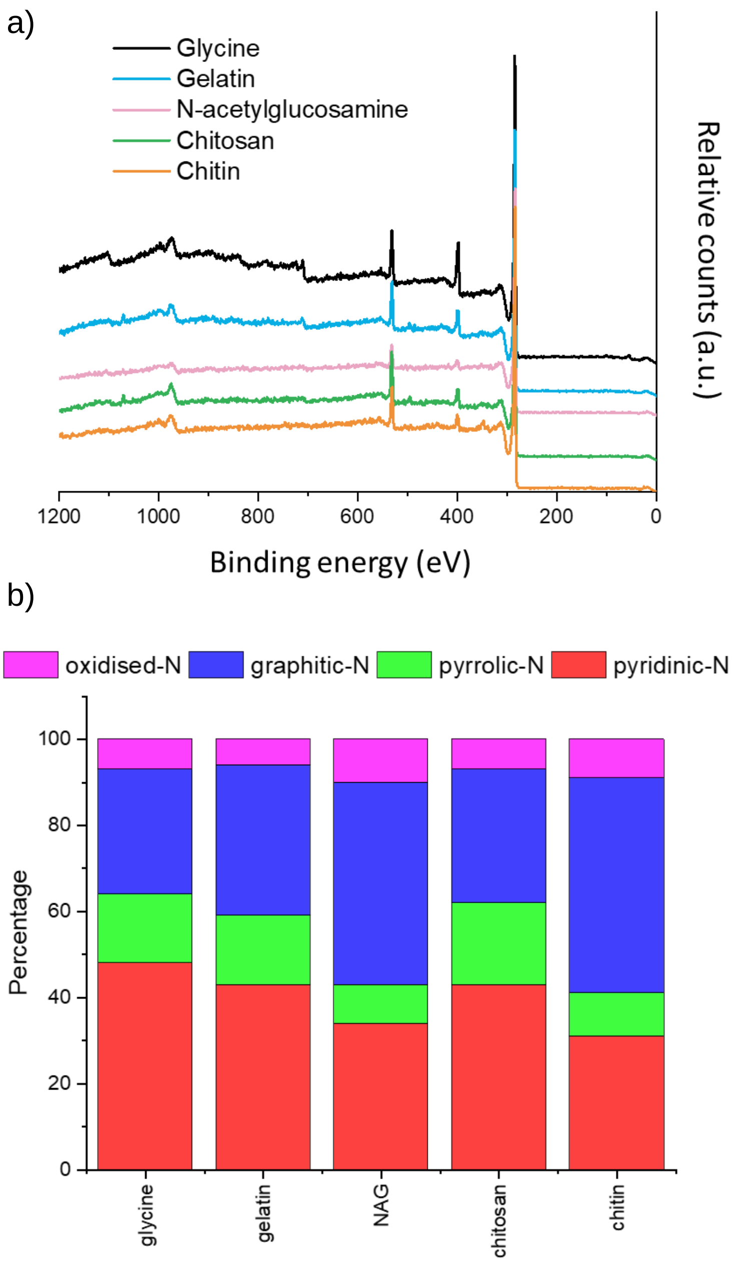

Figure 4.6: a) XPS survey spectra and b) relative distributions of nitrogen species calculated from XPS spectra of carbon samples produced from glycine, gelatin, N-acetylglucosamine, chitosan and chitin (5 g) and iron nitrate solution (0.68 mmol) and dwelled at 800 °C for 1 hr.

SAXS was used to assess the size of the iron-based particles within the carbon matrix (figure 4.7a). The resulting size distribution histograms for the glycine- and gelatin-derived carbons, calculated from fitting using McSAS, showed a large population of very small scattering features (radius <1 nm) (figure 4.7b and c). As SAXS arises from of varying electron density within a sample, various possible scattering interfaces that must be considered, such as the interface between the iron/iron carbide particles and the surrounding carbon matrix as well as the carbon/air interface. However, the size of the particles observed in SEM are consistent with the very small features observed in the size distribution histograms from SAXS, so it seems reasonable to suggest that this population (or at least part of it) with a radius < 1 nm is a result of the iron carbide/carbon scattering interface. This small particle size may be a reason why little graphitization is observed in the glycine- and gelatin-derived carbons; as was suggested in chapter 3, the catalyst particles must reach a certain critical size before they are catalytically active for the conversion of amorphous to graphitic carbon.

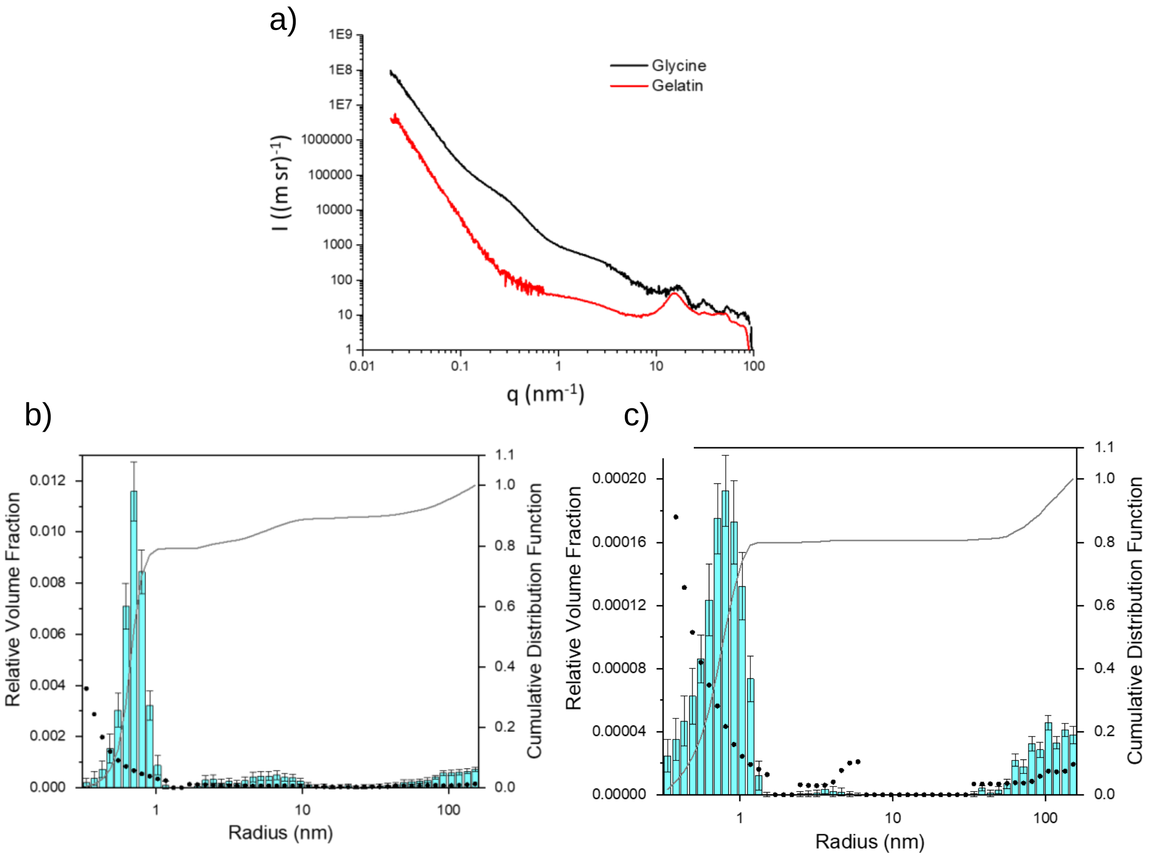

Figure 4.7: a) Raw SAXS patterns and resulting size distribution histograms calculated from McSAS fitting of SAXS data for carbons produced from b) glycine and c) gelatin (5 g) and iron nitrate solution (0.68 mmol), dwelled at 800 °C for 1 hr.

The histograms calculated from McSAS fitting of SAXS data for the N-acetylglucosamine-derived carbon show a range of different sized scattering features (figure 4.8b). This suggests that catalyst nanoparticle growth happens more quickly in the N-acetylglucosamine system. SAXS data for chitin-derived carbons show a large population of scattering features with radii between 1-10 nm, suggesting greater catalyst particle growth (figure 4.8d). The particles in both the N-acetylglucosamine and chitin-derived carbon may quickly reach the critical size to be active graphitization catalysts. This is consistent with the shift of the (002) reflection in PXRD to a sharper peak at approximately 26 °, more similar to that of graphite.

SAXS data for the chitosan-derived carbon shows a large population of scattering features with r < 1 nm (figure 4.8c). There is also a population of scattering features with a radius between 1-10 nm, suggesting that chitosan limits the growth of the catalyst particles. The observation of some features in the 1-10 nm range suggests that some catalyst particles may have grown sufficiently to act as graphitization catalysts, as some graphitic ordering is observed in the chitosan-derived carbon, especially when compared with the amorphous glycine- and gelatin-derived carbons.

Average crystallite sizes in the nitrogen-doped carbons calculated from Scherrer analysis of PXRD patterns (figure 4.3) are shown in table 4.4 for comparison. For the glycine, gelatin- and chitosan-derived carbons, Bragg peaks are unclear in the PXRD patterns so an average crystallite size could not be calculated. However, this does suggest that the crystals are likely to be extremely small in size, which is consistent with the observations in the SAXS data.

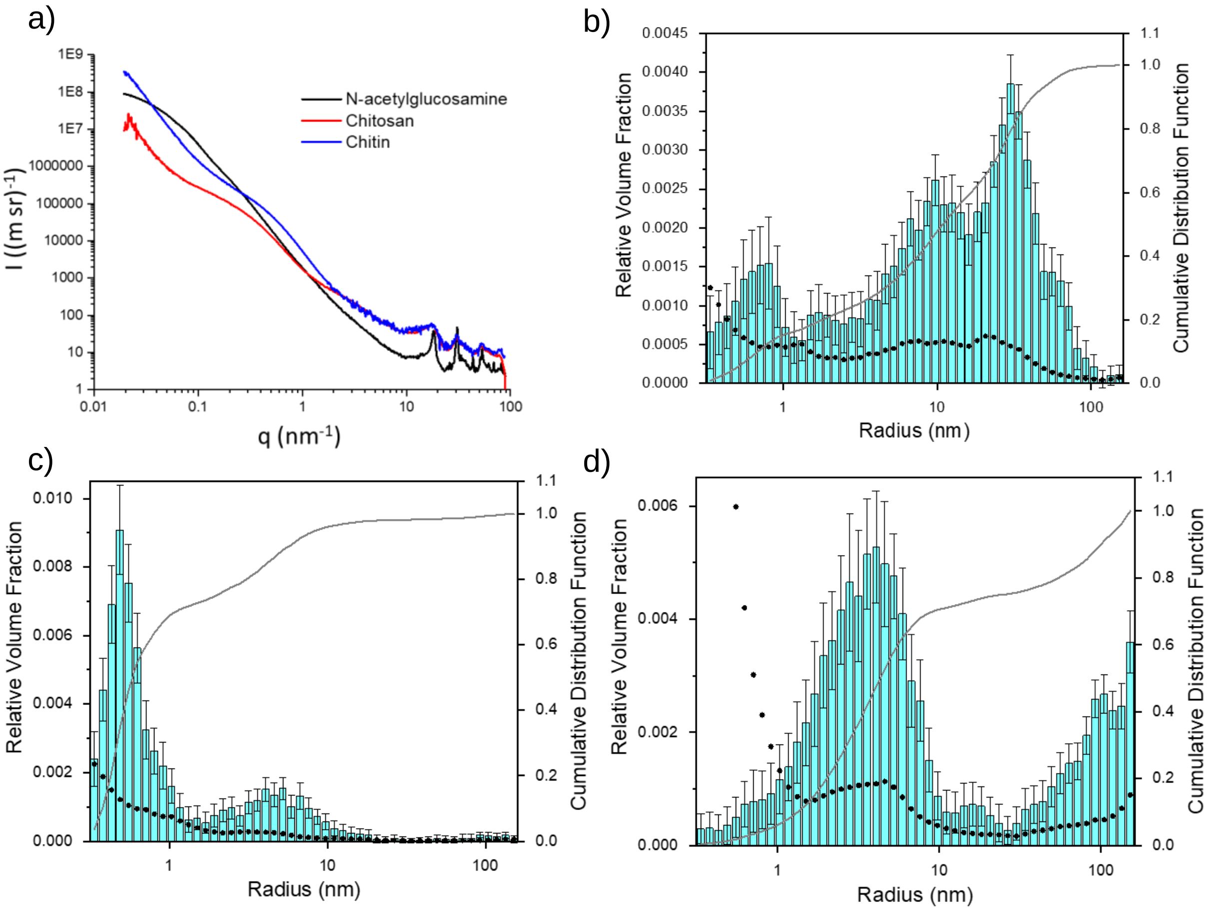

Figure 4.8: a) Raw SAXS patterns and resulting histograms calculated from McSAS fitting of SAXS data for carbons produced from b) N-acetylglucosamine, c) chitosan and d) chitin (5 g) and iron nitrate solution (0.68 mmol), dwelled at 800 °C for 1 hr.

Table 4.4: Average crystallite size of iron phases in carbons synthesized using different nitrogen-containing precursors (5 g) and iron nitrate solution (0.68 mmol), calculated from Scherrer analysis of PXRD patterns (figure 4.3).

Organic precursor	**Average crystallite size (nm)**	
	Fe_3C	**α-Fe**
Glycine	-	-
Gelatin	-	-
N-acetylglucosamine	28	-
Chitosan	-	-
Chitin	38	24

Nitrogen sorption measurements were used to assess the porosity of the carbon samples (figure 4.9). Glycine- and gelatin-derived carbons exhibit low porosity – the specific surface area of the gelatin-derived carbon is too low to calculate a reasonable value – while glycine-derived carbon has a specific surface area of just 27 m^2g^{-1}. N-acetylglucosamine-, chitosan- and chitin-derived carbons show greater porosity, adopting a more type IV isotherm shape with hysteresis due to capillary condensation, indicative of the presence of mesopores. N-acetylglucosamine-, chitosan- and chitin-derived carbons show specific surface area values of 246, 89 and 390 m^2g^{-1}, respectively. Other calculated adsorptive properties are reported in table 4.5 and these data mirror the sorption isotherms. The carbons that display a greater porosity are those that show a larger particle size in SAXS and a greater degree of graphitization, suggesting that the porosity, particularly on the mesopore scale, is a direct result of the conversion of amorphous to graphitic carbon within the samples.

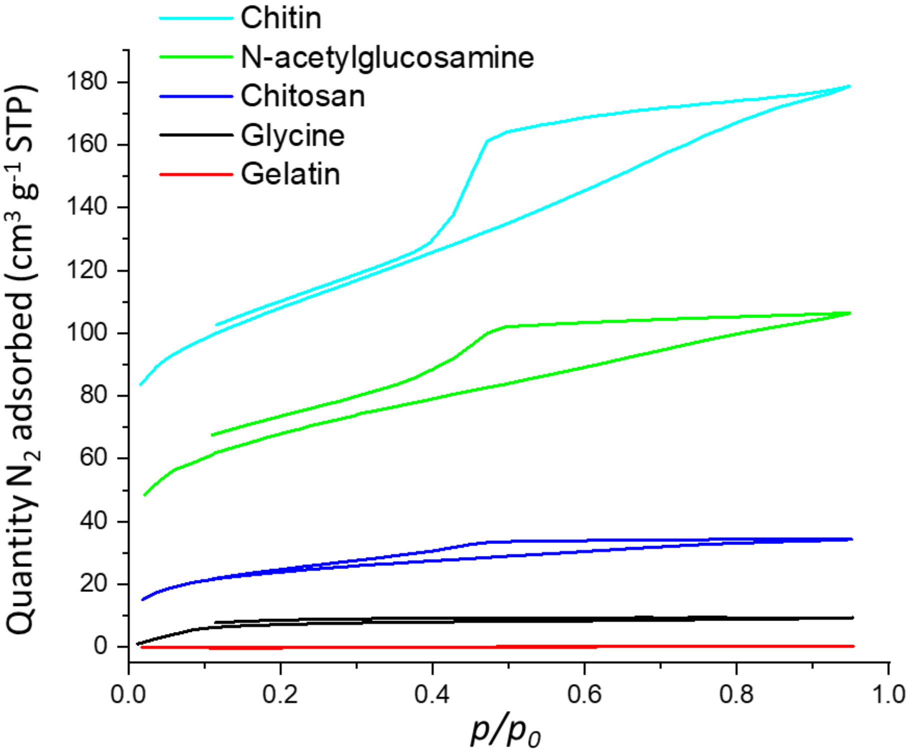

Figure 4.9: N_2 sorption data for carbons produced from glycine, gelatin, N-acetylglucosamine, chitosan and chitin (5 g) and iron nitrate solution (0.68 mmol), heated to 800 °C and dwelled for 1 hr.

Table 4.5: Adsorptive properties of carbons produced from glycine, gelatin, N-acetylglucosamine, chitosan and chitin (5 g) and iron nitrate solution (0.68 mmol), heated to 800 °C and dwelled for 1 hr.

Precursor	**S_{BET} (m^2g^{-1})**	**Max Q_{ads} (cm^3g^{-1})**	**V_{tot} (cm^3g^{-1})**	**S_{micro} (m^2g^{-1})**	**V_{micro} (cm^3g^{-1})**	**V_{micro}/V_{tot} (%)**
Glycine	27	9	0.015	4	0.001	7
Gelatin	-	-	-	-	-	-
N-acetylglucosamine	246	106	0.17	86	0.035	21
Chitosan	89	34	0.054	32	0.012	22
Chitin	390	180	0.28	173	0.073	26

TGA data shows the thermal decomposition of the various organic precursor/iron nitrate mixtures under a nitrogen atmosphere (figure 4.10). As glycine is a small molecule, it decomposes at a lower temperature than gelatin due to the larger size of the gelatin polymer chains. N-acetylglucosamine initially decomposes at a lower temperature than the polymeric species, chitosan and chitin, again due to the lower molecular weight. The variation in the decomposition behaviour of chitosan and chitin may be ascribed to the degree of acetylation. The structure of chitin contains many more N-acetyl groups. This increases the thermal stability of chitin compared with the deacetylated glucosamine units, which make up a large portion of the polymer chains in chitosan.[183]

The chitosan-derived carbon resulted in a greater mass of char residue than the chitin-derived carbon, an observation that has been previously reported in the literature. Arora *et al* suggested that the main decomposition event is a combination of two exothermic processes and ascribed this to thermal decomposition of amino and N-acetyl residues.[184] This contrasts with the decomposition of chitin, which is a single fast endothermic event, primarily due to the depolymerisation of polymeric chains into volatile low molecular weight molecules alongside the char. The authors suggested that this fast depolymerisation step in the chitin-derived carbon results in a lower percentage of char residue.[184]

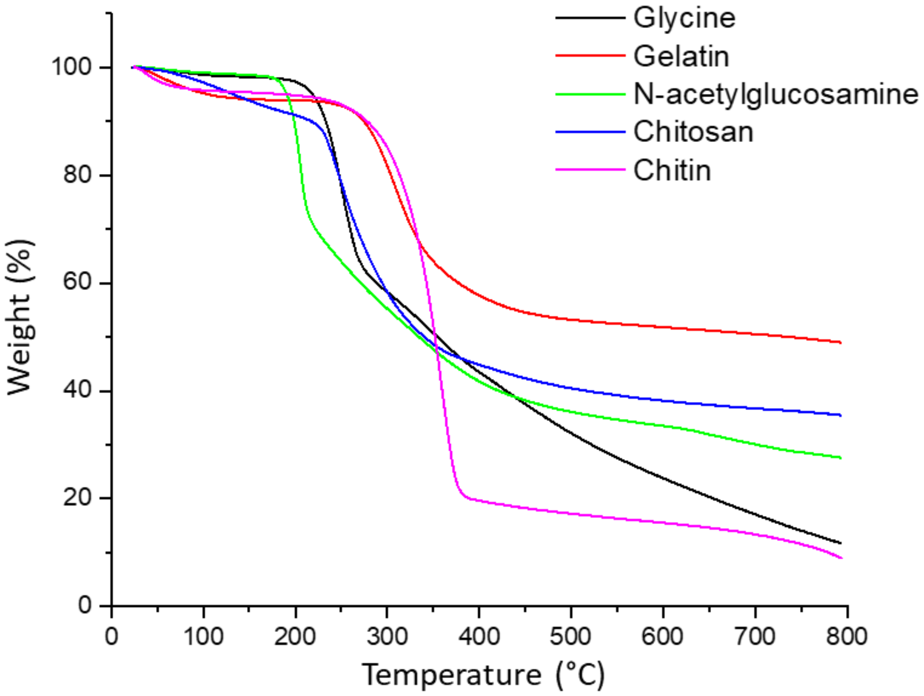

Figure 4.10: TGA data of carbons produced from glycine, gelatin, N-acetylglucosamine, chitosan and chitin (5 g) and iron nitrate solution (0.68 mmol), heated under a N_2 atmosphere at a rate of 5 °C/min.

In the case of N-acetylglucosamine, chitosan and chitin-derived carbons, the nature of the organic precursor appears to influence the size of the catalyst particles. This mirrors the results of the previous chapter, where particle size appeared to have a direct impact on the degree of graphitization of the carbons. Catalyst particle growth occurs quicker in both the N-acetylglucosamine- and chitin-derived carbons than the chitosan-derived carbons. This is likely due to the varying physical properties of the organic precursors. N-acetylglucosamine is a small molecule, so decomposes at a relatively low temperature of 200 °C (figure 4.10). Therefore, the major decomposition step of the precursor occurs before the initial nucleation of iron oxide nanoparticles, so these particles may grow without being hindered by large amounts of carbonaceous matter. Similar fast particle growth is observed in carbons derived from chitin. Although chitin is a polymer, with the major decomposition step occurring at a higher temperature of approximately 350 °C, chitin is insoluble in water, so when mixed with iron nitrate solution, the iron ions may coat the surface of the chitin rather than penetrating into the structure. As a result, the resulting iron oxide nanoparticles nucleate on the surface and are able to freely move and sinter.

In chitosan-derived carbons, catalyst particle growth proceeds more slowly. This is similar to observations of starch-derived carbons in the previous chapter. Chitosan forms a gel when dissolved in weak acetic acid solution, and upon addition of iron nitrate solution, iron ions can homogeneously disperse throughout the gel structure. Upon pyrolysis, as the initial iron oxide nanoparticles nucleate, they are surrounded by a large amount of carbon-rich matter, which decomposes at a temperature of 250 °C. The surrounding carbonaceous matter may restrict the growth of the iron oxide nanoparticles. Therefore, as they are carbothermally reduced to form iron carbide, they remain small and take longer to reach the critical size for graphitization.

However, the different thermal properties of the amino acid-based precursors, glycine and gelatin, seem to have little impact on the size of the catalyst particles. As glycine is a small molecule, it decomposes at a lower temperature than the polymeric gelatin; however, both precursors result in very small particle sizes. It is difficult to say definitively whether this is purely due to the nitrogen content of the amino acid-based precursors compared to the saccharide-based precursors as they have a significantly different structure. However, the higher nitrogen content does appear to be a contributing factor. Previous work studying a similar gelatin/iron nitrate system observed the formation of intermediate iron nitride phases.[168] Therefore, the possibility of iron nitride phases may also change the reaction pathway of the gelatin- and glycine-derived carbons, which may have an influence on the particle size in these systems.

4.3.2 Effect of increased iron content

The metal:organic ratio used so far in this chapter was sufficient to produce high levels of graphitization in cellulose- and glucose-derived carbons in the previous chapter. As little graphitic character was observed in the carbons derived from the nitrogen-containing organic precursors, the iron content was increased to see if more graphitization could be forced in these systems.

Carbon samples prepared using a higher iron content all show a considerably more intense peak corresponding to the (002) reflection of graphite in their PXRD patterns (figure 4.11). These peaks are still broader than what would be expected with a pure graphite sample, suggesting that there is considerable disorder within the carbon structures, but are much more similar to the diffraction patterns of carbons synthesized from glucose, starch and cellulose in the previous chapter. All five samples also show well-resolved peaks characteristic of iron carbide, along with a minor *α*-Fe phase, suggesting that these iron phases are likely to be responsible for graphitization. These peaks also allow for Scherrer analysis to be carried out to calculate an average crystallite size (table 4.6). For all five samples, the average crystallite sizes are approximately 30-40 nm, suggesting that at the higher iron concentration, the influence of the organic precursor on the particle size is less pronounced.

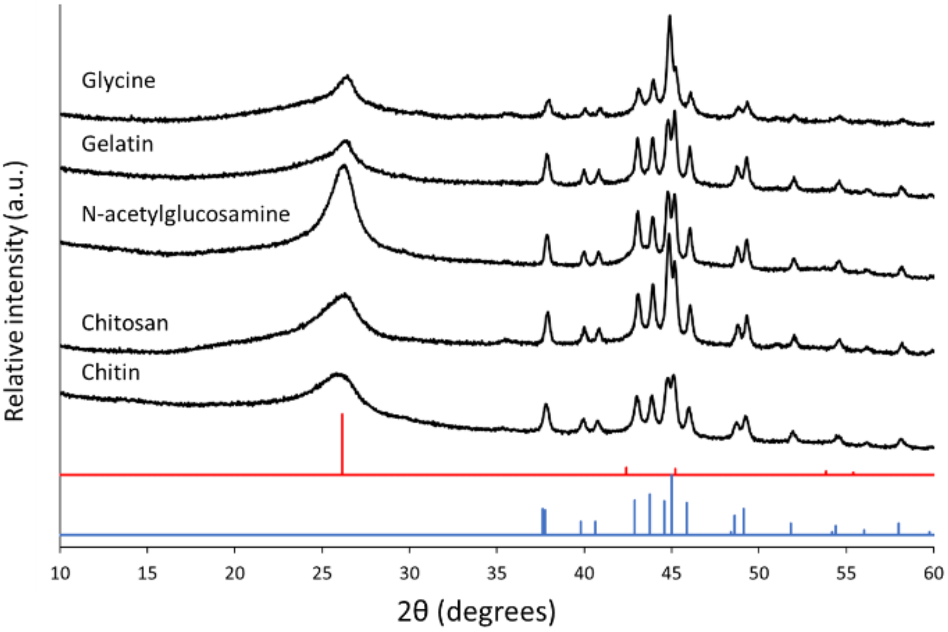

Figure 4.11: PXRD patterns of carbon/Fe_3C samples produced from glycine, gelatin, N-acetylglucosamine, chitosan and chitin (5 g) and iron nitrate solution (3.4 mmol), heated to 800 °C and dwelled for 1 hr.

Table 4.6: Average crystallite size of iron phases in carbons synthesized using different nitrogen-containing precursors (5 g) and iron nitrate solution (3.4 mmol), calculated from Scherrer analysis of PXRD patterns (figure 4.11).

Organic precursor	**Average crystallite size (nm)**	
	Fe_3C	**α-Fe**
Glycine	35	29
Gelatin	39	38
N-acetylglucosamine	38	39
Chitosan	42	32
Chitin	34	34

The increased graphitic character was confirmed by Raman spectra of the samples synthesized using a higher iron concentration, which show a sharpening in the D1 and G bands in all of the samples, indicating a greater degree of graphitic ordering (figure 4.12 and table 4.7).

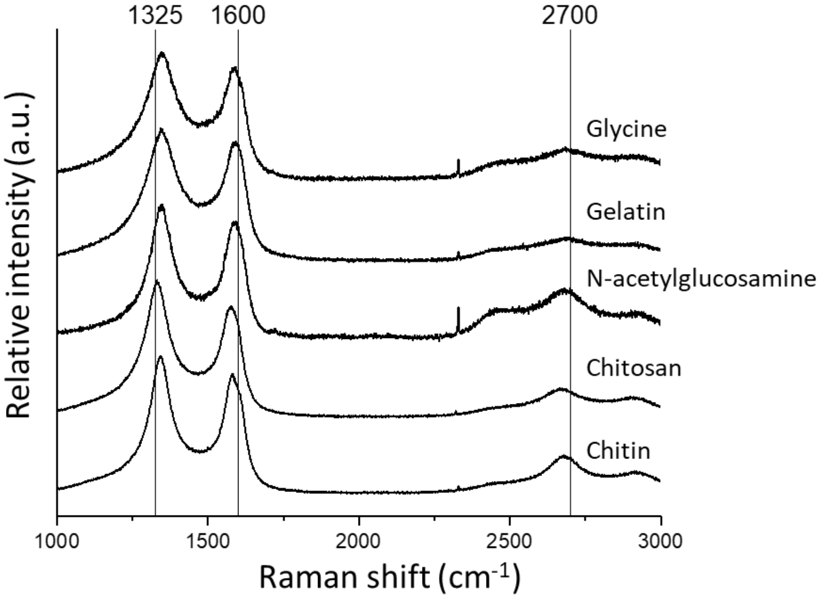

Figure 4.12: Raman spectra for carbon/Fe_3C samples produced from glycine, gelatin, N-acetylglucosamine, chitosan and chitin (5 g) and iron nitrate solution (3.4 mmol), heated to 800 °C for 1 hr.

Table 4.7: Results from fitting of Raman spectra in figure 4.12. All measurements were collected in triplicate on different locations and the average values are reported with uncertainty values.

Organic precursor	**Band**	**Peak position (cm^{-1})**	**FWHM (cm^{-1})**	**I_D/I_G**
Glycine	D1	1346 +/- 3	109 +/- 1	1.19 +/- 0.06
	G	1591 +/- 1	80 +/- 2	
Gelatin	D1	1348 +/- 2	125 +/- 3	1.30 +/- 0.05
	G	1595 +/- 1	75 +/- 1	
N-acetylglucosamine	D1	1348 +/- 2	96 +/- 5	1.17 +/- 0.03
	G	1594 +/- 2	77 +/- 2	
Chitosan	D1	1334 +/- 2	107 +/- 8	1.29 +/- 0.06
	G	1583 +/- 3	77 +/- 2	
Chitin	D1	1343 +/- 1	97 +/- 11	1.21 +/- 0.02
	G	1589 +/- 2	79 +/- 1	

Electron microscopy was used to confirm the nature of the graphitic nanostructures within the carbons. Gelatin- and chitin-derived carbons were examined to illustrate the differences in amino acid and saccharide-based precursors. SEM images of the gelatin-derived carbon synthesized using 3.4 mmol of iron nitrate show a greater number of iron-based particles, as expected, and the presence of what appear to be tubular structures (figure 4.13a). These are more visible in TEM images, which show graphitic “tubes” and “shells”, similar to structures seen in the previous chapter for glucose-, starch- and cellulose-derived carbons, alongside catalyst particles, which are visible as dark spots (figure 4.13c). Tubular structures are less visible in SEM images of the chitin-derived carbon (figure 4.13b); however, similar structures are clearly visible in TEM (figure 4.13d). Empty graphitic pores are present in both the gelatin- and chitin-derived carbons, suggesting that catalyst particle movement has occurred, where the particle has left a trail of graphitic carbon, as has been observed previously using ETEM.[79] Therefore, in the case of the gelatin- and chitin-derived carbons, the level of nitrogen does not impact the nature of the graphitic carbon nanostructure formed.

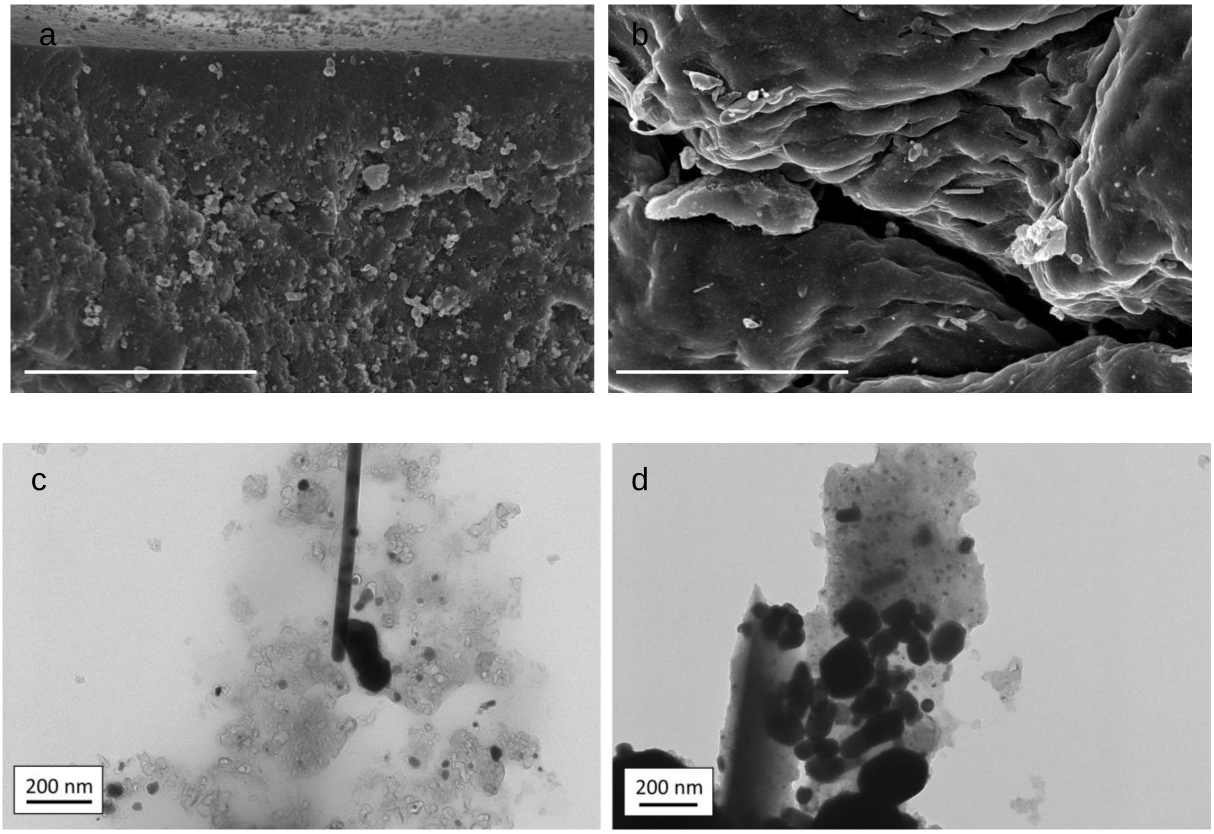

Figure 4.13: SEM and TEM images of carbons produced from a), c) gelatin and b), d) chitin (5 g) and iron nitrate solution (3.4 mmol), heated to 800 °C and dwelled for 1 hr. Scale bars in SEM images equals 5 µm.

Elemental analysis of the carbons prepared using the higher iron content shows a low nitrogen content in all five of the samples (table 4.8). A decrease in the carbon, hydrogen and nitrogen content is expected, purely from the larger amount of iron taking up a greater percentage of the total sample mass. However, in all five samples, the nitrogen content is less than expected, suggesting that it is expelled at some point during pyrolysis. As with the carbons produced with a lower iron content, the carbons produced from the amino acid-based precursors, glycine and gelatin, display a higher nitrogen content.

Table 4.8: Elemental analysis data for carbon samples produced from glycine, gelatin, N-acetylglucosamine, chitosan and chitin (5 g) and iron nitrate solution, heated to 800 °C and dwelled for 1 hr.

Precursor	**C%**		**H%**		**N%**	
	0.68 mmol Fe	**3.4 mmol Fe**	**0.68 mmol Fe**	**3.4 mmol Fe**	**0.68 mmol Fe**	**3.4 mmol Fe**
Glycine	70.7	66.9	0.8	0.7	15.1	6.4
Gelatin	69.6	74.2	3.5	0.6	13.8	2.3
N-acetylglucosamine	80.5	75.4	0.6	0.1	5.0	1.2
Chitosan	82.3	72.2	1.0	0.4	9.1	1.3
Chitin	79.0	75.6	0.8	0.2	5.8	1.3

Nitrogen sorption measurements of the carbons synthesized using the higher iron content (3.4 mmol) all show a type IV isotherm shape indicating the presence of mesopores (figure 4.14). This is consistent with the appearance of a significant (002) reflection peak in PXRD, again suggesting that iron-catalyzed graphitization has induced mesoporosity in the carbon samples. The most dramatic increase in porosity with increasing iron content is seen in gelatin-derived carbon. The gelatin-derived carbon produced with the higher iron content displays a high specific surface area of 414 m^2g^{-1} and a pore volume of 0.27 cm^3g^{-1}. This can be compared with the lower iron content sample, which had a porosity that was too low to calculate any reasonable values. Glycine-derived carbon, like gelatin-derived carbon, shows an increase in specific surface area from 27 m^2g^{-1} to 176 m^2g^{-1} with increasing iron content.

As the N-acetylglucosamine-derived carbons already showed some graphitization in the samples synthesized with the lower iron content, the change in porosity is less significant with the carbons produced using 0.68 mmol and 3.4 mmol, which displayed specific surface areas of 246 and 254 m^2g^{-1}, respectively. Chitin-derived carbon synthesized using the higher iron content also displays similar specific surface area values regardless of the iron content. However, the contribution to the total pore volume arising from micropores is lower (11 % compared to 26 %) at the higher iron content, likely due to the increased size of the iron-based catalyst particles that drive graphitization.

Chitosan-derived carbon shows an increase in specific surface area from 89 to 356 m^2g^{-1} with the increase in iron concentration. Again, this may be down to the greater number of mesopores introduced into the sample by graphitization.

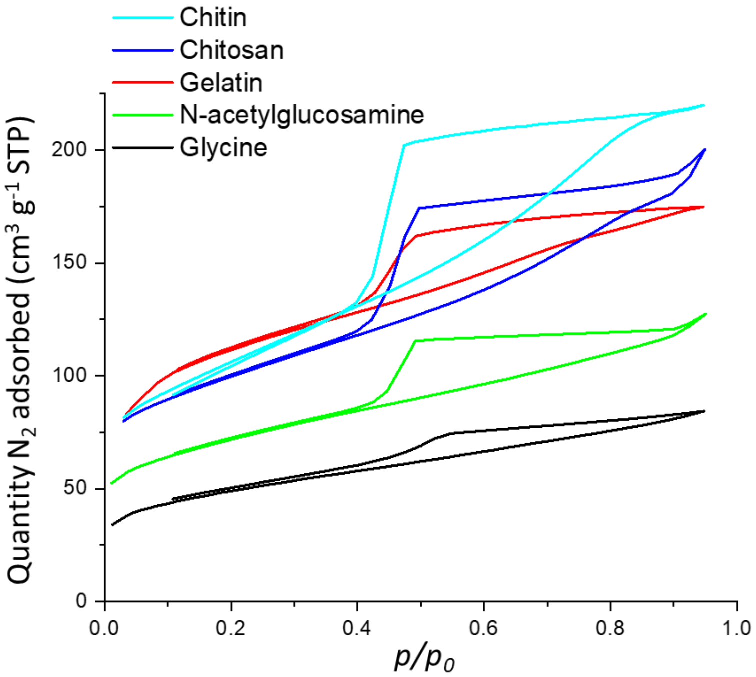

Figure 4.14: N_2 sorption isotherms for carbons produced from glycine, gelatin, N-acetylglucosamine, chitosan and chitin (5 g) and iron nitrate solution (3.4 mmol), heated to 800 °C and dwelled for 1 hr.

Table 4.9: Adsorptive properties of carbons produced from glycine, gelatin, N-acetylglucosamine, chitosan and chitin (5 g) and iron nitrate solution (3.4 mmol), heated to 800 °C and dwelled for 1 hr.

		Precursor				
	Iron concentration (mmol)	**Glycine**	**Gelatin**	**N-acetylglucosamine**	**Chitosan**	**Chitin**
S_{BET} (m^2g^{-1})	0.68	27	-	246	89	390
	3.4	179	414	254	356	374
Max Q_{ads} (cm^3g^{-1})	0.68	9	-	106	34	180
	3.4	85	176	128	201	221
V_{tot} (cm^3g^{-1})	0.68	0.015	-	0.17	0.054	0.28
	3.4	0.13	0.27	0.20	0.31	0.34
S_{micro} (m^2g^{-1})	0.68	4	-	86	32	173
	3.4	56	165	83	128	79
V_{micro} (cm^3g^{-1})	0.68	0.001	-	0.035	0.012	0.073
	3.4	0.023	0.06	0.036	0.055	0.036
V_{micro}/V_{tot} (%)	0.68	7	-	21	22	26
	3.4	18	22	18	18	11

4.3.3 Effect of synthesis conditions

To investigate the mechanism of graphitization of the various organic precursors, samples were heated to a range of temperatures between 500 °C and 800 °C.

4.3.3.1 Amino acid-based precursors

Figures 4.15 and 4.16 show PXRD patterns of samples synthesized from glycine and gelatin, respectively. In both systems, at temperatures below 700 °C, no peaks corresponding to any crystalline iron phases are visible, with the diffraction patterns solely consisting of broad features at approximately 25 ° and 45 ° 2θ, consistent with amorphous carbon. At 700 °C, peaks corresponding to iron carbide begin to emerge and become increasingly well defined as the temperature is increased to 800 °C, and further still as the dwell time increases, highlighted by Scherrer analysis in tables 4.10 and 4.11. As these iron carbide peaks sharpen at 800 °C, the main graphite peak also begins to sharpen and increase in intensity, particularly after a dwell time of 1 hr, suggesting that the iron carbide phase is responsible for the conversion of amorphous to graphitic carbon.

Interestingly, there is no evidence of the formation of iron nitride phases before the formation of iron carbide in either glycine- or gelatin-derived carbons, as previously seen in a study of the synthesis of iron carbides and nitrides from gelatin.[168,185] That work was carried out using synchrotron PXRD, so the lack of nitride phases here may be a result of the lower resolution lab X-ray diffractometer, or more likely due to the lower amount of iron used to produce the samples in our study. A similar result was reported by Giordano *et al* in the synthesis of molybdenum and tungsten carbide and nitride nanoparticles using urea as both the source of carbon and nitrogen.[186] At higher metal precursor:urea molar ratios, the nitride phases were favoured, whereas the carbide phases were favoured at low metal precursor:urea molar ratios.

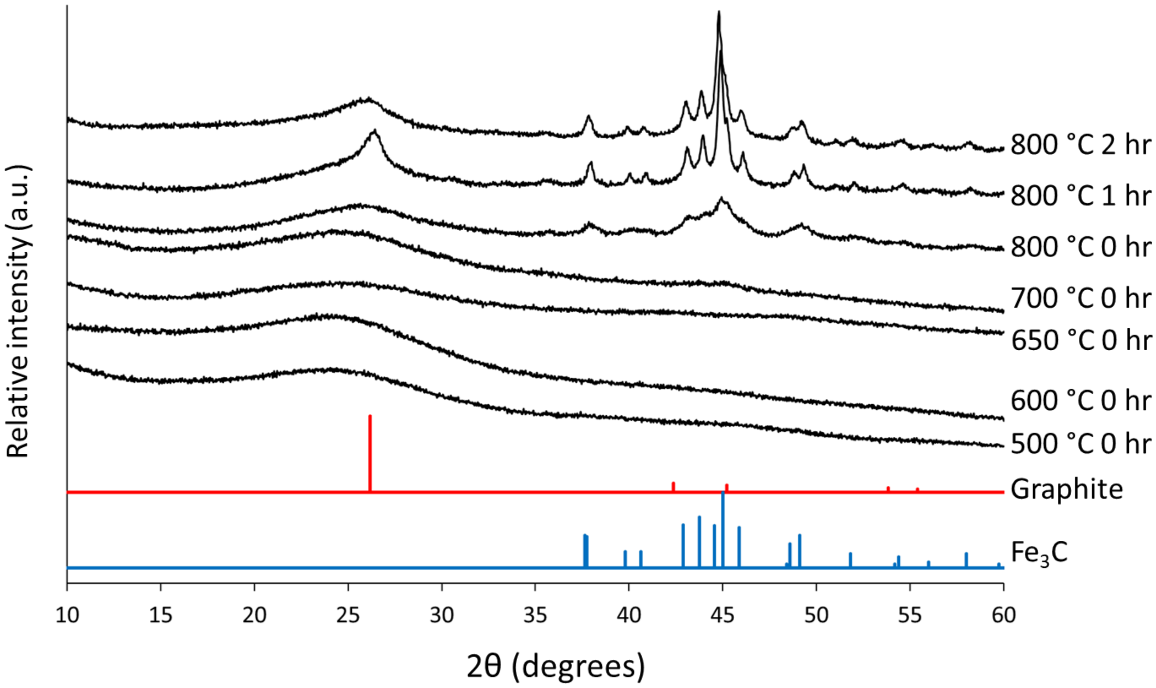

Figure 4.15: PXRD patterns for carbons produced from glycine (5 g) and iron nitrate solution (3.4 mmol), heated to different temperatures for various dwell times.

Table 4.10: Average crystallite size of iron phases in carbons synthesized using glycine (5 g) and iron nitrate solution (3.4 mmol) under different heating conditions, calculated from Scherrer analysis of PXRD patterns (figure 4.15).

Temperature (°C)/Dwell time (hr)	**Average crystallite size (nm)**	
	Fe_3C	***α*-Fe**
800 / 2	37	20
800 / 1	35	29

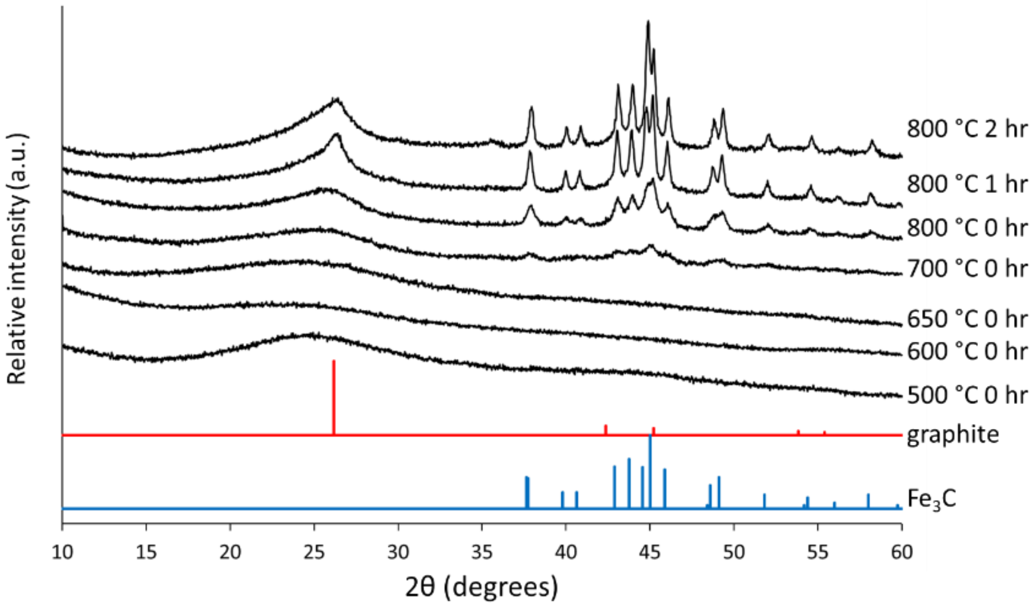

Figure 4.16: PXRD patterns for carbons produced from gelatin (5 g) and iron nitrate solution (3.4 mmol), heated to different temperatures for various dwell times.

Table 4.11: Average crystallite size of iron phases in carbons synthesized using gelatin (5 g) and iron nitrate solution (3.4 mmol) under different heating conditions, calculated from Scherrer analysis of PXRD patterns (figure 4.16).

Temperature (°C)/Dwell time (hr)	**Average crystallite size (nm)**	
	Fe_3C	***α*-Fe**
800 / 2	45	32
800 / 1	39	38
800 / 0	22	-

Figures 4.17a and b show Raman spectra for glycine- and gelatin-derived carbons synthesized under different conditions and the values extracted are displayed in tables 4.12 and 4.13 respectively. With increasing temperature and dwell time at 800 °C, the FWHM values for the peaks corresponding to the D1 and G peaks decrease as the carbon structure becomes increasingly ordered. Significant decreases in the FWHM of the peak corresponding to the G band occurs once the samples are held at 800 °C for 1 hr, at the same time as the main graphite peak emerges in the PXRD patterns, implying that this is due to the increase in the degree of graphitization (tables 4.12 and 4.13) .

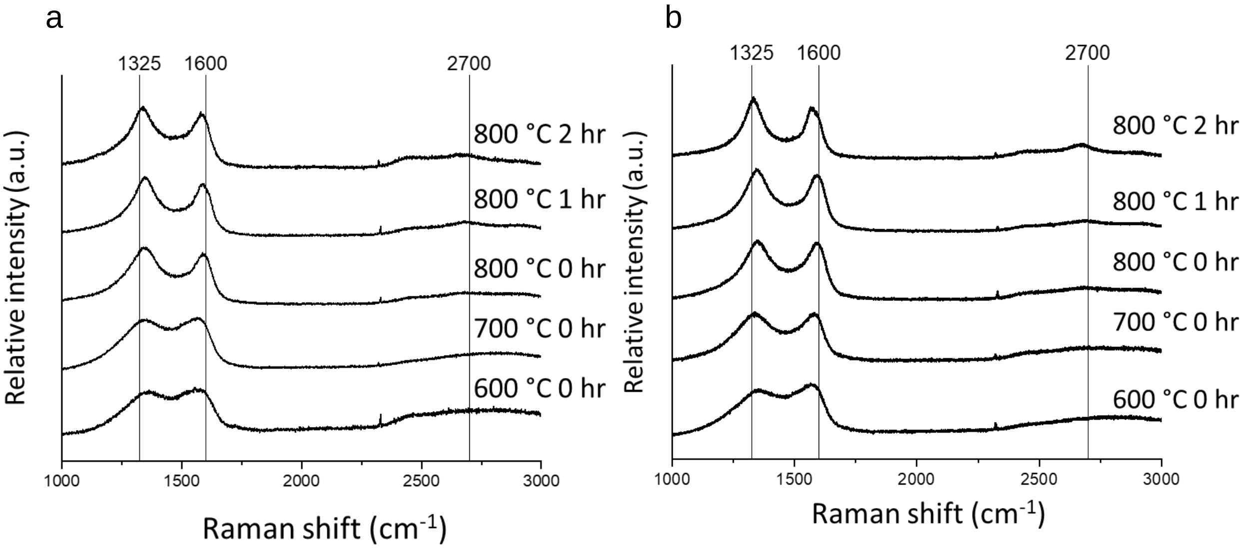

Figure 4.17: Raman spectra for carbons produced from a) glycine and b) gelatin (5 g) and iron nitrate solution (3.4 mmol), heated to different temperatures for various dwell times

Table 4.12: Results from fitting of Raman spectra of glycine-derived carbons in figure 4.17a. All measurements were collected in triplicate on different locations and the average values are reported with uncertainty values.

Temperature (°C)/Dwell time (hr)	**Band**	**Peak position (cm^{-1})**	**FWHM (cm^{-1})**	**I_D/I_G**
800 / 2	D1	1336 +/- 1	104 +/- 22	1.35 +/- 0.10
	G	1584 +/- 3	76 +/- 4	
800 / 1	D1	1346 +/- 3	109 +/- 1	1.19 +/- 0.06
	G	1591 +/- 1	80 +/- 2	
800 / 0	D1	1356 +/- 8	151 +/- 25	1.19 +/- 0.06
	G	1597 +/- 3	89 +/- 8	
700 / 0	D1	1359 +/- 7	195 +/- 5	1.09 +/- 0.10
	G	1585 +/- 1	106 +/- 3	
600 / 0	D1	1354 +/- 4	188 +/- 9	1.05 +/- 0.08
	G	1582 +/- 2	118 +/- 1	

Table 4.13: Results from fitting of Raman spectra of gelatin-derived carbons in figure 4.17b. All measurements were collected in triplicate on different locations and the average values are reported with uncertainty values.

Temperature (°C)/Dwell time (hr)	**Band**	**Peak position (cm^{-1})**	**FWHM (cm^{-1})**	**I_D/I_G**
800 / 2	D1	1334 +/- 1	110 +/- 8	1.37 +/- 0.06
	G	1582 +/- 2	73 +/- 2	
800 / 1	D1	1348 +/- 2	125 +/- 3	1.30 +/- 0.05
	G	1595 +/- 1	75 +/- 1	
800 / 0	D1	1353 +/- 2	134 +/- 4	1.11 +/- 0.04
	G	1597 +/- 1	83 +/- 2	
700 / 0	D1	1344 +/- 5	143 +/- 6	1.04 +/- 0.10
	G	1586 +/- 1	81 +/- 5	
600 / 0	D1	1364 +/- 12	178 +/- 12	0.99 +/- 0.13
	G	1587 +/- 2	96 +/- 2	

The ratio of the intensity of the peaks corresponding to the D1 and G bands (I_D/I_G) is often used as a measure of the degree of graphitization in graphitic materials, with a low value indicating a higher degree of graphitization. However, these values should be interpreted carefully in the case of nanocrystalline graphitic materials. As discussed in detail in the three-stage model proposed by Ferrari and Robertson, this interpretation is valid for materials structurally similar to graphite (i.e. stage 3 of the model); however, as amorphous carbon is converted to nanocrystalline graphite (i.e. stage 2 of the model), the I_D/I_G value actually increases.[163] This observation has also been noted by Bernard *et al*, who initially saw an increase in the I_D/I_G ratio in the Raman spectra of pyrolyzed saccharose-based chars.[187] Only once pyrolysis temperatures had increased to high temperatures (> 1500 °C) did the I_D/I_G ratio begin to decrease as the Raman spectra became more similar to that of graphite, so could be thought of as moving towards stage 3 of Ferrari and Robertson's model.[163] Glycine- and gelatin-derived carbons show an increase in the I_D/I_G ratio with increasing temperature and dwell time, consistent with the conversion of amorphous carbon to nanocrystalline graphite.

The porosity of the carbons was also examined using nitrogen sorption measurements. The glycine-derived carbons showed a significant increase in porosity between 700 and 800 °C, with the specific surface area increasing from 3 to 186 m^{2}g^{-1} (figure 4.18a and table 4.14). As the dwell time was increased, the mesoporosity of the carbons increased alongside the increase in the degree of graphitization shown in PXRD and Raman spectroscopy. The gelatin-derived carbons showed an even more substantial increase in porosity between the sample heated to 800 °C with a dwell time of 0 hr and the sample with a dwell time of 1 hr (figure 4.18b and table 4.15). This is also consistent with the point at which graphitic character is introduced into the carbon structure, indicating that the induced porosity is due to the graphitization process.

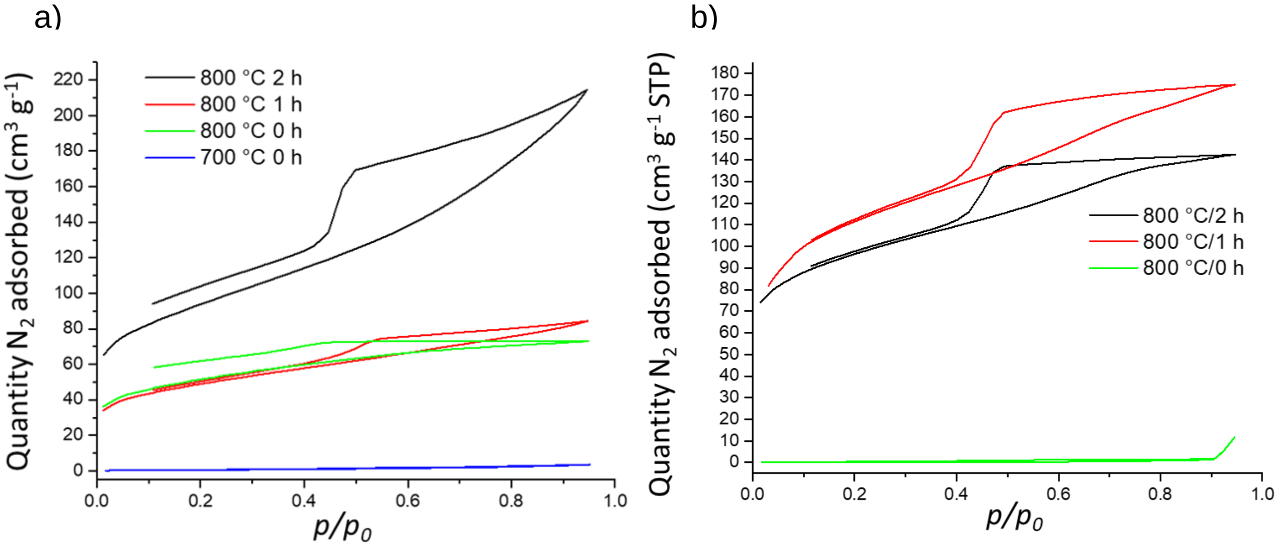

Figure 4.18: N$_2$ sorption isotherms for carbons produced from a) glycine and b) gelatin (5 g) and iron nitrate solution (3.4 mmol), heated to different temperatures for various dwell times

Table 4.14: Adsorptive properties of glycine-derived carbons in figure 4.18a calculated from N_2 sorption isotherms.

Temperature (°C)/Dwell time (hr)	**S_{BET} (m^2g^{-1})**	**Max Q_{ads} (cm^3g^{-1})**	**V_{tot} (cm^3g^{-1})**	**S_{micro} (m^2g^{-1})**	**V_{micro} (cm^3g^{-1})**	**V_{micro}/V_{tot} (%)**
800 / 2	336	216	0.33	81	0.036	11
800 / 1	176	85	0.13	56	0.023	18
800 / 0	186	73	0.11	65	0.027	25
700 / 0	3	4	0.006	0	0	0

Table 4.15: Adsorptive properties of gelatin-derived carbons in figure 4.18b calculated from N_2 sorption isotherms.

Temperature (°C)/Dwell time (hr)	**S_{BET} (m^2g^{-1})**	**Max Q_{ads} (cm^3g^{-1})**	**V_{tot} (cm^3g^{-1})**	**S_{micro} (m^2g^{-1})**	**V_{micro} (cm^3g^{-1})**	**V_{micro}/V_{tot} (%)**
800 / 2	352	143	0.22	171	0.07	32
800 / 1	414	176	0.27	165	0.06	22
800 / 0	Too low	12	0.02	NA	NA	NA

4.3.3.2 Saccharide-based precursors

Figures 4.19, 4.20 and 4.21 show PXRD patterns of a range of samples synthesized using N-acetylglucosamine, chitosan and chitin as the sources of carbon. In the N-acetylglucosamine-derived carbons, peaks corresponding to magnetite are present at 500 and 600 °C before well-defined peaks corresponding to iron carbide emerge at 700 °C. Scherrer analysis shows that the particle size of the iron phases are relatively large (> 30 nm) even at 600 °C (table 4.16). A peak for graphitic carbon then emerges in the PXRD pattern of the sample heated to 800 °C. The previous chapter’s study of iron-catalyzed graphitization of glucose, starch and cellulose showed that the reaction pathway of the iron species initially proceeds *via* nucleation of iron oxide nanoparticles, so it seems likely that a similar reaction pathway is occurring.

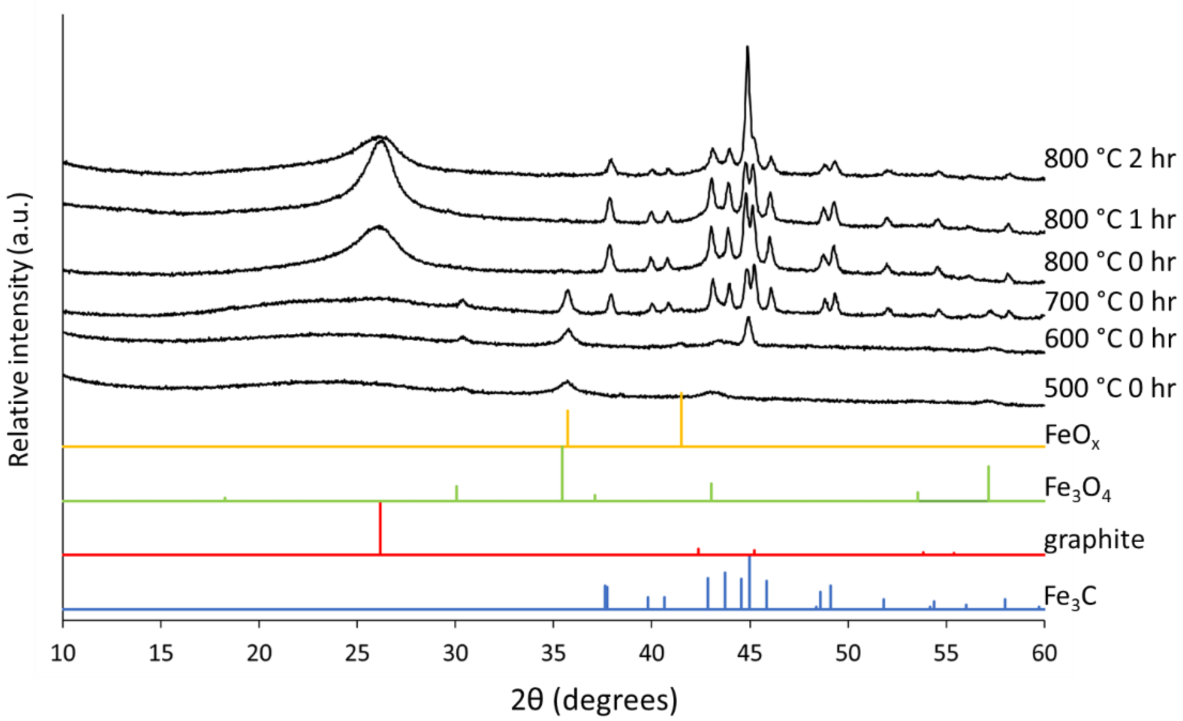

Figure 4.19: PXRD patterns for carbons produced from N-acetylglucosamine (5 g) and iron nitrate solution (3.4 mmol), heated to different temperatures for various dwell times.

Table 4.16: Average crystallite size of iron phases in carbons synthesized using N-acetylglucosamine (5 g) and iron nitrate solution (3.4 mmol) under different heating conditions, calculated from Scherrer analysis of PXRD patterns (figure 4.19).

Temperature (°C)/Dwell time (hr)	**Average crystallite size (nm)**		
	Fe_3O_4	**Fe_3C**	**α-Fe**
800 / 2	-	38	47
800 / 1	-	38	39
800 / 0	-	40	35
700 / 0	22	44	40
600 / 0	30	-	33

PXRD patterns of a series of chitosan-derived carbons (figure 4.20) show peaks corresponding to iron oxide phases after heating to temperatures of 500 and 600 °C. Broad peaks corresponding to iron carbide emerge in the samples heated to 650 and 700 °C. These peaks become better defined in the sample heated to 800 °C, suggesting an increase in particle size alongside the emergence of a graphitic carbon peak, which is shown by Scherrer analysis (table 4.17), as it was difficult to determine

FWHM values in the samples that had been heated to temperatures lower than 800 °C

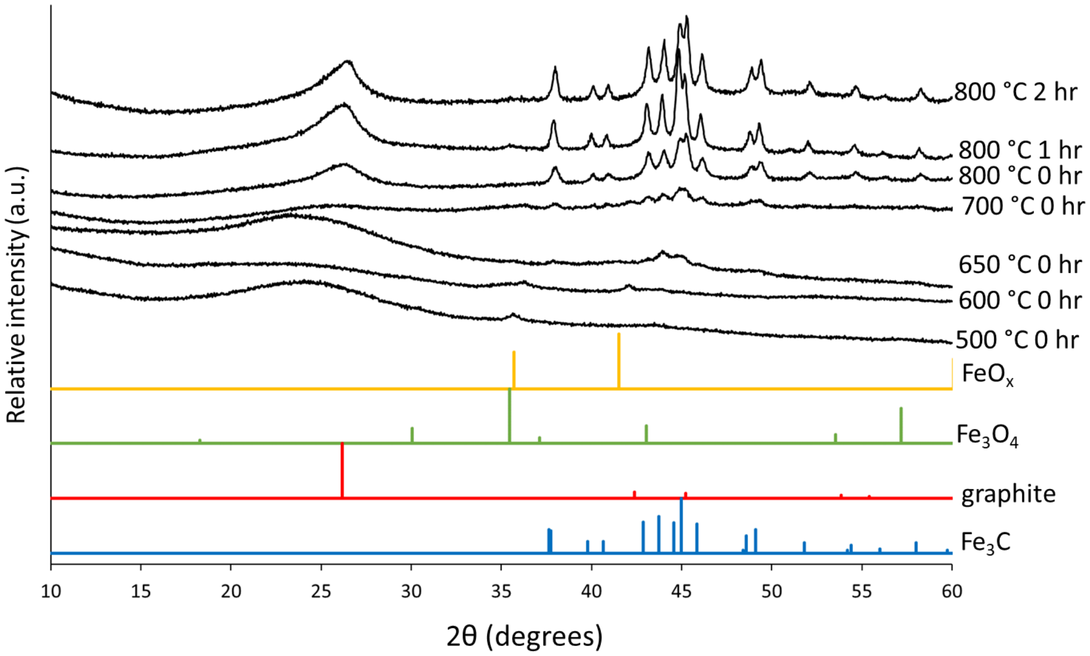

Figure 4.20: PXRD patterns for carbons produced from chitosan (5 g) and iron nitrate solution (3.4 mmol), heated to different temperatures for various dwell times.

Table 4.17: Average crystallite size of iron phases in carbons synthesized using chitosan (5 g) and iron nitrate solution (3.4 mmol) under different heating conditions, calculated from Scherrer analysis of PXRD patterns (figure 4.20).

Temperature (°C)/Dwell time (hr)	**Average crystallite size (nm)**	
	Fe_3C	**α-Fe**
800 / 2	38	27
800 / 1	42	32
800 / 0	24	26

PXRD patterns of chitin-derived carbons show the emergence of characteristic peaks corresponding to iron carbide at a relatively low temperature of 650 °C (figure 4.21). A graphitic carbon peak appears once the synthesis temperature reaches 700 °C. From 700 °C onwards, the graphitic carbon peak becomes slightly sharper and the peaks corresponding to iron carbide become better defined, suggesting growth in the size of the iron carbide particles (also shown by a general increase in crystallite size in Scherrer analysis in table 4.18) and an increase in the size of the graphitic carbon domains. At temperatures of 500-600 °C, weak intensity peaks corresponding to iron oxide phases such as wüstite are again visible.

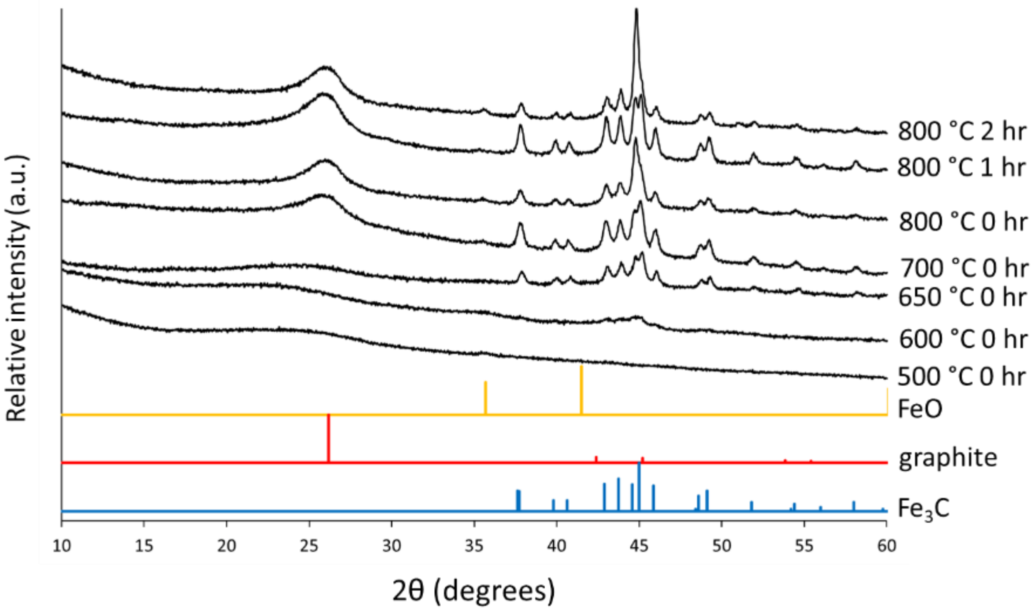

Figure 4.21: PXRD patterns for carbons produced from chitin (5 g) and iron nitrate solution (3.4 mmol), heated to different temperatures for various dwell times.

Table 4.18: Average crystallite size of iron phases in carbons synthesized using chitin (5 g) and iron nitrate solution (3.4 mmol) under different heating conditions, calculated from Scherrer analysis of PXRD patterns (figure 4.21).

Temperature (°C)/Dwell time (hr)	**Average crystallite size (nm)**	
	Fe_3C	**α-Fe**
800 / 2	55	32
800 / 1	34	34
800 / 0	29	24
700 / 0	25	33
650 / 0	31	26

Figures 4.22a, b and c show Raman spectra of N-acetylglucosamine-, chitosan- and chitin-derived carbons and resulting fitting values are displayed in tables 4.19, 4.20 and 4.21 respectively. As with the amino acid-based precursors, the peaks ascribed to the D1 and G bands are initially very broad at 600 °C. In the N-acetylglucosamine- and chitosan-derived carbons, the FWHM values decrease significantly, and the I_D/I_G ratio jumps between 700 and 800 °C, at the same point that the graphite peak in PXRD emerges, again suggesting that this is the point at which graphitization starts to occur (tables 4.19 and 4.20).

In the case of chitin-derived carbon, the major structural change is observed in Raman spectroscopy between 600 and 700 °C, again consistent with the early emergence of the graphitic carbon peak in PXRD (table 4.21). Interestingly, from this point onwards, the I_D/I_G decreases with temperature and hold time as the sample becomes more graphitic, a trend that fits more with stage 3 of the Ferrari and Robertson three-stage model as nanocrystalline graphite becomes more similar to graphite.[163]

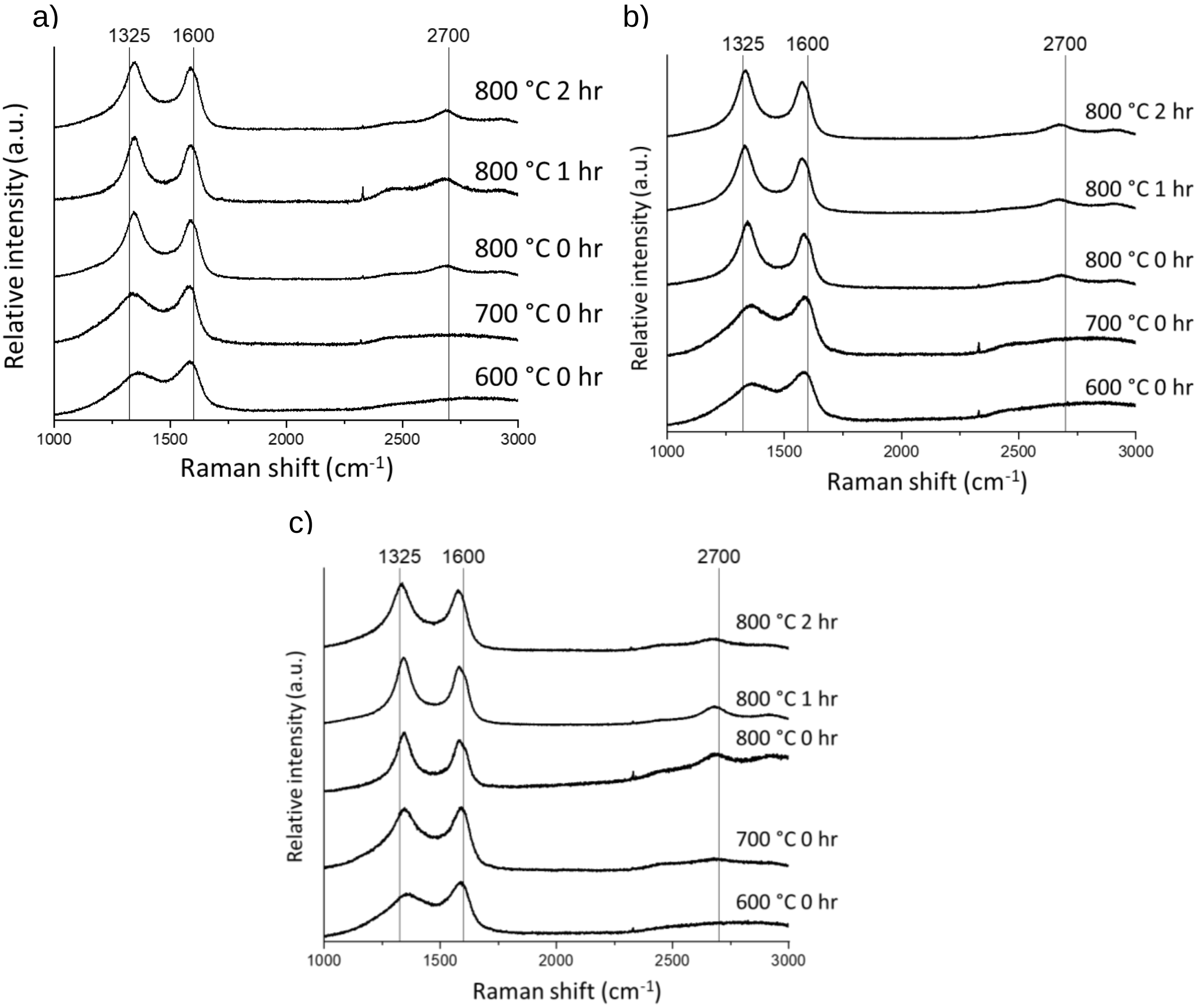

Figure 4.22: Raman spectra for carbons produced from a) N-acetylglucosamine, b) chitosan and c) chitin (5 g) and iron nitrate solution (3.4 mmol), heated to different temperatures for various dwell times

Table 4.19: Results from fitting of Raman spectra of N-acetylglucosamine-derived carbons in figure 4.22a. All measurements were collected in triplicate on different locations and the average values are reported with uncertainty values.

Temperature (°C)/Dwell time (hr)	**Band**	**Peak position (cm^{-1})**	**FWHM (cm^{-1})**	**I_D/I_G**
800 / 2	D1	1345 +/- 1	126 +/- 18	1.18 +/- 0.09
	G	1594 +/- 1	81 +/- 3	
800 / 1	D1	1348 +/- 2	96 +/- 5	1.17 +/- 0.03
	G	1594 +/- 2	77 +/- 2	
800 / 0	D1	1346 +/- 1	101 +/- 6	1.23 +/- 0.02
	G	1595 +/- 2	77 +/- 1	
700 / 0	D1	1342 +/- 4	166 +/- 8	0.99 +/- 0.11
	G	1583 +/- 1	85 +/- 5	
600 / 0	D1	1355 +/- 1	175 +/- 12	0.79 +/- 0.01
	G	1588 +/- 1	100 +/- 2	

Table 4.20: Results from fitting of Raman spectra of chitosan-derived carbons in figure 4.22b. All measurements were collected in triplicate on different locations and the average values are reported with uncertainty values.

Temperature (°C)/Dwell time (hr)	**Band**	**Peak position (cm^{-1})**	**FWHM (cm^{-1})**	**I_D/I_G**
800 / 2	D1	1334 +/- 1	98 +/- 5	1.38 +/- 0.04
	G	1581 +/- 1	76 +/- 1	
800 / 1	D1	1334 +/- 2	107 +/- 8	1.29 +/- 0.06
	G	1583 +/- 3	77 +/- 2	
800 / 0	D1	1346 +/- 3	102 +/- 7	1.25 +/- 0.05
	G	1593 +/- 4	77 +/- 2	
700 / 0	D1	1366 +/- 1	164 +/- 13	0.94 +/- 0.03
	G	1595 +/- 1	93 +/- 3	
600 / 0	D1	1369 +/- 2	184 +/- 6	0.94 +/- 0.04
	G	1593 +/- 1	92 +/- 3	

Table 4.21: Results from fitting of Raman spectra of chitin-derived carbons in figure 4.22c. All measurements were collected in triplicate on different locations and the average values are reported with uncertainty values.

Temperature (°C)/Dwell time (hr)	**Band**	**Peak position (cm^{-1})**	**FWHM (cm^{-1})**	**I_D/I_G**
800 / 2	D1	1334 +/- 1	95 +/- 7	1.16 +/- 0.09
	G	1582 +/- 1	76 +/- 3	
800 / 1	D1	1343 +/- 1	97 +/- 11	1.21 +/- 0.02
	G	1589 +/- 2	79 +/- 1	
800 / 0	D1	1343 +/-1	87 +/-6	1.34 +/- 0.10
	G	1589 +/- 1	72 +/- 3	
700 / 0	D1	1342 +/- 2	120 +/- 15	1.29 +/- 0.13
	G	1593 +/- 1	77 +/- 5	
600 / 0	D1	1362 +/- 2	159 +/- 30	0.73 +/- 0.19
	G	1592 +/- 1	89 +/- 1	

Nitrogen sorption measurements of N-acetylglucosamine-derived carbons (figure 4.23) showed low porosity after heating to 600 °C. The sample heated to 700 °C exhibits an isotherm with more of a type IV shape and a greater specific surface area and pore volume (table 4.22). In the samples heated to 800 °C, larger hysteresis loops are observed in the isotherms, indicative of greater mesoporosity as the degree of graphitization is increased.

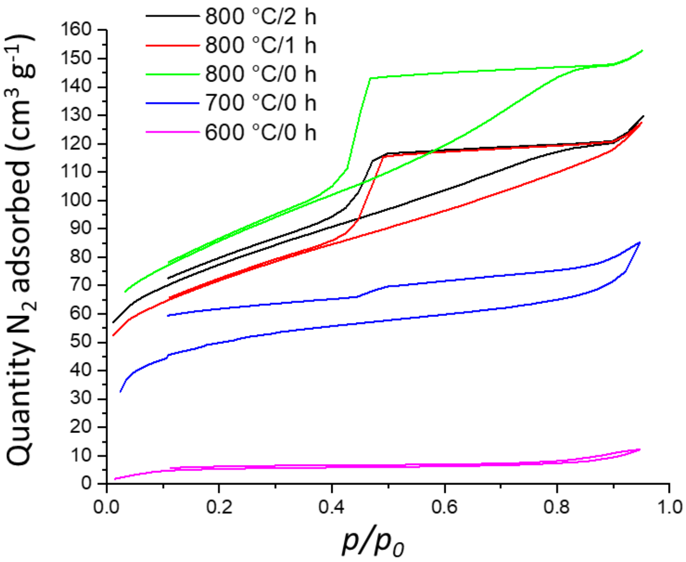

Figure 4.23: N_2 sorption isotherms for carbons produced from N-acetylglucosamine (5 g) and iron nitrate solution (3.4 mmol), heated to different temperatures for various dwell times.

Table 4.22: Adsorptive properties of N-acetylglucosamine-derived carbons from N_2 sorption isotherms in figure 4.23.

Temperature (°C)/Dwell time (hr)	**S_{BET} (m^2g^{-1})**	**Max Q_{ads} (cm^3g^{-1})**	**V_{tot} (cm^3g^{-1})**	**S_{micro} (m^2g^{-1})**	**V_{micro} (cm^3g^{-1})**	**V_{micro}/V_{tot} (%)**
800 / 2	277	130	0.20	101	0.043	22
800 / 1	254	128	0.20	83	0.036	18
800 / 0	303	154	0.24	93	0.041	17
700 / 0	184	86	0.13	75	0.029	22
600 / 0	22	12	0.02	8	0.002	10

The porosity of the chitosan-derived carbons is also consistent with the degree of graphitization observed in PXRD and Raman data. Low porosity is observed in the sample heated to 700 °C (figure 4.24), which does not show a significant graphitic carbon peak. Conversely, the samples heated to 800 °C all exhibit a graphitic carbon peak in their PXRD patterns and display type IV isotherms in nitrogen sorption experiments. The specific surface area and total pore volume increase and the relative microporosity of the carbons generally decreases with increasing dwell time as the graphitization process introduces mesoporosity into the carbon structure (table 4.23).

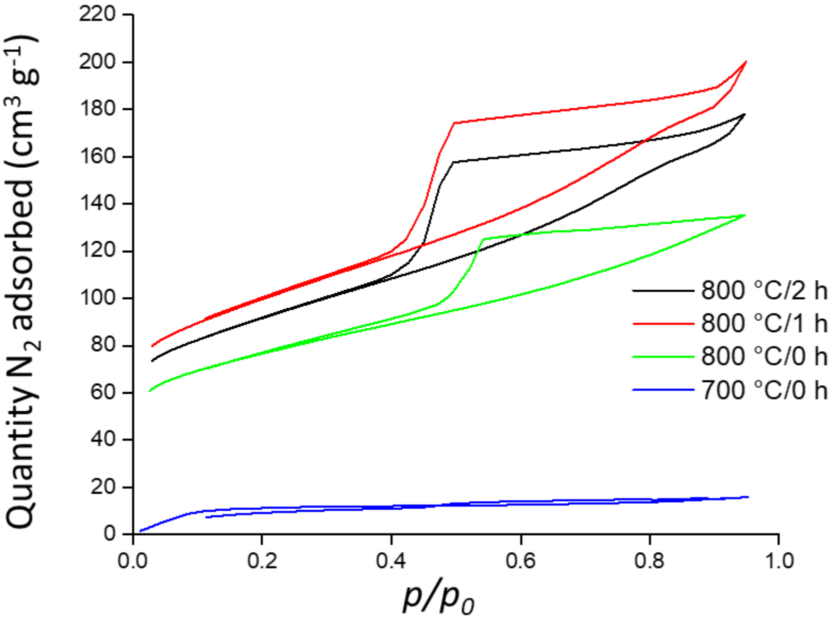

Figure 4.24: N_2 sorption isotherms for carbons produced from chitosan (5 g) and iron nitrate solution (3.4 mmol), heated to different temperatures for various dwell times

Table 4.23: Adsorptive properties of chitosan-derived carbons from N_2 sorption isotherms in figure 4.24.

Temperature (°C)/Dwell time (h)	**S_{BET} (m^2g^{-1})**	**Max Q_{ads} (cm^3g^{-1})**	**V_{tot} (cm^3g^{-1})**	**S_{micro} (m^2g^{-1})**	**V_{micro} (cm^3g^{-1})**	**V_{micro}/V_{tot} (%)**
800 / 2	328	178	0.28	118	0.051	18
800 / 1	356	201	0.31	128	0.055	18
800 / 0	276	136	0.21	113	0.048	23
700 / 0	45	16	0.025	15	0.004	16

As the chitin-derived carbons showed graphitic character at a relatively low temperature of 700 °C, significant mesoporosity is observed in the corresponding nitrogen sorption isotherm (figure 4.25). PXRD and Raman data showed that the degree of graphitization did not increase significantly after this point. This observation is mirrored in the nitrogen sorption data as the specific surface area and pore volumes remain relatively constant in the samples heated to temperatures of 700 and 800 °C (table 4.24).

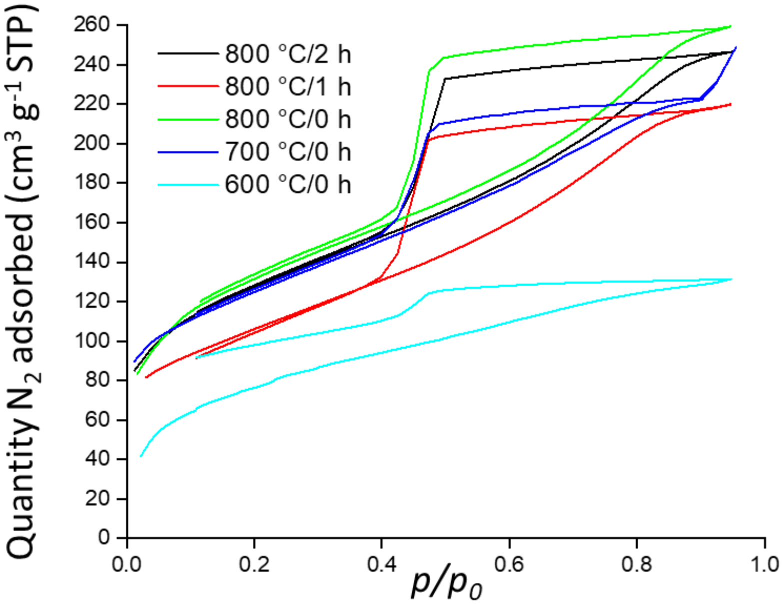

Figure 4.25: N_2 sorption isotherms for carbons produced from chitin (5 g) and iron nitrate solution (3.4 mmol), heated to different temperatures for various dwell times

Table 4.24: Adsorptive properties of chitin-derived carbons from N_2 sorption isotherms in figure 4.25.

Temperature (°C)/Dwell time (hr)	**S_{BET} (m^2g^{-1})**	**Max Q_{ads} (cm^3g^{-1})**	**V_{tot} (cm^3g^{-1})**	**S_{micro} (m^2g^{-1})**	**V_{micro} (cm^3g^{-1})**	**V_{micro}/V_{tot} (%)**
800 / 2	458	247	0.38	123	0.052	14
800 / 1	374	221	0.34	79	0.036	11
800 / 0	476	261	0.40	116	0.047	12
700 / 0	442	250	0.38	124	0.055	14
600 / 0	277	132	0.21	9	0.002	1

4.3.3.3 Comparing amino acid and saccharide-based precursors

Further analysis of gelatin- and chitin-derived carbons was carried out to compare the thermal behaviour of amino acid and saccharide-based precursors.

Elemental analysis of gelatin-derived carbons showed that there is a high nitrogen content until a dramatic decrease is observed between 700 and 800 °C, where nitrogen is expelled (table 4.25). Significant graphitization is only observed after the nitrogen has been expelled, suggesting that nitrogen within the carbon structure may hinder the production of graphitic nanostructures. The decrease in the nitrogen content in chitin-derived carbons is less pronounced as the nitrogen content is already relatively low at 650 °C, and the onset of graphitization occurs at a lower temperature of approximately 700 °C (table 4.26).

Table 4.25: Elemental analysis of carbons produced from gelatin (5 g) and iron nitrate solution (3.4 mmol), heated to different temperatures for various dwell times.

Temperature (°C) / hold time (hr)	**C%**	**H%**	**N%**
800 / 1	74.16	0.61	2.3
800 / 0	72.65	1.04	3.25
700 / 0	57.80	1.29	11.54
650 / 0	56.18	1.62	14.59

Table 4.26: Elemental analysis of carbons produced from chitin (5 g) and iron nitrate solution (3.4 mmol), heated to different temperatures for various dwell times.

Temperature (°C) / hold time (hr)	**C%**	**H%**	**N%**
800 / 1	75.55	0.22	1.25
800 / 0	70.64	1.94	4.68
700 / 0	68.98	0.75	3.49
650 / 0	63.15	1.96	6.13

TGA-MS data showed the different decomposition profiles of gelatin and chitin (figure 4.26a). Three mass loss steps were observed in the gelatin-derived carbon. At approximately 200 °C, a sharp mass loss is observed primarily due to the loss of CO_2, NH_3 and NO, before a large mass loss between 300-400 °C due to the loss of water. Between 700 and 800 °C, a further small mass loss is observed as the crystalline iron phases are formed and elemental analysis shows a significant loss in nitrogen content. No clear peaks are observed in the MS data, so this loss was presumed to be in the form of nitrogen lost to the atmosphere. TGA-MS data for the chitin-derived carbon mirrors the elemental analysis data during this region and shows a steady mass loss as the nitrogen content decreases rather than the sharp drop observed in the gelatin-derived carbon.

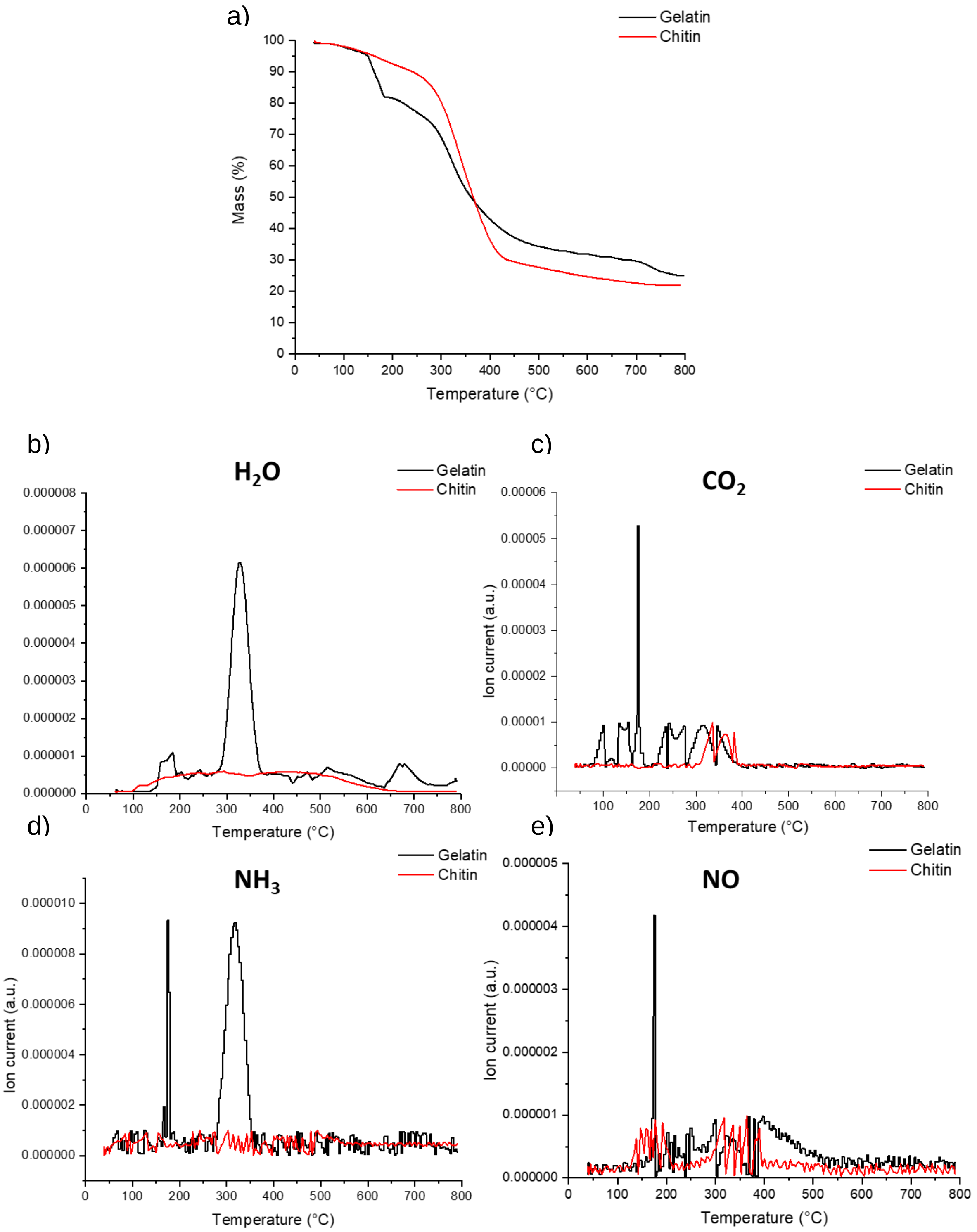

Figure 4.26: a) Mass loss, b) ion current signal at m/z = 18 amu, c) ion current signal at m/z = 44 amu, d) ion current signal at m/z = 17 amu and e) ion current signal at m/z = 30 versus temperature for carbons produced from gelatin and chitin (5 g) and iron nitrate solution (3.4 mmol), heated to different temperatures under N_2 for various dwell times.

4.4 Conclusions

Porous carbon materials containing graphitic structures can be produced from the nitrogen-containing precursors glycine, gelatin, N-acetylglucosamine, chitosan and chitin. Compared with the previous chapter's study of glucose, starch and cellulose – precursors that consist only of carbon, hydrogen and oxygen – a significantly greater amount of iron was required for the nitrogen-containing precursors in this study to induce a similar degree of graphitization and mesoporosity in the resulting carbons. This indicates that the presence of nitrogen hinders the formation of graphitic nanostructures.

The amino acid-based precursors, glycine and gelatin, are more resistant to graphitization than the saccharide-based precursors. SAXS data showed extremely small particle sizes in glycine- and gelatin-derived carbons, suggesting catalyst particles may take longer to reach the critical size to become catalytically active, as reported previously. Amino acid-based precursors are structurally different to saccharide-based precursors, and it was shown previously that precursor structure has a significant impact on graphitization, but it seems likely that the higher nitrogen content in the amino acid-based structures is a significant factor in hindering graphitization, particularly as significant graphitization only occurs once a high proportion of nitrogen is expelled from the structure.

The results of this chapter highlight the importance of understanding the structure of organic precursors in iron-catalyzed graphitization. The content of heteroatoms such as nitrogen, along with the precursor's physical properties, can significantly influence the graphitization process, with some precursors offering a greater degree of control over particle size and porosity. This is particularly important when using biomass-based precursors for iron-catalyzed graphitization, which contain a variety of chemical compositions. Understanding the factors that influence graphitization may help to identify appropriate feedstocks for the production of graphitic carbons.

Table 4.27: Summary of key findings in chapter 4.

Key Finding	**Evidenced by:**
Nitrogen-containing precursors require a greater iron content to drive graphitization	• Lack of characteristic peak for graphitic carbon in PXRD until iron nitrate concentration is increased
Precursors with high nitrogen content produce carbons with higher nitrogen content	• Elemental analysis • XPS survey spectra
Amino acid-based precursors more resistant to graphitization than saccharide-based precursors	• Slower/later growth of characteristic peak for graphitic carbon in PXRD • Slower/later development of graphitic character as observed in Raman spectroscopy • Slower/later growth of mesoporosity in N_2 sorption isotherms
Smaller particle sizes in amino acid-derived carbons	• Scherrer analysis of PXRD data • Size distribution histograms extracted from SAXS data
Tubular graphitic nanostructures in both gelatin- and chitin-derived carbon	• SEM • TEM
Graphitization occurred once a large proportion of nitrogen was expelled	• Elemental analysis • TGA-MS

Chapter 5 - *In situ* mechanistic study of iron-catalyzed graphitization

5.1 Introduction

The exact mechanism of iron-catalyzed graphitization remains an area of dispute and various mechanisms have been proposed, particularly as a variety of precursors have been investigated.[18,72] The most popular mechanism is the dissolution-precipitation mechanism, in which a molten Fe_xC_y particles dissolves the surrounding amorphous carbon until it reaches a point of supersaturation.[188] Carbon is then precipitated out in the form of graphitic nanostructures such as hollow tubes. The movement of seemingly liquid or liquid-like nanoparticles through a carbon matrix, and the subsequent formation of hollow graphitic structure has been observed in *in situ* TEM studies.[79]

There are many examples throughout the literature, highlighted in chapter 1, in which the onset of graphitization occurs at temperatures considerably lower than the melting point of pure iron (1538 °C).[143] Therefore, alternative theories have suggested that the catalyst particles must be in a solid state.[145] *In situ* PXRD studies have also shown the presence of crystalline phases during the onset of graphitization in some systems, suggesting that at least a proportion of the metal species is in the solid state.[189]

An alternative mechanism proposed is the carbide formation-decomposition mechanism, in which iron carbide is the phase responsible for graphitization.[141] Due to the metastable nature of the iron carbide phase, some authors suggest that iron carbide continually forms and decomposes into a more thermodynamically stable, pure iron phase alongside graphitic carbon.

Some authors have suggested that both mechanisms may occur but at different temperatures. Gomez-Martin *et al* suggested that in the iron-catalyzed graphitization of MDF wood, iron carbide is responsible for graphitization at a temperature of 700-750 °C.[189] At temperatures above 750 °C, iron carbide decomposes into γ-Fe and the dissolution-precipitation mechanism is more likely to be responsible for graphitization.[189]

In this chapter, the mechanism of iron-catalyzed graphitization is studied, focusing on the onset of graphitization at temperatures of approximately 700-800 °C. The same glucose, starch and cellulose systems from chapter 3 are examined using *in situ* ETEM and *in situ* synchrotron PXRD to probe the mechanism of graphitization.

5.2 Experimental

5.2.1 Sample preparation

Samples were prepared in the same manner as in chapter 3. For glucose samples, 5 g of D-(+)-glucose was dissolved in 20 ml of DI water in a beaker with gentle heating to 40 °C and stirring for 10 min. 1.35 g (3.4 mmol) of iron (III) nitrate nonahydrate was dissolved in 4 ml of DI water and this was added to the glucose solution, followed by stirring for 10 min. The mixture was dried in an oven at 70 °C for 24 hr. The resulting brown, caramel-like sample was placed in an alumina boat crucible then heated in a tube furnace at a rate of 5 °C/min under a nitrogen atmosphere with a flow rate of 1 l/min to 400 °C. The samples were then cooled completely to room temperature.

For starch samples, the procedure was the same, except 5 g of potato starch was dissolved in 45 ml of DI water at 70 °C and stirred for 10 min. 1.35 g (3.4 mmol) of iron (III) nitrate nonahydrate was again dissolved in 4 ml of DI water and this was added to the starch mixture, followed by stirring for 10 min. The mixture was dried (as in glucose samples) to produce an orange solid, which was subjected to the same heating procedure as glucose samples.

For cellulose samples, 1.35 g (3.4 mmol) of iron (III) nitrate nonahydrate was dissolved in 15 ml of DI water at room temperature and the resulting solution was added to a beaker containing 5 g of cellulose fibres (powder). The mixture was manually stirred for 10 min until the solution had been absorbed. The sample was dried to give a yellow powder and pyrolyzed as above. Before the *in situ* measurements, the cellulose/iron nitrate mixture was pyrolyzed to 400 °C under a nitrogen atmosphere. Cellulose fibres and iron nitrate decompose at temperatures of 300-350 °C and 130-160 °C, respectively, so pre-heating to 400 °C was used to remove the majority of the gases that would be expelled during pyrolysis, which may have affected the integrity of the vacuum system within the ETEM and potentially damage the filament or damage the capillary setup in the synchrotron PXRD experiments. in chapter 3, no crystalline phases were observed in PXRD until iron oxide phases formed at approximately 600 °C. Therefore, 400 °C was deemed to be an appropriate temperature for the pre-treatment. As expected, no Bragg peaks were observed in the PXRD pattern of the resulting cellulose-derived carbon (appendix C – figure 8.13).

5.2.2 In situ ETEM

Small portions of sample (≈ 50 mg) were dispersed in ethanol (≈ 1 ml) by sonication for 10 min. One drop of the dispersion was pipetted on to a silicon nitride TEM grid. ETEM experiments were performed using a FEI Titan 80-300 instrument at Brookhaven National Laboratory and a double-tilt DENS Solutions MEMS-based heating holder was used to heat the sample.

5.2.3 In situ synchrotron PXRD

PXRD experiments were performed in the Materials Science Powder Diffraction (BL04 - MSPD) beamline of the ALBA-CELLS synchrotron (Cerdanyola del Vallés, Spain). Beam energy was 30 keV with a wavelength of 0.41271 Å as confirmed using a silicon standard. The experimental setup was based on the capillary flow cell design described by Chupas *et al*.[190] Samples were packed in quartz capillaries of 1 mm diameter and mounted using graphite ferrules. The samples were heated using a FMB Oxford hot air blower under a 2 ml/min flow rate of nitrogen at a heating rate of 10 °C/min to 400 °C then 5 °C/min to 800 °C. The sample was then dwelled at 800 °C for 2 hr before cooling to room temperature at a cooling rate of 20 °C/min. A diffraction pattern was collected approximately every 1 min during the heating/dwelling/cooling cycle.

5.2.3.1 Rietveld refinement

Phase composition was calculated using Rietveld refinement of synchrotron PXRD data using TOPAS 6. Instrumental profiles were obtained by performing a refinement of a nickel standard. Diffraction patterns were refined by allowing scale factors, lattice parameters and size-related broadening terms to vary. In order to describe the background from amorphous carbon, a linear background and four broad pseudo-Voigt peaks were used at 5.6. 11.4, 13.0 and 19.7 ° 2θ, the positions and widths of which were refined. Refinements with $R_{wp} < 5\%$ were obtained in all cases

5.3 Results and discussion

5.3.1 In situ ETEM

In situ ETEM was used to probe the mechanism of iron-catalyzed graphitization on the nanoscale. Upon heating of the cellulose-derived carbon within the ETEM, dark particles likely corresponding to iron phases embedded within a matrix of carbon become visible (figure 5.1). As the temperature is increased to between 700 and 800 °C, some of these particles are observed to become mobile and move through the carbon matrix (figure 5.2). Once moving, the particles appear to leave behind trails of graphitic carbon, as has been observed in similar systems both *in* and *ex situ*. Not all of the particles become mobile in the timeframe of the *in situ* footage, and it is difficult to say whether these particles were already mobile and stopped moving or remained stationary throughout the heating procedure. In PXRD studies of similar systems, both pure iron and iron carbide phases are often present during graphitization. Some authors have suggested that γ-Fe is responsible for catalyzing the graphitization process,[139] while others have suggested that Fe_3C is the active species[140] or that it may be a combination of phases and the different phases may result in different graphitic nanostructures.[137]

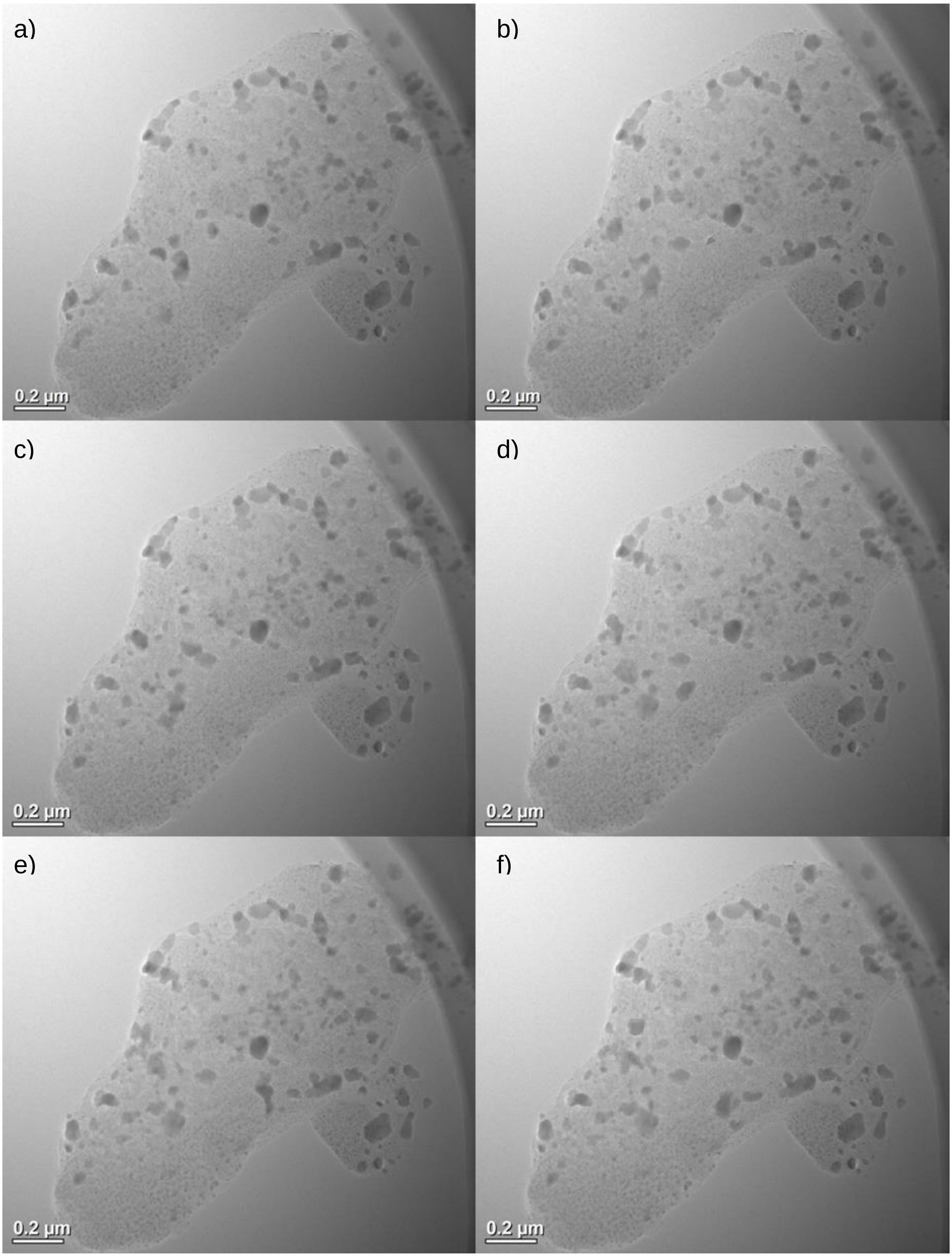

Figure 5.1: Snapshots of in situ ETEM footage after a) 0, b) 1, c) 2, d) 3, e) 4 and f) 5 s of carbon produced from cellulose (5 g) and iron nitrate solution (3.4 mmol), heated to 800 °C.

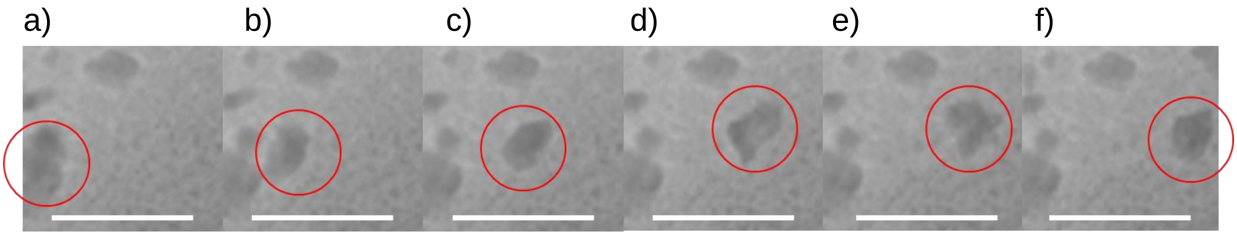

Figure 5.2: Magnified Snapshots of in situ ETEM footage after a) 0, b) 1, c) 2, d) 3, e) 4 and f) 5 s of cellulose-derived carbon heated to 800 °C. Scale bar = 200 nm.

Due to the dynamic nature of the system, it was difficult to determine the chemical nature of the mobile particles either by collecting higher resolution images to observe any lattice fringes or by using selected area electron diffraction. Therefore, from these results alone, the exact chemical nature of the catalytic particle could not be determined exactly.

The fast motion of the catalyst particles proceeded in a seemingly liquid-like manner, at temperatures considerably lower than the melting temperature of iron, similar to previous *in situ* ETEM studies in both iron-catalyzed graphitization and CVD systems, suggesting that a similar process may be occurring in both routes. The heating effect of the high energy electron beam within the TEM must be taken into account when considering these results. However, as similar tubular graphitic nanostructures were observed *ex situ*, it seems reasonable to suggest that the mobile behaviour of catalyst particles is independent of any electron beam heating effects.

5.3.2 In situ synchrotron PXRD

In situ synchrotron PXRD was used to study the chemical nature of the iron phases during graphitization.

5.3.2.1 Cellulose-derived carbon

Diffraction patterns were collected approximately every minute throughout the pyrolysis procedure and sequential refinements were carried out in TOPAS to determine the chemical composition of the iron species throughout the heating procedure. Firstly, in the cellulose-derived carbon, the sample remained largely amorphous up until approximately 750 °C (figure 5.3). Therefore, sequential Rietveld refinements were carried out from 750 °C, and the relative populations of the iron phases Fe_3C, α-Fe and γ-Fe were tracked over time along with the intensity of the peak corresponding to the (002) reflection of graphite at 6.8 ° 2θ. An example of a Rietveld refinement is shown in figure 5.4 and other examples are included in Appendix C.

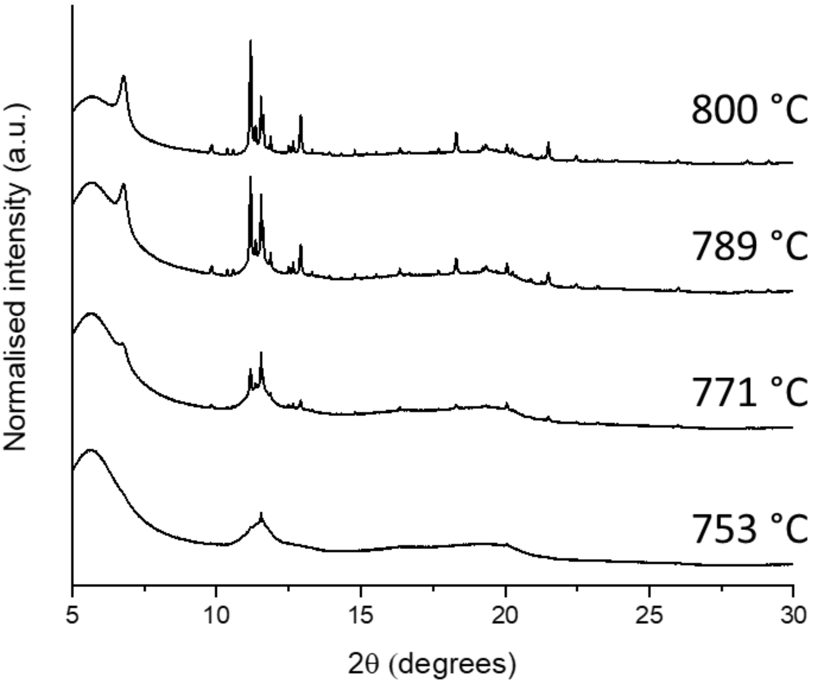

Figure 5.3: In situ PXRD patterns of carbon produced from cellulose (5 g) and iron nitrate solution (3.4 mmol) at a selection of temperatures between 750 and 800 °C.

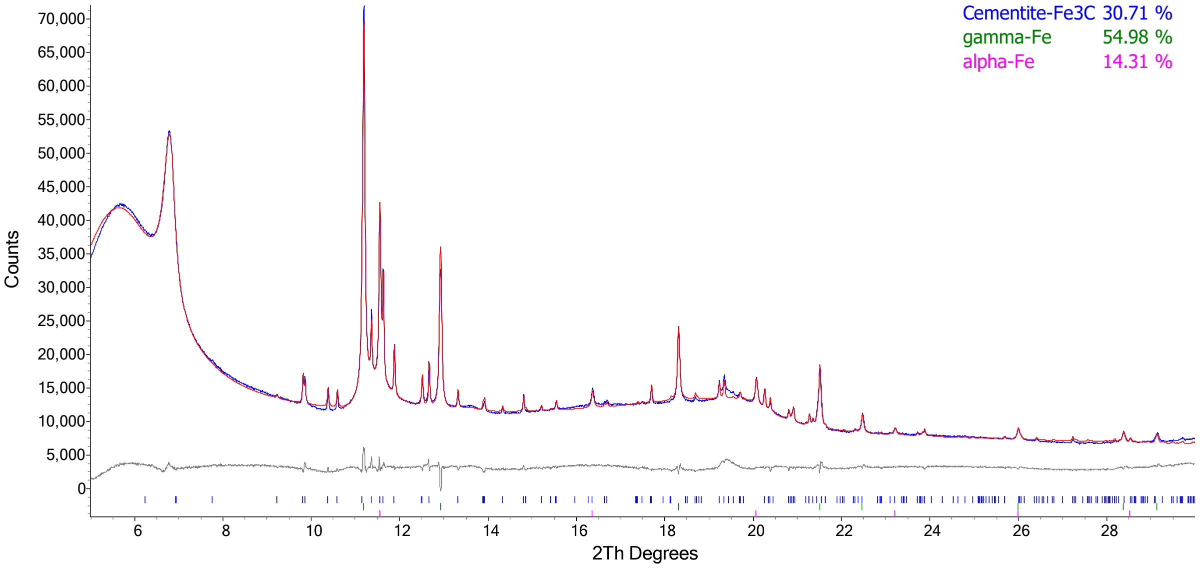

Figure 5.4: Rietveld refinement of diffraction data for cellulose-derived carbon acquired after 0 min at 800 °C. Raw diffraction data is shown in red, calculated data is shown in blue and the difference curve in grey. Tick marks refer to Fe_3C, γ-Fe and α-Fe and match the colours in the legend.

Starting from 750 °C, refinement results of the cellulose-derived carbon system show that the iron species is primarily in the form of α-Fe. As the temperature is increased, α-Fe converts to the higher temperature iron phase, γ-Fe along with a lower molar fraction of Fe_3C. The transition from α-Fe to γ-Fe is consistent with the iron-carbon phase diagram for bulk systems, in which for low carbon contents, α-Fe transforms to γ-Fe at 910 °C.[143] This transition is accompanied by fast growth in the intensity of the graphitic carbon peak, shown in figure 5.5, suggesting a correlation between the two phases and that the γ-Fe phase may be responsible for graphitization. As the sample is less crystalline at temperatures of 750-760 °C, the error bars in the relative molar fractions of the iron phase are much larger in this temperature range, which is the likely cause of the kink in the data at approximately 760 °C, rather than an actual feature of the data.

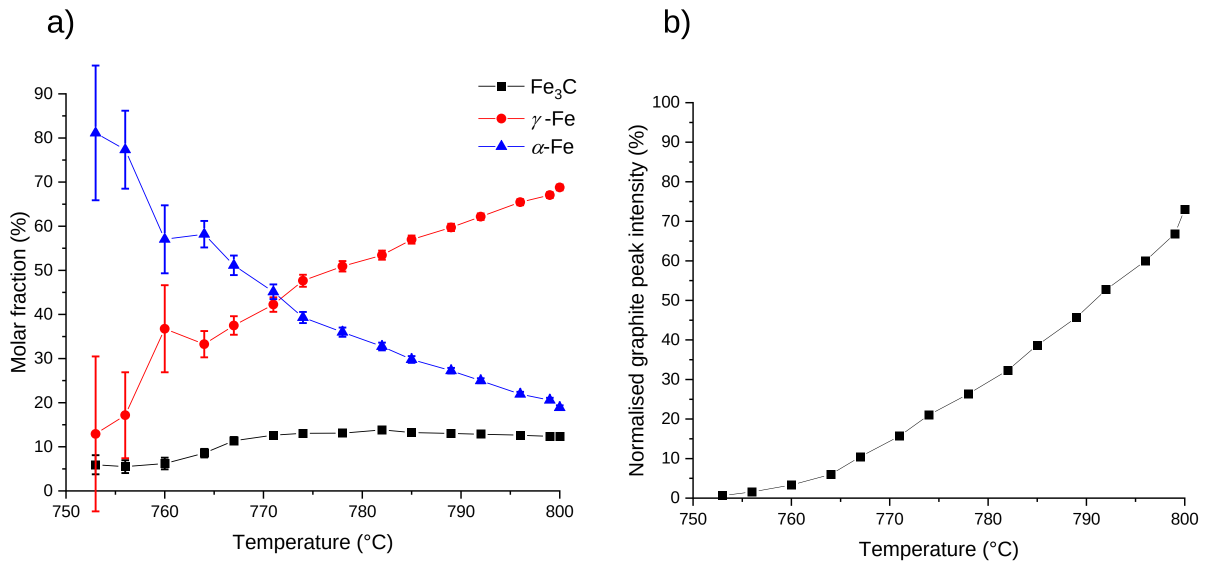

Figure 5.5: a) Plot of molar fractions of iron phases and b) normalised graphite peak intensity versus temperature. Graphite peak intensity is normalised to maximum intensity reached during heating cycle. Values calculated from sequential Rietveld refinements of in situ synchrotron PXRD patterns of cellulose-derived carbon.

By the time the cellulose-derived carbon reaches 800 °C, the graphite peak is very close to reaching its maximum intensity, suggesting that the graphitization process had almost reached completion. This is similar to the *ex situ* PXRD results for cellulose-derived carbons in chapter 3, where significant graphitization was observed after a dwell time of 0 hr at 800 °C. Refinement results calculated from PXRD patterns collected every minute as the sample was dwelled at 800 °C show that the intensity of the graphitic carbon peak remains approximately constant after the first 5 minutes at 800 °C (figure 5.7b). The relative molar fractions of the iron phases also remain approximately constant over the dwell time of 2 hr (figure 5.7a).

A sudden change in the molar fractions of the iron phases occurred after 100 min at 800 °C. During the experimental procedure, the capillary cell was rotated so that the sample as a whole was exposed to the hot air blower and to improve the statistics of the data collection. The sudden change in the molar fractions of the iron phases at 100 min was ascribed to the sample powder moving within the capillary, resulting in a different area of the sample being exposed to the X-ray beam. Therefore, this sudden change was assumed to be an artefact resulting from the experimental setup rather than a real feature of the data.

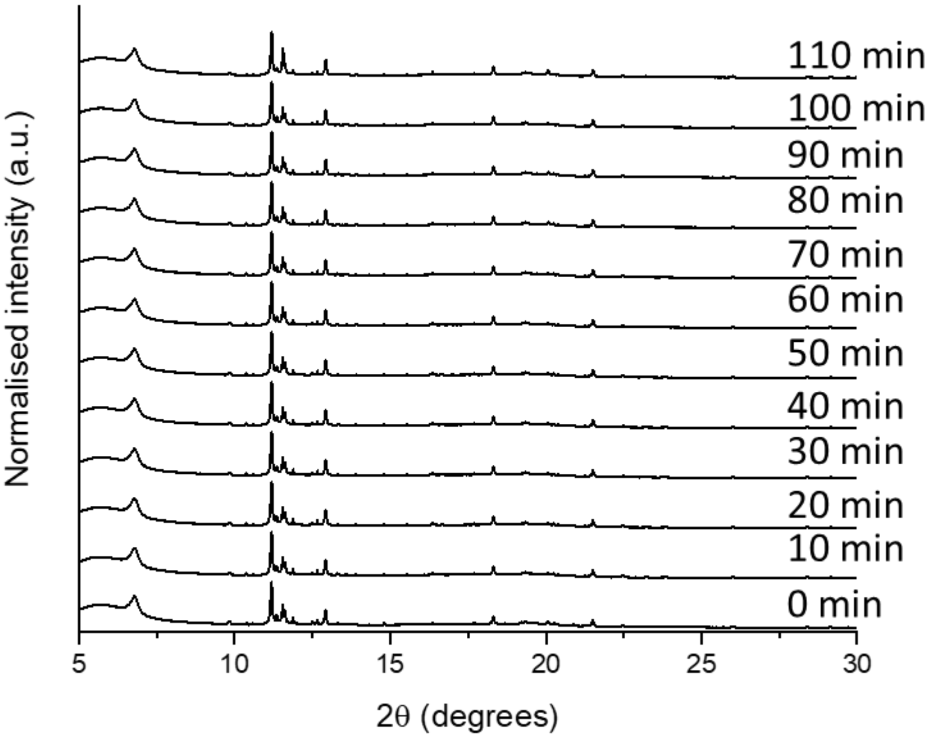

Figure 5.6: In situ PXRD patterns of carbon produced from cellulose (5 g) and iron nitrate solution (3.4 mmol) at a selection of dwell times at 800 °C.

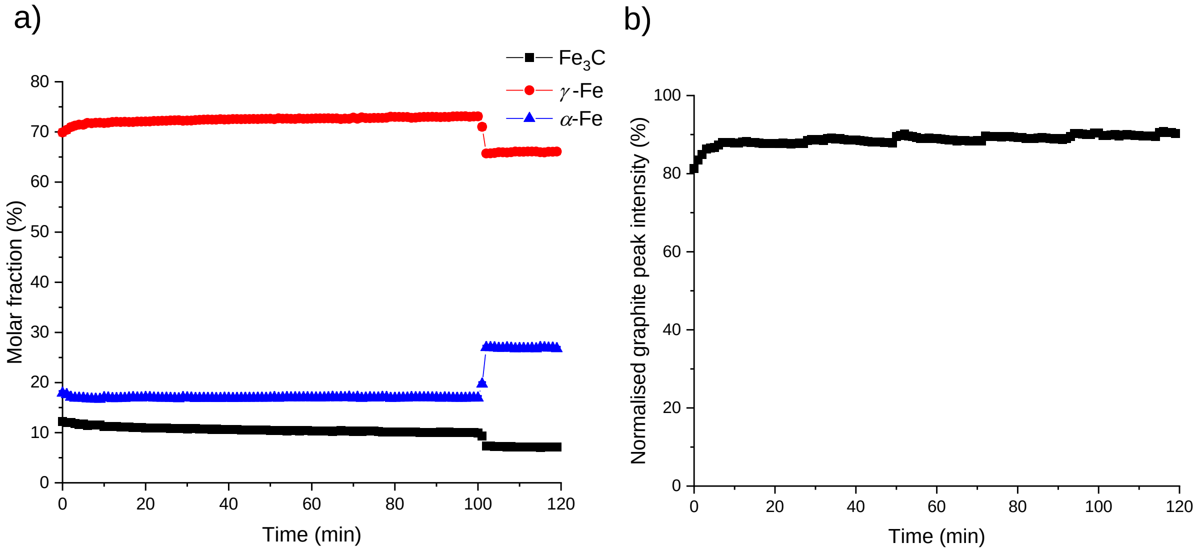

Figure 5.7: a) Plot of molar fractions of iron phases and b) normalised graphite peak intensity versus time at 800 °C. Graphite peak intensity is normalised to maximum intensity reached during heating cycle. Values calculated from sequential Rietveld refinements of in situ synchrotron PXRD patterns of cellulose-derived carbon.

Upon cooling the cellulose-derived carbon, the γ-Fe phase mostly transforms back to the lower temperature α-Fe phase (figure 5.9a). Upon this transition, a further small increase in the intensity of the graphitic carbon peak was observed (figure 5.9b). Gomez-Martin *et al* observed similar results in iron-catalyzed graphitization of MDF wood and attributed the additional graphitization to the decreased solubility of carbon in the α-Fe phase compared to the γ-Fe phase and the precipitation of graphitic carbon around the iron particles.[189]

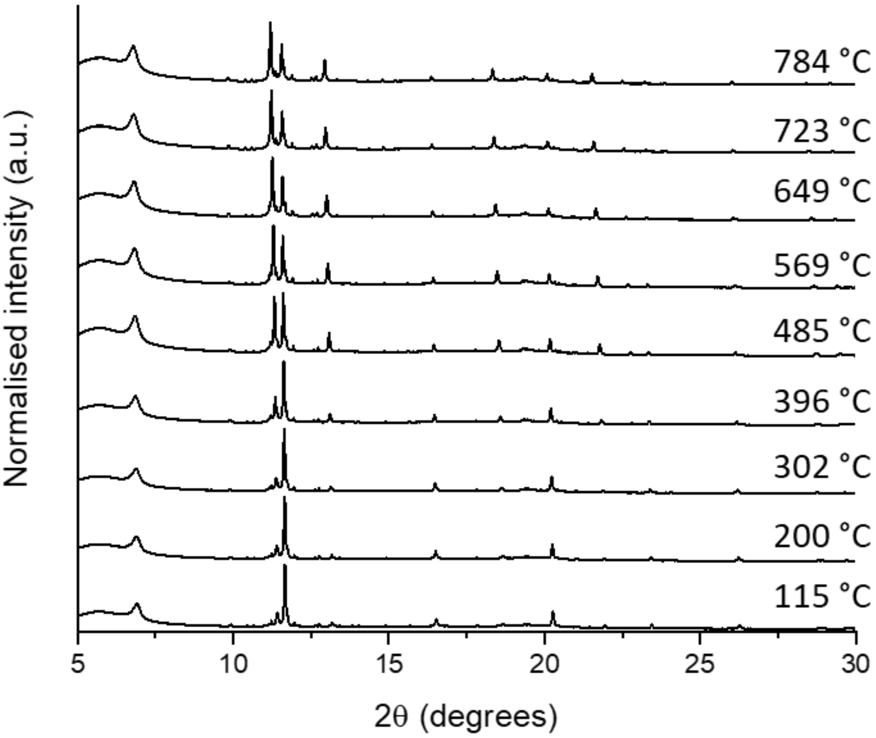

Figure 5.8: In situ PXRD patterns of carbon produced from cellulose (5 g) and iron nitrate solution (3.4 mmol) at a selection of temperatures during cooling.

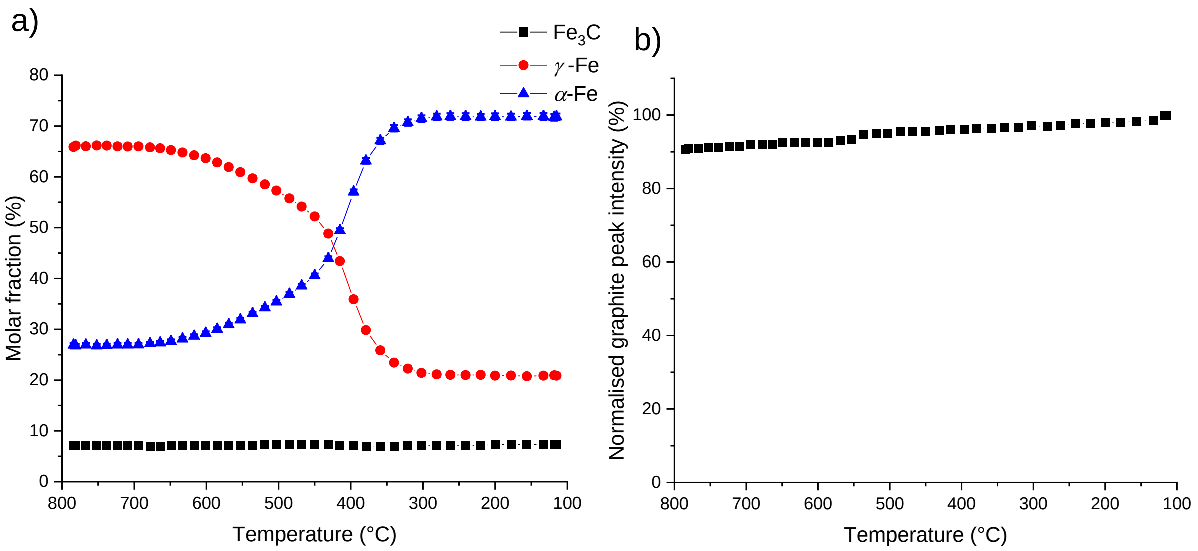

Figure 5.9: a) Plot of molar fractions of iron phases and b) normalised graphite peak intensity versus temperature during cooling. Graphite peak intensity is normalised to maximum intensity reached during heating cycle. Values calculated from sequential Rietveld refinements of in situ synchrotron PXRD patterns of cellulose-derived carbon.

5.3.2.2 Starch-derived carbon

In starch-derived carbon, at temperatures below 800 °C, only very broad and poorly resolved peaks were observed in the PXRD patterns. Therefore, Rietveld refinements were performed on the PXRD patterns collected once the sample reached 800 °C (figure 5.9). Upon reaching 800 °C, the results of the Rietveld refinements (figure 5.11a) show that the iron species was predominantly in the form of *α*-Fe. As the dwell time increased, the relative molar fraction of *α*-Fe decreased, while the relative molar fraction of Fe_3C increased. The molar fraction of *γ*-Fe also increased slightly in the first 20 minutes before it decreased over the following 100 minutes at 800 °C, converting into Fe_3C.

Unlike the cellulose-derived carbon, at temperatures below 800 °C, the intensity of the graphitic carbon peak was relatively low upon reaching 800 °C. As the dwell time was increased, the intensity of the graphitic carbon peak gradually increased (figure 5.11b).

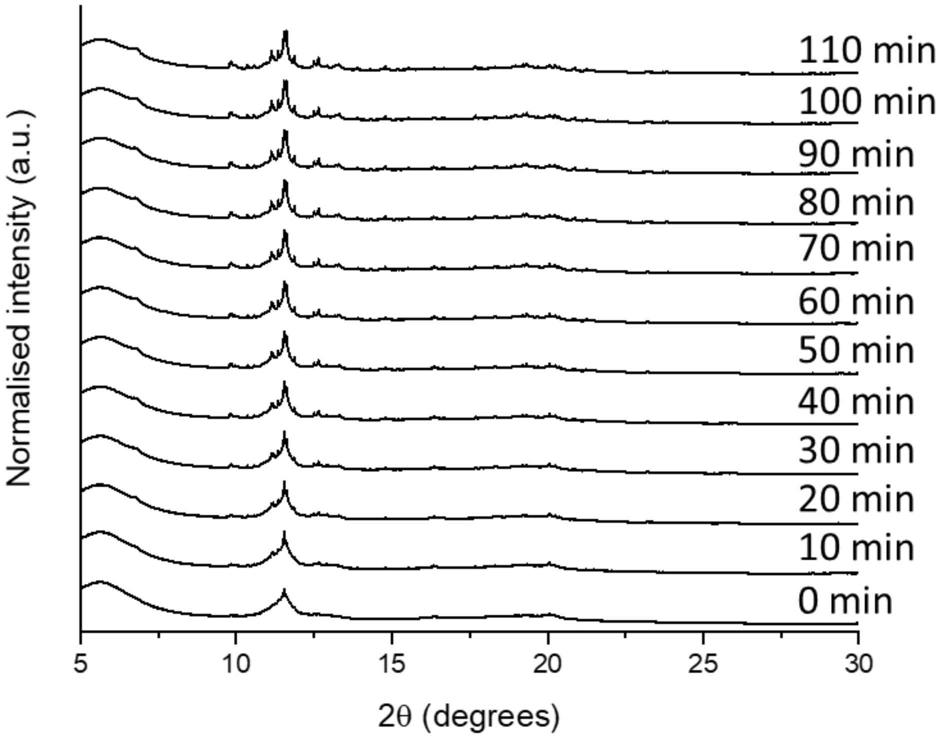

Figure 5.10: In situ PXRD patterns of carbon produced from starch (5 g) and iron nitrate solution (3.4 mmol) at a selection of dwell times at 800 °C.

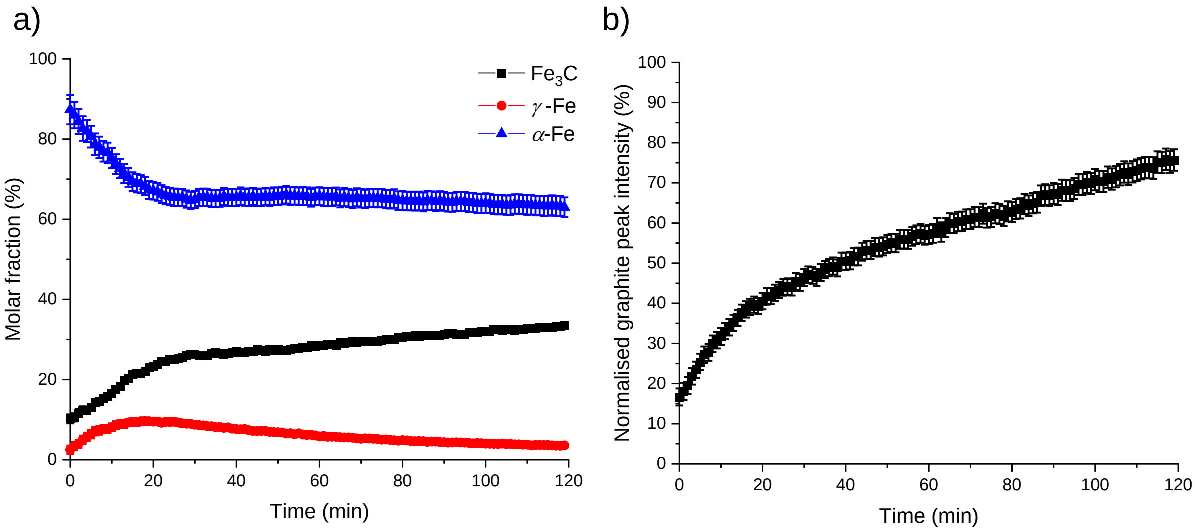

Figure 5.11: a) Plot of molar fractions of iron phases and b) normalised graphite peak intensity versus time at 800 °C. Graphite peak intensity is normalised to maximum intensity reached during heating cycle. Values calculated from sequential Rietveld refinements of in situ synchrotron PXRD patterns of starch-derived carbon.

As the starch-derived carbon sample was cooled from 800 °C, the relative molar fractions remained relatively constant (figure 5.13a). The proportion of Fe_3C

decreased slightly, resulting in a slight increase in the molar fraction of γ-Fe. During cooling, the graphite peak intensity also continued to increase gradually, likely as carbon is ejected from the Fe_3C phase (figure 5.13b). The differences in the cellulose- and starch-derived carbons may be attributed to smaller particle sizes causing a different chemical pathway and will be discussed in more detail below.

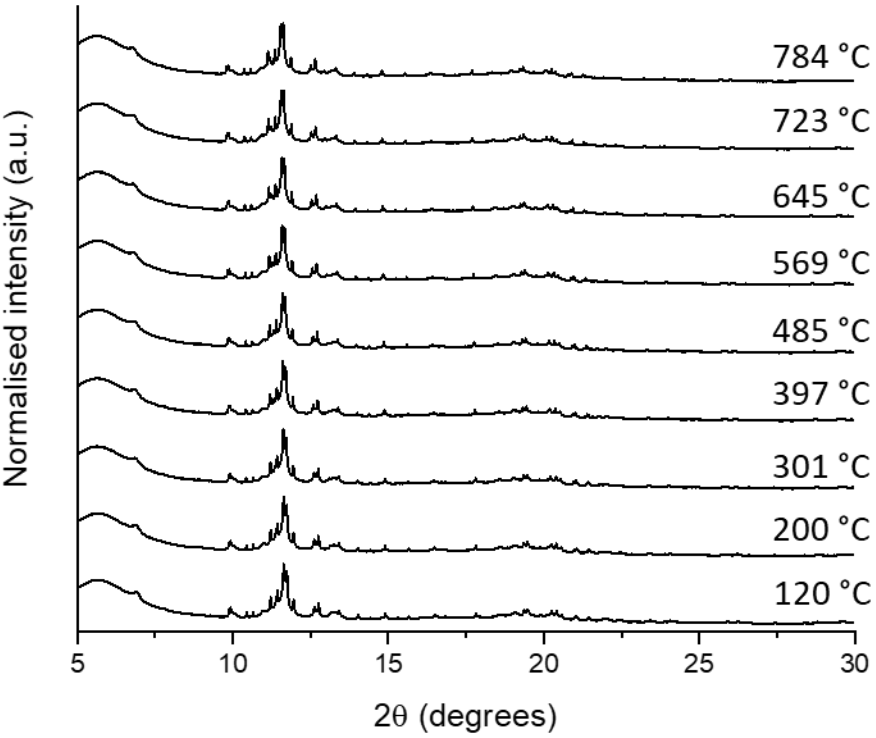

Figure 5.12: In situ PXRD patterns of carbon produced from starch (5 g) and iron nitrate solution (3.4 mmol) at a selection of temperatures during cooling.

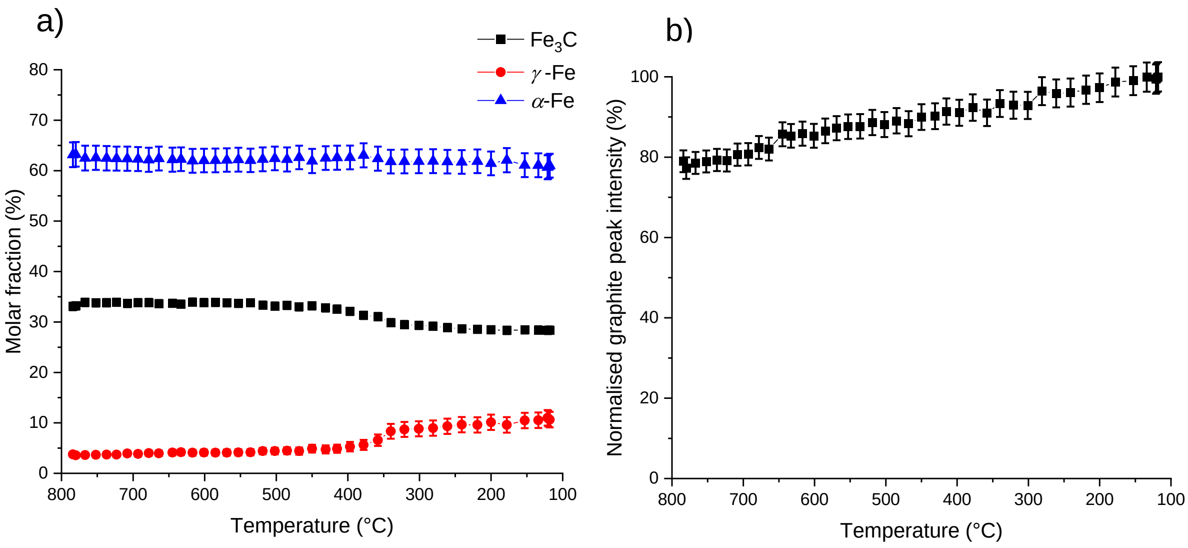

Figure 5.13: a) Plot of molar fractions of iron phases and b) normalised graphite peak intensity versus temperature. Graphite peak intensity is normalised to maximum intensity reached during heating cycle. Values calculated from sequential Rietveld refinements of in situ synchrotron PXRD patterns of starch-derived carbon.

5.3.2.3 Glucose-derived carbon

Like the cellulose-derived carbon, the glucose-derived carbon showed fast graphitization with significant growth of the graphitic carbon peak occurring as the sample was heated from 750-800 °C, as shown in figures 5.14 and 5.15b. However, the relative proportions of the iron phases were different. The primary phase present at 750 °C was *α*-Fe, which partially transformed to *γ*-Fe and Fe_3C with increasing temperature, as in the cellulose-derived carbon, but the *α*-Fe phase still had the highest molar fraction once the sample reached 800 °C (figure 5.15a).

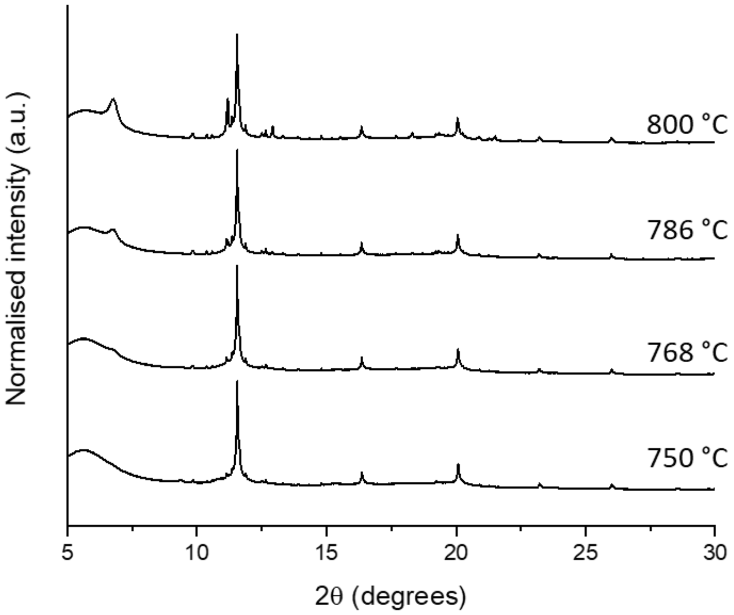

Figure 5.14: In situ PXRD patterns of carbon produced from glucose (5 g) and iron nitrate solution (3.4 mmol) at a selection of temperatures during heating.

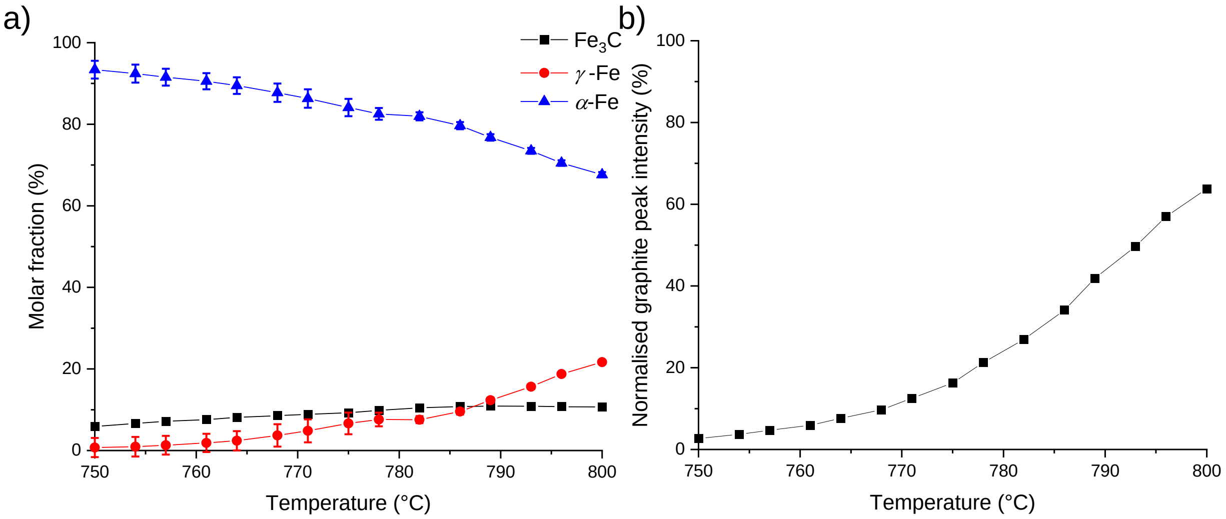

Figure 5.15: a) Plot of molar fractions of iron phases and b) normalised graphite peak intensity versus temperature. Graphite peak intensity is normalised to maximum intensity reached during heating cycle. Values calculated from sequential Rietveld refinements of in situ synchrotron PXRD patterns of glucose-derived carbon.

As the glucose-derived carbon sample was heated to 800 °C, the graphite peak intensity was close to its maximum and remained relatively constant after the first 20 minutes at 800 °C (figure 5.17b). Also, during the first 20 minutes at 800 °C, the molar fraction of *α*-Fe decreases and partially converts to *γ*-Fe (figure 5.17a). However, a large proportion of the iron species remained in the *α*-Fe phase throughout the 2 hr dwell time at 800 °C.

A stepwise growth can be noted in the peak intensity of the graphitic carbon peak (figure 5.17b). As with the cellulose-derived carbon, this behaviour was again assumed to be due to movement of the sample powder within the capillary during the heating procedure and not considered to be a real feature in the refinement data.

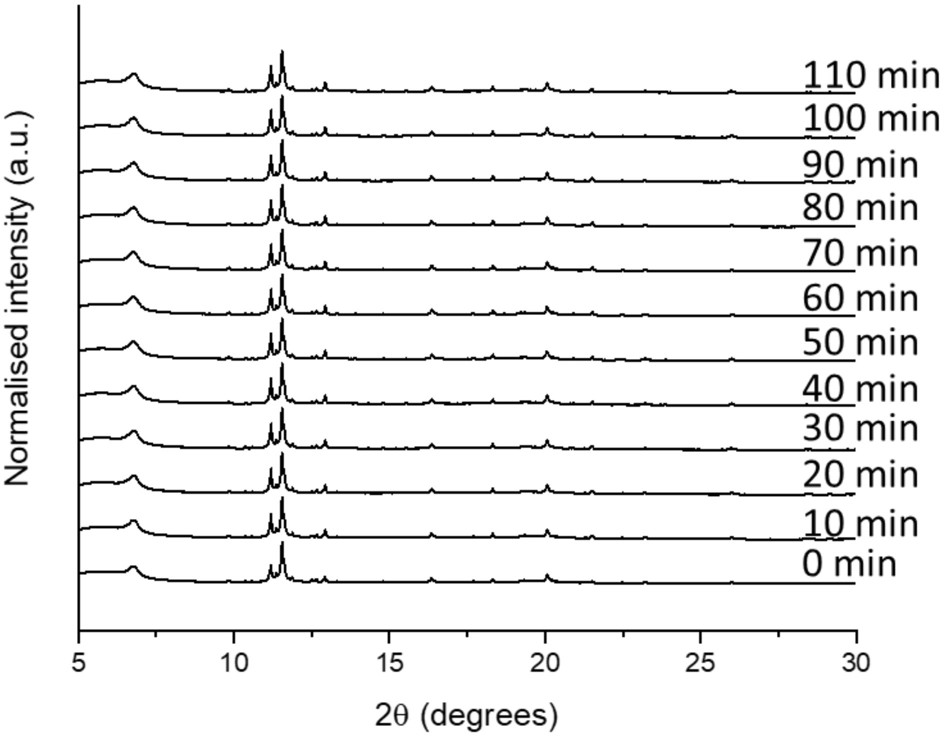

Figure 5.16: In situ PXRD patterns of carbon produced from glucose (5 g) and iron nitrate solution (3.4 mmol) at a selection of dwell times at 800 °C.

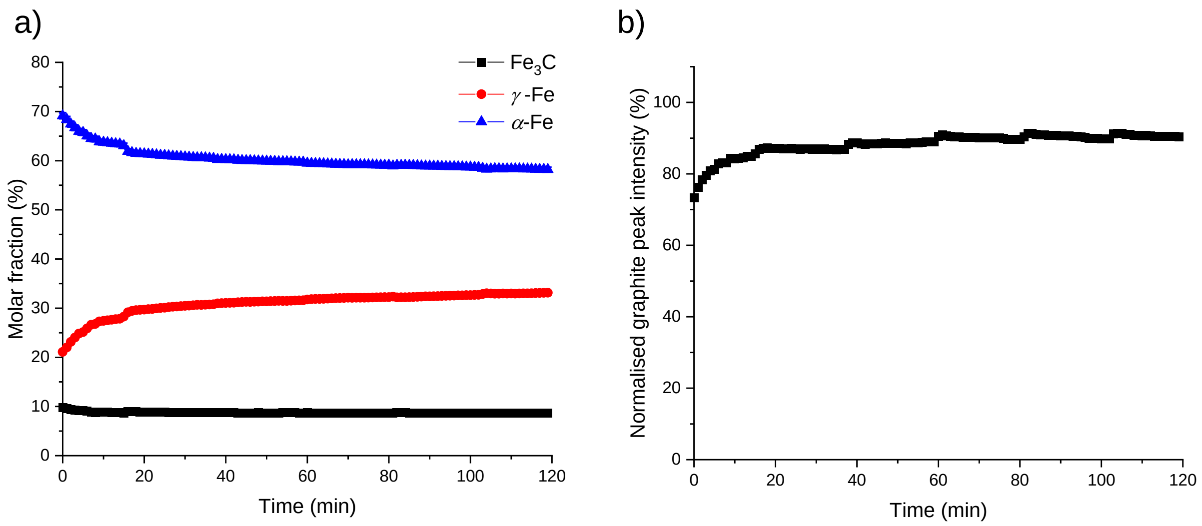

Figure 5.17: a) Plot of molar fractions of iron phases and b) normalised graphite peak intensity versus time at 800 °C. Graphite peak intensity is normalised to maximum intensity reached during heating cycle. Values calculated from sequential Rietveld refinements of in situ synchrotron PXRD patterns of glucose-derived carbon.

Like the cellulose-derived carbon, as the glucose-derived carbon was cooled to room temperature, a significant proportion of the *γ*-Fe phase converts to *α*-Fe (figure 5.19a). However, the conversion is less pronounced as the molar fraction of *α*-Fe remained high throughout the dwell time. Alongside this conversion, the intensity of the graphite peak increases, likely as carbon is precipitated out of the iron nanoparticles in the form of graphitic carbon as the solubility of carbon within the iron species decreases (figure 5.19b).

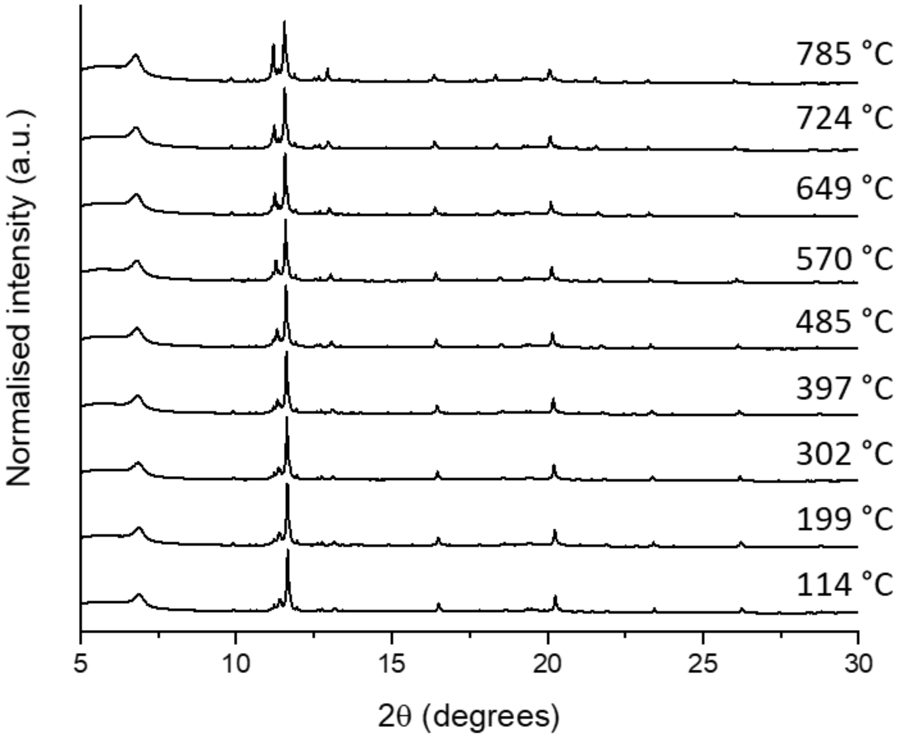

Figure 5.18: In situ PXRD patterns of carbon produced from glucose (5 g) and iron nitrate solution (3.4 mmol) at a selection of temperatures during cooling.

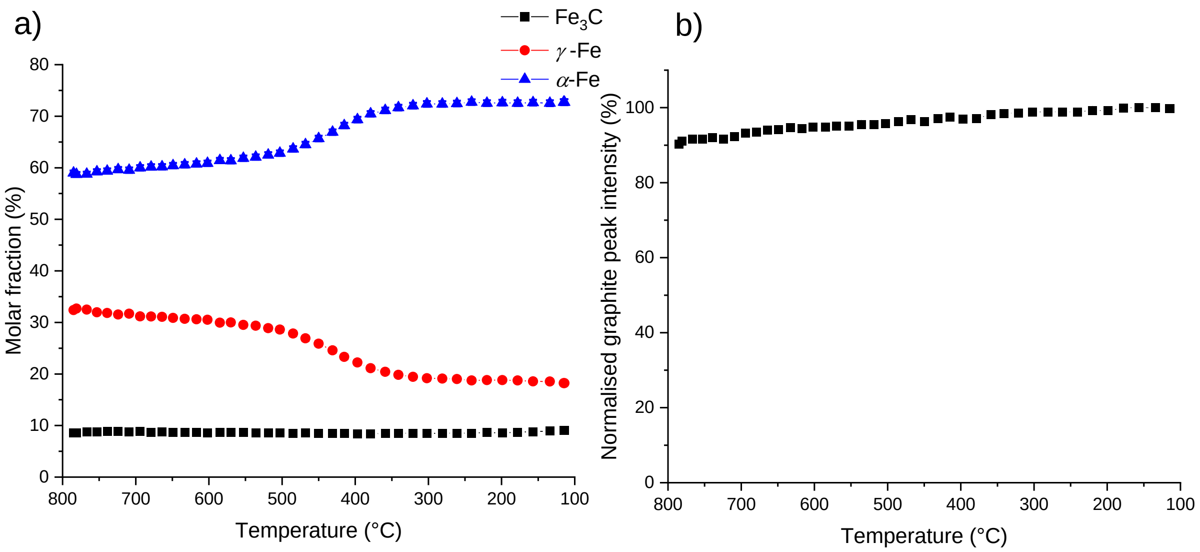

Figure 5.19: a) Plot of molar fractions of iron phases and b) normalised graphite peak intensity versus temperature. Graphite peak intensity is normalised to maximum intensity reached during heating cycle. Values calculated from sequential Rietveld refinements of in situ synchrotron PXRD patterns of glucose-derived carbon.

5.3.3 Insights into the chemical nature of the graphitization catalyst in the three systems

Considering the mechanism of graphitization occurring in the cellulose-, starch- and glucose-derived carbons, it is clear that different reaction pathways are occurring in the different systems. Combining the results of the Rietveld refinements shown earlier in Figure 5.20a shows that at the onset of graphitization in the cellulose-derived carbon system, the low temperature *α*-Fe phase transforms into a mixture of *γ*-Fe with some Fe_3C. The intensity of the graphitic carbon peak increases rapidly alongside the growth of the *γ*-Fe phase (figure 5.20b) and, once the sample reached 800 °C, the degree of graphitization and the molar fraction of *γ*-Fe reached their maxima. This suggests that *γ*-Fe is the primary phase responsible for the conversion of amorphous carbon to nanostructured graphitic carbon structures.

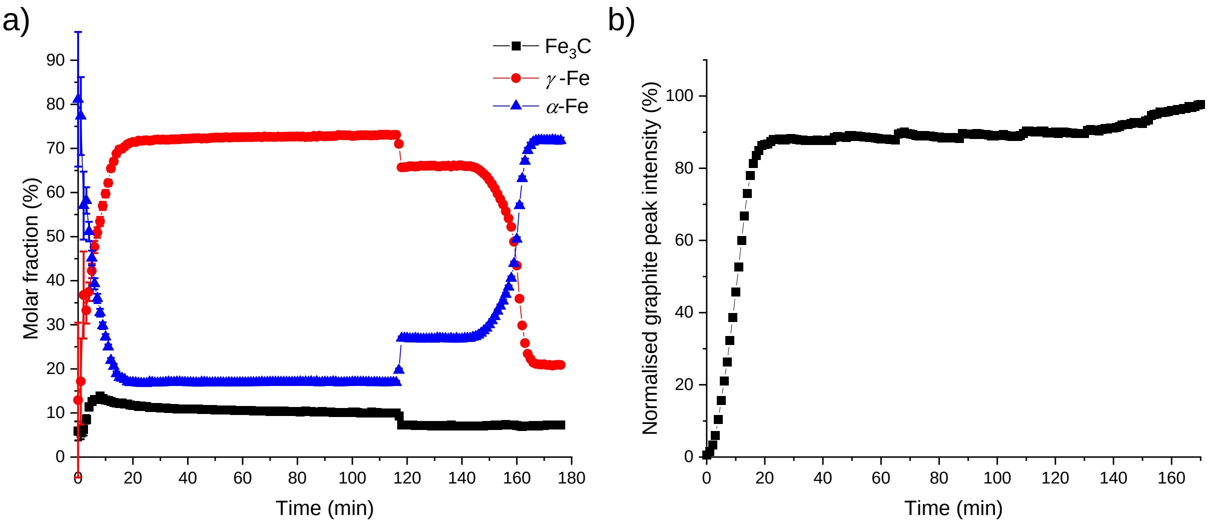

Figure 5.20: a) Plot of molar fractions of iron phases and b) normalised graphite peak intensity versus time across whole pyrolysis procedure. Graphite peak intensity is normalised to maximum intensity reached during heating cycle. Values calculated from sequential Rietveld refinements of in situ synchrotron PXRD patterns of cellulose-derived carbon.

The starch-derived carbon system clearly showed different behaviour to the cellulose-derived carbon system. As with the cellulose-derived carbon, the graphitic carbon peak emerged as a proportion of the *α*-Fe phase is transformed into *γ*-Fe and Fe_3C

(figure 5.21a). However, the proportion of *α*-Fe converted was much lower, and a molar fraction of approximately 60 % *α*-Fe was maintained throughout the dwell time at 800 °C. Of the proportion of the *α*-Fe that underwent a phase transformation, only a small proportion formed the *γ*-Fe phase and a greater molar fraction of Fe_3C was formed.

Upon reaching 800 °C, the graphitic carbon peak slowly grew in intensity as the sample was dwelled at 800 °C (figure 5.21b). One explanation for the slow graphitization process in the starch system is the low *γ*-Fe content. If *γ*-Fe was the active catalytic phase, as was seemingly the case in the cellulose-derived carbon system, then a low catalyst loading may have resulted in a slower graphitization process.

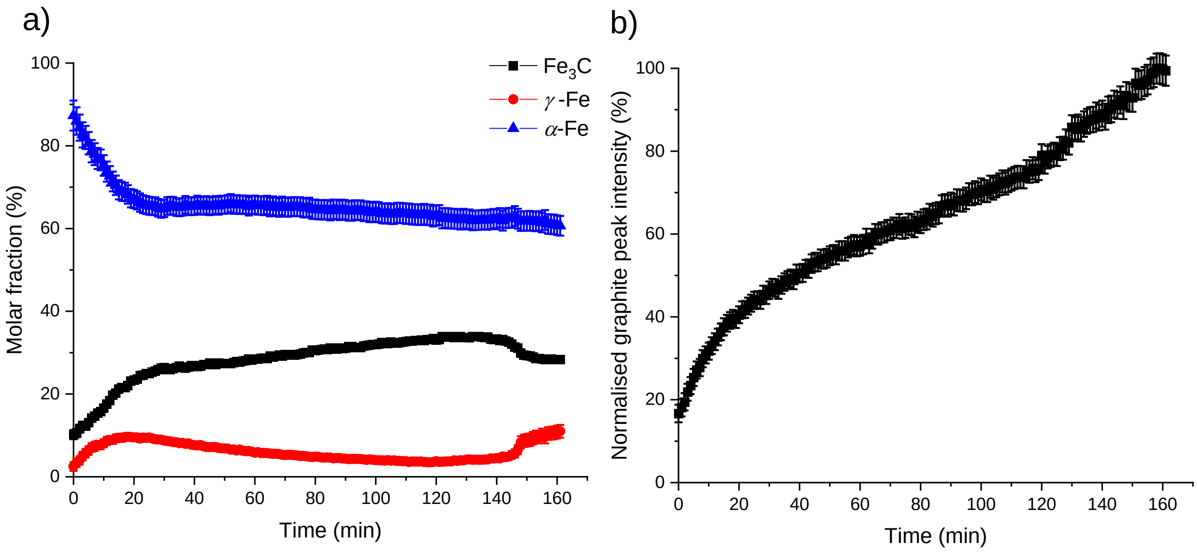

Figure 5.21: a) Plot of molar fractions of iron phases and b) normalised graphite peak intensity versus time across whole pyrolysis procedure. Graphite peak intensity is normalised to maximum intensity reached during heating cycle. Values calculated from sequential Rietveld refinements of in situ synchrotron PXRD patterns of starch-derived carbon.

In the glucose-derived carbon, the onset of graphitization again occurred as *α*-Fe transformed into a mixture of *γ*-Fe and Fe_3C (figure 5.22). As with the starch-derived carbon, a large fraction of the *α*-Fe did not undergo a phase transformation. However, the fraction of the *α*-Fe that did transform preferentially formed *γ*-Fe over Fe_3C. Graphitization then proceeded quickly as the proportion of *γ*-Fe increased, again suggesting that *γ*-Fe was the likely catalytically active species.

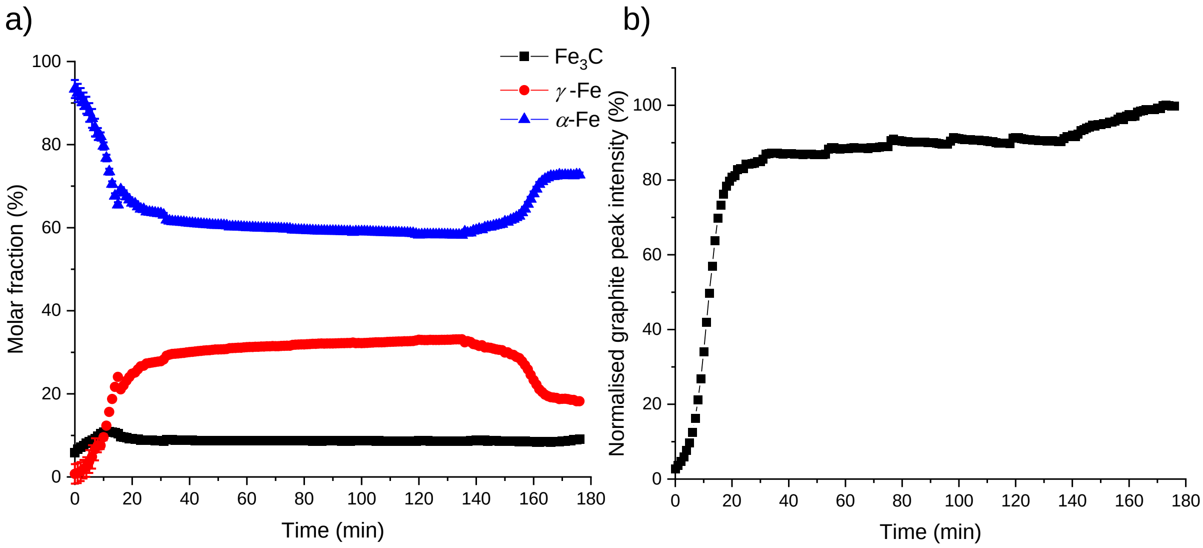

Figure 5.22: a) Plot of molar fractions of iron phases and b) normalised graphite peak intensity versus time across whole pyrolysis procedure. Graphite peak intensity is normalised to maximum intensity reached during heating cycle. Values calculated from sequential Rietveld refinements of in situ synchrotron PXRD patterns of glucose-derived carbon.

A study by Wirth et al investigated the phase of iron-based catalyst nanoparticles during carbon nanotube growth via CVD using a combination of *in situ* PXRD and ETEM, as in this chapter.[191] The authors reported that two different pathways could be followed to give varying relative concentrations of the iron phases and rationalized this behaviour using the iron-carbon and iron carbide-carbon phase diagrams. One pathway occurred at a slightly higher temperature (pathway A in figure 5.23) and one at a slightly lower temperature (pathway B in 5.23). In pathway A, as carbon content is increased, point a_1 is crossed (the *α*-Fe/*γ*-Fe coexistence line) before point a_2 (*α*-Fe/iron carbide); therefore, *γ*-Fe initially forms preferentially over Fe_3C, and *γ*-Fe and *α*-Fe exist in equilibrium. As the carbon content increases further, point a_4 is reached (*γ*-Fe/carbon coexistence line). After this point, the *γ*-Fe particles become supersaturated with carbon and carbon nanotube nucleation occurs from the *γ*-Fe particles. Carbon nanotube nucleation occurs before reaching point a_5 (the γ-Fe/Fe_3C solidus), and as there is a large difference between point a_4 and a_5, the γ-Fe particle is stable against Fe_3C nucleation. Point a_5 is not reached as the carbon nanotube provides a sink for excess carbon.[191]

Conversely, in pathway B, the difference between point b_1 (α-Fe/C coexistence line) and b_2 (α-Fe/Fe_3C coexistence line) is much smaller. Therefore, Fe_3C nucleation is more favourable, followed by carbon nanotube growth. The authors suggest that at temperatures far above and below the eutectoid temperature, carbon nanotube growth would be dominated by mostly metallic or carbide catalyst particles respectively, whereas close to the eutectoid temperature, the relative pathway is dictated by kinetic effects.[191]

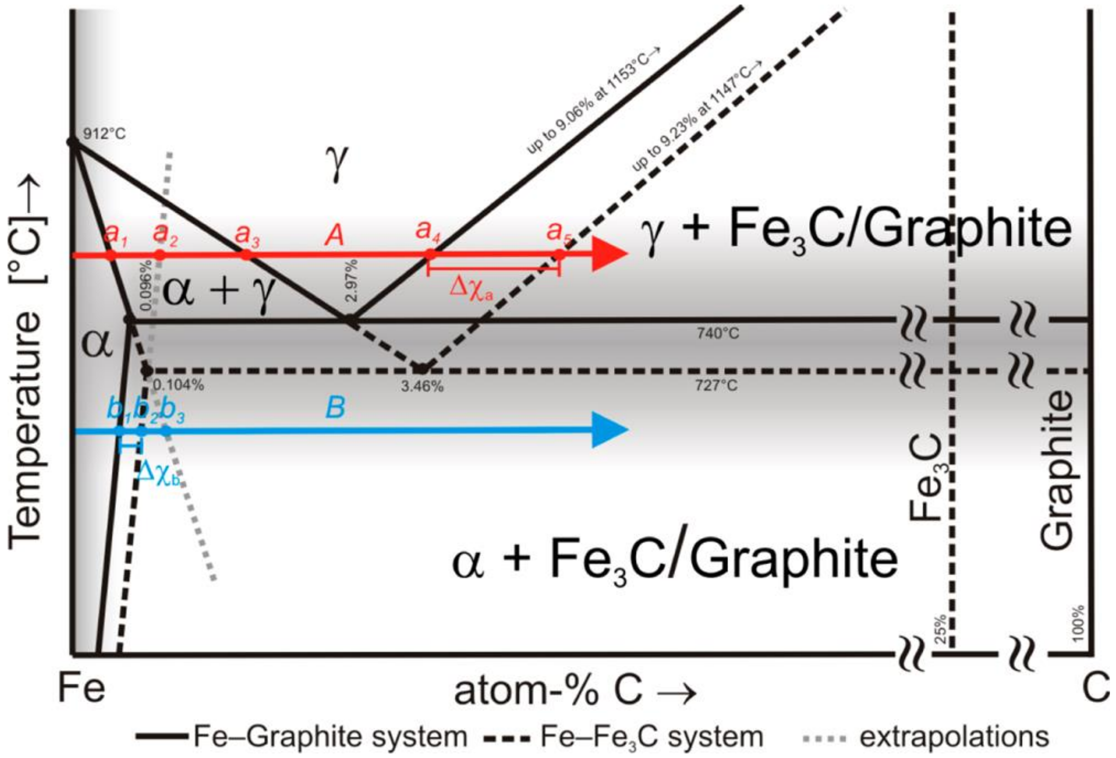

Figure 5.23: Schematic phase diagram adapted with permission from ref. 191.

Considering the three systems in this chapter, the cellulose-derived carbon system proceeded *via* a pathway similar to pathway A, unlike the starch-derived carbon system, which proceeded *via* a pathway more similar to pathway B. Therefore, the different systems may be located at different positions on the iron-carbon phase diagram.

In chapter 3, the different behaviour of the starch-derived carbon system was attributed to the smaller size of the catalyst particles, and the idea that particles must reach a critical size in order to become catalytically active. The temperature of phase transitions and solubilities in binary phase transitions has been shown to be affected by particle size.[192,193] Therefore, the variation in particle size in the three systems, especially in the case of the starch-derived carbon, may influence which pathway is the most kinetically favourable.

5.4 Conclusions

The TEM results within this chapter have suggested that iron-based catalyst particles display liquid-like, dynamic behaviour during graphitization in cellulose-derived carbon. However, *in situ* PXRD results show the presence of crystalline iron phases at the onset of graphitization, indicating that the catalyst particles are likely to be in a solid state. This is further evidenced by the observation that graphitization occurred alongside solid-solid phase transformations, suggesting that these are likely to be the driving force for graphitization.

Cellulose-, starch- and glucose-derived carbon systems from chapter 3 were shown to proceed *via* different reaction pathways, resulting in different rates of graphitization. The variation in the reaction pathways was rationalized by considering the different systems to occupy different spaces on the iron-carbon phase diagram, similar to the work of Wirth *et al*, possibly due to variations in particle sizes between the systems.[191]

Graphitization was observed to occur more quickly in the systems with higher molar fractions of γ-Fe than Fe_3C. One explanation may be that only γ-Fe is an active catalytic phase, as the starch-derived carbon had a low γ-Fe content and a slow graphitization step. Alternatively, as in the study of Wirth *et al*, graphitization may proceed from both γ-Fe and Fe_3C particles, but the carbide route is a kinetically slower process.[191]

Future work should focus on improving the experimental setup of the *in situ* ETEM with the aim of obtaining footage of high enough quality that it would be possible to observe lattice fringes or perform SAED to provide further information regarding the physical and chemical nature of the catalyst particles during graphitization. It would also be useful to perform similar experiments on both the glucose- and starch-derived carbon systems to see whether similar catalyst movement would be observed in these systems. Further investigation into the starch-derived carbon system would be particularly instructive as the graphitization process was observed to be significantly slower than the other two systems.

Table 5.1: Summary of key findings in chapter 5.

Key Finding	**Evidenced by:**
Catalyst particles in cellulose-derived carbon were mobile during graphitization	• Movement of iron-based particles observed in real time in ETEM experiments
Catalyst particles likely in solid state during graphitization	• Presence of Bragg peaks at the onset of graphitization during *in situ* synchrotron PXRD
Graphitization slower in starch-derived carbon system	• Slower growth of characteristic peak for graphitic carbon during *in situ* synchrotron PXRD
Higher γ-Fe content resulted in faster graphitization than systems with high Fe_3C content	• Different rates of growth of characteristic peak for graphitic carbon during *in situ* synchrotron PXRD • Different molar fractions of iron phases in the different systems calculated from Rietveld refinement of *in situ* synchrotron PXRD data

Chapter 6 – Modelling the melting behaviour of catalyst particles in iron-catalyzed graphitization

6.1 Introduction

Understanding the mechanistic aspects of iron-catalyzed graphitization is crucial to be able to optimize the synthetic routes to produce tailorable nanostructured graphitic carbon materials. If the movement of the nanoparticle catalyst particles can be understood, it may be possible to control the movement and introduce directional order into the resulting tubular nanostructures.

One aspect of the mechanism that remains an area of dispute is the physical nature of the catalyst particles during graphitization. Even with more sophisticated experimental studies, distinguishing between a solid and liquid nanoparticle in such a dynamic system remains a challenge. The work in chapter 5 displayed the movement of the catalyst nanoparticles in ETEM experiments during the conversion of amorphous carbon to graphitic carbon nanostructures, potentially suggesting that the catalyst particles may be in a liquid or liquid-like state. However, synchrotron PXRD also showed the presence of crystalline phases at the onset of graphitization, suggesting a solid catalyst species.

6.1.1 Nanoparticle melting

The melting behaviour of objects on the nanoscale is often considerably different to that of the bulk material. This idea was first explored over 100 years ago, when Pawlow derived an equation to describe and predict the decrease in melting point of “melting point depression” of spherical nanoparticles with decreasing size.[194]

The first experimental evidence for this melting point depression was reported by Takagi in 1954.[195] Since then, Pawlow’s formula (equation 6.1) has been widely used as a model for nanoparticle melting.

$$T_m(R) = T_m\left(1 - \frac{C}{R}\right)$$

(6.1)

In equation 6.1, R is the particle radius, T_m is the bulk melting temperature of the material, $T_m(R)$ is the melting temperature of a particle with a specific radius and C is a constant that is related to the surface energies (γ_{sv} and γ_{lv}), atomic density (ρ) and latent heat (L) as shown in equation 6.2:

$$C \approx 2(\gamma_{sv} - \gamma_{lv})/\rho L$$

(6.2)

Atoms on the surface play an important role in the melting behaviour of a material. In 1842, Faraday suggested that a liquid-like layer on the surface of ice can exist at temperatures below the bulk melting temperature.[196] Studies have since shown that surface melting is a common occurrence in various crystalline materials, including metals. Due to the greater surface:volume ratio in nanoparticles, the influence of the surface is far more pronounced than in a corresponding bulk material. Simulations performed by Ding *et al*, for example, suggest that surface melting occurs in iron nanoparticles – the thickness of the surface melt increases until the structure totally collapses at the melting temperature.[197]

Various studies into the melting behaviour of iron nanoparticles have been reported in the literature using a variety of different interatomic potentials. However, the inclusion of carbon is an area that has been less well explored, particularly in the context of nanoparticles. The bulk iron-carbon phase diagram shows that pure iron undergoes some solid-solid phase transformations before undergoing melting (figure 6.1). At temperatures below 910 °C, pure iron adopts a BCC structure (α-Fe), which converts to FCC (γ-Fe) between 910-1394 °C.[143] Above 1394 °C, the FCC phase converts to a different BCC phase (δ-Fe) at 1394 °C, before undergoing melting at 1538 °C.[143]

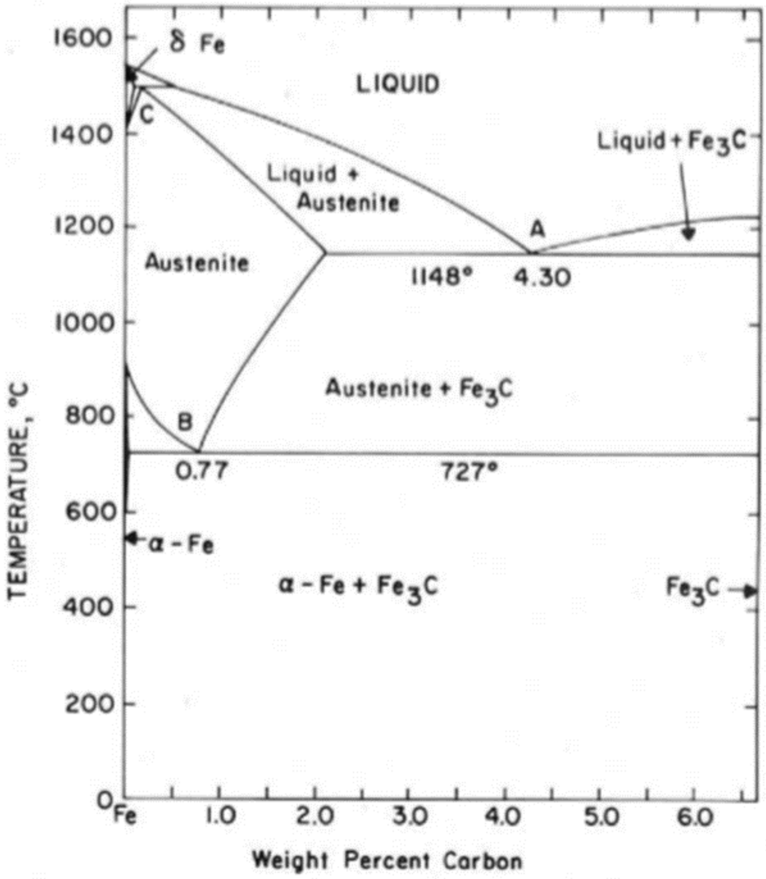

Figure 6.1: Bulk iron-carbon phase diagram reproduced from ref. 143.

The bulk iron-carbon phase diagram shows that the introduction of carbon initially lowers the melting temperature. However, Fe_3C does not have a well-defined melting temperature as it is a metastable phase that often decomposes to iron and carbon before undergoing melting. The iron-carbon phase diagram also shows a eutectic point at 1420 K, where liquid iron, carbon and Fe_3C co-exist in equilibrium, so some studies use this value as the melting temperature for Fe_3C.

Many studies of nanoparticle melting focus on freestanding nanoparticles to minimize the computational cost of the simulations. However, experimentally, nanoparticles are almost always either in contact with a substrate or embedded within a solid matrix, as is the case in iron-catalyzed graphitization syntheses. Therefore, it is important to consider the influence that the surrounding material may have on the melting behaviour of the nanoparticles. Studies such as the work of Ding *et al*[149] and Shibuta *et al*[198] have explored substrate-supported iron nanoparticles and showed that the presence of a substrate generally increases the melting temperature of the nanoparticles. In this chapter, the melting behaviour of both freestanding and supported iron and iron carbide nanoparticles are explored in the context of iron-catalyzed graphitization systems.

6.2 Molecular dynamics

The simulations in this chapter were all run using classical molecular dynamics, a deterministic simulation method that follows the trajectory of a system which obeys Newton’s classical laws of motion. The motion of atoms or molecules are simulated with respect to the forces acting upon them, such as intra- or intermolecular forces.

In molecular dynamics simulations, the initial positions of the atoms are defined, and each atom is assigned a velocity. This can be achieved by defining an initial temperature of the simulation and generating a Gaussian distribution of velocities, which are randomly assigned to each atom. Alternatively, positions and velocities may be used from a previous simulation. The atom trajectory is defined by the positions and momenta as a function of time, and each point in the trajectory corresponds to a configuration with potential energy, $V(t)$.

The general molecular dynamics cycle is as follows:

1. Define initial positions at timestep 0 and initial velocities – if the initial positions of all atoms are known, determine the atomic distances.
2. From the atomic distances, calculate energies by taking the sum of all the interactions from each pair of atoms.
3. From the energies, calculate the force acting upon the atoms by taking the sum of all the forces acting upon each atom.
4. Apply Newton's second law of motion to calculate acceleration ($F = ma$).
5. Calculate the new positions and velocities after a small increment of time (*dt*). Integrate the acceleration to get new positions after *dt*. Repeat the above process to calculate the energies, forces and acceleration at the new position.

6.2.1 Empirical potentials

The interactions between particles are described by interatomic potentials, which fall into various categories. Two relevant categories are discussed here: Lennard-Jones and the embedded atom model (EAM).

6.2.1.1 Lennard-Jones

A commonly used, mathematically simple interatomic potential is the Lennard-Jones potential. This considers a repulsive and attractive component that is dependent on the distance between a pair of atoms. The Lennard-Jones potential is usually written in terms of the well depth and the distance of closest approach, which can be used to calculate the energy of an atom (equation 6.3).

$$U_{L-J} = 4\varepsilon \left(\left(\frac{\sigma}{R}\right)^{12} - \left(\frac{\sigma}{R}\right)^{6}\right) \tag{6.3}$$

In equation 6.3, $U_{L\text{-}J}$ is the potential energy, ε is the potential well depth, R is the atomic distance and σ is the distance of closest approach. The repulsive term arises from Pauli's exclusion principle, which states that electrons cannot overlap the same space, so the potential energy tends to infinity with decreasing interatomic distance. In practice, rather than using an exponential term, a power of 12 term is used to reduce computing time.

The attractive term comes from weak van der Waals forces between atoms, which increase as the interatomic distance is decreased. In practice, a cut-off is introduced whereby the interactions from atoms positioned beyond a certain distance are assumed to be negligible, so are not included in the calculations.

The parameter ε determines the strength of the interactions between particles. A deeper well indicates a stronger pair-wise interaction.

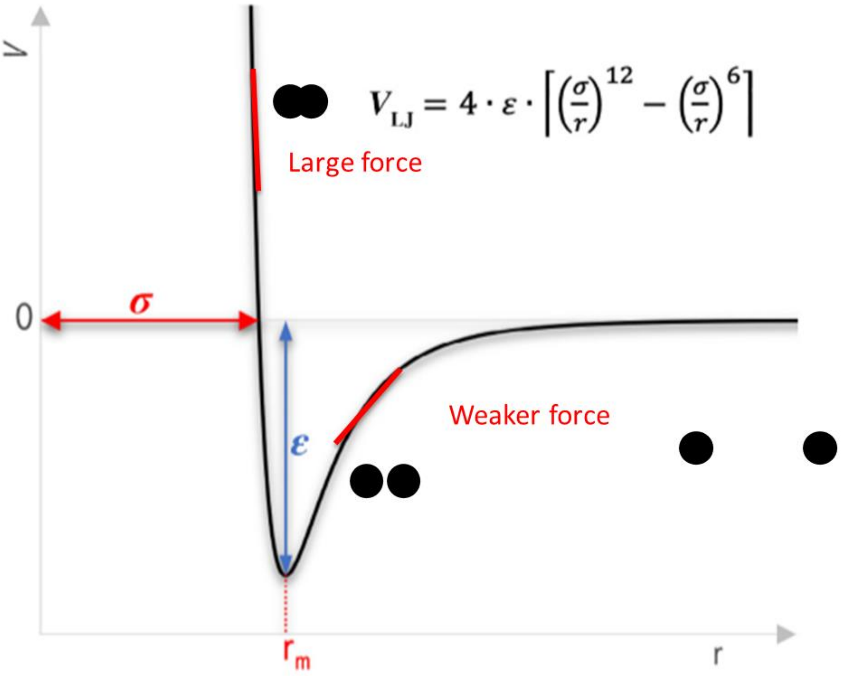

Figure 6.2: Schematic of the Lennard-Jones potential adapted with permission from ref. 199.

The total energy of the system, U_{LJ} can be approximated by a sum of the energies of all particles:

$$U_{LJ} = \sum_{i=1}^{N-1} \sum_{j=i+1}^{N} U_{ij}$$

(6.4)

The force acting on a particle (*i*) can be calculated by integrating the energy of the particle with respect to its position. Considering two interacting particles, *i* and *j*, the force that atom *j* is exerting on *i* is given by equation 6.5.

$$F_{j \rightarrow i} = - grad\, U_{ij}$$

(6.5)

The negative sign indicates that a negative slope (or repulsive interaction) will give a positive force and a positive slope (or attractive interaction) will result in a negative force.

The total force acting on particle *i,* (F_i) can be calculated by summing the force exerted by all the particles that are within the relevant cut-off distance ($F_{j \rightarrow i}$).

$$F_i = \sum_{j \neq i} F_{j \rightarrow i}$$

(6.6)

The calculated forces can be used to calculate the particle's acceleration by applying Newton's second law of motion, $F = ma$.

6.2.1.2 EAM

Pair-wise potentials such as Lennard-Jones do not consider the environment of the particle so are generally only useful for giving approximations of the interactions in a system where the exact nature of the components may not be the area of interest in the simulation. For example, Lennard-Jones potentials would not be relevant for modelling the interactions within a metal cluster, in which the potential energy of an atom positioned on the surface should be greater than the potential energy of an atom located within the bulk.

The EAM potential considers the energy of embedding an atom into the electron density of neighbouring atoms, so the general formula contains an additional embedding energy term alongside a pair-wise term.[200]

$$U = \sum U_i \tag{6.7}$$

$$U_i = F_i(\rho_i) + \frac{1}{2}\sum_{j \neq i} \varphi_{ij}(r_{ij}) \tag{6.8}$$

In equation 6.8, φ_{ij} is a two-body term and describes the short-range electrostatic pair interaction between atoms i and j and $F(\rho_i)$ refers to the energy of embedding atom in the local electron density (ρ_i) of neighbouring atoms.

For simplicity, the electron density is approximated by a linear superposition of the surrounding neighbours, where the parameter $f_j(r_{ij})$ in equation 6.9 denotes the contribution to the embedding energy of atom *i* from the electron density of all atoms *j*.

$$\rho_i = \sum_{j \neq i} f_j(r_{ij})$$

(6.9)

6.2.2 Numerical implementation

In molecular dynamics simulations, an integration algorithm is used to numerically solve the classical equations of motion. One of the most common integration algorithms, is the velocity-Verlet algorithm.[201] This particular algorithm is based on the Verlet algorithm,[202] which is derived from a Taylor expansion of the positions of a particle (r_i) at times ($t + \delta t$) and ($t - \delta t$), where v_i and a_i correspond to the velocity and acceleration of particle *i*, respectively.

$$r_i(t + \delta t) = r_i(t) + v_i(t)\delta t + \frac{1}{2} a_i(t)\delta t^2 + \cdots$$

(6.10)

$$r_i(t - \delta t) = r_i(t) - v_i(t)\delta t + \frac{1}{2} a_i(t)\delta t^2 - \cdots$$

(6.11)

In reality, the Taylor expansions would result in further derivative terms to increasing powers. However, if the timestep (*t*) is small enough, then equations 6.10 and 6.11 can be approximated to only include the second order terms. In the case of molecular dynamics simulations, this generally requires a timestep in the order of femtoseconds.

Equations 6.10 and 6.11 can be combined to give a single equation, 6.12, which is known as the Verlet integrator.

$$r_i(t + \delta t) = 2r_i(t) - r_i(t - \delta t) + a_i(t)\delta t^2$$

(6.12)

The velocity of particle *i* can then be calculated separately by considering the change in position of the particle over time using equation 6.13.

$$v_i(t) = \frac{r_i(t + \delta t) - r_i(t - \delta t)}{2\delta t}$$

(6.13)

To implement the Verlet algorithm, it is necessary to know the positions of the particle at two timesteps. However, when starting a molecular dynamics simulation, only the initial positions are known. Therefore, a more convenient form of the Verlet algorithm, known as the “velocity-Verlet algorithm”, is often used instead (equations 6.14 and 6.15).

$$r_i(t + \delta t) = r_i(t) + v_i(t)\delta t + \frac{1}{2}a_i(t)\delta t^2$$

(6.14)

$$v_i(t + \delta t) = v_i(t) + \frac{1}{2}(a_i(t) + a_i(t + \delta t))\delta t$$

(6.15)

The velocity-Verlet algorithm can be derived from the original Verlet algorithm and allows for the calculation of the consequent positions of the particle from only the initial position. The positions and velocities are also both calculated at each timestep, which allows for a more efficient simulation.

6.2.3 Langevin thermostat

The temperature of all the simulations in this chapter was controlled using the Langevin thermostat.[203] This thermostat simulates Brownian motion, in which interactions are modelled with a background solvent. The total force on each atom, F_{total}, is described by a combination of three parameters, F_c, F_f and F_r.

$$F_{total} = F_c + F_f + F_r \tag{6.16}$$

F_c is a conservative force, which is determined by the particle-particle interactions and is dependent on the specific interatomic potential used. F_f corresponds to a frictional or drag force and is related to the viscosity of the background solvent. Finally, F_r refers to a force due to solvent atoms randomly colliding with the particle and this is dictated by the desired temperature in the simulation.

6.2.4 Periodic boundary conditions

To reduce the computing cost and avoid any effect from interactions with the edges of the simulation box, periodic boundary conditions are often used. The simulation box can be infinitely multiplied in up to three dimensions and particles can move freely between the identical boxes. If a particle moves out of the simulation box, it will re-enter the box from the other side. An important consideration is that as the boundary of the simulation box is not rigid, a particle in box A in figure 6.3's nearest neighbour may in fact be in an adjacent simulation box (B, for example). These conditions allow for simulation of a large system without drastically reducing the computational efficiency.

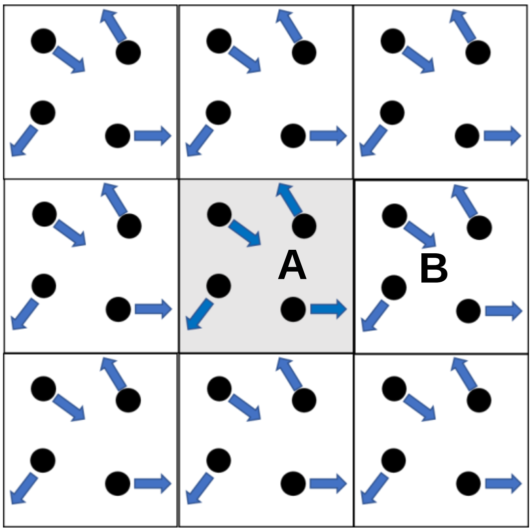

Figure 6.3: Schematic showing periodic boundary conditions. Actual simulation box (A) used in simulation is coloured in grey.

6.3 Experimental

6.3.1 Simulation details

A classical molecular dynamics method using LAMMPS was employed to study the melting behaviour of free and substrate-supported iron and iron carbide clusters. LAMMPS is an open-source molecular dynamics program developed at Sandia National Laboratories.[204]

6.3.1.1 Freestanding clusters

Clusters of BCC iron, FCC iron and Fe_3C were constructed in LAMMPS using lattice parameters and atomic positions extracted from crystallographic data, and a spherical cluster with a certain radius was defined (figure 6.4).

For pure iron clusters, the iron-iron interactions were modelled using the Asadi MEAM potential.[205] For iron-carbon clusters, the MEAM potential reported by Liyanage *et al* was used to describe the iron-iron, iron-carbon and carbon-carbon interactions.[206]

The classical equations of motion were integrated using a timestep of 2.0 fs and the temperature was controlled using the Langevin thermostat. Periodic boundary conditions were employed in the x, y and z directions.

The clusters were initially annealed at the starting temperature for 10 ns before the start of a simulation. Heating and cooling simulations were then carried out at a rate of 16 K/ns and statistical averages were generated. Trajectories were visualized using OVITO.[207]

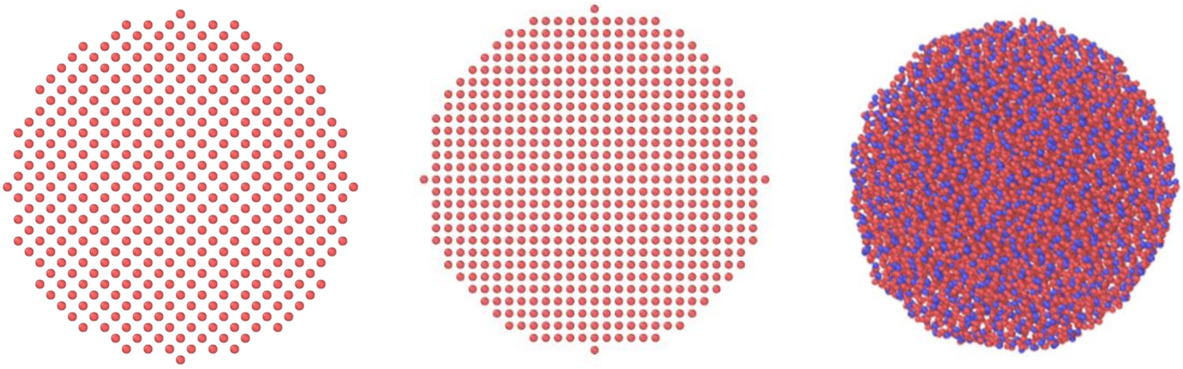

Figure 6.4: a) Body-centred cubic Fe cluster made up of 4285 atoms constructed from crystallographic data, b) face-centred cubic Fe cluster made up of 5775 atoms constructed from crystallographic data and c) Fe_3C cluster made up of 8987 atoms constructed from crystallographic data.

6.3.1.2 Substrate-supported clusters

The same procedure was carried out to construct clusters with a BCC iron, FCC iron or Fe_3C iron carbide structure and the same Asadi and Liyanage potentials were used to describe the interactions within the cluster. A fixed wall substrate was introduced along the z-plane of the simulation box and periodic boundary conditions were only employed in the x and y directions. The cluster-substrate interaction was described using a Lennard-Jones 12-6 potential. The distance of closest approach (σ) in the Lennard-Jones potential was fixed at 2.91 Å as it is the sum of the Van der Waals radii of iron and carbon. The well depth (ε) was varied from 0.05 to 1.0 eV to model the variable strength of interaction between the clusters and the substrate.

The classical equations of motion were also integrated using a timestep of 2.0 fs. The angular momentum of the clusters in the x-y plane was fixed at each step to prevent movement of the cluster along the substrate during the simulation. To reduce computational cost, only the atoms within the nanoparticles were heated in the NVE ensemble using a Langevin thermostat.

The clusters were initially annealed at a fixed distance of 2σ from the substrate at the starting temperature of the simulation for 10 ns. The cluster was then relaxed at the initial temperature for 5 ns to allow it to wet onto the substrate. Heating and cooling procedures were then carried out as with the freestanding clusters.

6.3.2 Characterizing melting

The melting and freezing transitions of the clusters were characterized by plotting caloric curves (i.e. E(T) versus T). The phase transition was identified by a sharp change in energy corresponding to the absorption of latent heat.

Separately, the phase transition temperature was also determined from the heat capacities, C_V, which were calculated from the fluctuations of energy using equation 6.17, where E corresponds to energy, T is the temperature and k_B is the Boltzmann constant.

$$C_V = \frac{< E^2 > - < E >^2}{k_B T^2}$$

(6.17)

The two methods were used to determine the temperature at which melting or freezing occurred and the results were compared. To avoid effects of superheating/supercooling, melting and freezing simulations were run for each cluster at the same heating/cooling rate. For most of the clusters tested, there was some level of hysteresis, where the freezing transition occurs at a lower temperature than the melting transition. This is a common phenomenon due to the fast heating and cooling rates required for molecular dynamics simulations and was accounted for by applying equation 6.18, where T_c^+ = T of melting transition and T_c^- = T of freezing transition, to calculate an equilibrium melting temperature, T_m.[208]

$$T_m = T_{c^+} - \sqrt{T_{c^+}T_{c^-}} + T_{c^-}$$

(6.18)

6.3.2.1 RDF

The radial distribution function (RDF), *g(r),* is a measure of the probability of finding a particle at distance *r* from a particle that is positioned at position *r* = 0 and can be calculated from molecular dynamics trajectories as all of the atomic positions are known quantities. The RDF can be used to assess the structural order with a cluster. Solid, crystalline clusters will likely display defined peaks to a greater distance from position *r* = 0 than molten or amorphous clusters so the RDF can be used to identify structural changes.

In a multi-component system, the total RDF calculated for the cluster can be split into partial RDFs for each pairwise interaction. For example, in a binary system with two atomic species, A and B, the total RDF, *g(r),* is equal to:

$$g(r) = c_A^2 g_{AA}(r) + 2c_A c_B g_{AB}(r) + c_B^2 g_{BB}(r)$$

(6.19)

Where, c_A and c_B denote the concentrations of the two atomic species and $g_{AA}(r)$, $g_{AB}(r)$ and $g_{BB}(r)$ refer to the partial RDFs for the pairwise A-A, A-B and B-B interactions, respectively.

6.3.2.2 Common neighbour analysis

Common neighbour analysis is a method in which atoms in a particular environment, such as FCC, HCP, BCC or icosahedral can be identified.[209, 210] Each pair of atoms within a cluster is assigned a set of three indices, which describes the specific local environment of the pair. In particular, this gives information about the number of neighbours common to both atoms and the number of bonds between these common neighbours. The values of the indices correspond to a particular structure type, so can be used to assign structures to specific atoms. Atoms that do not meet the requirements of the specified structure types are considered to be amorphous.

6.4 Results and discussion

6.4.1 Freestanding BCC iron clusters

Caloric curves and plots of heat capacities for BCC clusters during heating simulations show a clear increase in the temperature of the melting transition with increasing cluster size (figure 6.5a). All of these transitions could be matched to a maximum in the plots of heat capacity (figure 6.6a). Cooling simulations also show clear transitions corresponding to the solidification transition (figures 6.5b and 6.6b). However, there was less correlation between the solidification temperature and the size of the cluster, with solidification occurring in the 1000-1200 K temperature range for all of the clusters. Therefore, the larger clusters generally showed greater hysteresis than the smaller clusters.

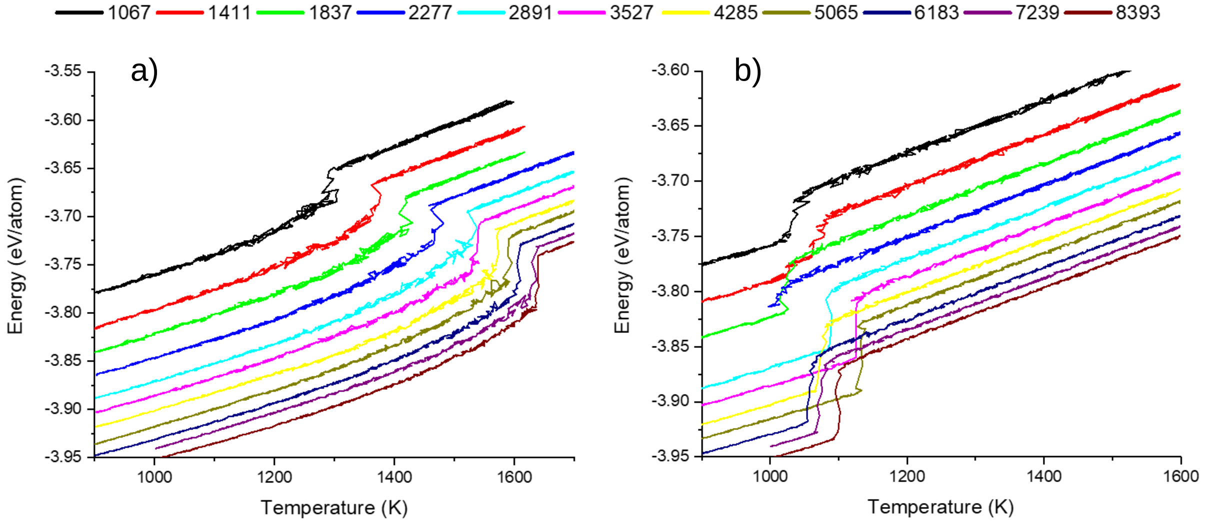

Figure 6.5: Caloric curves calculated from a) heating and b) cooling simulations of BCC clusters of various sizes. The number in the legend indicates the number of atoms in the cluster.

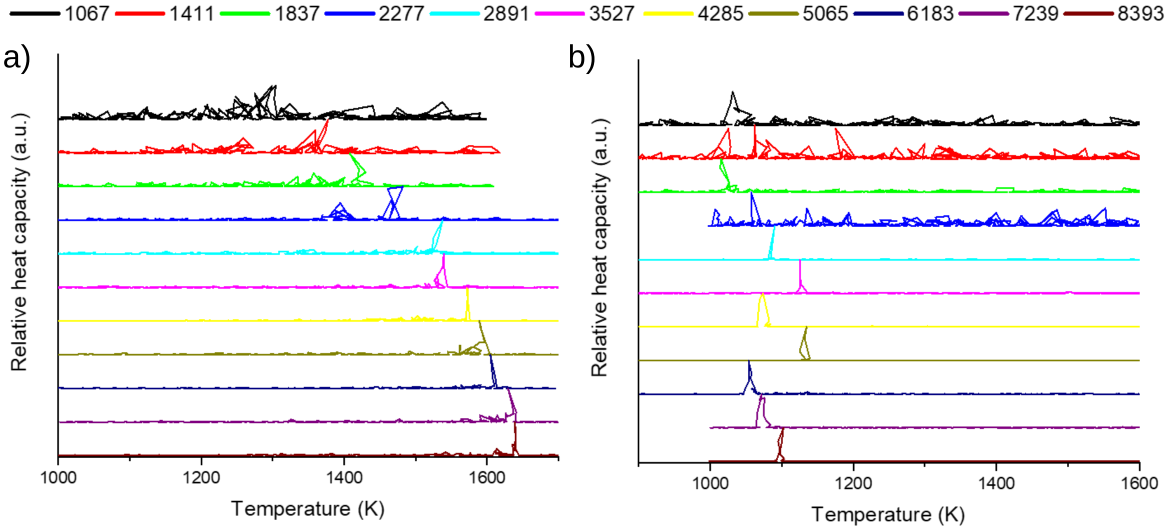

Figure 6.6: Plots of heat capacities calculated from a) heating and b) cooling simulations of BCC Fe clusters of various sizes. The number in the legend indicates the number of the atoms in the cluster.

RDFs were also used to confirm the melting/solidification temperature range of the clusters. Figure 6.7 shows an example of RDFs calculated at temperature intervals of 100 K in heating and cooling simulations of a BCC cluster. The RDFs from the heating simulation show that the cluster loses its structural order past a distance of 10 Å between 1600 and 1700 K, indicating a structural change. For this particular cluster, the melting temperature was found to be 1639 K from caloric curves and plots of the heat capacity, which is consistent with the melting transition. RDFs calculated from the cooling simulations show the biggest change between 1100 and 1000 K. The solidification temperature from caloric curves and heat capacity plots was found to be 1102 K, so the major structural change may be expected to occur between 1100 and 1200 K.

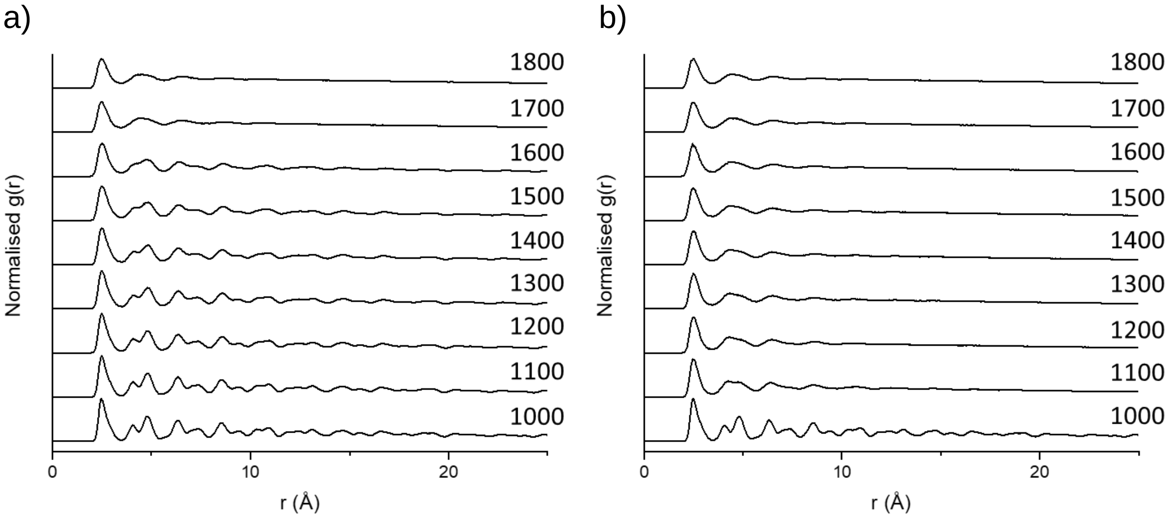

Figure 6.7: Radial distribution functions calculated from a) heating and b) cooling simulations of BCC Fe cluster containing 8393 atoms. Caloric curves and heat capacity plots show melting temperature to be 1639 K and solidification temperature to be 1102 K.

Common neighbour analysis of the atoms in the same cluster during the simulation, mirrored the results of the RDFs. During heating, the cluster gradually lost its structure and became molten, as the number of BCC atoms decreased with increasing temperature until all the atoms in the cluster became amorphous between 1600 and 1700 K (figures 6.8 and 6.10). Common neighbour analysis from the cooling simulation shows that the cluster remained completely amorphous until 1100 K, when a small amount of BCC atoms formed, consistent with the solidification temperature of 1102 K from the caloric and heat capacity data (figures 6.9 and 6.10). As the cluster was cooled to 1000 K, the number of atoms with the BCC structure type increases rapidly, hence a significant change in structure is observed in the RDFs between 1100 and 1000 K.

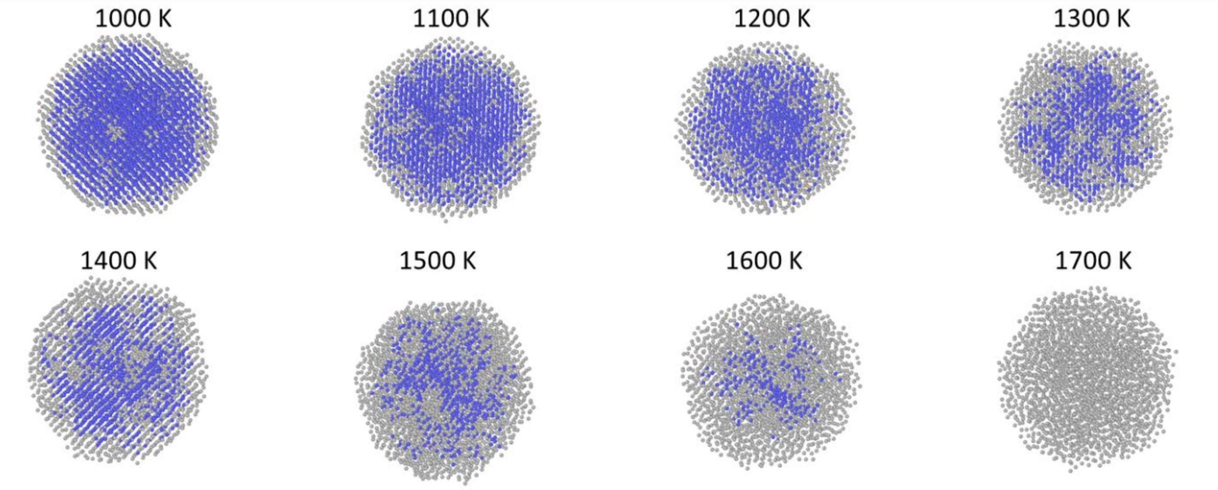

Figure 6.8: Snapshots of common heating simulation of BCC Fe cluster containing 8393 atoms. Amorphous atoms are coloured in grey and BCC atoms in blue.

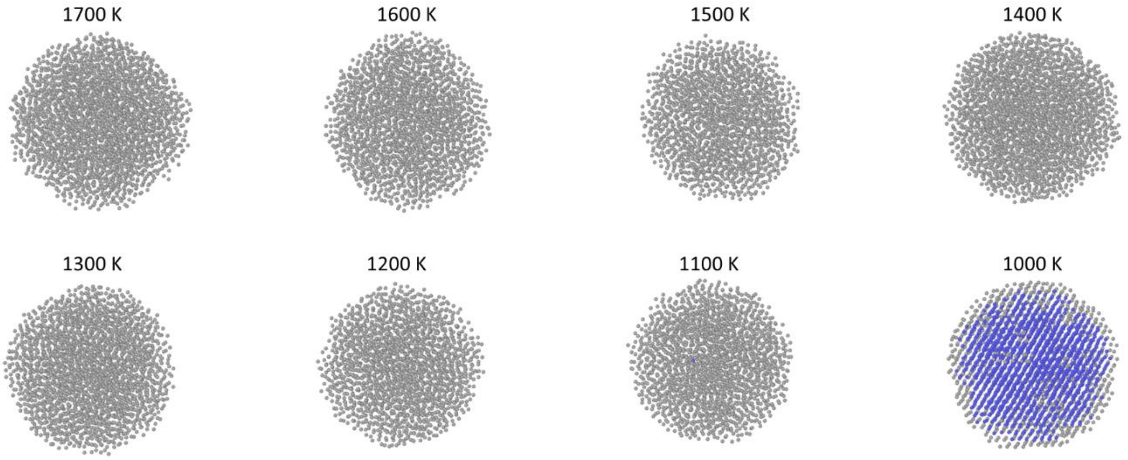

Figure 6.9: Snapshots of cooling simulation of BCC Fe cluster containing 8393 atoms. Amorphous atoms are coloured in grey and BCC atoms in blue.

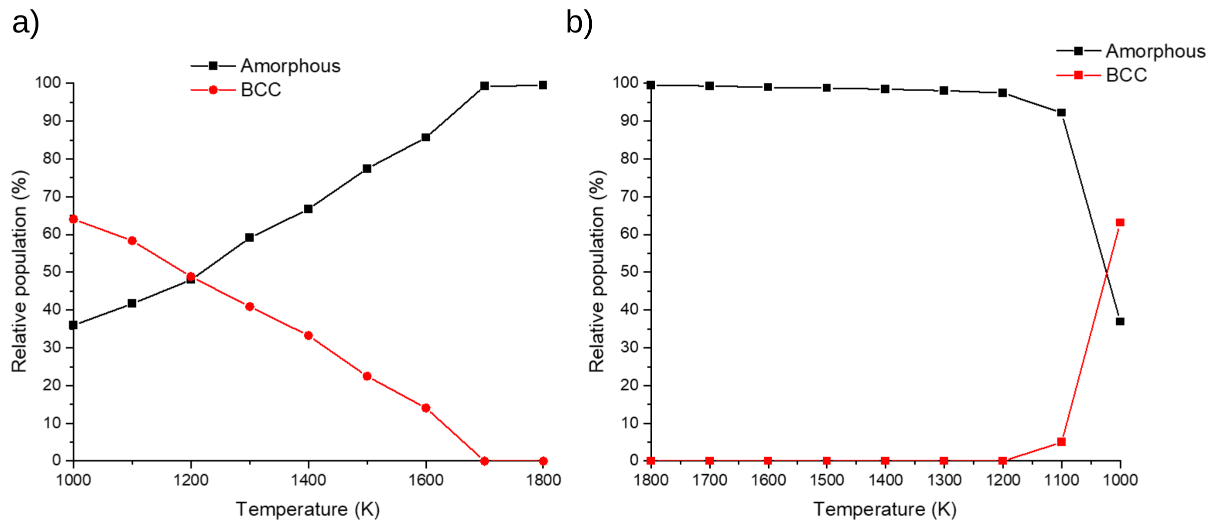

Figure 6.10: Plots of common neighbour analysis calculated from a) heating and b) cooling simulations of BCC Fe cluster containing 8393 atoms.

For each cluster, the equilibrium melting temperature was calculated using equation 6.18 and the resulting data gave reasonable agreement with Pawlow's formula (figure 6.11). From fitting the equilibrium melting temperature data, a bulk melting temperature of 1624 K was extracted. This value is lower than the experimental melting temperature of 1811 K for bulk iron; however, this is not uncommon for EAM potentials and the exact bulk melting temperature can vary significantly between different interatomic potentials. Therefore, the variation in the melting temperatures in this chapter must be interpreted with the bulk melting temperature of 1624 K in mind.

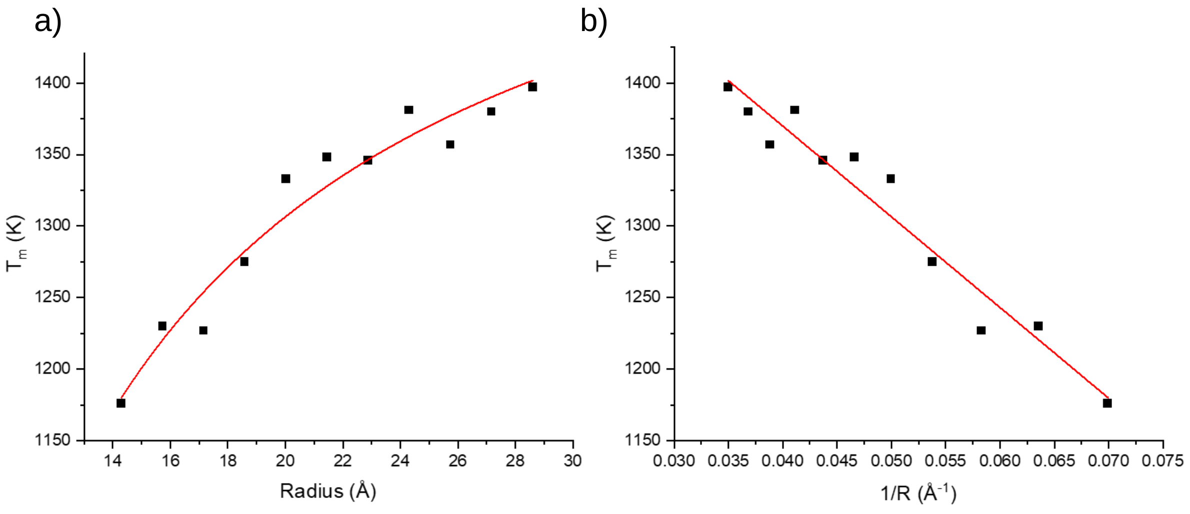

Figure 6.11: Equilibrium melting temperature (T_m) vs a) cluster radius and b) 1/cluster radius for BCC Fe clusters. Data was fitted using Pawlow's formula (equation 6.1))

6.4.2 Freestanding FCC iron clusters

The same procedure was carried out using FCC iron clusters as the initial configuration. During the initial minimisation procedure, the structure of the FCC iron clusters quickly transformed from FCC to BCC at 1100 K, as shown by common neighbour analysis (figures 6.12 and 6.13).

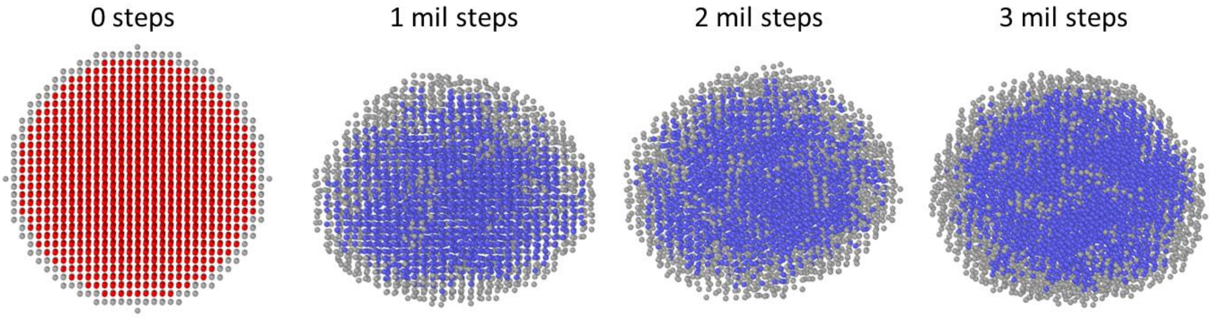

Figure 6.12: Snapshots of cluster consisting of 8589 atoms with initial FCC structure annealed at 900 K. Amorphous atoms are coloured in grey, BCC atoms in blue and FCC

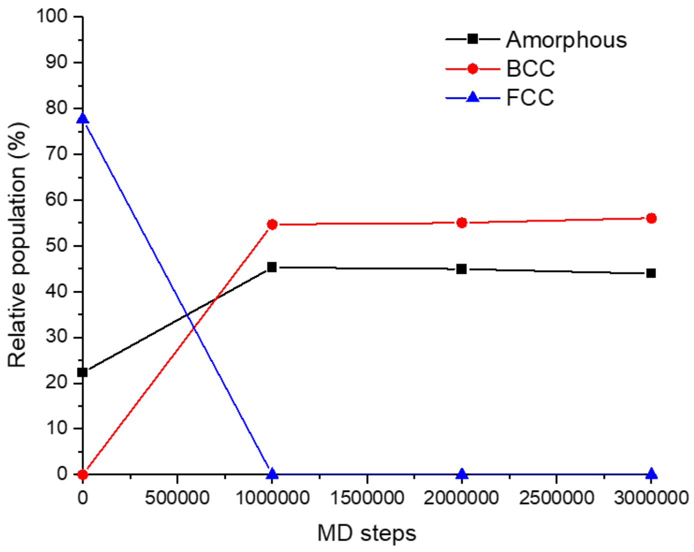

Figure 6.13: Common neighbour analysis of cluster consisting of 8589 atoms with an initial FCC structure and held at 1100 K.

The bulk iron-carbon phase diagram (figure 6.1) suggests that the most favourable structure at 1100 K, or 827 °C, is the BCC structure, so this is not unexpected.[143] However, *in situ* PXRD in the previous chapter showed that the FCC phase formed in some systems at temperatures of approximately 750 °C. Common neighbour analysis performed on heating and cooling simulations of the clusters with an initial FCC structure showed that upon heating, the number of BCC atoms gradually decreased, as with the BCC clusters before undergoing melting (figure 6.14a). Upon cooling, the BCC iron structure reformed, rather than the initial FCC structure (figure 6.14b). Some authors have reported the conversion of BCC from FCC iron clusters before undergoing melting.[211] However, this conversion occurred during the energy minimization step here so was not observed in the heating simulations.

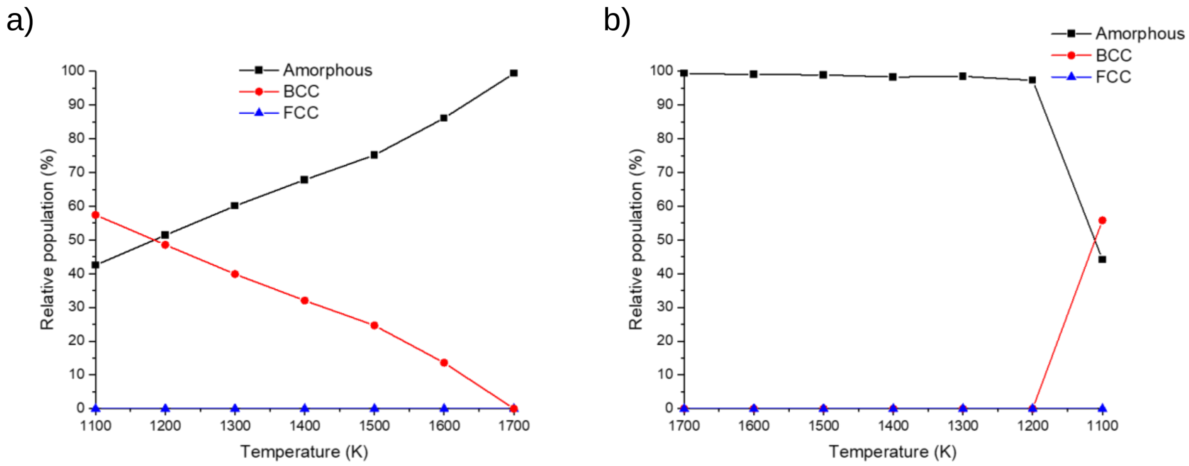

Figure 6.14: Plots of relative populations of atom structure types during a) heating and b) cooling simulations of an iron cluster containing 8589 atoms with an initial FCC structure.

Using the same method as with the BCC iron clusters, equilibrium melting temperatures were calculated from heating and cooling simulations of iron clusters with an initial FCC structure. Fitting the resulting data in figure 6.15 with Pawlow's formula (equation 6.1) yielded a bulk melting temperature of 1638 K, similar to the value of 1624 K calculated from clusters with an initial BCC structure (appendix D – figure 8.19). Therefore, due to the minimization step involved in the simulations, in which the cluster would adopt a BCC arrangement of atoms, the configuration of the input structure had little impact on the melting behaviour of the clusters.

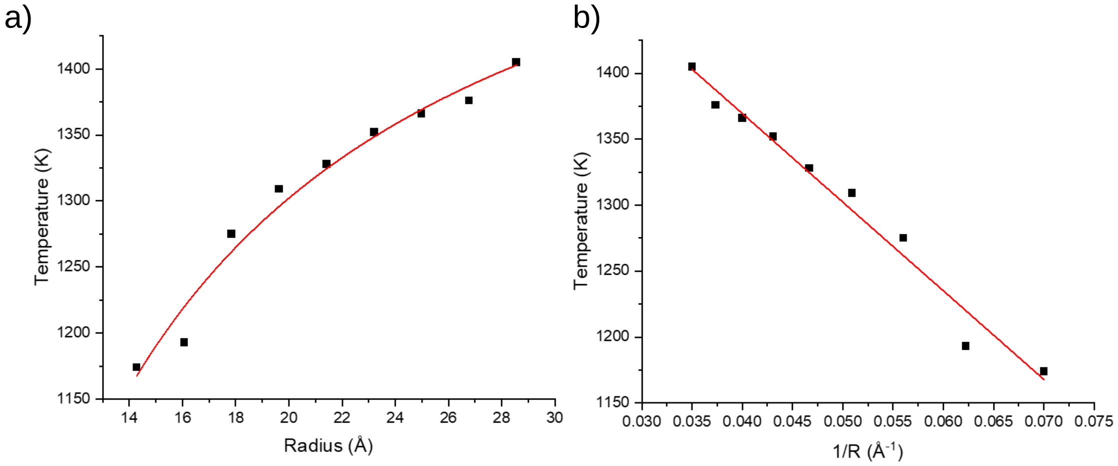

Figure 6.15: Plots of equilibrium melting temperature vs a) cluster radius and b) 1/cluster radius calculated from heating and cooling simulations of iron clusters containing 8589 atoms with an initial FCC structure.

6.4.3 Freestanding Fe_3C clusters

Simulations involving Fe_3C were carried out using the Liyanage potential.[206] Simulations of elemental iron phases were also run using this potential as a test and a similar melting point depression was observed as the previously used Asadi potential.[205] However, a higher bulk melting temperature of 2230 K was observed (appendix D – figure 8.20).

In heating simulations, a clear jump in energy was observed in the caloric curves, corresponding to a melting transition that could be matched to a maximum in heat capacity plots (figure 6.16a and 6.17a). However, the freezing transition in cooling simulations was less well defined. The energy decreased linearly with decreasing temperature without a sudden decrease in energy, making it difficult to assign a specific solidification point (figure 6.16b and 6.17b).

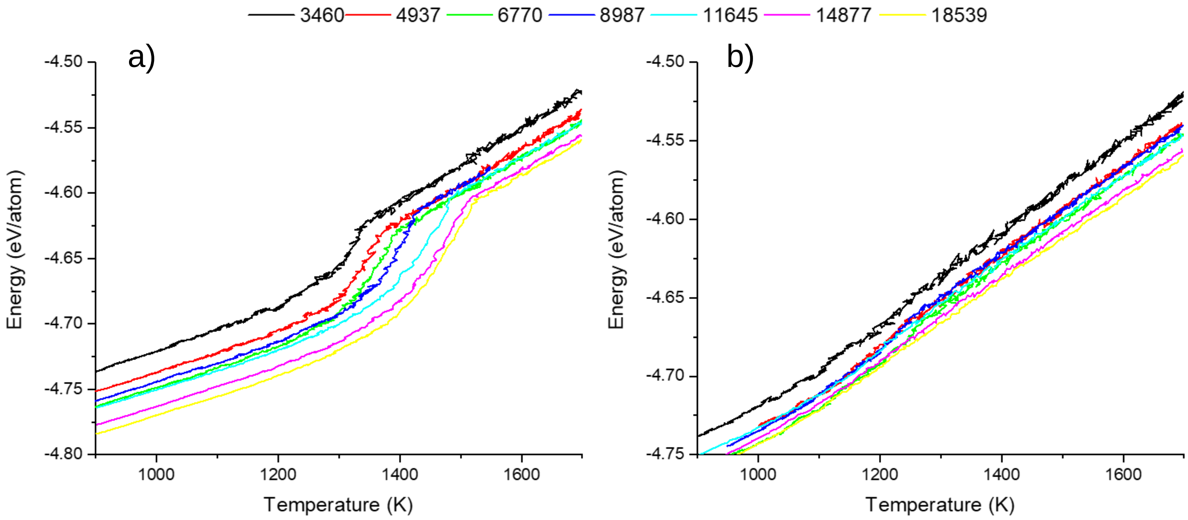

Figure 6.16: Caloric curves for a) heating and b) cooling simulations of Fe_3C clusters of various sizes. The number in legend indicates the number of atoms in the cluster.

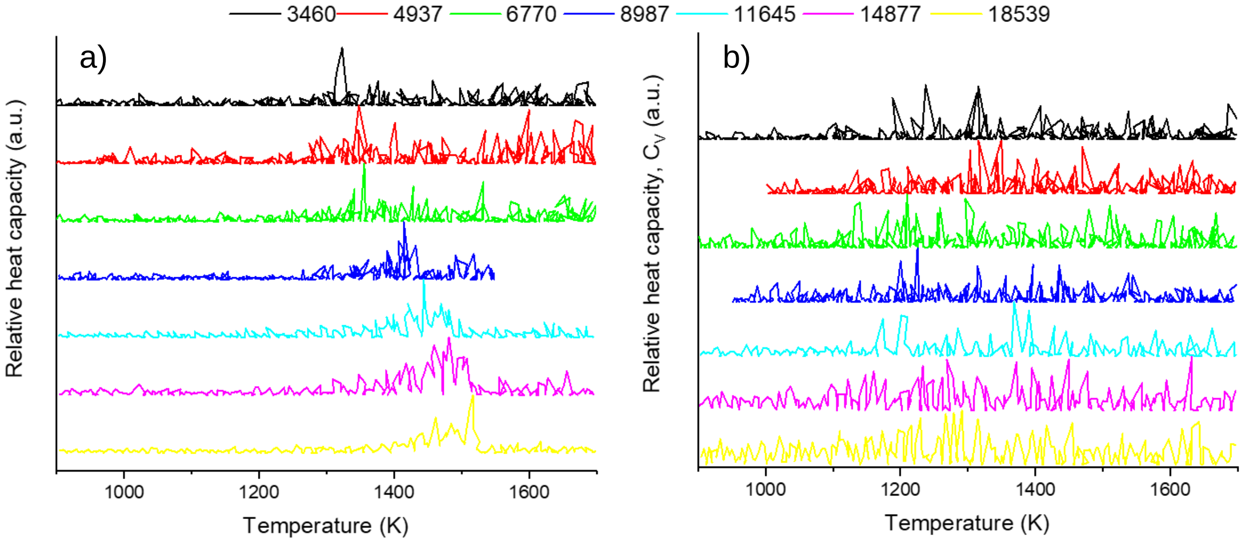

Figure 6.17: Plots of heat capacities calculated from a) heating and b) cooling simulations of Fe_3C cluster of various sizes. The number in the legend indicates the number of atoms in the cluster.

RDFs showed similar results to the caloric curves and plots of heat capacities. RDFs from the heating simulation showed a structural change between 1400 and 1500 K, which could be ascribed to the melting temperature (figure 6.18a). The RDFs calculated from the cooling simulation showed a gradual change in the local structure of the cluster, which did not reform the initial local structure in the heating simulations (figure 6.18b). It was not possible to perform common neighbour analysis as the structure of the atoms could not be assigned to any of the structure types, so all atoms were seemingly 100 % amorphous throughout both the heating and cooling simulations.

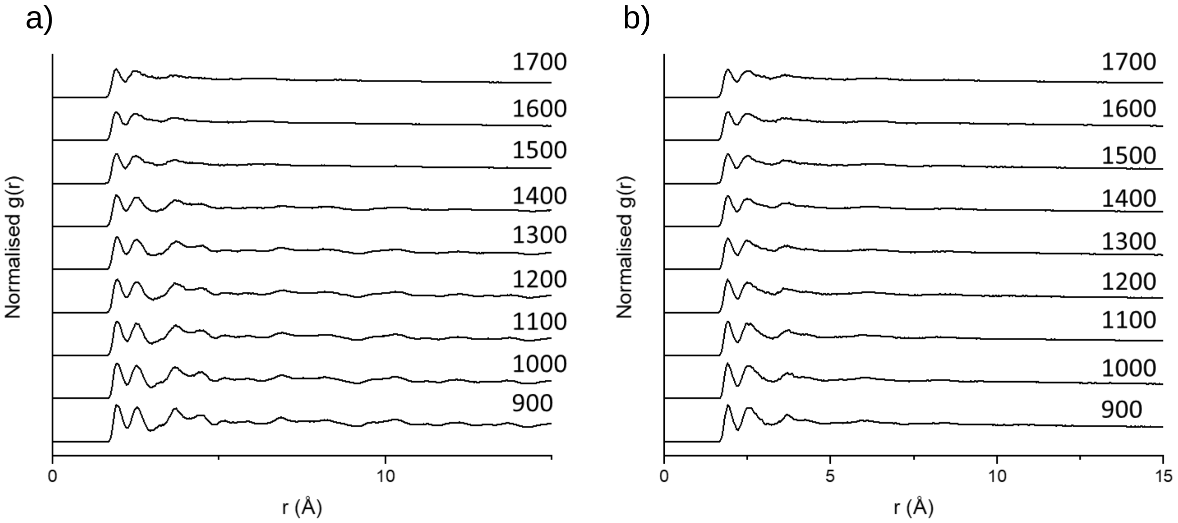

Figure 6.18: Radial distribution functions during a) heating and b) cooling simulations of Fe_3C cluster consisting of 18539 atoms.

The reason why there is no obvious freezing point in the Fe_3C iron carbide simulations may be due to the metastable nature of the phase. Fe_3C has no well-defined melting temperature and experimentally will decompose into BCC iron and carbon after a long period of time at temperatures of approximately 923-973 K. It does, however, have a eutectic point at 1420 K, in which liquid iron, FCC iron and Fe_3C may coexist.[143]

A bulk melting temperature of 1425 K was assigned by Liyanage *et al*, consistent with the eutectic point, as a guide in the simulations.[206] Liyanage *et al* performed a two-phase simulation in which half of the simulation box was filled with solid Fe_3C atoms and the other half was filled with liquid atoms (figure 6.19). The box was held at various temperatures to see which phrase, solid or liquid would become dominant.[206]

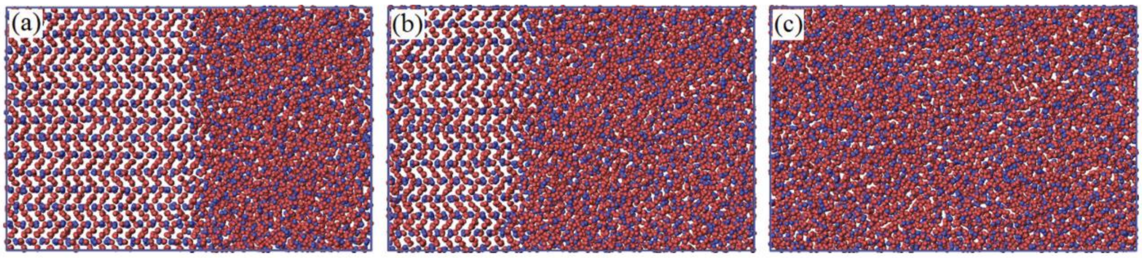

Figure 6.19: Snapshots of the two-phase MD simulation at 1430 K carried out by Liyanage et al. Red spheres are Fe atoms, and blue atoms are C atoms. a) Initial state of the simulation box, which contains both liquid and solid phases of Fe_3C. b) Intermediate state of the simulation box at 20 ns, as the liquid phase propagates to the solid phase. C) Final state of the simulation box at 30 ns, when the entire system has turned into a liquid phase. Figure adapted from ref. 206.

In Liyanage *et al*'s simulations, the half of the box that contained solid Fe_3C iron carbide atoms may have acted as a seed for nucleation at temperatures below the melting temperature. The simulations run in this thesis are analogous to a homogeneous nucleation process, and the nucleation barrier is too great to overcome spontaneously without the presence of a surface to nucleate onto. Alternatively, the rate of nucleation of the Fe_3C phase may be kinetically limited. Considering the extremely short timescales involved in molecular dynamics simulations (in the order of nanoseconds) it may be that the solid Fe_3C phase would form if the cluster was held at a temperature below the melting point for a longer period of time, outside the timescales possible in molecular dynamics.

However, plotting the melting temperatures derived from heating simulations of Fe_3C clusters showed an increase in the melting temperature of the clusters with increasing particle size, as was expected (figure 6.20). Some of the cluster melting temperatures were found to be greater than the bulk melting temperature of 1425 K, determined by Liyanage *et al*.[206] However, if it were possible to observe a freezing transition in the cooling simulations, the equilibrium melting temperature would likely be closer to this value as the possible superheating effects would be eliminated.

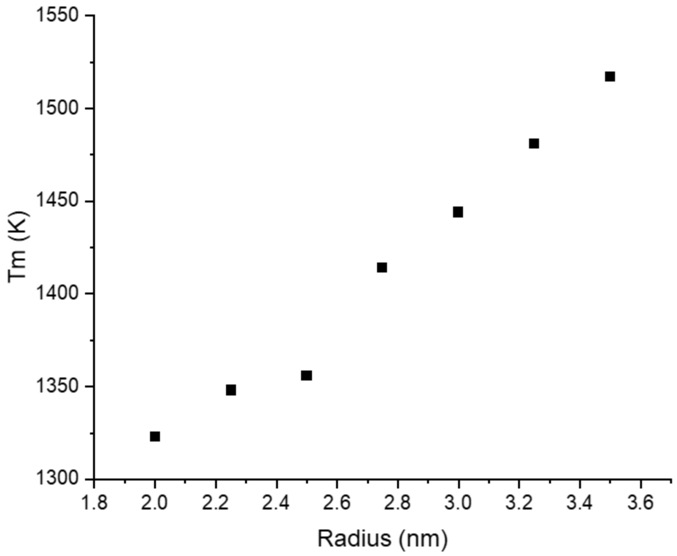

Figure 6.20: Plot of the temperature of the melting transition for Fe_3C clusters of various sizes.

6.4.4 Variable carbon content

According to the dissolution-precipitation mechanism, amorphous carbon is dissolved into the catalyst particle during graphitization and is redeposited as graphitic carbon once the catalyst particle becomes supersaturated. Therefore, in a real-life iron-catalyzed graphitization system, as well as the perfect crystalline iron phases, *α*-Fe, *γ*-Fe and Fe_3C, analogues of these structures with a variable carbon content are likely to be present during graphitization. To examine the effect of carbon content, a series of clusters consisting of the same number of total atoms, but varying carbon contents were constructed, and a similar heating/cooling procedure was performed.

Caloric curves calculated from the heating simulations all showed a clear jump in the energy, which could be matched to a spike in plots of the heat capacities for each of the clusters tested, allowing for a melting transition temperature to be identified (figures 6.21a and 6.22a). Caloric curves calculated from cooling simulations also showed clear transitions that matched a maximum in the heat capacity plots for all clusters, apart from the cluster with a 5.1 wt% carbon content (figures 6.21b and

6.22b). The caloric curve for this cluster showed a steady decrease in energy as the cluster was cooled, rather than a clear step, therefore making it difficult to assign a solidification temperature, or an equilibrium melting temperature.

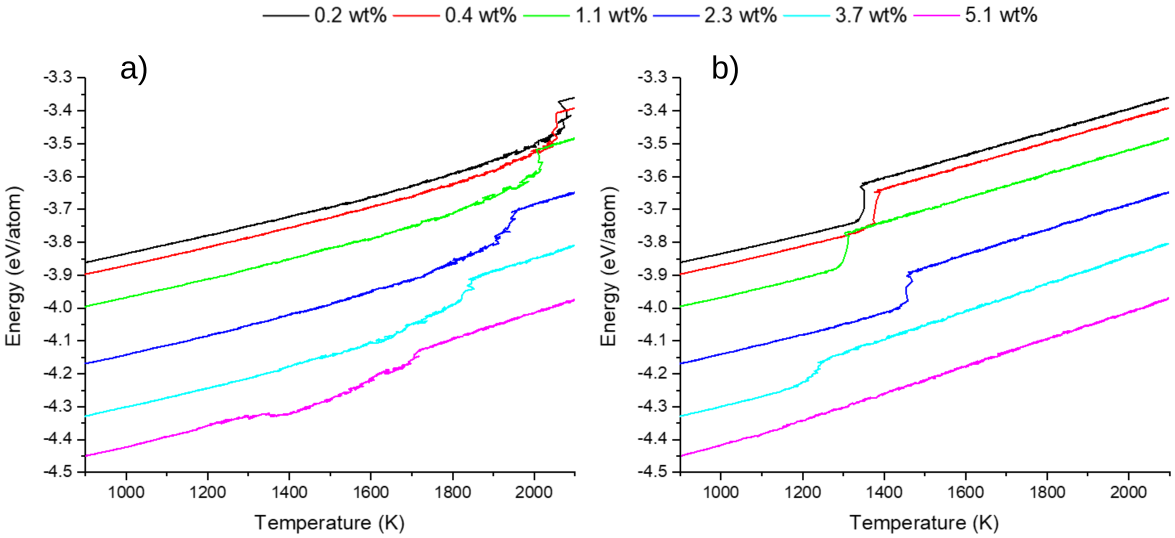

Figure 6.21: Caloric curves calculated from a) heating and b) cooling simulations of clusters containing 3527 atoms with varying carbon content.

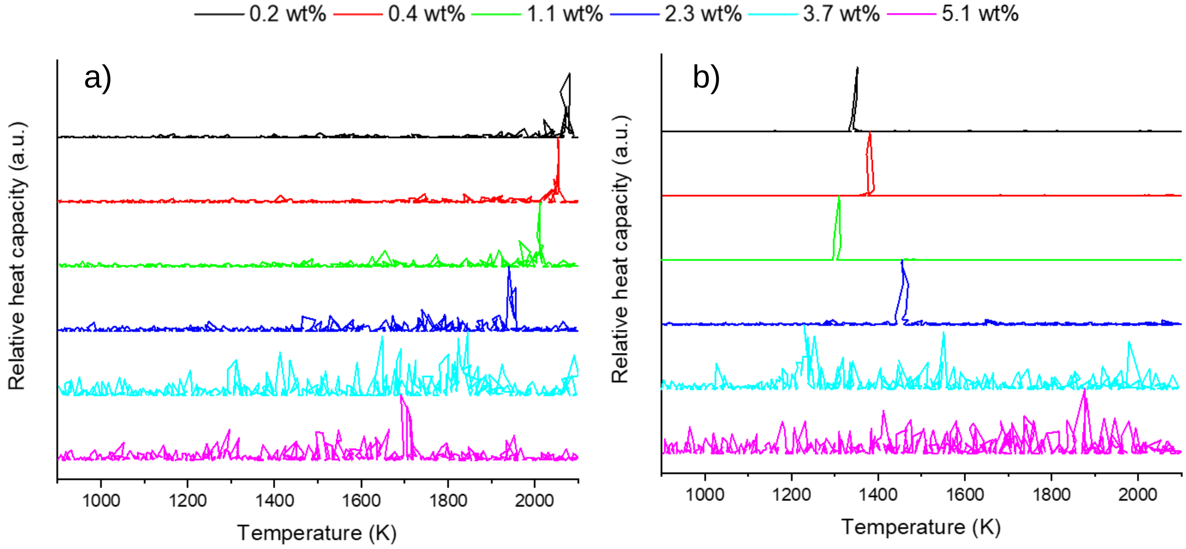

Figure 6.22: Plots of relative heat capacities calculated from a) heating and b) cooling simulations of clusters containing 3527 atoms with varying carbon content.

For all of the clusters tested, common neighbour analysis only showed the presence of either amorphous or BCC structure types. Other structure types such as FCC, HCP and icosahedral were included in the analysis but only amorphous and BCC were identified. As may be expected, the initial proportion of BCC atoms in the cluster decreased as more carbon was introduced into the cluster. For all of the clusters apart from the cluster with a carbon content of 5.1 wt%, the heating simulations showed a gradual decrease in the number of BCC atoms with increasing temperature until no BCC atoms remained (figure 6.23). Also, as with the previous free iron cluster simulations, in the cooling simulations, a sudden increase in the number of BCC atoms was observed as the cluster solidified (figure 6.24).

Unexpectedly, the cluster with 5.1 wt% carbon showed an increase in the number of BCC atoms in the heating simulations from 0 % to approximately 20 % at 1400 K. This structural rearrangement could also be observed in the caloric curve as a slight increase in the energy of the cluster. After this point, the cluster followed the same behaviour as the others, as the number of BCC atoms decreased until it fully melted between 1700 and 1800 K. However, as with the Fe_3C clusters (which have a carbon content of 6.67 wt%), no BCC atoms emerged during the cooling simulation, so it was not possible to assign a specific solidification temperature. Interestingly, the bulk iron-carbon shows a eutectic point at 4.3 wt% carbon at approximately 1400 K (or 1130 °C), the same point at which solidification in cooling simulations was no longer observed.[143] On the iron-carbon phase diagram, at carbon concentrations above 4.3 wt%, the primary iron phase is Fe_3C. Therefore, as with the earlier Fe_3C simulations, the spontaneous nucleation of the Fe_3C phase is not observed within the timescale of the molecular dynamics simulations.

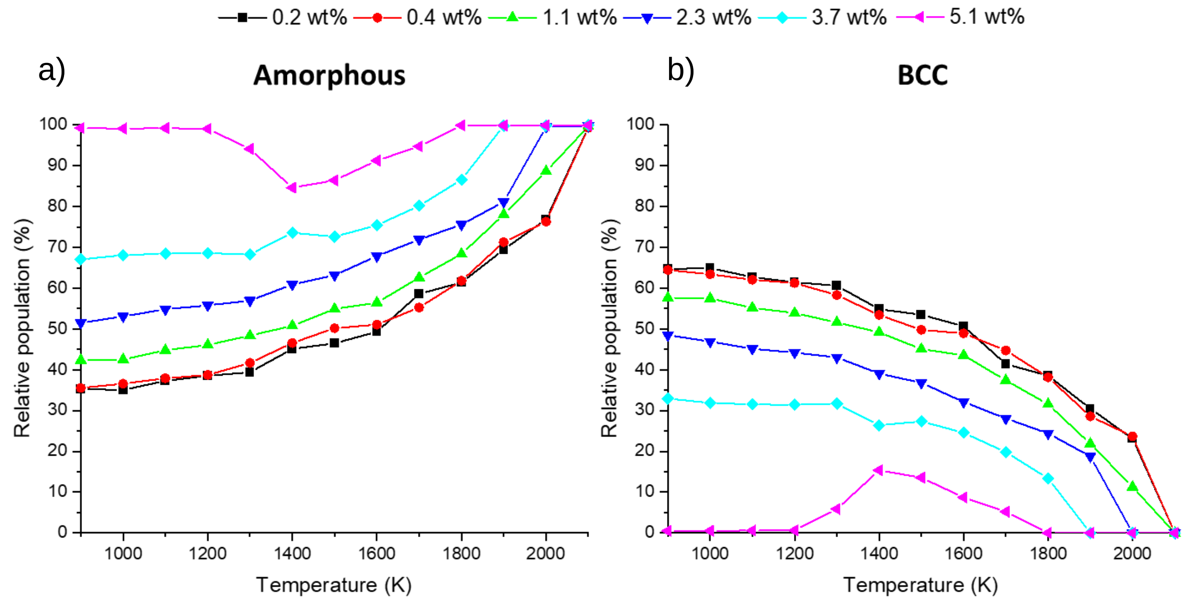

Figure 6.23: Plots of relative population of a) amorphous and b) BCC structure types calculated from common neighbour analysis in heating simulations of clusters containing 3527 atoms with varying carbon content.

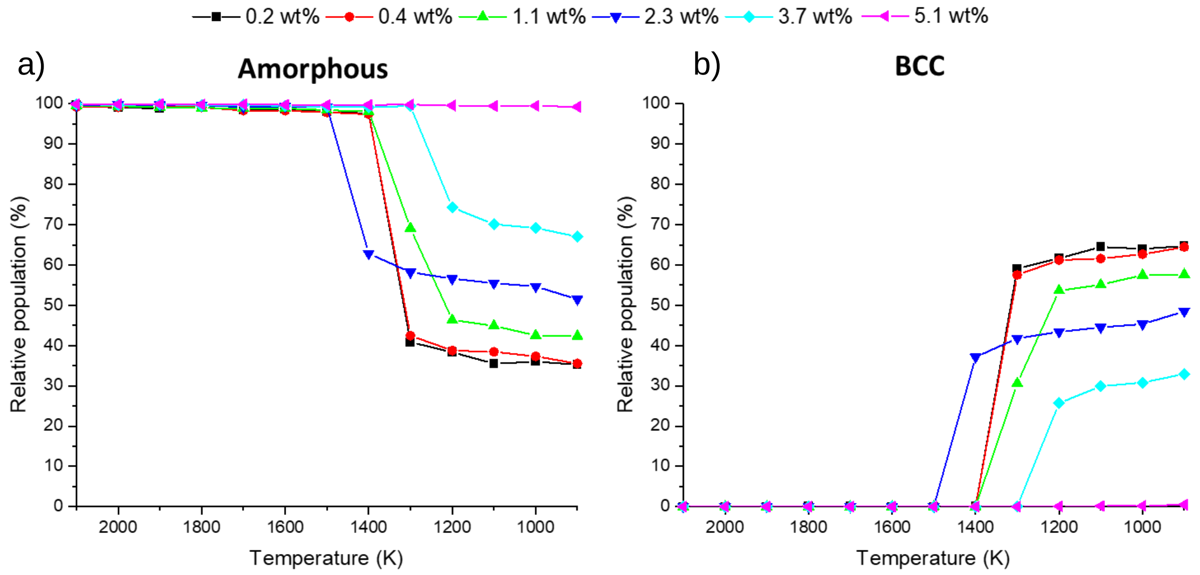

Figure 6.24: Plots of relative population of a) amorphous and b) BCC structure types calculated from common neighbour analysis in cooling simulations of clusters containing 3527 atoms with varying carbon content.

Plots of the resulting data showed that the melting temperature of the clusters decreased with increasing carbon content (figure 6.25). This is an observation that was previously observed by Ding *et* al[212] and Curtarolo *et al*[213] and is consistent with the iron-carbon phase diagram up to the eutectic point at 4.3 wt% carbon.[143]

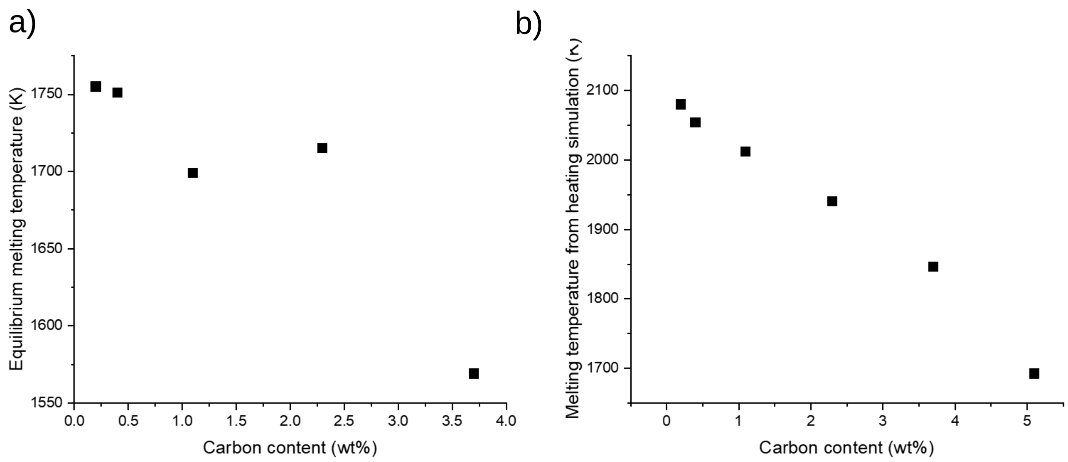

Figure 6.25: Plots of a) equilibrium melting temperature and b) melting temperature calculated from heating simulations of clusters containing 3527 atoms versus carbon content of cluster.

6.4.5 Introduction of substrate

6.4.5.1 BCC iron clusters

In a real-life graphitization system, the iron/iron carbide nanoparticles are not simply in a freestanding state but are surrounded by a large amount of carbon. In the ETEM footage shown in chapter 5, as well as in a previous study of iron-catalyzed graphitization of cellulose filter paper,[79] the catalyst nanoparticles could be seen to interact with the surrounding carbon matrix and "peel" off the carbon, leaving behind a trail of graphitic carbon. The interaction between metal nanoparticles and a substrate has previously been shown to influence the melting behaviour of the nanoparticles.[149,198] Therefore, in an attempt to model this, simulations were carried out in the presence of a fixed substrate to represent the surrounding carbon atoms. Only the iron/iron carbide cluster, not the substrate, was coupled to the thermostat. This is because carbon has a much higher melting temperature than iron, so it was assumed that the surrounding carbon would not undergo melting. Further, only heating the cluster considerably reduced the computational cost. The substrate used in these simulations consisted of a fixed wall with no atomic or structural information and the cluster-substrate interaction strength was modelled with a Lennard-Jones 12-6 potential, where the strength of the cluster-substrate interaction, ε, could be varied.

Figure 6.27 shows that the wetting behaviour of a BCC iron cluster onto the model substrate varied with varying interaction strength. The contact angle of the particle on the substrate was calculated, assuming that the cluster surface was spherical. A greater interaction strength resulted in a lower contact angle, indicating a greater degree of wetting. The contact angle of the particle on the substrate was independent of the size of the particle, in agreement with Young's equation (equation 6.20), which shows that the contact angle, θ_c, is only dependent on the relative surface energies. In equation 6.20, γ_{SV} is the surface energy of the solid-vapour interface, γ_{CS} is surface energy of the cluster-substate interface and γ_{CV} is the surface energy of the cluster-vapour interface.

$$cos\theta_c = \frac{\gamma_{SV} - \gamma_{CS}}{\gamma_{CV}} \tag{6.20}$$

Increasing the interaction strength of the cluster and the substrate decreases the surface energy of the cluster-substrate interface, while the other surface energies remain constant. The contact angle should decrease, and the particle should wet the substrate more strongly.

The effective radius of curvature, R_{eff}, is a parameter that has been described in previous melting studies of supported nanoparticles.[149, 150] The R_{eff} refers to the radius of the sphere extrapolated from the surface of the supported cluster when in the liquid state. The height, h, and width, w, of the supported clusters can be measured during the simulations. For clusters that do not strongly wet the substrate, i.e. where $h \geq w/2$, the R_{eff} is simply equal to $w/2$. However, for clusters that wet the substrate strongly, i.e. where $h < w/2$, the R_{eff} can be calculated using equation 6.21. The contact angle can then be calculated using equation 6.22. The resulting contact angles and effective radius of curvature values are displayed in figures 6.27a and b respectively.

$$R_{eff} = h(1 + \left(\frac{w}{2}\right)^2 (h)^{-2}/2 \tag{6.21}$$

$$\theta_c = cos^{-1}(1 - \frac{h}{R_{eff}}) \tag{6.22}$$

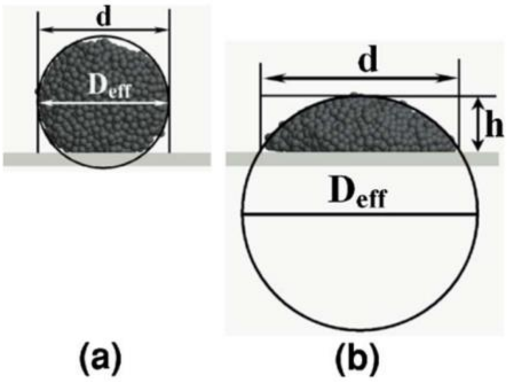

Figure 6.26: Illustration of the effective diameter, D_{eff}, obtained from the cluster curvature for weak (a) and strong (b) substrate adhesions. Figure adapted with permission from reference 149.

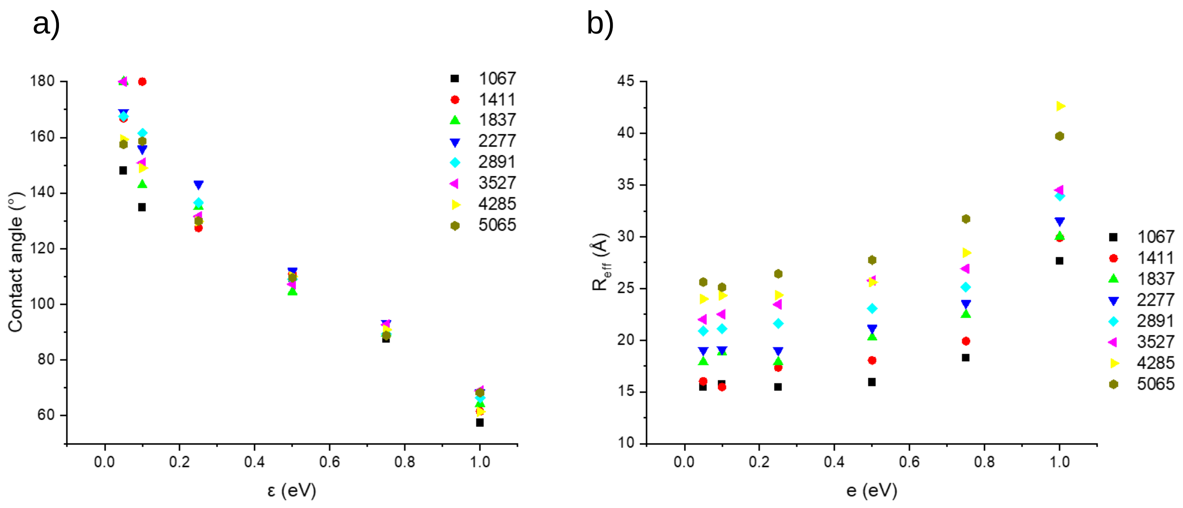

Figure 6.27: Plots of a) contact angles and b) effective radius of curvature vs the cluster-substrate interaction strength for BCC Fe clusters of various sizes. Number in legend indicates the number of atoms in the cluster.

As with the free clusters, heating and cooling simulations were run to extract equilibrium melting temperatures. As an example, figures 6.28 and 6.29 show the results of heating and cooling simulations of BCC iron clusters consisting of 5065 atoms and varying interaction strengths.

Caloric curves (figure 6.28) and plots of the heat capacities (figure 6.29) showed that the temperature of the melting/freezing transition generally increased with increasing interaction strength in both the heating and cooling simulations. The amount of hysteresis was reduced with increasing interaction strength, likely due to the presence of fewer surface atoms in the clusters with a greater cluster-substrate interaction strength. The atoms close to the substrate were somewhat fixed; therefore, the freezing transition was more favourable and occurred earlier and at a higher temperature in the simulation.

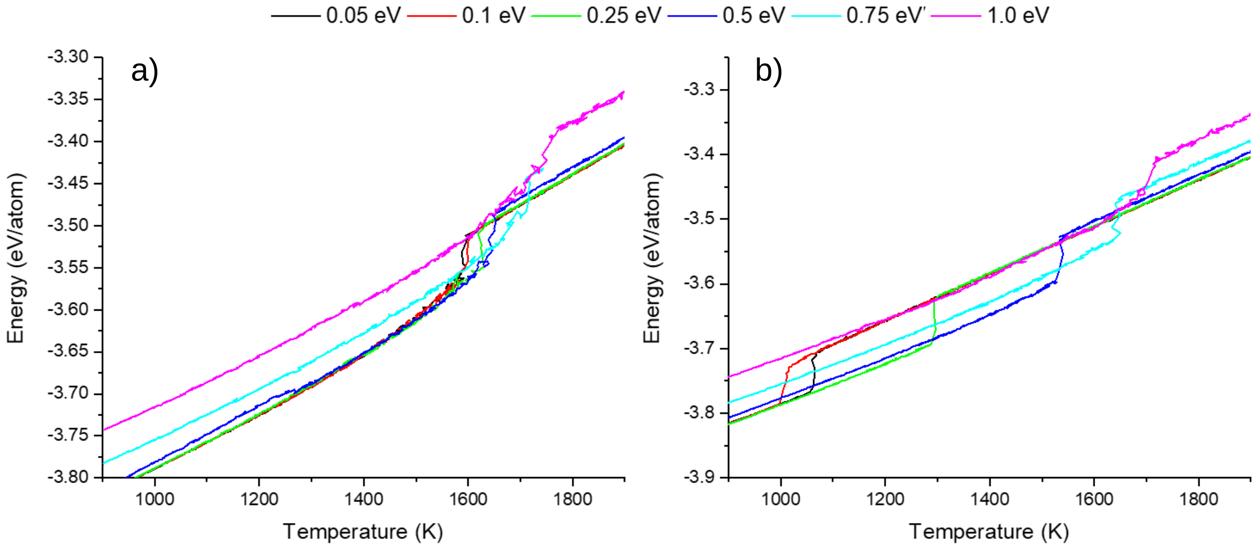

Figure 6.28: Caloric curves calculated from a) heating and b) cooling simulations of BCC Fe clusters consisting of 5065 atoms supported on a fixed wall substrate. Value in legend indicates cluster-substrate interaction strength.

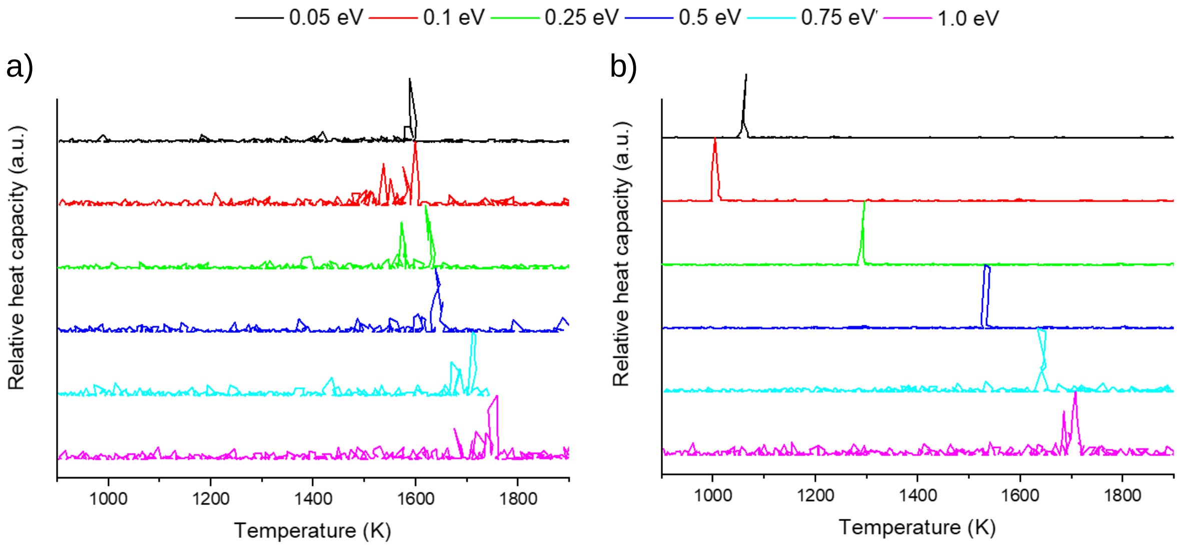

Figure 6.29: Plots of heat capacities versus temperature calculated from a) heating and b) cooling simulations of BCC Fe clusters consisting of 5065 atoms supported on a fixed wall substrate. Value in legend indicates cluster-substrate interaction strength.

Common neighbour analysis calculated from a heating simulation of a cluster with a cluster-substrate interaction strength of 0.05 eV showed the gradual reduction in the number of atoms with a BCC structure type, until 100 % atoms reached an amorphous state by 1600 K (figures 6.30 and 6.32a). As observed previously with the free nanoparticles, the atoms remained in an amorphous state during the cooling simulation until a sharp increase in the number of BCC atoms at the solidification point (figures 6.31 and 6.32b).

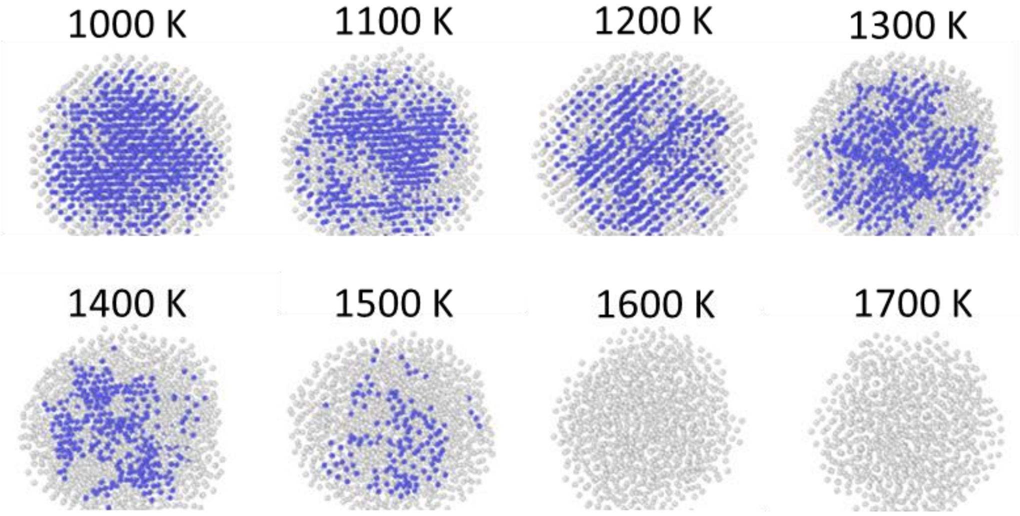

Figure 6.30: Snapshots of heating simulation of BCC Fe cluster consisting of 5065 atoms supported on a fixed wall substrate with an interaction strength of 0.05 eV. Amorphous atoms are coloured in grey, BCC atoms in blue.

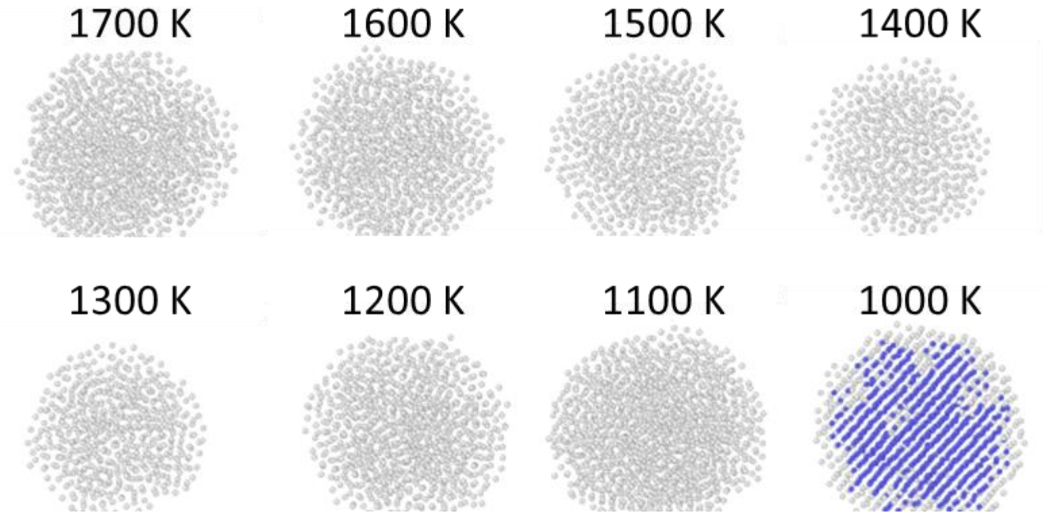

Figure 6.31: Snapshots of cooling simulation of BCC Fe cluster consisting of 5065 atoms supported on a fixed wall substrate with an interaction strength of 0.05 eV. Amorphous atoms are coloured in grey, BCC atoms in blue.

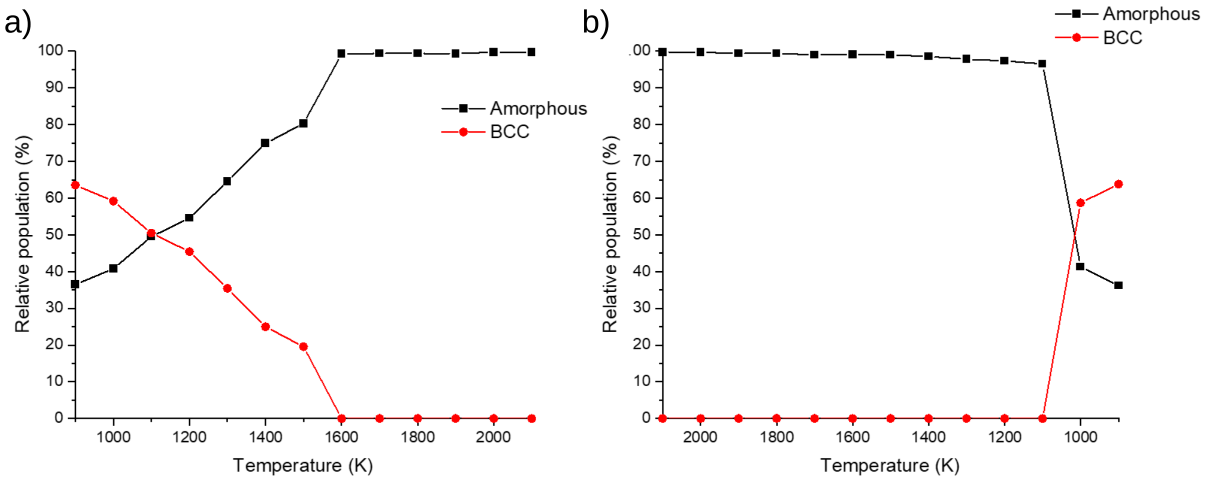

Figure 6.32: Plots of relative populations of structure types calculated by common neighbour analysis from a) heating and b) cooling simulations of BCC Fe clusters consisting of 5065 atoms supported on a fixed wall substrate with an interaction strength of 0.05 eV.

Common neighbour analysis of a cluster with a cluster-substrate interaction strength of 1.0 eV again showed consistent behaviour with the caloric curves and plots of heat capacities. As with the 0.05 eV cluster, in the heating simulation, the number of BCC atoms gradually decreased with increasing temperature until all of the atoms became amorphous between 1700 and 1800 K (figures 6.33 and 6.35a). During the cooling simulation, the increase in the number of BCC atoms occurred more gradually and at a higher temperature than the cluster with a cluster-substrate interaction strength of 0.05 eV, with the atoms closest to the substrate generally nucleating first. The BCC structure then gradually grew outwards until the majority of the atoms in the cluster displayed the BCC structure (figures 6.34 and 6.35b).

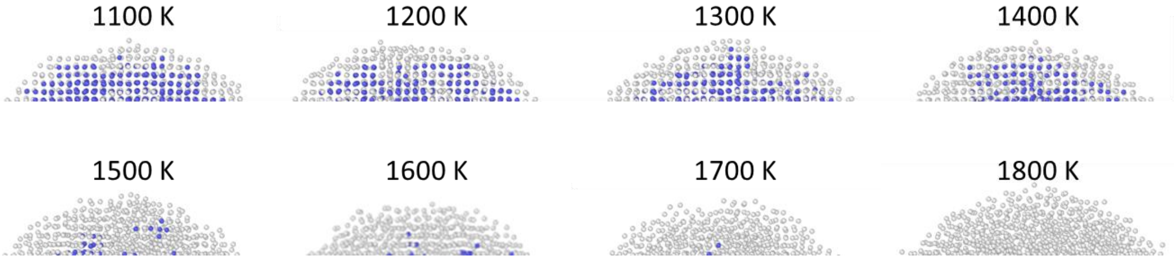

Figure 6.33: Snapshots of heating simulation of BCC Fe cluster consisting of 5065 atoms with a cluster-substrate interaction strength of 1.0 eV. Amorphous atoms are coloured in grey, BCC atoms in blue.

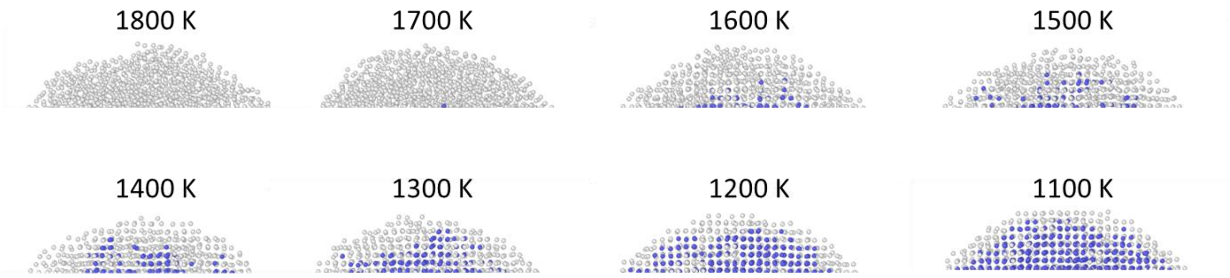

Figure 6.34: Snapshots of cooling simulation of BCC Fe cluster consisting of 5065 atoms with a cluster-substrate interaction strength of 1.0 eV. Amorphous atoms are coloured in grey, BCC atoms in blue.

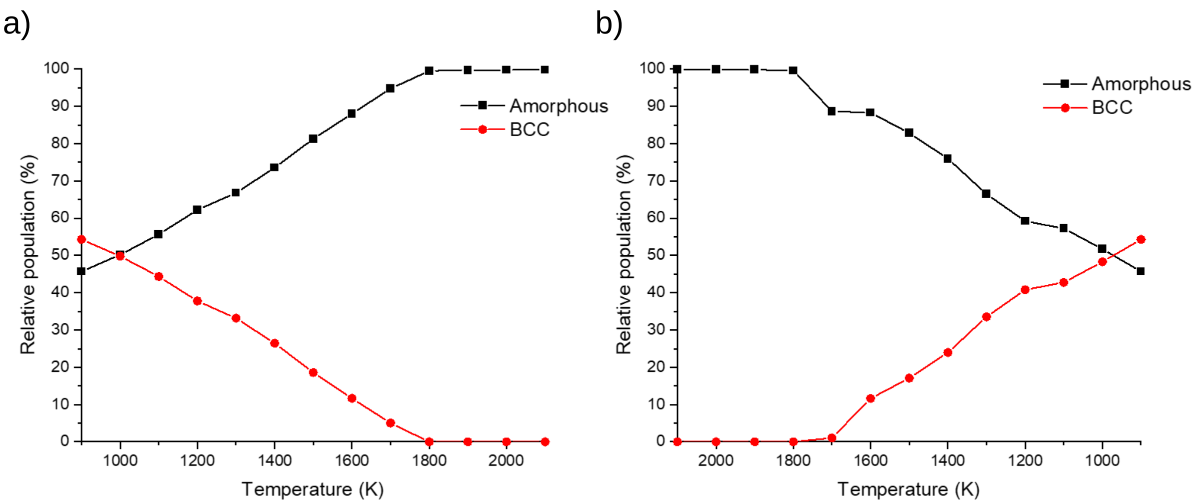

Figure 6.35: Common neighbour analysis calculated from a) heating and b) cooling simulation of BCC Fe cluster consisting of 5065 atoms supported on a fixed wall substrate with a cluster-substrate interaction strength of 1.0 eV.

The results derived from heating and cooling simulations of a range of cluster sizes showed that the equilibrium melting temperature increased with increasing cluster-substrate interaction strength, as with previous results of supported Fe clusters (figure 6.36). The equilibrium melting temperature also shows a Pawlow-like relationship with R_{eff} (figure 6.37).

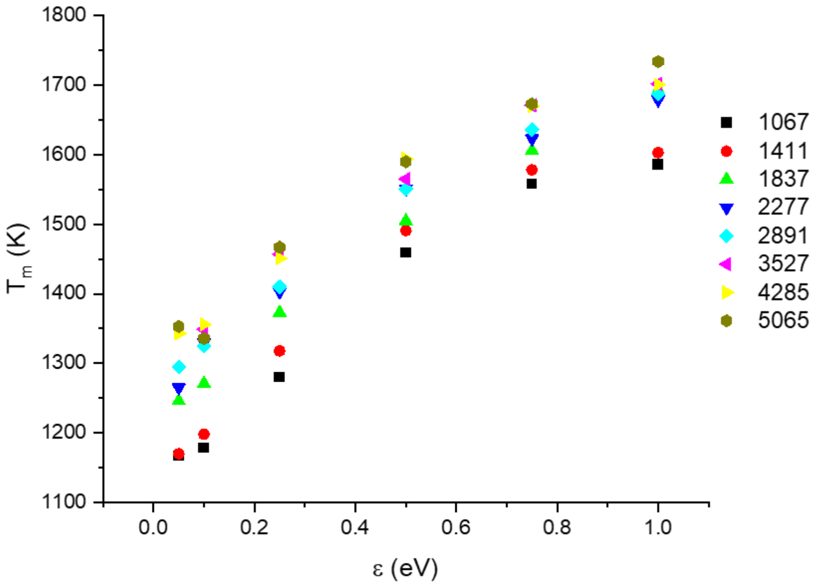

Figure 6.36: Plot of equilibrium melting temperature vs cluster-substrate interaction strength for BCC Fe clusters of various sizes.

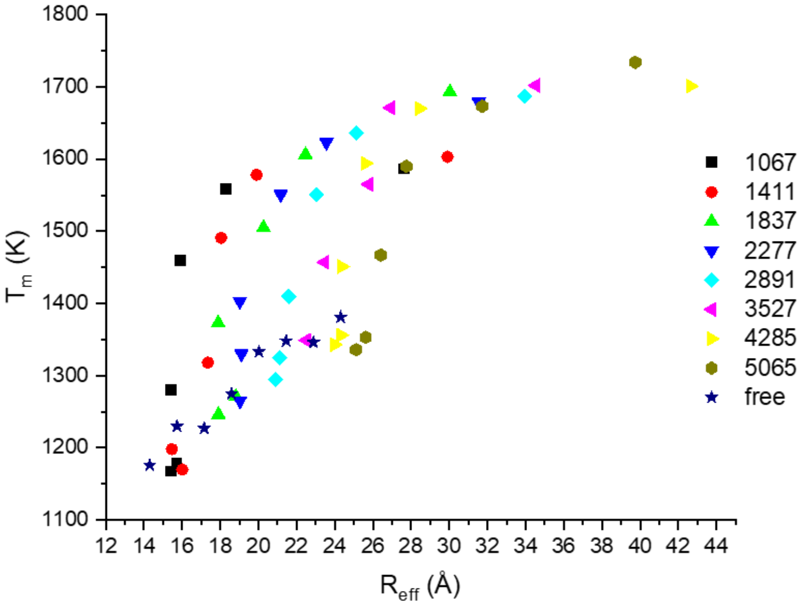

Figure 6.37: Plot of equilibrium melting temperature vs effective radius of curvature (R_{eff}) for Fe clusters with an initial BCC structure of various sizes.

In a similar study by Shibuta *et al*, albeit using a Finnis-Sinclair potential rather than a MEAM potential to model the iron-iron interactions, the melting temperature determined from heating simulations of BCC iron clusters supported on a fixed wall substrate versus the effective radius of curvature gave good agreement with Pawlow's formula.[198] However, the solidification temperature was more sensitive to the cluster-substrate interaction strength.

The work presented in this chapter showed a similar result, as a plot of the melting temperatures from heating simulations vs the effective radius of curvature showed good correlation with Pawlow's formula (figure 6.38a). Compared to the solidification temperatures from cooling simulations vs effective radius of curvature, which showed poor correlation with Pawlow's formula (figure 6.38b) but showed a monotonic increase in solidification temperature with increasing cluster-substrate interaction strength (figure 6.39b). Shibuta *et al* suggested that this behaviour is consistent with classical nucleation theory as a lower contact angle favours faster nucleation.[198] Therefore, solidification is more favourable and less undercooling (or hysteresis) is observed for the stronger cluster-substrate interactions.

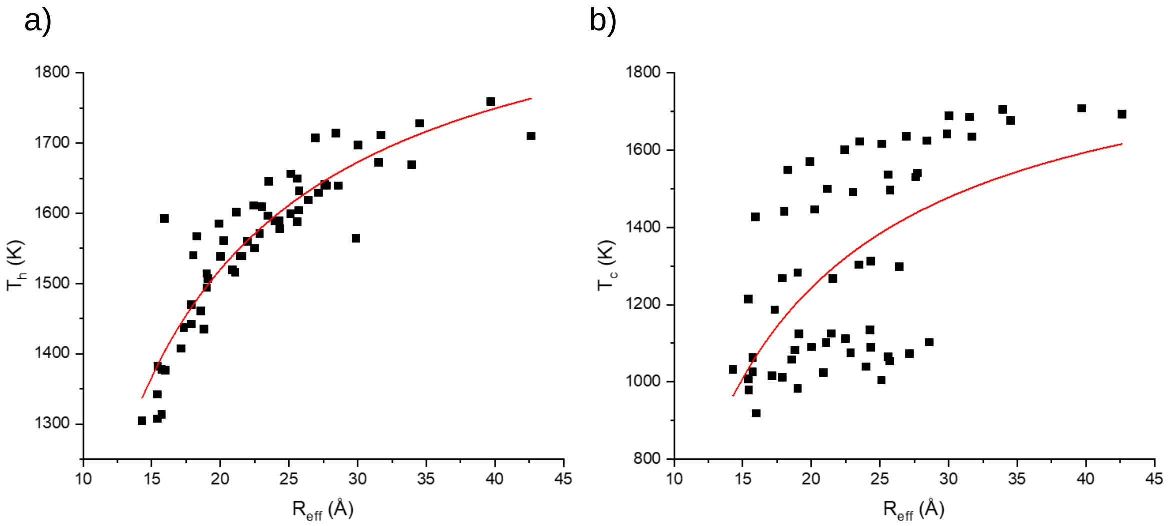

Figure 6.38: Plots of a) melting temperatures and b) solidification temperatures versus effective radius of curvature calculated from heating and cooling simulations respectively of Fe clusters with an initial BCC structure. Data fitted using Pawlow's formula.

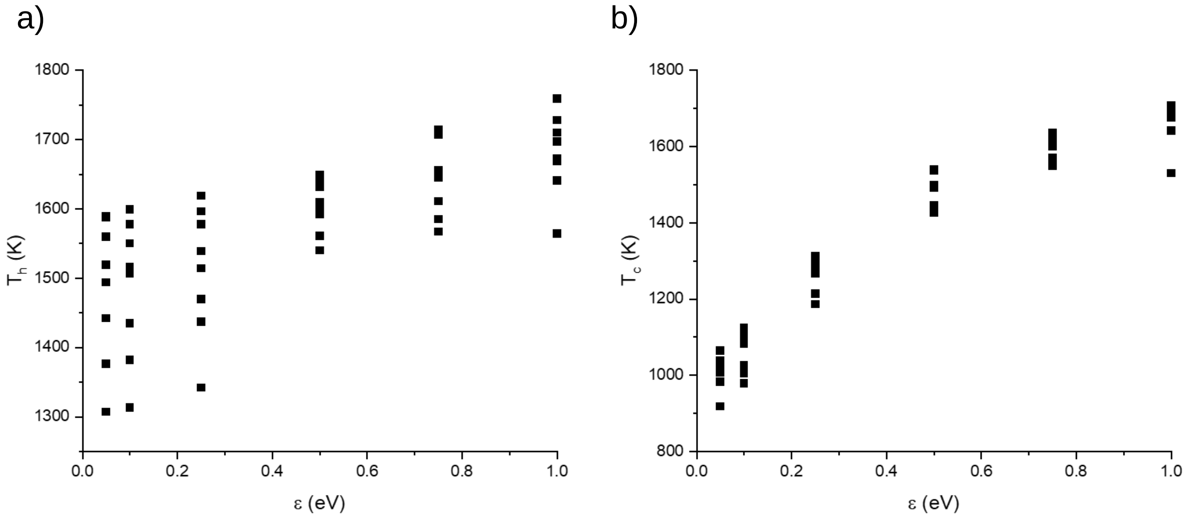

Figure 6.39: Plots of a) melting temperatures and b) solidification temperatures versus cluster-substrate interaction strength calculated from heating and cooling simulations respectively of Fe clusters with an initial BCC structure.

6.4.5.2 Fe_3C clusters

The same procedure was carried out with Fe_3C using the same Liyanage potential used for the freestanding nanoparticles to describe the cluster interactions and a Lennard-Jones 12-6 potential to describe the cluster-substrate interactions.[206] As with BCC iron clusters, increasing the cluster-substrate interaction strength increased the wetting of the Fe_3C clusters onto the substrate, resulting in a decrease in the contact angle and an increase in the effective radius of curvature (figure 6.40).

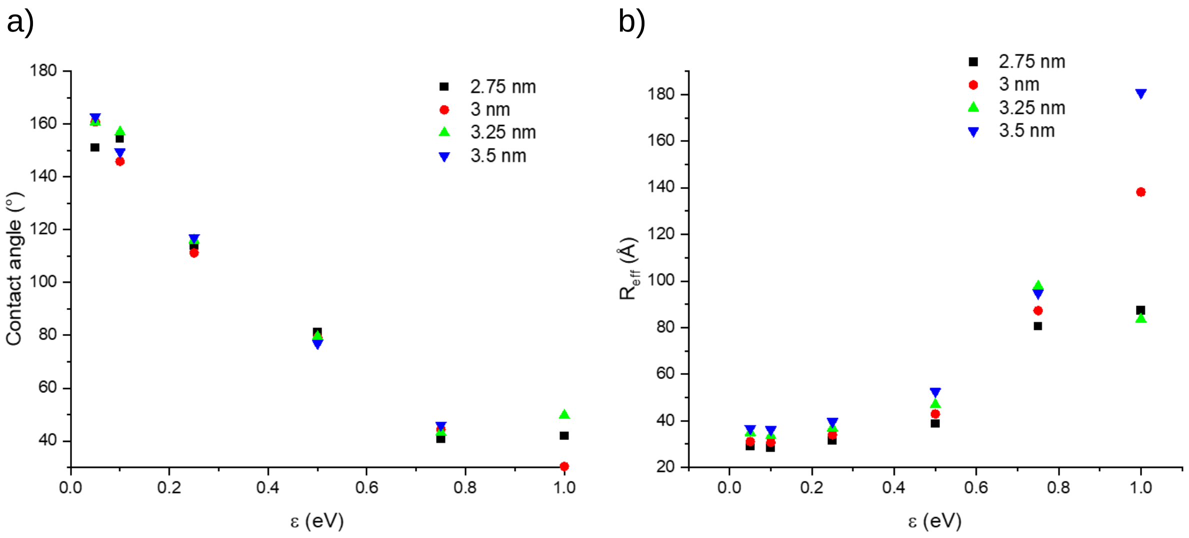

Figure 6.40: Plots of a) contact angle and b) effective radius of curvature versus cluster-substrate interaction strength for a range of Fe_3C clusters of various sizes.

As it was impossible to assign a solidification temperature in the cooling simulations of freestanding Fe_3C clusters, only heating simulations of supported Fe_3C clusters were considered here. Sharp increases in energy in caloric curves (figure 6.41a) could be matched to a spike in the heat capacity (figure 6.41b) for all of the clusters, so it was possible for a melting temperature was assigned.

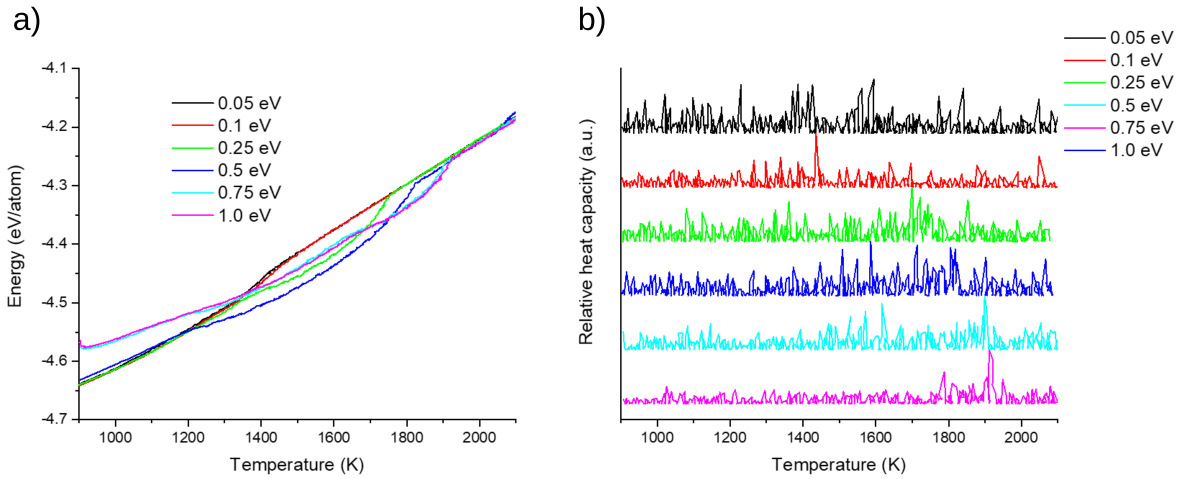

Figure 6.41: a) Caloric curves and b) plots of heat capacities calculated from heating simulations of Fe_3C clusters consisting of 14877 atoms supported on a fixed wall substrate with various cluster-substrate interaction strength.

Plots of the resulting melting temperatures for a range of cluster sizes showed that the melting temperature initially increased sharply with increasing cluster-substrate interaction strength (figure 6.42a) and effective radius of curvature (figure 6.42b) then increased more gradually, similar to the trend observed for supported BCC clusters, indicating similar melting behaviour.

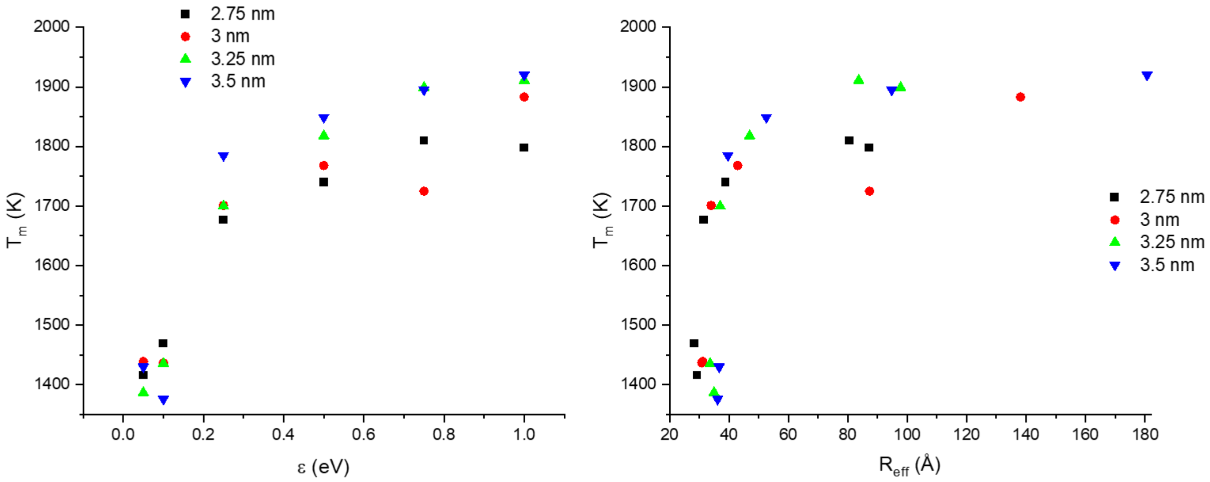

Figure 6.42: Plot of equilibrium melting temperature vs a) cluster-substrate interaction strength and b) effective radius of curvature (R_{eff}) for Fe_3C clusters of various sizes.

6.5 Conclusions

The molecular dynamics simulations performed in this chapter have shown that particle size and cluster-substrate interaction strength have a significant influence on the melting behaviour of Fe_xC_y clusters. For freestanding iron clusters, the equilibrium melting temperature showed good agreement with Pawlow's formula for the melting of spherical nanoparticles.[194] The initial configuration of the iron cluster, i.e. whether the cluster had a BCC or FCC structure, had little bearing on the melting behaviour of the clusters, as FCC clusters quickly transformed to a BCC structure during the minimization step. This suggests that the BCC structure was the most thermodynamically stable for the Asadi potential used in these simulations.[205] Cooling simulations also always reformed the BCC structure, similar to what may be expected from the bulk iron-carbon phase diagram.[143]

Introducing carbon into the clusters generally decreased the melting temperatures of the clusters, as had been previously observed in studies by Ding *et al*[212] and Curtarolo *et al*[213] and as is consistent with the bulk iron-carbon phase diagram.[143] For carbon contents greater than approximately 4 wt%, it became difficult to assign a solidification temperature as no sharp decrease in the energy was observed in caloric curves, so it was only possible to examine the melting transition in heating simulations. According to the iron-carbon phase diagram, beyond 4.3 wt% carbon, the most stable iron phase is Fe_3C, and perfect Fe_3C clusters also showed similar behaviour.[143]

The iron-carbon phase diagram is complicated, with many possible phases, and few interatomic potential available can be used to describe the melting behaviour of iron-carbon systems so further research is required to fully understand the melting/solidifying behaviour of iron clusters with a relatively high carbon content. However, the reasons as to why the Fe_3C phase did not easily reform are possibly due to the complexity of the unit cell resulting in a significant thermodynamic or kinetic barrier that prevents spontaneous nucleation of the Fe_3C phase within the timescale of the molecular dynamics simulations. Even with this in mind, the results of the simulations in this chapter showed that the melting temperature of Fe_3C clusters decreased with decreasing cluster size, as expected for freestanding spherical nanoparticles.

The introduction of a fixed wall substrate with a cluster-substrate interaction strength described by a Lennard-Jones potential had a strong influence on the melting and solidifying behaviour of the clusters. For BCC iron clusters, the melting transition followed a Pawlow-like trend with the effective radius of curvature, rather than the initial cluster radius, similar to previous reports from Ding *et al*[149] and Shibuta *et al*.[198]

The solidification temperature of the supported clusters was more strongly influenced by the cluster-substrate interaction strength than the effective radius of curvature. The degree of hysteresis between the melting and solidifying transitions decreased with increasing cluster-substrate interaction strength. As Shibuta *et al* had previously reported, this observation was rationalized by the theory of heterogeneous nucleation, as solidification of the atoms close to the substrate was more favourable than for surface atoms.[198] This resulted in a faster rate of nucleation in the clusters with a greater cluster-substrate interaction strength, so a solid cluster was formed earlier in the cooling simulation and at a higher temperature.

Importantly, similar trends were observed in heating simulations of supported Fe_3C clusters as the melting temperature generally increased with increasing cluster-substrate interaction strength as well as increasing effective radius of curvature so the same conclusions could be applied to both pure iron and iron carbide clusters.

In the context of iron-catalyzed graphitization syntheses, graphitization is generally observed to occur at temperatures of approximately 800 °C (or 1073 K), generally catalyzed by nanoparticles with radii of 5-50 nm. The results of these simulations suggest that, on a purely size-based argument, iron, iron carbide or clusters with a carbon content between the two phases are unlikely to be in a liquid state at the reaction temperatures unless they are extremely small.

The introduction of a substrate generally has a stabilising effect on the clusters and increases the melting temperature of both iron and iron carbide clusters with increasing cluster-substrate interaction strength, so the surrounding carbon matrix in iron-catalyzed graphitization systems may result in similar behaviour. Of course, the substrate used in this study had no atomic or structural information, so an amorphous carbon or graphitic carbon substrate may result in different melting behaviour. For example, Schebarchov *et al* showed that favourable epitaxy between nickel nanoparticles and a graphene substrate resulted in a further increase in melting temperature.[150] Unfavourable epitaxy may actually reduce the melting temperature of a cluster; however, this is beyond the scope of this study and may be an interesting avenue to explore in future work. These results, in combination with the presence of crystalline phases that can be observed during graphitization in *in situ* synchrotron PXRD studies in chapter 5, suggest that the solid state is more likely than a fully liquid catalyst particle during graphitization.

Table 6.1: Summary of key findings in chapter 6.

Key Finding	Evidenced by:
Melting temperature of freestanding iron and iron carbide nanoparticles increases with particle size	• Temperature of phase transitions in caloric curves • Temperature of the maxima in plots of heat capacity • Increase in the temperature at which the particle loses long range structure, shown by radial distribution functions • Increase in the temperature at which all atoms become amorphous in common neighbour analysis
Introducing carbon into iron particle decreases melting temperature	• Temperature of phase transition in caloric curves • Temperature of the maxima in plots of heat capacities • Decrease in the temperature at which all atoms become amorphous in common neighbour analysis
Iron particles with carbon content greater than 4wt% do not spontaneously re-form upon cooling	• Lack of phase transition in caloric curves from cooling simulations • No clear maximum in plots of heat capacities from cooling simulations • No re-forming of common structure types in common neighbour analysis of cooling simulations
Stronger cluster-substrate interactions increase the melting temperature of cluster	• Temperature of phase transition in caloric curves • Temperature of the maxima in plots of heat capacities • Increase in the temperature at which all atoms become amorphous in common neighbour analysis

Chapter 7 – Concluding remarks

7.1 – Thesis summary

The main aim of this thesis was to provide insight into the mechanistic aspects of the production of nanostructured graphitic carbons *via* iron-catalyzed graphitization so that the route can be developed to produce tailorable carbon nanostructures. To achieve this aim, systematic studies of precursors and reaction conditions were carried out to assess the effect of experimental parameters on the resulting carbon nanostructure. Also, *in situ* experimental and computational studies were performed to provide information on the chemical and physical nature of the catalyst nanoparticle during graphitization.

Chapter 3 presented a study into the effect of precursor structure on porous carbons produced by iron-catalyzed graphitization was presented. Carbons produced from three compositionally similar but structurally different organic precursors – glucose, starch and cellulose – were examined. The choice of organic precursor had a direct effect on the porosity of the resulting carbon material. Glucose- and cellulose-derived carbons were predominantly mesoporous, while starch-derived carbons contained a mixture of micro and mesopores under the same reaction conditions. This difference was ascribed to the constrained growth of the catalyst nanoparticles within the starch-derived carbon system. It was proposed that the catalyst particles must reach a critical size in order to become catalytically active, so the slower growth in the starch-derived system resulted in a slower graphitization step that generated a mixture of graphitic nanostructures and turbostratic carbon. The results highlighted the importance of the physical properties of the organic precursor, and that the starch-derived carbon system offers greater scope for controlling the structural and textural properties of the resulting graphitic carbon material.

Chapter 4 further explored the influence of precursor structure, particularly focusing on organic precursors containing nitrogen functionality, features commonly found in bio-derived materials. Two classes of material were examined: saccharide- and amino acid-based precursors. The results of this chapter showed that the presence of nitrogen within the precursor structure hinders the graphitization process, so a greater amount of iron is required to drive graphitization in nitrogen-containing systems compared to systems containing only carbon, hydrogen and oxygen. The amino acid-based precursors were found to be more resistant to graphitization and SAXS data showed the presence of extremely small iron-based particles in these systems. This offered further evidence to the argument that catalyst nanoparticles must reach a critical size in order to become catalytically active.

In chapter 5, the organic precursors studied in chapter 3 (glucose, starch and cellulose) were investigated *in situ*. The dynamic, liquid-like movement of catalyst nanoparticles to produce tubular graphitic nanostructures was observed in real time using *in situ* ETEM, confirming the fast graphitization step observed *ex situ* in chapter 3. Graphitization was also shown to proceed quickly in cellulose-derived carbons using *in situ* synchrotron PXRD. Importantly, crystalline iron phases were observed at the onset of graphitization, suggesting a large proportion of the nanoparticles were in the solid state. All three systems examined were shown to proceed *via* a slightly different reaction pathway with varying relative concentrations of iron phases, possibly due to the variations in particle size causing the different systems to occupy different locations on the iron-carbon phase diagram. Graphitization was shown to occur faster in systems with a high content of γ-Fe, potentially suggesting that this is the primary catalyst phase. However, the three systems were also shown to contain both γ-Fe and iron carbide. Therefore, an alternative explanation may be that both phases are catalytically active, but that the iron carbide route is a kinetically slower process.

In chapter 6, building on the experimental observations from chapter 5, the physical nature of the catalyst nanoparticle was examined using molecular dynamics. Simulations were performed to extract melting temperatures of freestanding iron and iron carbide as well as nanoparticles with intermediate carbon contents. The melting temperature was shown to decrease with decreasing nanoparticle size, fitting well with Pawlow's theory of melting point depression in spherical nanoparticles.[194] The introduction of carbon into the structure was shown to reduce the melting temperature of the nanoparticle up to approximately 4 wt% carbon, fitting with the bulk iron-carbon phase diagram. At carbon concentrations higher than 4 wt%, precise equilibrium melting temperatures were more difficult to determine as iron carbide becomes the most stable phase, and spontaneous nucleation of iron carbide did not occur within the timescales of the simulations. However, even with this in mind, the results of all the simulations showed that for freestanding nanoparticles, the melting point depression was not significant enough to produce a liquid state at the reaction temperatures in iron-catalyzed graphitization systems purely on a size-based argument.

The introduction of a substrate was also examined to model the effect of the surrounding carbon matrix on the melting behaviour of catalyst nanoparticles. The results of the simulations showed that the melting temperature of both iron and iron carbide nanoparticles increased with increasing cluster-substrate interaction strength. This observation was rationalized by considering that the effective radius of curvature of the substrate-supported nanoparticles has a greater correlation with the melting temperature than the corresponding initial radius of the freestanding nanoparticle.

These results further support the argument that the catalyst nanoparticles are more likely to be in the solid state than the liquid state during graphitization in iron-catalyzed graphitization systems.

7.2 Suggestions for future work

7.2.1 Further investigation of starch-derived carbon system toward assessing application performance

In chapter 3, the starch-derived carbon system was found to have the greatest potential for structural control of the resulting graphitic carbon nanostructure. Building on the observations in this thesis, future work should be directed towards assessing the performance of these materials in real-world applications. For example, the starch-derived carbons containing areas of graphitic ordering along with turbostratic regions may be interesting to explore for application as a sodium-ion battery anode material. Therefore, work should be carried out to explore the influence of properties such as surface area and degree of graphitization on sodium storage behaviour and how experimental conditions may be optimized to enhance performance.

7.2.2 In situ studies of nitrogen-containing precursors

In chapter 4, the presence of nitrogen within the organic precursor was shown to inhibit the graphitization process. To explore this further, it would be useful to perform *in situ* experiments to probe the precise reaction pathway in real time in the different nitrogen-containing systems. It would be particularly interesting to see whether any metastable iron nitride phases are formed, which are not observed *ex situ*. The iron species are likely to be small in size and potentially poorly crystalline so ideally a synchrotron X-ray source would be used for *in situ* PXRD experiments, as in chapter 5.

7.2.3 Development of in situ ETEM experiments

Due to time and equipment constraints, it was only possible to carry out ETEM experiments on the cellulose-derived carbon system. One of the aims of these experiments was to see whether lattice fringes could be identified in the catalyst particles to provide evidence that the catalyst particles were in the solid state. However, the dynamic nature of the cellulose-derived carbon system made the ETEM measurements particularly challenging.

One reason for this is due to the setup inside a TEM. For imaging in TEM, it is necessary to prepare a thin sample so that a large number of electrons are able to pass through it – these are used to construct an image of the sample. However, in practice, it is extremely difficult to prepare a truly two-dimensional sample, so the resulting image is essentially a two-dimensional silhouette image of a three-dimensional sample. Therefore, thicker areas of the sample appear darker than thinner areas as fewer electrons can pass through. For the Brookhaven experiments, it was only possible to visualize the catalyst nanoparticles within the thinner areas of the carbon matrix. As these catalyst nanoparticles were mobile, they would often start in thin areas of carbon but move into thicker areas and become invisible, making it difficult to track the trajectory of the particles. Also, because of the three-dimensional sample, rather than just moving in the x and y dimensions across the sample grid, the particles could also move in the z-direction (i.e., in the direction down the microscope column), therefore moving out of focus as they travelled outside of the focal plane. It was also difficult to predict which of the particles would become mobile and which would remain stationary. *Ex situ* measurements show that not all of the nanoparticles become mobile and produce graphitic nanotubes and the same was observed *in situ*, possibly due to some of the nanoparticles not having reached the critical size needed to become catalytically active. Due to the slower graphitization step observed in the starch-derived carbon system, it may be easier to study the movement of the catalyst nanoparticles, so future work may focus on this system.

To address some of the challenges faced while performing the experiments at Brookhaven, some preliminary work was carried out to construct a model system. Previous *ex situ* and *in situ* PXRD data of saccharide-based carbon systems showed that the reaction pathway of the iron species proceeded *via* magnetite before forming the catalytically active γ-Fe or iron carbide species. There are examples throughout the literature of synthetic routes to produce suspensions of monodisperse magnetite nanoparticles. The issue of polydispersity could thus be addressed by synthesising magnetite nanoparticles of a specific size that can act as the source of iron, rather than using iron nitrate solution. Although the nanoparticles are likely to grow as they are heated and undergo conversion to γ-Fe or iron carbide, the results of chapter 3 of this thesis showed that an important step for allowing control of the catalyst particle size is the nucleation of the iron oxide species. Therefore, if the iron oxide nanoparticles are of a small, uniform size initially, the resulting catalyst nanoparticles may remain a similar size.

As for the source of carbon in the model system, rather than using the same organic precursors as in the previous experiments, a sputtered amorphous carbon film on a standard copper TEM grid was used as the source of carbon. In a previous *in situ* ETEM study on a cellulose-derived carbon system, it was observed that the sputtered carbon coating could be graphitized by the catalyst nanoparticles formed from iron nitrate solution. As the sputtered carbon is extremely thin, particularly compared to the mass of biomass-derived carbon from glucose-, starch- and cellulose-derived carbon systems, the idea was that the graphitization process could only proceed in the x and y directions of the sample grid so should be easier to visualize as particle should not get lost in the thicker regions of the sample. Optical microscopy images showed that the structure of a sputtered carbon-coated copper TEM remained largely intact after pyrolysis to 800 °C under argon (appendix E – figures 8.21 and 8.22).

Magnetite nanoparticles were synthesized in a method used by Sun *et al* (experimental details in appendix E).[214] TEM images of the synthesized magnetite nanoparticles showed a consistent size, with a diameter of approximately 10 nm (figure 7.1).

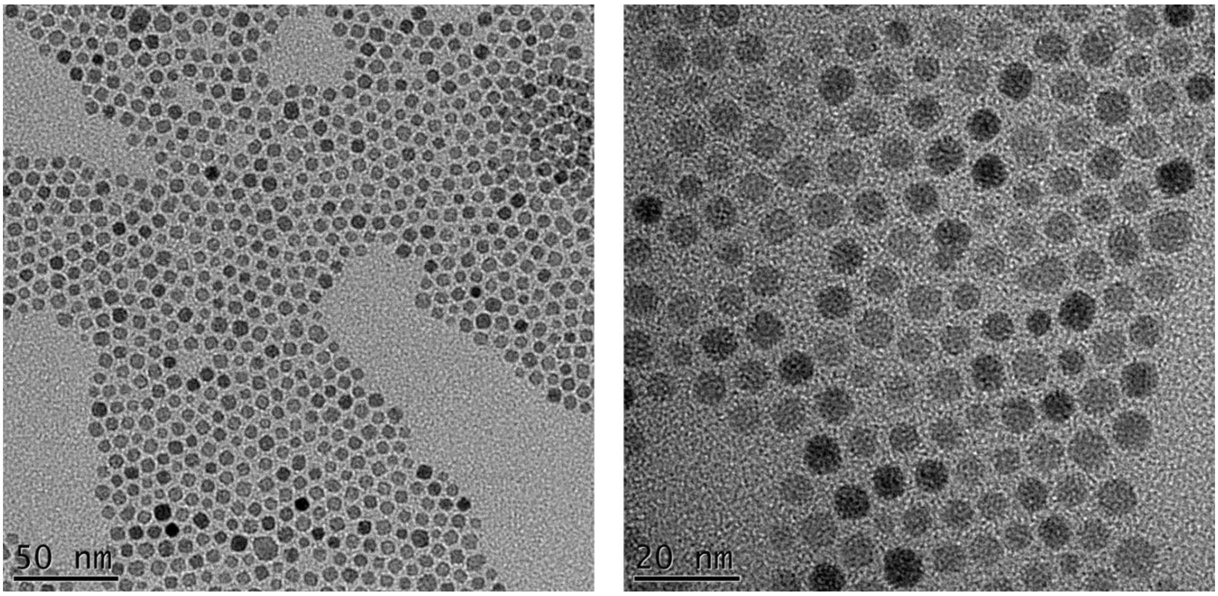

Figure 7.1: TEM images of as synthesised magnetite nanoparticles.

The magnetite nanoparticle suspension was deposited onto amorphous carbon-coated copper TEM grids and subjected to pyrolysis to 800 °C under a flow of argon. TEM images of the grids after pyrolysis showed tracks of what appeared to be graphitic carbon, suggesting that the iron-based nanoparticles catalyzed conversion of the amorphous carbon coating (figure 7.2). Therefore, future *in situ* ETEM experiments should be carried out on the theoretically simpler model system to possibly identify lattice fringes in the catalyst nanoparticles.

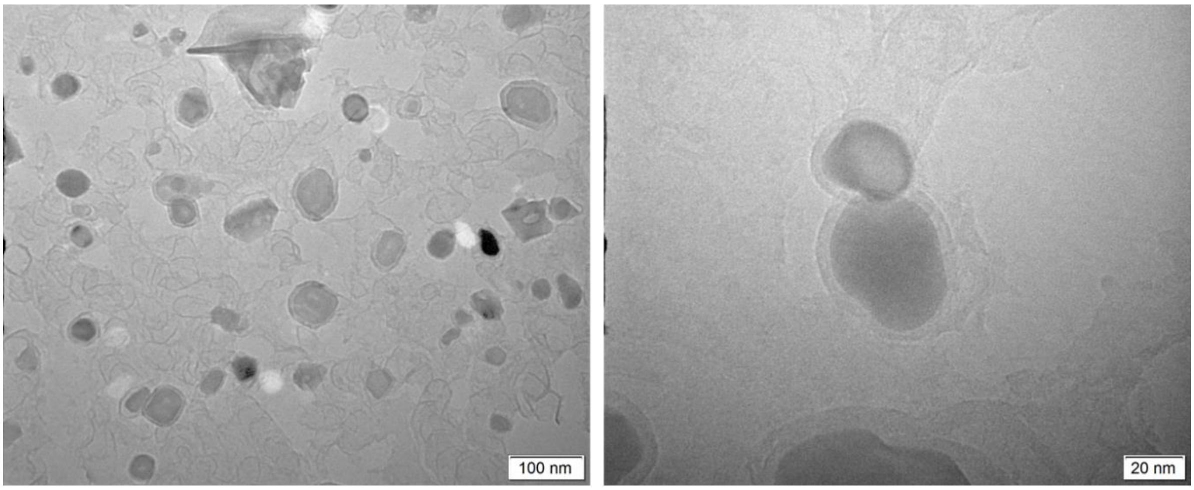

Figure 7.2: TEM images of magnetite nanoparticles deposited onto copper TEM grid after heating to 800 °C under Ar.

7.2.4 Further MD studies

Finally, the results of chapter 6 showed that the presence of a substrate had a significant impact on the melting behaviour of iron and iron carbide nanoparticles. The substrate used in this thesis had no structural information. Therefore, it would be interesting to assess whether different melting behaviour would be observed for particles supported on amorphous carbon or graphitic carbon substrates, particularly as epitaxial strain has previously been shown to have an impact.

Chapter 8 – Appendices

8.1 Appendix A - The effect of precursor structure on porous carbons produced by iron-catalyzed graphitization of biomass

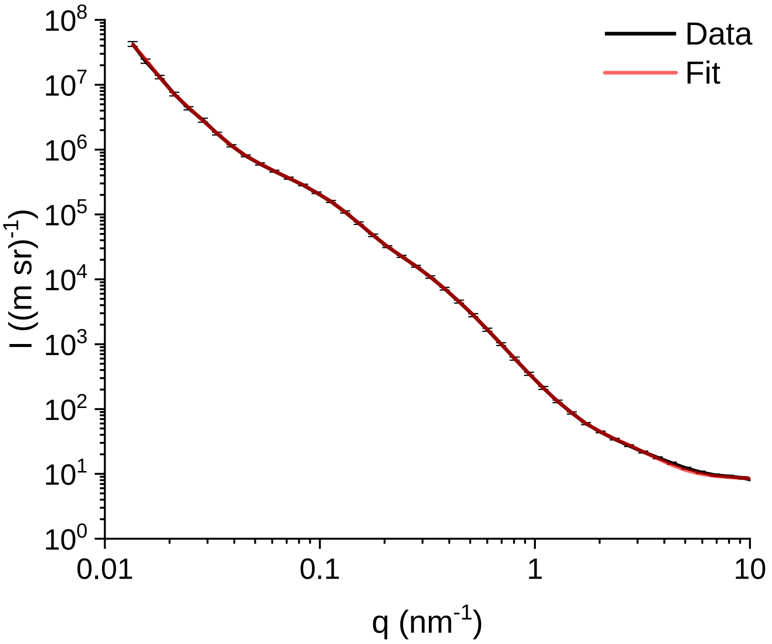

Figure 8.1: Raw SAXS data vs Monte Carlo fit for carbon produced from starch (5 g) and iron nitrate solution (0.68 mmol) and dwelled at 800 °C for 1 hr.

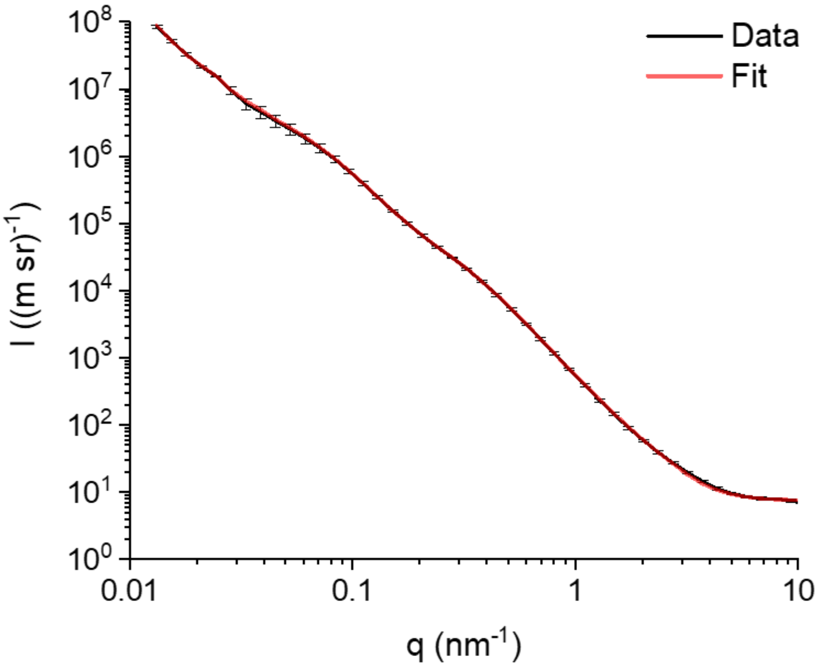

Figure 8.2: Raw SAXS data vs Monte Carlo fit for carbon produced from cellulose (5 g) and iron nitrate solution (0.68 mmol) and dwelled at 800 °C for 1 hr.

8.2 Appendix B - The influence of nitrogen in the synthesis of porous carbons by iron-catalyzed graphitization

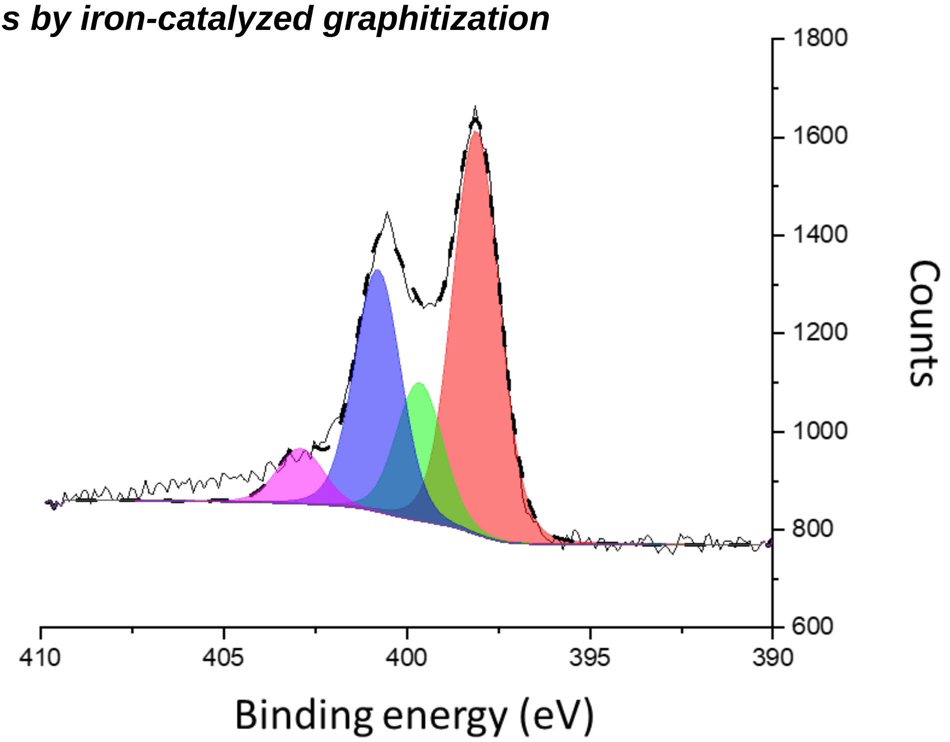

Figure 8.3: Deconvoluted N1s XPS spectrum for carbon produced from glycine (5 g) and iron nitrate solution (0.68 mmol), dwelled at 800 ° C for 1 hr. Grey line is raw spectra and dashed line is fitted spectra. Purple peak refers to oxidized-N, graphitic-N is blue, pyrrolic-N is green and pyridinic-N is red.

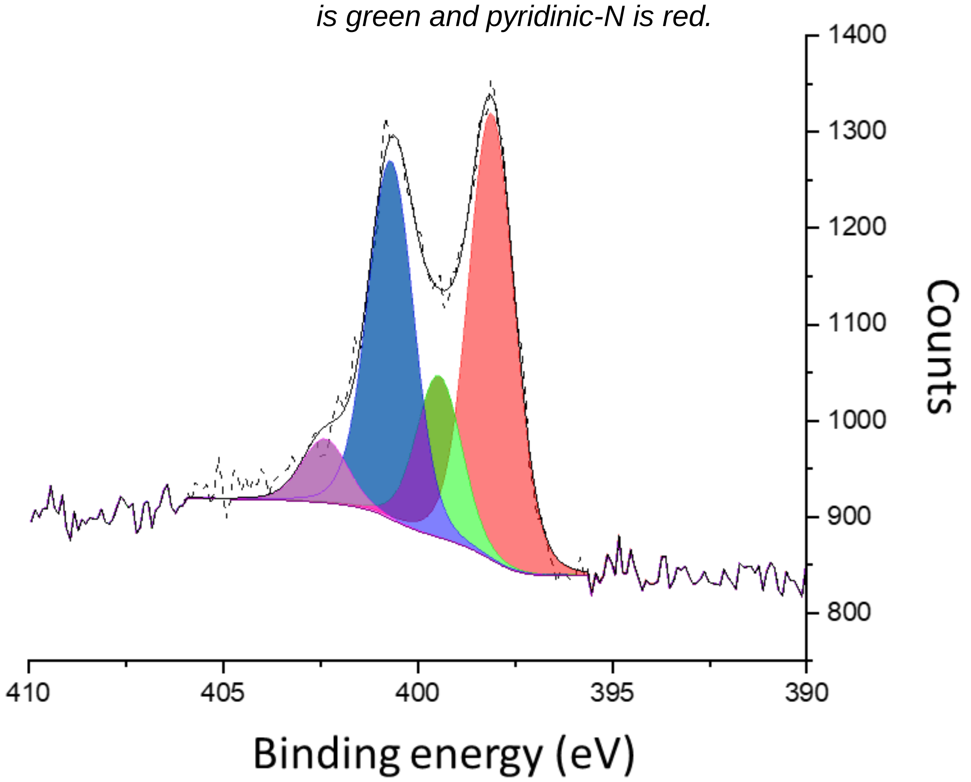

Figure 8.4: Deconvoluted N1s XPS spectrum for carbon produced from gelatin (5 g) and iron nitrate solution (0.68 mmol), dwelled at 800 °C for 1 hr. Grey line is raw spectra and dashed line is fitted spectra. Purple peak refers to oxidized-N, graphitic-N is blue, pyrrolic-N is green and pyridinic-N is red.

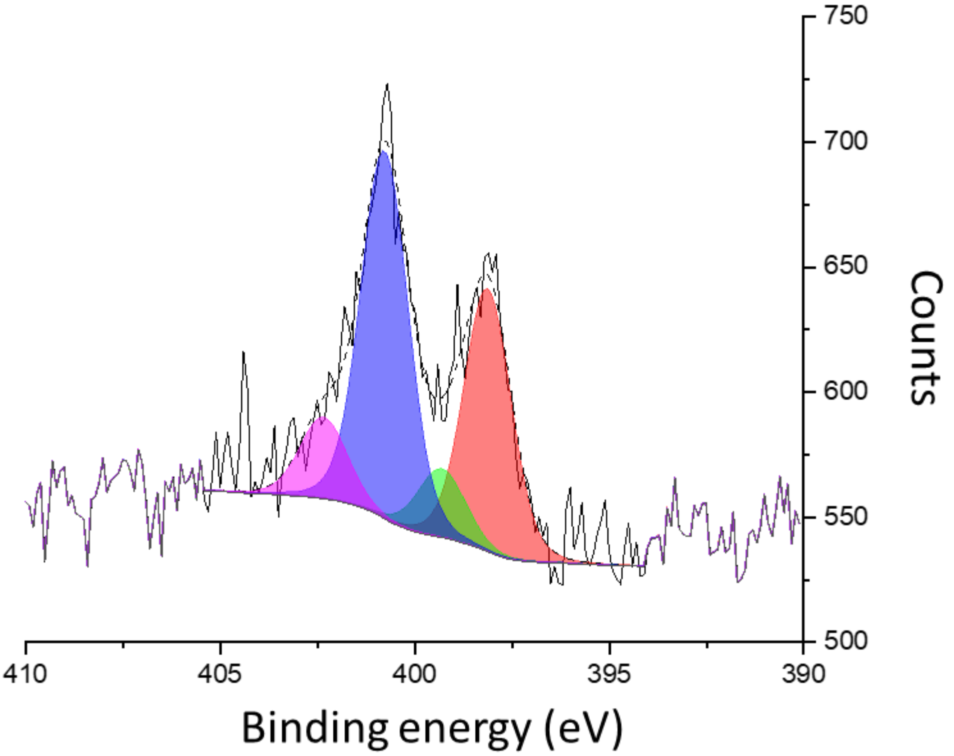

Figure 8.5: Deconvoluted N1s XPS spectrum for carbon produced from N-acetylglucosamine (5 g) and iron nitrate solution (0.68 mmol), dwelled at 800 °C for 1 hr. Grey line is raw spectra and dashed line is fitted spectra. Purple peak refers to oxidized-N, graphitic-N is blue, pyrrolic-N is green and pyridinic-N is red.

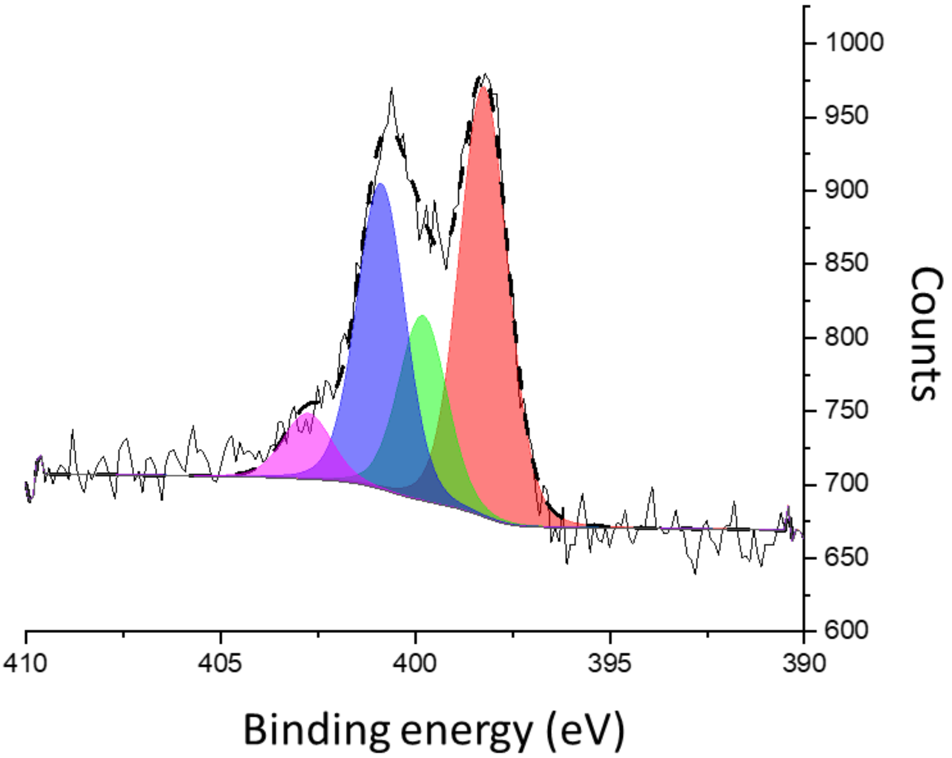

Figure 8.6: Deconvoluted N1s XPS spectrum for carbon produced from chitosan (5 g) and iron nitrate solution (0.68 mmol), dwelled at 800 °C for 1 hr. Grey line is raw spectra and dashed line is fitted spectra. Purple peak refers to oxidized-N, graphitic-N is blue, pyrrolic-N is green and pyridinic-N is red.

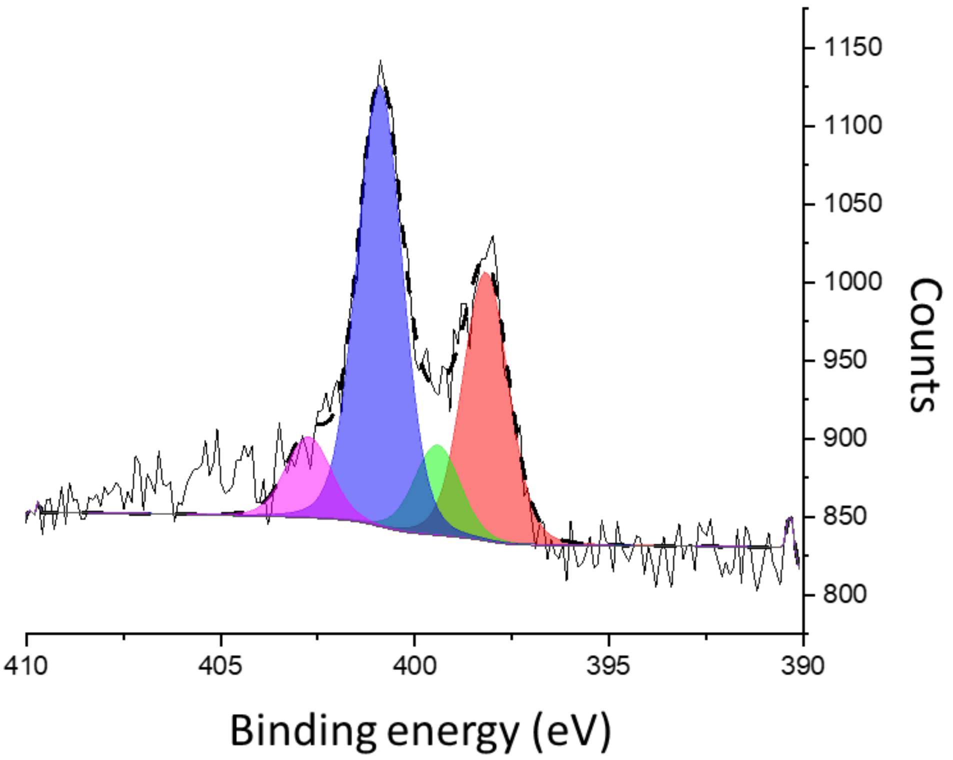

Figure 8.7: Deconvoluted N1s XPS spectra for carbon produced from chitin (5 g) and iron nitrate solution (0.68 mmol), dwelled at 800 °C for 1 hr. Grey line is raw spectra and dashed line is fitted spectra. Purple peak refers to oxidized-N, graphitic-N is blue, pyrrolic-N is green and pyridinic-N is red.

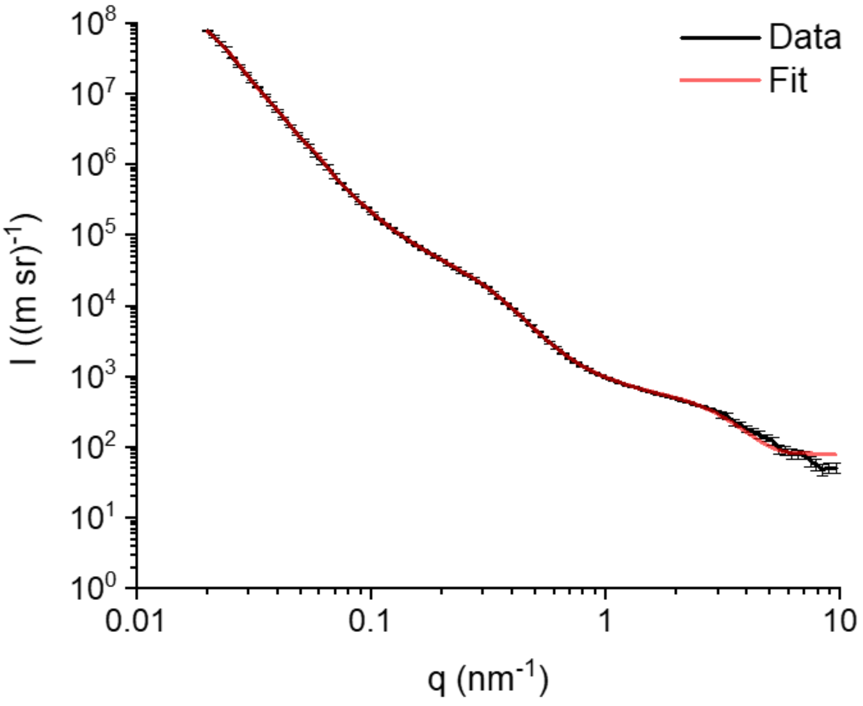

Figure 8.8: Raw SAXS data vs Monte Carlo fit for carbon produced from glycine (5 g) and iron nitrate solution (0.68 mmol), dwelled at 800 °C for 1 hr.

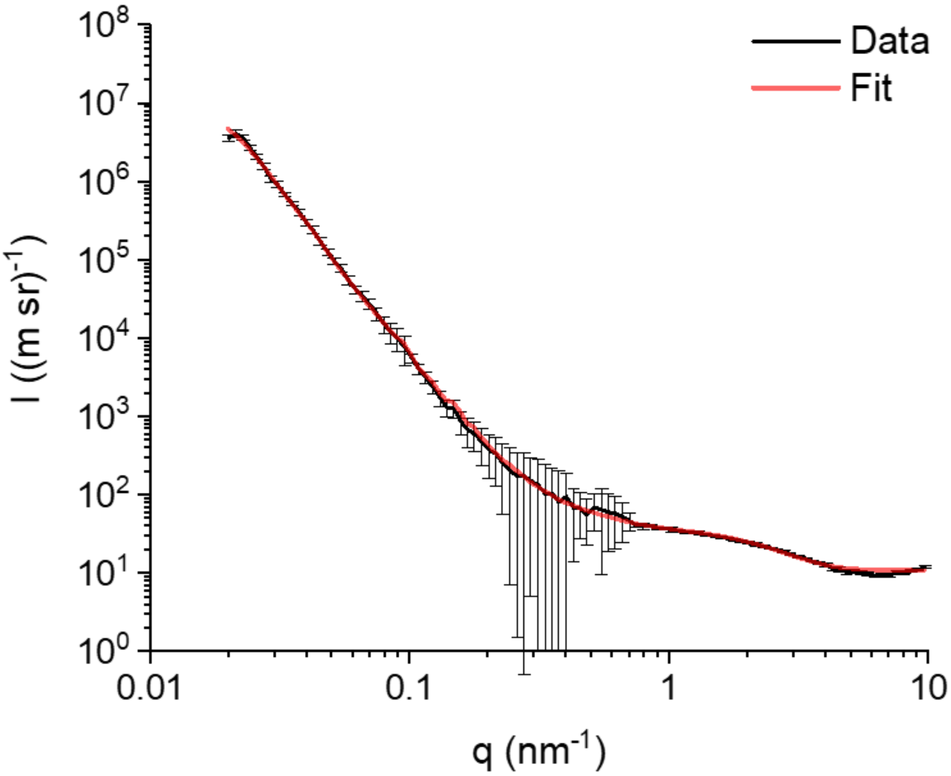

Figure 8.9: Raw SAXS data vs Monte Carlo fit for carbon produced from gelatin (5 g) and iron nitrate solution (0.68 mmol), dwelled at 800 °C for 1 hr.

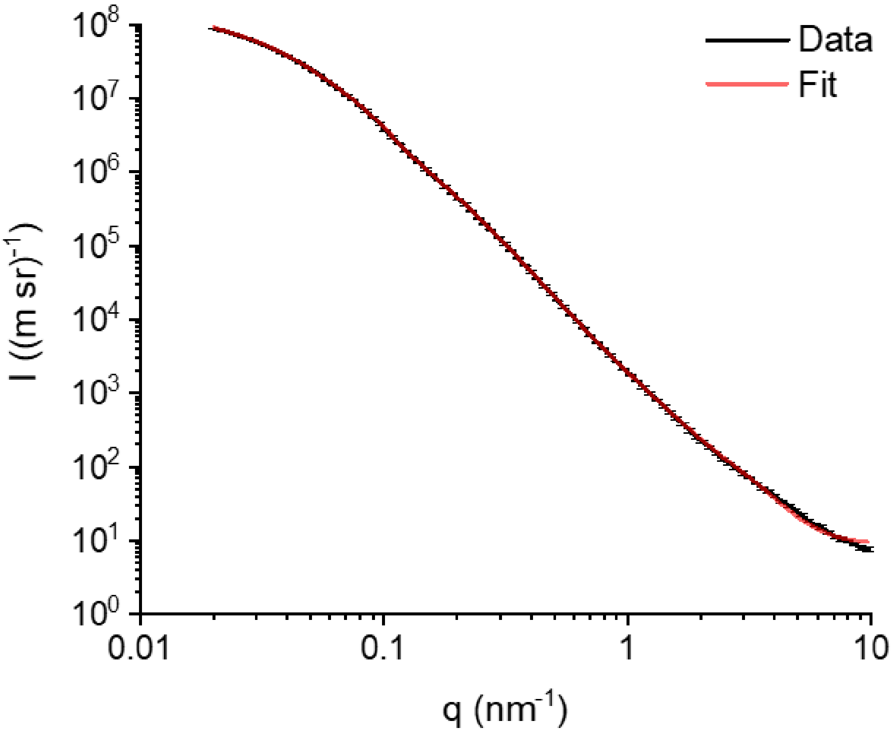

Figure 8.10: Raw SAXS data vs Monte Carlo fit for carbon produced from N-acetylglucosamine (5 g) and iron nitrate solution (0.68 mmol), dwelled at 800 °C for 1 hr..

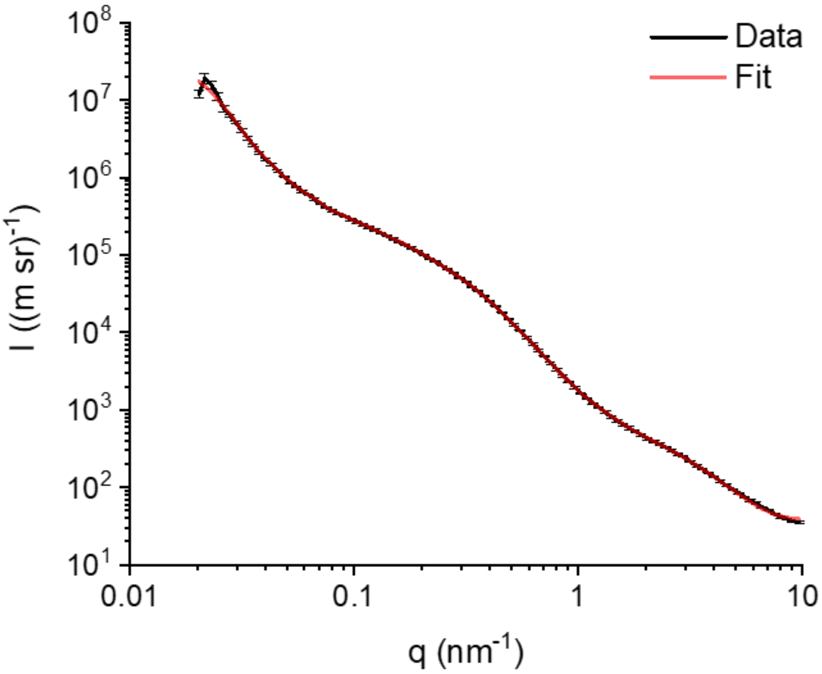

Figure 8.11: Raw SAXS data vs Monte Carlo fit for carbons produced from N-acetylglucosamine (5 g) and iron nitrate solution (0.68 mmol), dwelled at 800 °C for 1 hr.

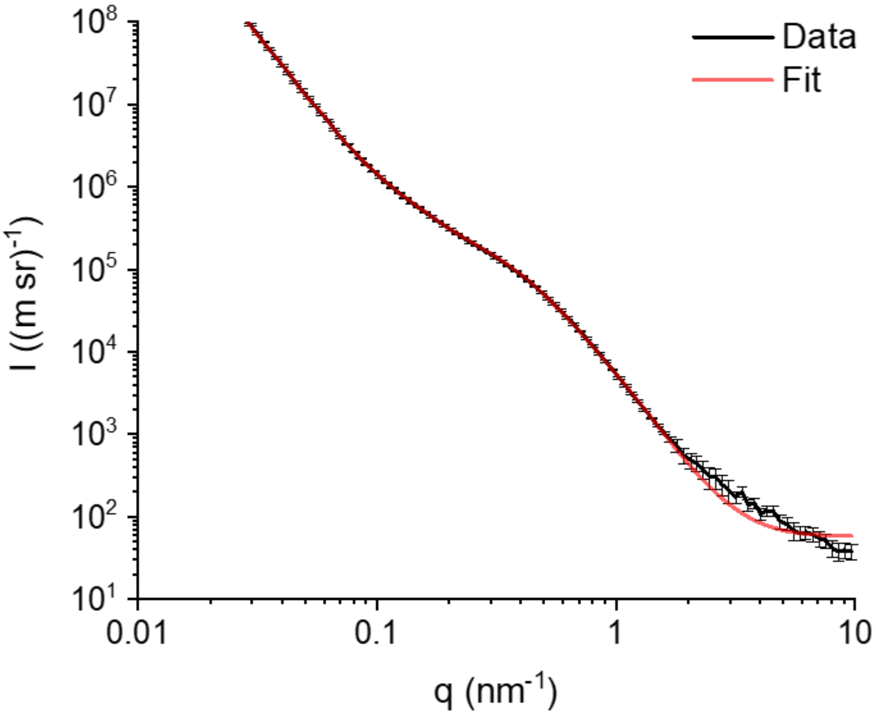

Figure 8.12: Raw SAXS data vs Monte Carlo fit for carbons produced from chitosan (5 g) and iron nitrate solution (0.68 mmol), dwelled at 800 °C for 1 hr.

8.3 Appendix C - In situ mechanistic study of iron-catalyzed graphitization

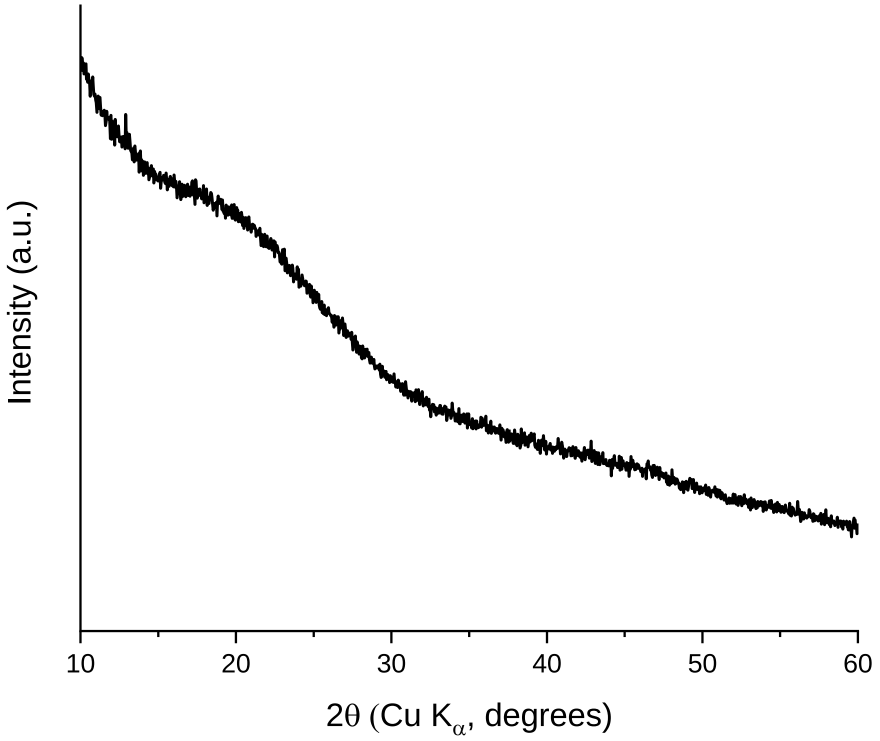

Figure 8.13: PXRD pattern of carbon produced from cellulose (5 g) and iron nitrate solution (3.4 mmol), heated to 400 °C.

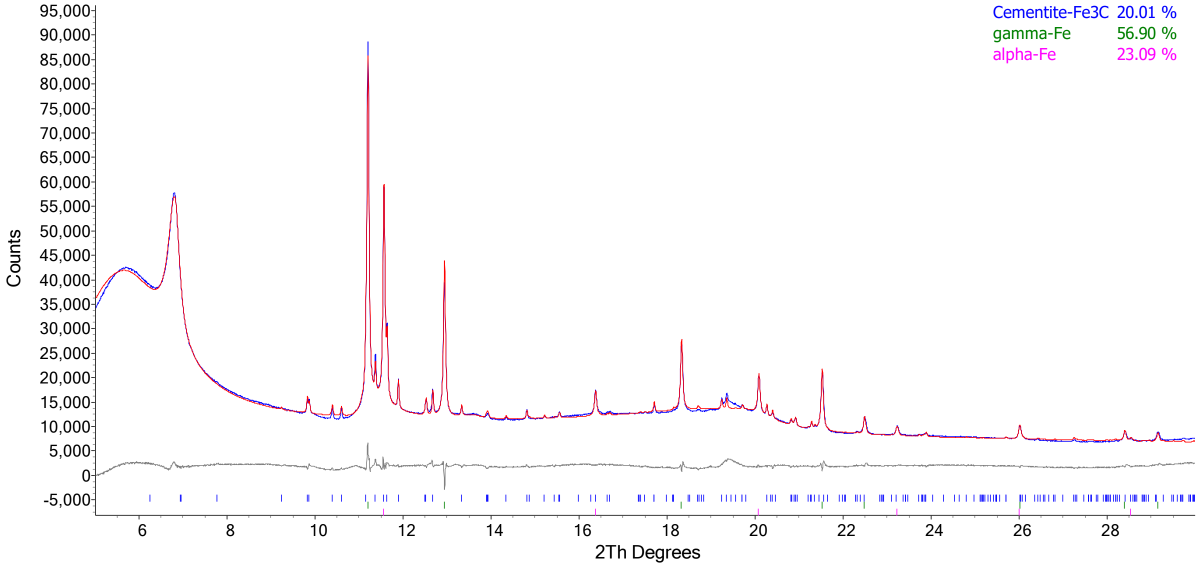

Figure 8.14: Rietveld refinement of diffraction data for cellulose-derived carbon acquired after 120 min at 800 °C. Raw diffraction data is shown in red, calculated data is shown in blue and the difference curve in grey. Tick marks refer to Fe_3C, γ-Fe and α-Fe and match the colours in the legend.

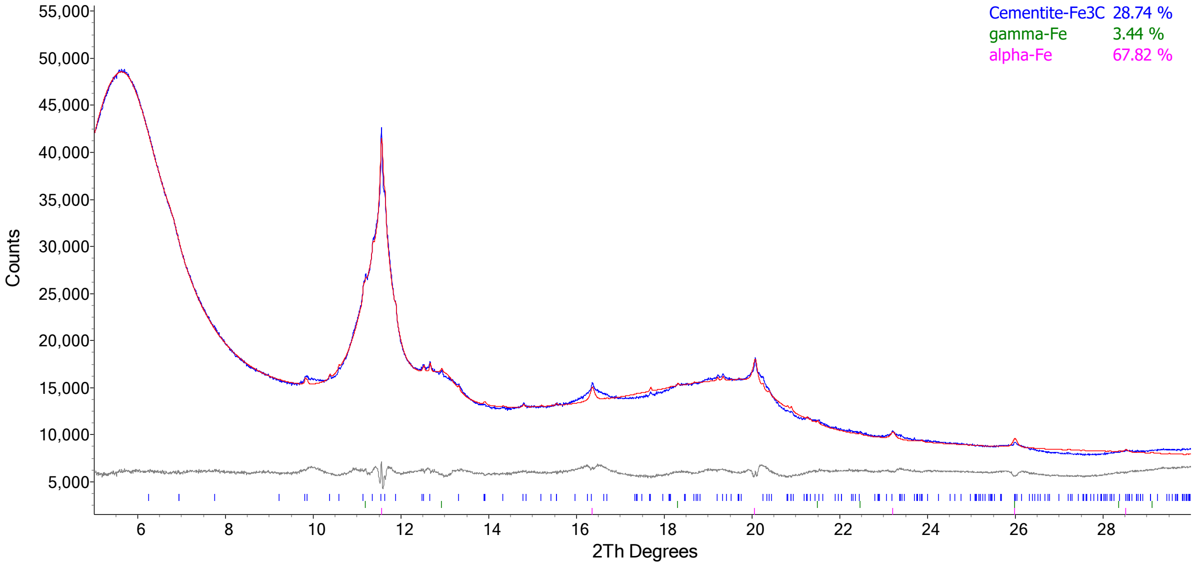

Figure 8.15: Rietveld refinement of diffraction data for starch-derived carbon acquired after 0 min at 800 °C. Raw diffraction data is shown in red, calculated data is shown in blue and the difference curve in grey. Tick marks refer to Fe_3C, γ-Fe and α-Fe and match the colours in the legend.

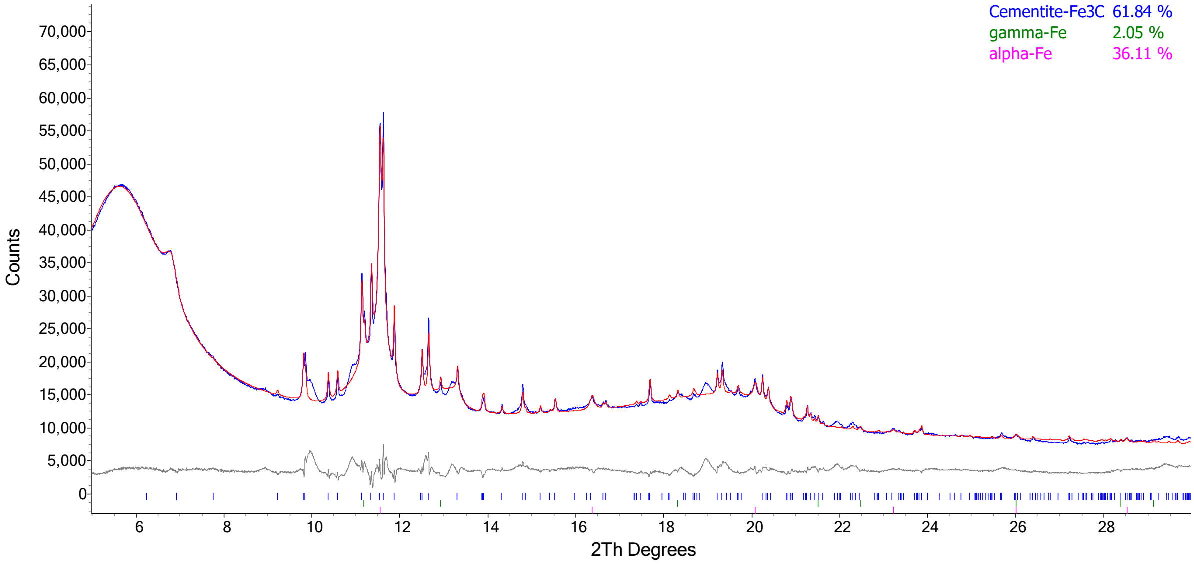

Figure 8.16: Rietveld refinement of diffraction data for starch-derived carbon acquired after 120 min at 800 °C. Raw diffraction data is shown in red, calculated data is shown in blue and the difference curve in grey. Tick marks refer to Fe_3C, γ-Fe and α-Fe and match the colours in the legend.

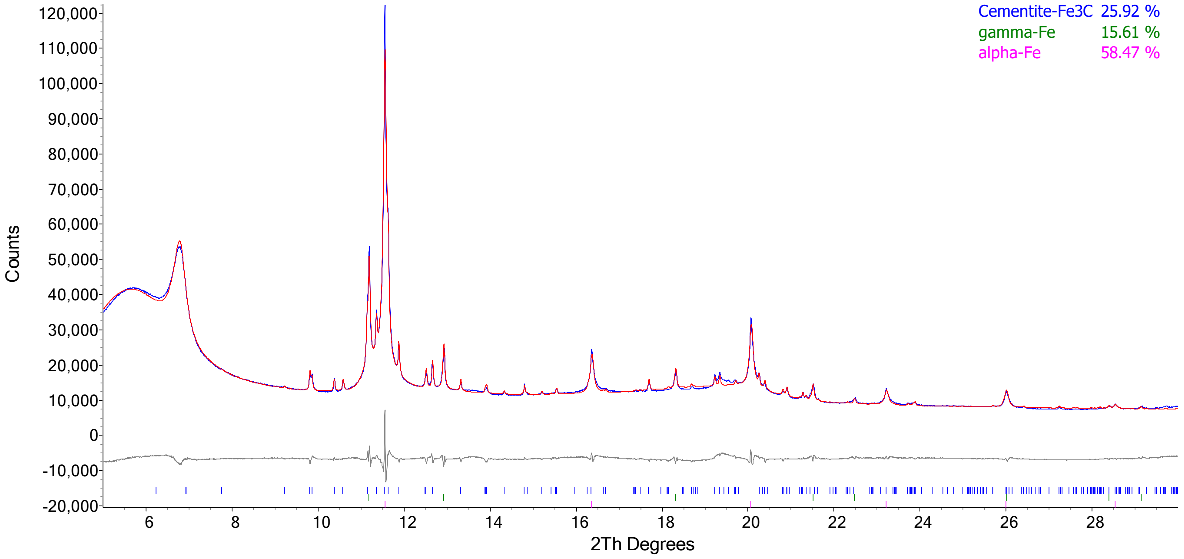

Figure 8.17: Rietveld refinement of diffraction data for glucose-derived carbon acquired after 0 min at 800 °C. Raw diffraction data is shown in red, calculated data is shown in blue and the difference curve in grey. Tick marks refer to Fe_3C, γ-Fe and α-Fe and match the colours in the legend.

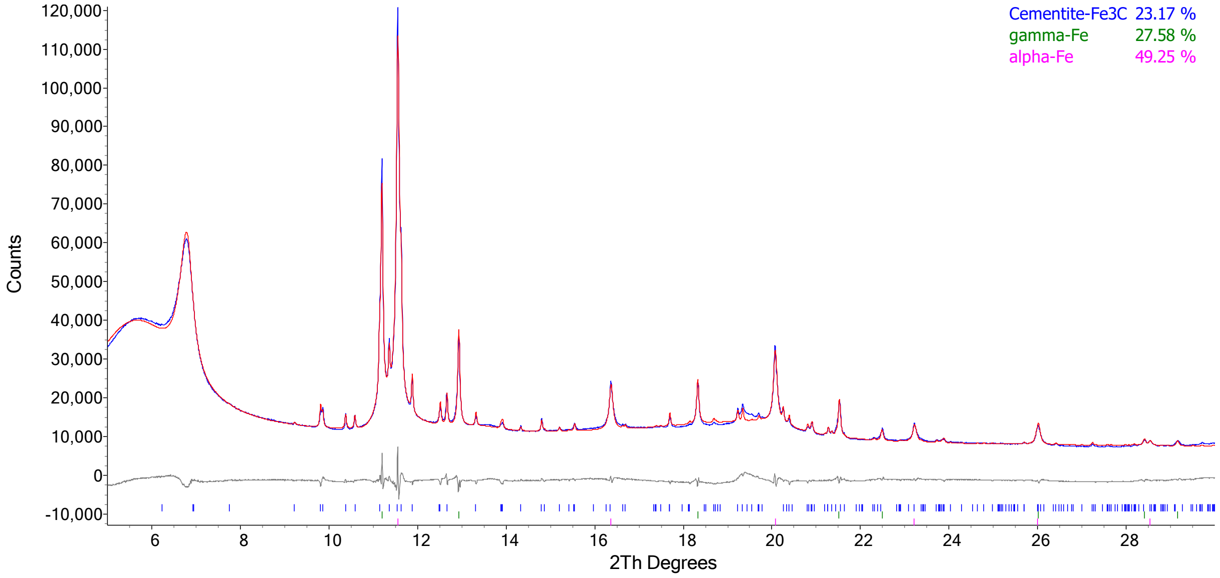

Figure 8.18: Rietveld refinement of diffraction data for glucose-derived carbon acquired after 120 min at 800 °C. Raw diffraction data is shown in red, calculated data is shown in blue and the difference curve in grey. Tick marks refer to Fe_3C, γ-Fe and α-Fe and match the colours in the legend.

8.4 Appendix D - Modelling the melting behaviour of catalyst particles in iron-catalyzed graphitization

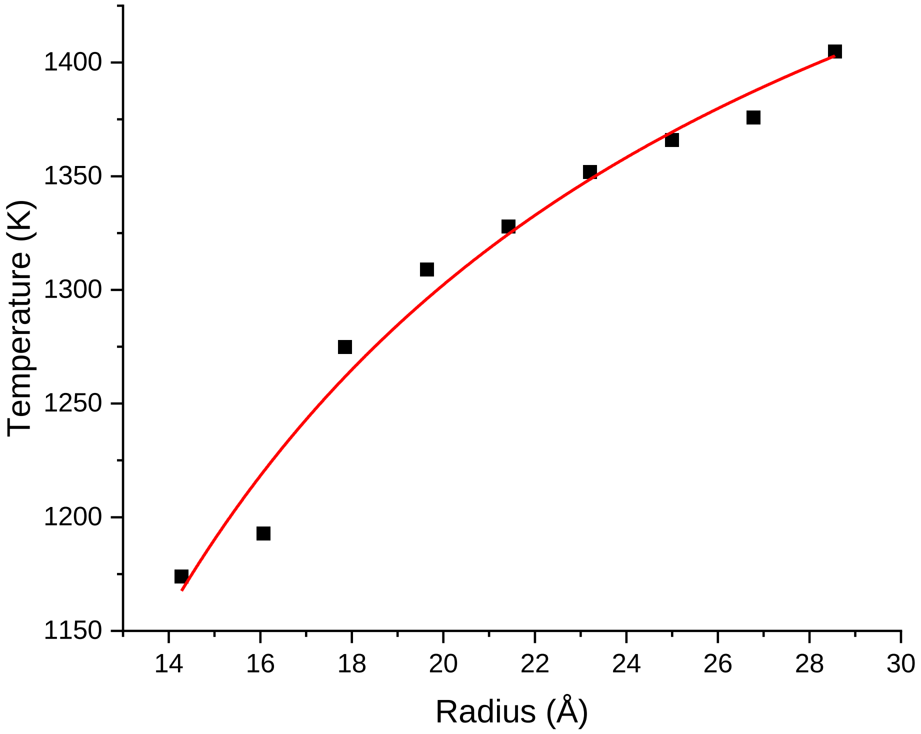

Figure 8.19: Plot of equilibrium melting temperature vs radius of cluster for a range of Fe cluster sizes, with an initial FCC structure. Bulk melting temperature from fitting with Pawlow formula = 1638 K.

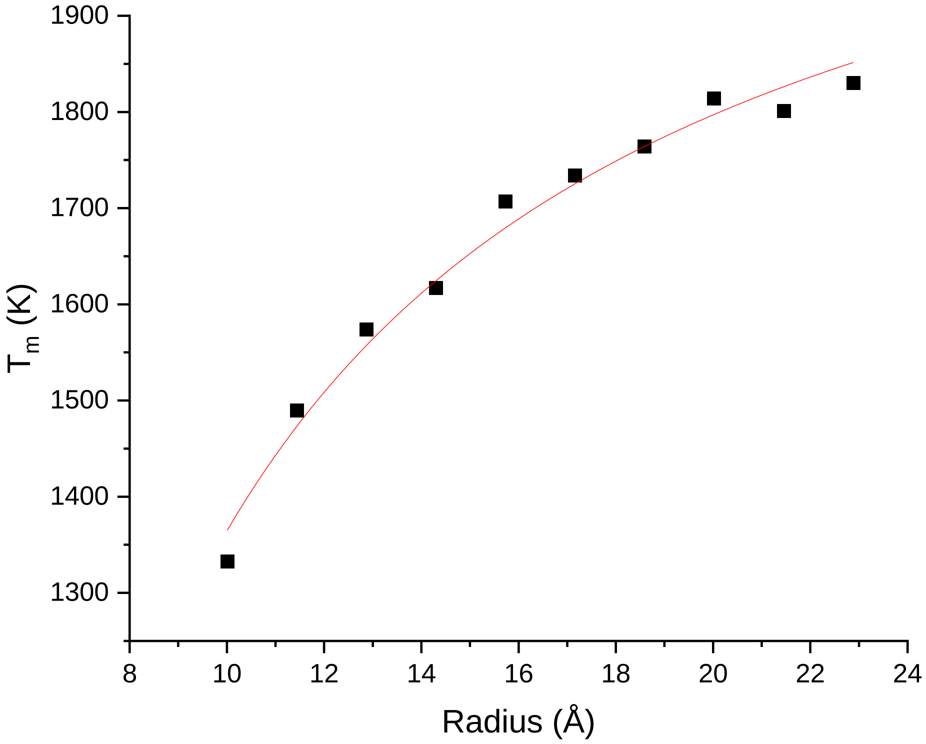

Figure 8.20: Plot of equilibrium melting temperature vs radius of cluster for a range of Fe cluster sizes, using Liyanage potential. Bulk melting temperature from fitting with Pawlow formula = 2230 K.

8.5 Appendix E – Concluding remarks

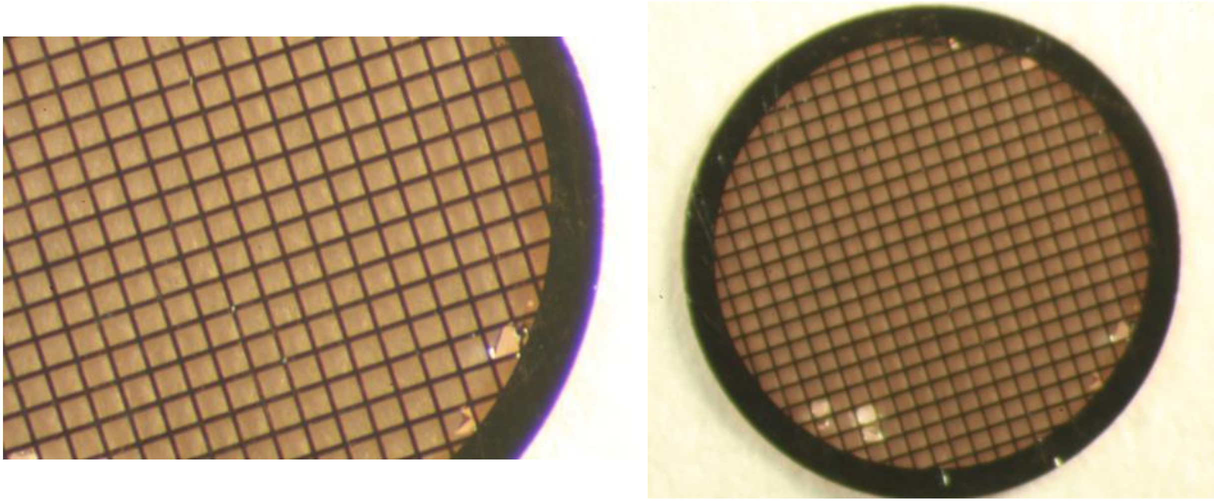

Figure 8.21: Optical microscopy images of a sputtered carbon-coated copper TEM grid before heating.

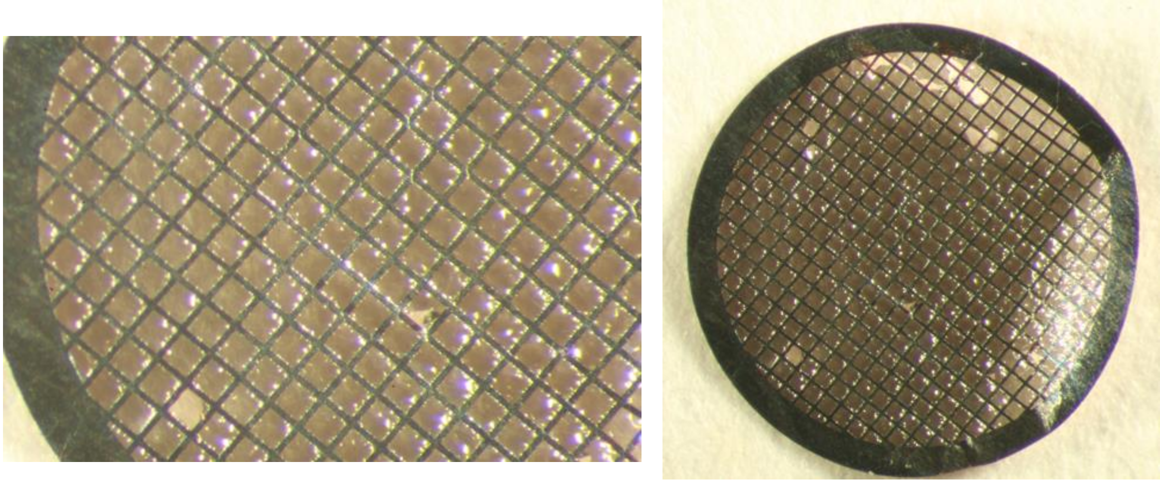

Figure 8.22: Optical microscopy images of a sputtered carbon-coated copper TEM grid after heating to 800 °C under argon.

Iron (II) acetate was used as the iron precursor and reacted with 1,2-dodecanediol in diphenyl ether with two surfactants, oleic acid and oleylamine, added into the reaction mixture to increase the electrostatic repulsions between the formed nanoparticles to avoid agglomeration. The reaction was carried out under a nitrogen atmosphere to avoid over-oxidation and the formation of Fe_2O_3 and the mixture was initially heated to 200 °C for 30 min before heating to reflux at 265 °C for 30 min. The nanoparticles were then precipitated with ethanol and separated by centrifugation before being dispersed in hexane with the addition of extra oleic acid and oleylamine to aid dispersion. A portion of the precipitated nanoparticles were dried in air at room temperature and PXRD showed that Fe_3O_4 was successfully produced.

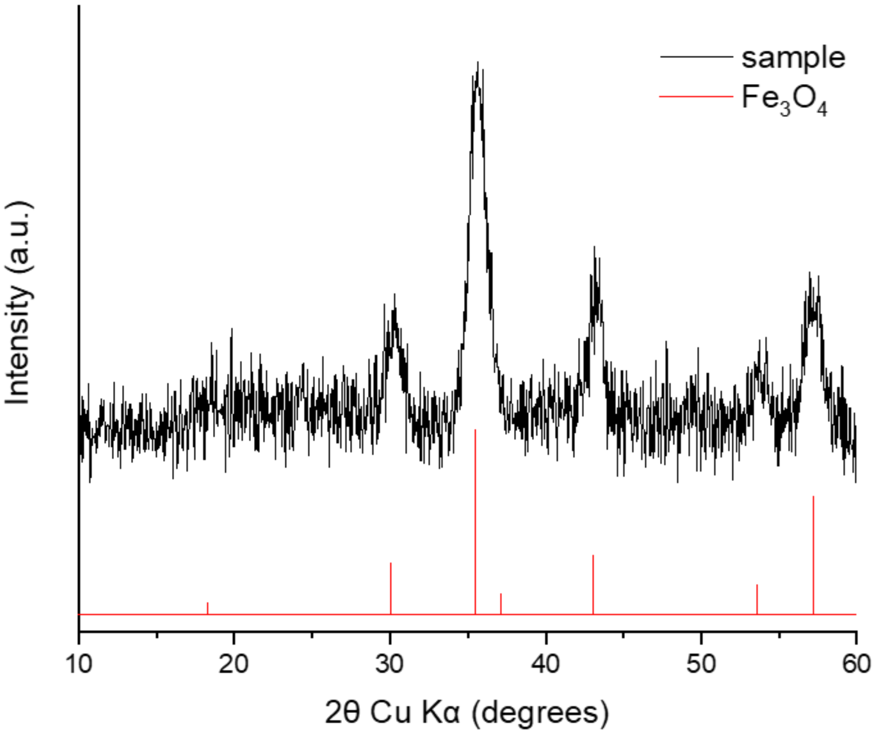

Figure 8.23: PXRD pattern of synthesised Fe_3O_4 nanoparticles.

Chapter 9 - Bibliography

---

[1] X. Hu, X. Sun, S. J. Yoo, B. Evanko, F. Fan, S. Cai. C. Zheng, W. Hu and G. D. Stucky, *Nano Energy*, 2019, **56**, 828-839.

[2] Y. Hu, J. O. Jensen, W. Zhang, L. N. Cleemann, W. Xing, N. J. Bjerrum and Q. Li, *Angew. Chem., Int. Ed.*, 2014, **53**, 3675-3679.

[3] B. Li, L. Yang, C. Q. Wang, Q. P. Zhang, Q. C. Liu, Y. D. Li and R. Xhao, *Chemosphere*, 2017, **175**, 332-340.

[4] S. Iijima, *Nature*, 1991, **354**, 56-58.

[5] T. Guo, P. Nikolaev, A. Thess, D. T. Colbert and R. E. Smalley, *Chem. Phys. Lett.,* 1995, **243**, 49-54.

[6] *IUPAC Gold Book*, https://goldbook.iupac.org/html/C/C00894.html, (accessed July 2022).

[7] E. Fitzer, K.-H. Köchling, H. P. Boehm and H. Marsh, *Pure Appl. Chem.*, 1995, **67**, 473–506.

[8] H. Pan, M. Pruski, B. C. Gerstein, F. Li and J. S. Lannin, *Phys. Rev. B: Condens. Matter Mater. Phys.*, 1991, **44**, 6741–6745.

[9] R. Van Noorden, *Nature*, 2011, **469**, 14–16.

[10] M. Monthioux, *Carbon*, 2020, **160**, 405–406.

[11] H. W. Kroto, J. R. Heath, S. C. O'Brien, R. F. Curl and R. E. Smalley, *Nature*, 1985, **318**, 162-163.

[12] A. Bianco, H.-M. Cheng, T. Enoki, Y. Gogotsi, R. H. Hurt, N. Koratkar, T. Kyotani, M. Monthioux, C. R. Park, J. M. D. Tascon and J. Zhang, *Carbon*, 2013, **65**, 1–6.

[13] K. Dasgupta and D. Sathiyamoorthy, *Mater. Sci. Technol.,* 2003, **19**, 995-1002.

[14] R. E. Franklin, *Proc. R. Soc. London, Ser. A*, 1951, **209**, 196–218.

---

[15] P. J. F. Harris, *J. Mater. Sci.*, 2013, **48**, 565–577.

[16] S. J. Townsend, T. J. Lenosky, D. A. Muller, C. S. Nichols and V. Elser, *Phys. Rev. Lett.*, 1992, **69**, 921–924.

[17] A. P. Terzyk, S. Furmaniak, P. J. F. Harris, P. A. Gauden, J. Włoch, P. Kowalczyk and G. Rychlicki, *Phys. Chem. Chem. Phys.*, 2007, **9**, 5919–5927.

[18] R. D. Hunter, J. Ramirez-Rico and Z. Schnepp, *J. Mater. Chem. A*, 2022, **10**, 4489-4516.

[19] Y. Nishi, *Chem. Rec.*, 2001, **1**, 406–413.

[20] W.-J. Liu, H. Jiang and H.-Q. Yu, *Energy Environ. Sci.*, 2019, **12**, 1751–1779.

[21] C. Liedel, *ChemSusChem*, 2020, **13**, 2110–2141.

[22] S. W. Kim, D. H. Seo, X. Ma, G. Ceder and K. Kang, *Adv. Energy Mater.,* 2012, **2**, 710-721.

[23] H. Tonnoir, D. Huo, R. L. S. Canevesi, V. Fierro, A. Celzard and R. Janot, *Mater. Today Chem.,* 2022, **23**, 100614.

[24] X. Yin, Y. Zhao, X. Wang, X. Feng, Z. Lu, Y. Li, H. Long, J. Wang, J. Ning and J. Zhang, *Small,* 2022, **18**, 2105568.

[25] M. Shao, Q. Chang, J.-P. Dodelet and R. Chenitz, *Chem. Rev.*, 2016, **116**, 3594–3657.

[26] D. Guo, R. Shibuya, C. Akiba, S. Saji, T. Kondo and J. Nakamura, *Science*, 2016, **351**, 361-365.

[27] L. Sun, C. Tan, L. Wang, J. Zou, G. Mu and H. Fu, *J. Mater. Chem.,* 2011, **21**, 7232-7239.

[28] W. Chen, L. Duan and D. Zhu, *Environ. Sci. Technol.*, 2007, **41**, 8295–8300.

[29] H. J. Wang, A. L. Zhou, F. Peng, H. Yu and J. Yang, *J. Colloid Interface Sci.*, 2007, **316**, 277-283.

---

[30] N. Arora and N. N. Sharma, *Diamond Relat. Mater.*, 2014, **50**, 135–150.

[31] N. I. Alekseyev and G. A. Dyuzhev, *Carbon*, 2003, **41**, 1343–1348.

[32] J. Prasek, J. Drbohlavova, J. Chomoucka, J. Hubalek, O. Jasek, V. Adam and R. Kisek, *J. Mater. Chem.*, 2011, **21**, 15872–15884.

[33] J. Kong, A. M. Cassell and H. J. Dai, *Chem. Phys. Lett.,* 1998, **292**, 567-574.

[34] G. D. Nessim, *Nanoscale*, 2010, **2**, 1306-1323.

[35] J. Yang and S. Zuo, *Diamond Relat. Mater.*, 2019, **95**, 1–4.

[36] M. Sevilla, C. Sanchís, T. Valdés-Solís, E. Morallón and A. B. Fuertes, *Carbon*, 2008, **46**, 931–939.

[37] M. J. Xie, J. Yang, J. Y. Liang, X. F. Guo and W. P. Ding, *Carbon*, 2014, **77**, 215–225.

[38] R. D. Hunter, J. L. Rowlandson, G. J. Smales, B. R. Pauw, V. P. Ting, A. Kulak and Z. Schnepp, *Mater. Adv.*, 2020, **1**, 3281–3291.

[39] M. N. Obrovac, X. Zhao, L. T. Burke and R. A. Dunlap, *Electrochem. Commun.*, 2015, **60**, 221–224.

[40] H. Niu, Y. Wang, X. Zhang, Z. Meng and Y. Cai, *ACS Appl. Mater. Interfaces*, 2012, **4**, 286–295.

[41] Z. Tian, C. Wang, J. Yue, X. Zhang and L. Ma, *Catal. Sci. Technol.*, 2019, **9**, 2728–2741.

[42] J. Hoekstra, A. M. Beale, F. Soulimani, M. Versluijs-Helder, J. W. Geus and L. W. Jenneskens, *New J. Chem.*, 2015, **39**, 6593–6601.

[43] R. Atchudan, S. Perumal, T. N. J. I. Edison and Y. R. Lee, *Mater. Lett.*, 2016, **166**, 145–149.

[44] C. Defilippi, M. O. A. Mukadam, S. A. Nicolae, M. R. Lees and C. Giordano, *Materials*, 2019, **12**, 323.

---

[45] Z. Cao, M. Qin, C. Zuo, Y. Gu and B. Jia, *J. Colloid Interface Sci.*, 2017, **491**, 55–63.

[46] S. Juvanen, A. Sarapuu, S. Vlassov, M. Kook, V. Kisand, M. Käärik, A. Treshchalov, J. Aruväli, J. Kozlova, A. Tamm, J. Leis and K. Tammeveski, *ChemElectroChem*, 2021, **8**, 2288–2297.

[47] I.-A. Choi, D.-H. Kwak, S.-B. Han, J.-Y. Park, H.-S. Park, K.-B. Ma, D.-H. Kim, J.-E. Won and K.-W. Park, *Appl. Catal., B*, 2017, **211**, 235–244.

[48] J. J. Shi, X. M. Hu, M. R. Madsen, P. Lamagni, E. T. Bjerglund, S. U. Pedersen, T. Skrydstrup and K. Daasbjerg, *ACS Appl. Nano Mater.*, 2018, **1**, 3608–3615.

[49] H. Khani, N. S. Grundish, D. O. Wipf and J. B. Goodenough, *Adv. Energy Mater.*, 2020, **10**, 1903215.

[50] M. Xiao, J. Zhu, L. Feng, C. Liu and W. Xing, *Adv. Mater.*, 2015, **27**, 2521–2527.

[51] C. W. Huang, L. C. Hsu and Y. Y. Li, *Nanotechnology*, 2006, **17**, 4629–4634.

[52] K. Inomata and Y. Otake, *Microporous Mesoporous Mater.*, 2011, **143**, 60-65.

[53] M. Sevilla and A. B. Fuertes, *Carbon*, 2006, **44**, 468-478.

[54] J. J. Li, Y. Liang, B. J. Dou, C. Y. Ma, R. J. Lu, Z. P. Hao, Q. Xie, Z. Q. Luan and K. Li, *Mater. Chem. Phys.,* 2013, **138**, 484-489.

[55] A. M. Wang, J. W. Ren, B. F. Shi, G. Z. Lu and Y. Q. Wang, *Microporous Mesoporous Mater.*, 2012, **151**, 287-292.

[56] H. Marsh, D. Crawford and D. W. Taylor, *Carbon*, 1983, **21**, 81–87.

[57] J. I. Ozaki, K. Nozawa, K. Yamada, Y. Uchiyama, Y. Yoshimoto, A. Furuichi, T. Yokoyama, A. Oya, L. J. Brown and J. D. Cashion, *J. Appl. Electrochem.*, 2006, **36**, 239–247.

[58] Z. Tang, Y. Song, X. He and J. Yang, *Mater. Lett.*, 2012, **89**, 330–332.

---

[59] C. G. Renda, R. Bertholdo, T. Venancio, A. P. Luz, V. C. Pandolfelli and A. A. Lucas, *Ceram. Int.*, 2019, **45**, 12196–12204.

[60] B. Zhang, C. Liu, W. Kong and C. Qi, *Frontiers of Materials Science*, 2016, **10**, 147–156.

[61] J. Qi, L. H. Jiang, Q. W. Tang, S. Zhu, S. L. Wang, B. L. Yi and C. Q. Sun, *Carbon*, 2012, **50**, 2824–2831.

[62] J. S. Li, J. Gu, H. J. Li, Y. Liang, Y. X. Hao, X. Y. Sun and L. J. Wang, *Microporous Mesoporous Mater.*, 2010, **128**, 144–149.

[63] A. Abdelwahab, J. Castelo-Quibén, J. F. Vivo-Vilches, M. Pérez-Cadenas, F. J. Maldonado-Hódar, F. Carrasco-Marín and A. F. Pérez-Cadenas, *Nanomaterials*, 2018, **8**, 266.

[64] A. Chen, Y. Yu, T. Xing, R. Wang, Y. Zhang and Q. Li, *J. Mater. Sci.*, 2015, **50**, 5578–5582.

[65] G. Hasegawa, K. Kanamori and K. Nakanishi, *Mater. Lett.*, 2012, **76**, 1–4.

[66] M. M. Gaikwad, M. Kakunuri and C. S. Sharma, *Mater. Today Commun.*, 2019, **20**, 100569.

[67] W. Kicinski, M. Norek and M. Bystrzejewski, *J. Phys. Chem. Solids*, 2013, **74**, 101–109.

[68] N. I. Maksimova, O. P. Krivoruchko, G. Mestl, V. I. Zaikovskii, A. L. Chuvilin, A. N. Salanov and E. B. Burgina, *J. Mol. Catal. A: Chem.*, 2000, **158**, 301–307.

[69] Y.-H. Chung and S. Jou, *Mater. Chem. Phys.*, 2005, **92**, 256–259.

[70] F. Cesano, M. M. Rahman, F. Bardelli, A. Damin and D. Scarano, *ChemistrySelect*, 2016, **1**, 2536–2541.

[71] J. Hoekstra, A. M. Beale, F. Soulimani, M. Versluijs-Helder, D. van de Kleut, M. Koelewijn, J. W. Geus and L. W. Jenneskens, *Carbon*, 2016, **107**, 248–260.

---

[72] Q. C. Yan, J. H. Li, X. F. Zhang, E. Hassan, C. J. Wang, J. L. Zhang and Z. Y. Cai, *J. Nanopart. Res.*, 2018, **20**, 223.

[73] Q. G. Yan, J. H. Li, X. F. Zhang, J. L. Zhang and Z. Y. Cai, *Nanomater. Nanotechnol.*, 2018, **8**, 1–12.

[74] X. F. Zhang, Q. G. Yan, J. H. Li, I. W. Chu, H. Toghiani, Z. Y. Cai and J. L. Zhang, *Polymers*, 2018, **10**, 183.

[75] S. W. Zhang, M. Y. Zeng, J. X. Li, J. Li, J. Z. Xu and X. K. Wang, *J. Mater. Chem. A*, 2014, **2**, 4391-4397.

[76] G. Daniel, T. Kosmala, F. Brombin, M. Mazzucato, A. Facchin, M. C. Dalconi, D. Badocco, P. Pastore, G. Granozzi and C. Durante, *Catalysts*, 2021, **11**, 390.

[77] Z. Schnepp, Y. Zhang, M. J. Hollamby, B. R. Pauw, M. Tanaka, Y. Matsushita and Y. Sakka, *J. Mater. Chem. A*, 2013, **1**, 13576–13581.

[78] J. Hoekstra, A. M. Beale, F. Soulimani, M. Versluijs-Helder, J. W. Geus and L. W. Jenneskens, *J. Phys. Chem. C*, 2015, **119**, 10653–10661.

[79] S. Glatzel, Z. Schnepp and C. Giordano, *Angew. Chem., Int. Ed.*, 2013, **52**, 2355–2358.

[80] K. Lotz, A. Wutscher, H. Dudder, C. M. Berger, C. Russo, K. Mukherjee, G. Schwaab, M. Havenith and M. Muhler, *ACS Omega*, 2019, **4**, 4448–4460.

[81] J. Hoekstra, M. Versluijs-Helder, E. J. Vlietstra, J. W. Geus and L. W. Jenneskens, *ChemSusChem*, 2015, **8**, 985–989.

[82] S. Shi, W. Che, K. Liang, C. Xia and D. Zhang, *J. Anal. Appl. Pyrolysis*, 2015, **115**, 1–6.

[83] A. N. Prusov, S. M. Prusova, A. G. Zakharov, A. V. Bazanov and V. K. Ivanov, *Fibre Chem.*, 2018, **50**, 154–160.

---

[84] S. Xia, N. Cai, W. Lu, H. Zhou, H. Xiao, X. Chen, Y. Chen, H. Yang, X. Wang, S. Wang and H. Chen, *J. Cleaner Prod.*, 2021, **329**, 129735.

[85] Q. Yan, X. Zhang, J. Li, E. Hassan, C. Wang, J. Zhang and Z. Cai, *J. Mater. Sci.*, 2018, **53**, 8020–8029.

[86] X. Zhang, Q. Yan, J. Li, J. Zhang and Z. Cai, *Materials*, 2018, **11**, 139.

[87] S. T. Neeli and H. Ramsurn, *Carbon*, 2018, **134**, 480–490.

[88] J. Zhao, Y. Liu, X. Quan, S. Chen, H. Yu and H. Zhao, *Appl. Surf. Sci.*, 2017, **396**, 986–993.

[89] A. Gutiérrez-Pardo, J. Ramírez-Rico, R. Cabezas-Rodríguez and J. Martínez-Fernández, *J. Power Sources*, 2015, **278**, 18–26.

[90] E. Thompson, A. E. Danks, L. Bourgeois and Z. Schnepp, *Green Chem.*, 2015, **17**, 551–556.

[91] R. D. Hunter, J. Davies, S. J. A. Hérou, A. Kulak and Z. Schnepp, *Philos. Trans. R. Soc., A*, 2021, **379**, 20200336.

[92] W.-J. Liu, K. Tian, Y.-R. He, H. Jiang and H.-Q. Yu, *Environ. Sci. Technol.*, 2014, **48**, 13951–13959.

[93] M. Sevilla, C. Sanchís, T. Valdés-Solís, E. Morallón and A. B. Fuertes, *J. Phys. Chem. C*, 2007, **111**, 9749–9756.

[94] A. Gomez-Martin, A. Gutierrez-Pardo, J. MartinezFernandez and J. Ramirez-Rico, *Fuel Process. Technol.*, 2020, **199**, 106279.

[95] A. Gutiérrez-Pardo, J. Ramírez-Rico, R. Cabezas-Rodríıguez and J. Martínez-Fernández, *J. Power Sources*, 2015, **278**, 18–26.

[96] A. Gomez-Martin, J. Martinez-Fernandez, M. Ruttert, A. Heckmann, M. Winter, T. Placke and J. Ramirez-Rico, *ChemSusChem*, 2018, **11**, 2776–2787.

---

[97] L. Ma, Y. Xu, Y. Liu, H. Zhang, J. Yao, N. Li, C. M. Li, W. Zhou and J. Jiang, *ACS Sustainable Chem. Eng.*, 2019, **7**, 17919–17928.

[98] Y. Gong, D. Li, C. Luo, Q. Fu and C. Pan, *Green Chem.*, 2017, **19**, 4132–4140.

[99] L. Sun, C. Tian, M. Li, X. Meng, L. Wang, R. Wang, J. Yin and H. Fu, *J. Mater. Chem. A,* 2013, **1**, 6462–6470.

[100] Q. Liu, J. Gu, W. Zhang, Y. Miyamoto, Z. Chen and D. Zhang, *J. Mater. Chem.*, 2012, **22**, 21183–21188.

[101] S. Zhang, Y. Su, S. Zhu, H. Zhang and Q. Zhang, *J. Anal. Appl. Pyrolysis*, 2018, **135**, 22–31.

[102] Y. Liu, J. Ruan, S. Sang, Z. Zhou and Q. Wu, *Electrochim. Acta*, 2016, **215**, 388–397.

[103] F. Wu, R. Huang, D. Mu, B. Wu and Y. Chen, *Electrochim. Acta*, 2016, **187**, 508–516.

[104] X. Li, E. Cui, Z. Xiang, L. Yu, J. Xiong, F. Pan and W. Lu, *Colloids Surf., A*, 2020, **819**, 152952.

[105] L. Chen, T. Ji, L. Mu, Y. Shi, L. Brisbin, Z. Guo, M. A. Khan, D. P. Young and J. Zhu, *RSC Adv.*, 2016, **6**, 2259-2269.

[106] Z. Yan, C. Dai, M. Zhang, X. Lu, X. Zhao and J. Xie, *Int. J. Hydrogen Energy*, 2019, **44**, 4090–4101.

[107] Y. Cai, Y. Luo, H. Dong, X. Zhao, Y. Xiao, Y. Liang, H. Hu, Y. Liu and M. Zheng, *J. Power Sources*, 2017, **353**, 260–269.

[108] I. Major, J. M. Pin, E. Behazin, A. Rodriguez-Uribe, M. Misra and A. Mohanty, *Green Chem.*, 2018, **20**, 2269–2278.

---

[109] E. Petala, Y. Georgiou, V. Kostas, K. Dimos, M. A. Karakassides, Y. Deligiannakis, C. Aparicio, J. Tuček and R. Zbořil, *ACS Sustainable Chem. Eng.*, 2017, **5**, 5782–5792.

[110] X. Zhang, H. Li, K. Zhang, Q. Wang, B. Qin, Q. Cao and L. Jin, *J. Electrochem. Soc.*, 2018, **165**, A2084–A2092.

[111] S. Xia, K. Li, H. Xiao, N. Cai, Z. Dong, C. Xu, Y. Chen, H. Yang, X. Tu and H. Chen, *Bioresour. Technol.*, 2019, **287**, 121444.

[112] W. Tian, Q. Gao, Y. Tan and Z. Li, *Carbon*, 2017, **119**, 287–295.

[113] M. A. Ahsan, A. R. Puente Santiago, A. Rodriguez, V. Maturano-Rojas, B. Alvarado-Tenorio, R. Bernal and J. C. Noveron, *J. Cleaner Prod.*, 2020, **275**, 124141.

[114] S. Xia, N. Cai, J. Wu, H. Xiao, J. Hu, X. Chen, Y. Chen, H. Yang, X. Wang and H. Chen, *Fuel Process. Technol.*, 2020, **209**, 106543.

[115] K. Suzuki, Y. Saito, N. Okazaki and T. Suzuki, *Sci. Rep.*, 2020, **10**, 12131.

[116] A. S. Kamal, N. H. Jabarullah and R. Othman, *Mater. Today: Proc.*, 2020, **31**, 211–216.

[117] J. He, D. Zhang, Y. Wang, J. Zhang, B. Yang, H. Shi, K. Wang and Y. Wang, *Appl. Surf. Sci.*, 2020, **515**, 146020.

[118] B. S. Purwasasmita, F. Tafwidli and R. Septawendar, *J. Aust. Ceram. Soc.*, 2013, **49**, 119–126.

[119] X. Zhang, K. Zhang, H. Li, Q. Cao, L. Jin and P. Li, *J. Power Sources*, 2017, **344**, 176–184.

[120] M. Sevilla, C. Salinas Martínez-de Lecca, T. Valdés-Solís, E. Morallón and A. B. Fuertes, *Phys. Chem. Chem. Phys.*, 2008, **10**, 1433–1442.

[121] A. Leonhardt, M. Ritschel, D. Elefant, N. Mattern, K. Biedermann, S. Hampel, C. Müller, T. Gemming and B. Buchner, *J. Appl. Phys.*, 2005, **98**, 074315.

---

[122] Z. H. Li, H. Y. Zhang, H. P. Zhu, L. Q. Li and H. Y. Liao, *J. Mater. Sci.*, 2016, **51**, 5676–5684.

[123] K. T. Lee, X. Ji, M. Rault and L. F. Nazar, *Angew. Chem., Int. Ed.*, 2009, **48**, 5661–5665.

[124] J. Song, M. Sun, Q. Chen, J. Wnag, G. Zhang and Z. Xue, *J. Phys. D: Appl. Phys.*, 2004, **37**, 5–9.

[125] Z. M. Sheng, M. H. Hu, Z. Y. Dai, C. Y. Hong, C. K. Chang, Q. Z. Chen and X. J. Chang, *Microporous Mesoporous Mater.*, 2016, **234**, 224–229.

[126] J. N. Wang, L. Zhang, J. J. Niu, F. Yu, Z. M. Sheng, Y. Z. Zhao, H. Chang and C. Pak, *Chem. Mater.*, 2007, **19**, 453–459.

[127] A. O. Baskakov, I. S. Lyubutin, S. S. Starchikov, V. A. Davydov, L. F. Kulikova, T. B. Egorova and V. N. Agafonov, *Inorg. Chem.*, 2018, **57**, 14895–14903.

[128] S. S. Starchikov, V. A. Zayakhanov, A. L. Vasiliev, S. Lyubutin, A. O. Baskakov, Y. A. Nikiforova, K. O. Funtov, M. V. Lyubutina, L. F. Kulikova, V. N. Agafonov and V. A. Davydov, *Carbon*, 2021, **178**, 708–717.

[129] H. Dai, A. G. Rinzler, P. Nikolaev, A. Thess, D. T. Colbert and R. E. Smalley, *Chem. Phys. Lett.*, 1996, **260**, 471-475.

[130] M. A. Ribas, F. Ding, P. B. Balbuena and B. I. Yakobson, *J. Chem. Phys.*, 2009, **131**, 224501.

[131] F. Ding, A. Rosen, E. E. B. Campbell, L. K. L. Falk and K. Bolton, *J. Phys. Chem. B*, 2006, **110**, 7666-7670.

[132] F. Ding, A. Rosen and K. Bolton, *J. Chem. Phys.*, 2004, **121**, 2775–2779.

[133] Z. Yu, D. Chen, B. Tøtdal and A. Holmen, *Catal. Today*, 2005, **100**, 261–267.

[134] S. Hofmann, G. Csanyi, A. C. Ferrari, M. C. Payne and J. Robertson, *Phys. Rev. Lett.*, 2005, **95**, 036101.

---

[135] A. A. Puretzky, D. B. Geohegan, S. Jesse, I. N. Ivanov and G. Eres, *Appl. Phys. A: Mater. Sci. Process.*, 2005, **81**, 223–240.

[136] Y. Wang, B. Li, P. S. Ho, Z. Yao and L. Shi, *Appl. Phys. Lett.*, 2006, **89**, 183113.

[137] Z. He, J.-L. Maurice, A. Gohier, C. S. Lee, D. Pribat and C. S. Cojocaru, *Chem. Mater.*, 2011, **23**, 5379–5387.

[138] T. Ichihashi, M. Ishida, Y. Ochiai and J. Fujita, J. Vac. Sci. *Technol., B: Microelectron. Nanometer Struct.–Process., Meas., Phenom.*, 2004, **22**, 3221–3223.

[139] C. T. Wirth, S. Hofmann and J. Robertson, *Diamond Relat. Mater.*, 2009, **18**, 940–945.

[140] H. Yoshida, S. Takeda, T. Uchiyama, H. Kohno and Y. Homma, *Nano Lett.*, 2008, **8**, 2082—2086.

[141] C. P. Deck and K. Vecchio, *Carbon*, 2006, **44**, 267-275.

[142] R. S. Wagner and W. C. Ellis, *Appl. Phys. Lett.*, 1964, **4**, 89–90.

[143] G. J. Long and H. P. Leighly, *J. Chem. Educ.*, 1982, **59**, 948–953.

[144] O. P. Krivoruchko and V. I. Zaikovskii, *Mendeleev Commun.*, 1998, **3**, 97–99.

[145] A. R. Harutyunyan, T. Tokune and E. Mora, *Appl. Phys. Lett.*, 2005, **87**, 051919.

[146] M. Takagi, *J. Phys. Soc. Jpn.*, 1954, **9**, 359–363.

[147] F. Ding, A. Rosen and K. Bolton, *Carbon*, 2005, **43**, 2215–2217.

[148] F. Ding, K. Bolton and A. Rosen, *Eur. Phys. J. D*, 2005, **34**, 275–277.

[149] F. Ding, A. Rosen, S. Curtarolo and K. Bolton, *Appl. Phys. Lett.*, 2006, **88**, 133110.

[150] D. Schebarchov and S. C. Hendy, *Phys. Rev. B: Condens. Matter Mater. Phys.*, 2011, **84**, 085407.

[151] H. Rietveld, *J. Appl. Crystallogr., 1969,* ***2****, 65-71.*

[152] L. B. McCusker, R. B. Von Dreele, D. E. Cox, D. Louer and P. Scardi, *J. Appl. Crystallogr*, 1999, **32**, 36-50.

---

[153] R. Von, *J. Appl. Crystallogr*, 1997, **30**, 517-525.

[154] M. Thommes, K. Kaneko, A. V. Neimark, J. P. Olivier, F. Rodriguez-Reinoso, J. Rouquerol and K. S. W. Sing, Physisorption of gases, with special reference to the evaluation of surface area and pore size distribution (IUPAC Technical Report), 2015, DOI: 10.1515/pac-2014-1117.

[155] ISO. Determination of the Specific Surface Area of Solids by Gas Adsorption. BET Method. ISO 9277, 2010, pp. 1–24.

[156] ISO. Pore size distribution and porosity of solid materials by mercury porosimetry and gas adsorption – Part 3: Analysis of micropores by gas adsorption. ISO 15901-3, 2007, pp. 1–27.

[157] R. C. Pettersen, in The Chemistry of Solid Wood, ed. R. Rowell, ACS, Washington, 1984, ch. 2, pp. 57–126.

[158] N. Singh, J. Singh, L. Kaur, N. Singh Sodhi and B. Singh Gill, Food Chem., 2003, 81, 219–231.

[159] P. J. Jenkins and A. M. Donald, Carbohydr. Res., 1998, 308, 133–147.

[160] K. Leppanen, S. Andersson, M. Torkkeli, M. Knaapila, N. Kotelnikova and R. Serimaa, Cellulose, 2009, 16, 999–1015.

[161] J. L. Rowlandson, K. J. Edler, M. Tian and V. P. Ting, *ACS Sustainable Chem. Eng.*, 2020, **8**, 2186-2195.

[162] A. Sadezky, A. Muckenhuber, H. Grothe, R. Niessner and U. Pöschl, *Carbon*, 2005, **43**, 1731-1742.

[163] A. C. Ferrari and J. Robertson, *Phys. Rev. B: Condens. Matter Mater. Phys.,* 2000, **61**, 14095-14107.

[164] N. Shimodaira and A. Masui, *J. Appl. Phys.,* 2002, **92**, 902-909.

---

[165] I. Bressler, B. R. Pauw and A. F. Thunemann, *J. Appl. Crystallogr.*, 2015, **48**, 962-969.

[166] ISO. Pore size distribution and porosity of solid materials by mercury porosimetry and gas adsorption – Part 2: Analysis of mesopores and macropores by gas adsorption. ISO 15901-2, 2006, pp. 1-30.

[167] G. Laudisio, R. K. Dash, J. P. Singer, G. Yushin, Y. Gogotsi and J. E. Fischer, *Langmuir*, 2006, **22**, 8945-8950.

[168] Z. Schnepp, A. E. Danks, M. J. Hollamby, B. R. Pauw, C. A. Murray and C. C. Tang, *Chem. Mater.*, 2015, **27**, 5094-5099.

[169] S. Kudo, Z. Zhou, K. Yamasaki, K. Norinaga and J. Hayashi, *Catalysts*, 2013, **3**, 757-773.

[170] W. S. Ratnayake and D. S. Jackson, *J. Agric. Food Chem.*, 2006, **54**, 3712-3716.

[171] C. W. B. Bezerra, L. Zhang, K. Lee, H. Liu, A. L. B. Marques, E. P. Marques, H. Wang and J. Zhang, *Electrochim. Acta,* 2008, **53**, 4937-4951.

[172] S. S. Shah, S. M. A. Nayem, N. Sultana, A. J. S. Ahammad and M. A. Aziz, *ChemSusChem*, 2022, **15**, e202101282.

[173] G. Li, J. Yu, W. Yu, L. Yang, X. Zhang, X. Liu, H. Liu and W. Zhou, *Small*, 2020, **16**, 2001980.

[174] S. Xia, W. Guo, N. Cai, L. Sun, H. Zhou, W. Lu, X. Chen, J. Zhang, Y. Chen, H. Yang, F. Sun, D. Wang, X. Wang, S. Wang and H. Chen, *Fuel Process. Technol.,* 2021, **224**, 107028.

[175] Y. Goto, Y. Nakayasu, H. Abe, Y. Katsuyama, T. Itoh and M. Watanabe, *Phil. Trans. R. Soc. A*, 2021, **379**, 20200348.

[176] L. K. Shrestha, R. G. Shrestha, R. Chaudhary, R. R. Pradhananga, B. M. Tamrakar, T. Shrestha, S. Maji, R. L. Shrestha and K. Ariga, *Nanomaterials,* 2021, **11**, 3175.

---

[177] Y. Tan, X. Wang, S. Song, M. Sun, Y. Xue and G. Yang, *ACS Omega*, 2021, **6**, 24814-24825.

[178] D. Menga, J. L. Low, Y. Li, I. Arcon, B. Koyuturk, F. Wagner, F. Ruiz-Zepeda, M. Gaberscek, B. Paulus and T. P. Fellinger, *J. Am. Chem. Soc.,* 2021, **143**, 18010-18019.

[179] N. Fairley, V. Fernandez, M. Richard-Plouet, C. Guillot-Deudon, J. Walton, E. Smith, D. Flahaut, M. Greiner, M. Biesinger, S. Tougaard, D. Morgan and J. Baltrusaitis, *Applied Surface Science Advances*, 2021, **5**, 100112.

[180] A. Cuesta, P. Dhamelincourt, J. Laureyns, A. Martínez-Alonso and J. M. D. Tascón, *Carbon*, 1994, **32**, 1523-1532.

[181] S. A. Chernyak, A. S. Ivanov, K. I. Maskalov, A. V. Egorov, Z. Shen, S. S. Savilov and V. L. Lunin, *Phys. Chem. Chem. Phys.,* 2017, **19**, 2276-2285.

[182] J. Casanovas, J. M. Ricart, J. Rubio, F. Illas and J. M. Jiménez-Mateos, *J. Am. Chem. Soc.,* 1996, **118**, 8071-8076.

[183] Y. Qiao, S. Chen, Y. Liu, H. Sun, S. Jia, J. Shi, C. M. Pedersen, Y. Wang and X. Hou, *Carbohydr. Polym.*, 2015, **133**, 163-170.

[184] S. Arora, S. Lal, S. Kumar, M. Kumar and M. Kumar, *Arch. Appl. Sci. Res.*, 2011, **3**, 188-201.

[185] M. S. Chambers, D. S. Keeble D. Fletcher, J. A. Hriljac and Z. Schnepp, *Inorg. Chem.*, 2021, **60**, 7062-7069.

[186] C. Giordano, C. Erpen, W. Yap and M. Antonietti, *Nano Lett.*, 2008, **8**, 4659-4663.

[187] S. Bernard, O. Beyssac, K. Benzerara, N. Findling, G. Tzvetkov and G. E. Brown, *Carbon*, 2010, **48**, 2506-2516.

[188] Q. C. Yan, J. H. Li, X. F. Zhang, E. Hassan, C. J. Wang, J. L. Zhang and Z. Y. Cai, *J. Nanopart. Res.*, 2018, **20**, 223.

---

[189] A. Gomez-Martin, Z. Schnepp and J. Ramirez-Rico, *Chem. Mater.,* 2021, **33**, 3087-3097.

[190] P. J. Chupas, K. W. Chapman, C. Kurtz, J. C. Hanson, P. L. Lee and C. P. Grey, *J. Appl. Crystallogr.,* 2008, **41**, 822-824.

[191] C. T. Wirth, B. C. Bayer, A. D. Gamalski, S. Esconjauregui, R. S. Weatherup, C. Ducati, C. Baehtz, J. Robertson and S. Hofmann, *Chem. Mater.,* 2012, **24**, 4633-4640.

[191] S. Xiong, W. Qi, B. Huang, M. Wang, Z. Li and S. Liang, *J. Phys. Chem. C,* 2012, **116**, 237-241.

[192] S. Xiong, W. Qi, B. Huang, M. Wang, Z. Li and S. Liang, *J. Phys. Chem. C,* 2012, **116**, 237-241.

[193] A. S. Shirinyan, A. M. Gusak and M. Wautelet, *Acta Mater.,* 2005, **53**, 5025-5032.

[194] P. Pawlow, *Z. Phys. Chem.,* 1909, **65**, 1-35.

[195] M. Takagi, *J. Phys. Soc. Jpn.,* 1954, **9**, 359-363.

[196] M. Faraday, Experimental researches in chemistry and physics. Taylor & Francis, 1859.

[197] F. Ding, K. Bolton and A. Rosen, *Eur. Phys. J. D,* 2005, **32**, 275-277.

[198] Y. Shibuta and T. Suzuki, *Chem. Phys. Lett.,* 2010, **486**, 137-143.

[199] C. Sikorska and N. Gaston, *J. Comput. Chem.,* 2020, **41**, 1985-2000.

[200] M. S. Daw and M. I. Baskes, *Phys. Rev. Lett.*, 1983, **50**, 1285-1288.

[201] W. C. Swope, H. C. Andersen, P. H. Berens and K. R. Wilson, *J. Chem. Phys.,* 1982, **76**, 637-649.

[202] L. Verlet, *Phys. Rev.*, 1967, **159**, 98.

[203] T. Schneider and E. Stoll, *Phys. Rev. B*, 1978, **17**, 1302-1322.

[204] A. P. Thompson, H. M. Aktulga, R. Berger, D. S. Bolintineanu, W. M. Brown, P. S. Crozier, P. J. in ‘t Veld, A. Kohlmeyer, S. G. Moore, T. D. Nguyen, R. Shan, M. J.

Stevens, J. Tranchida, C. Trott and S. J. Plimpton, *Comput. Phys. Commun.,* 2022, **271**, 108171.

[205] E. Asadi. M. A. Zaeem, S. Nouranian and M. I. Baskes, *Phys. Rev. B,* 2015, **91**, 024105.

[206] L. S. I. Liyanage, S. -G. Kim, J. Houze, S Kim, M. A. Tschopp, M. I. Baskes and M. F. Horstemeyer, *Phys. Rev. B,* 2014, **89**, 094102.

[207] A. Stukowski, *Modell. Simul. Mater. Sci. Eng.,* 2010, **18**, 015012.

[208] S. N. Luo, A. Strachan and D. C. Swift, *J. Chem. Phys.,* 2004, **120**, 11640-11649.

[209] D. Faken and H. Jónsson, *Comp. Mater. Sci.*, 1994, **2**, 279-286.

[210] J. Honeycutt and H. Andersen, *J. Phys. Chem.*, 1987, **91**, 4950-4963.

[211] L. Wu, Y. Zhang, Y. Wen, Z. Zhong and S. Sun, *Chem. Phys. Lett.,* 2011, **502**, 207-210.

[212] F. Ding, K. Bolton and A. Rosen, *J. Vac. Sci. Technol., A*, 2004, **22**, 1471-1476.

[213] S. Curtarolo, N. Awasthi, W. Setyawan, N. Li, A. Jiang, T. Y. Tan, E. Mora, K. Bolton and A. R. Harutyunyan, *Phys. Procedia,* 2010, **6**, 16-26.

[214] S. Sun, H. Zeng, D. B. Robinson, S. Raoux, P. M. Rice, S. X. Wang and G. Li, *J. Am. Chem. Soc.*, 2004, **126**, 273-279.